ALMA MATER STUDIORUM
UNIVERSITÁ DI BOLOGNA

Dottorato di Ricerca in

Chimica

Ciclo XXXIII

Settore Concorsuale: 03/C1 (sec. 03/B1)

Settore Scientifico Disciplinare: CHIM/06 (sec. CHIM/03)

Advanced Functional Organic-Inorganic Hybrid (Nano)Materials: from Theranostics to Organic Electronics and Additive Manufacturing

PRESENTATA DA:

Mirko Maturi

SUPERVISORE

Prof. Mauro Comes Franchini

COORDINATORE DOTTORATO

Prof.ssa Domenica Tonelli

Esame finale anno 2021

SUMMARY

PREFACE

(ABSTRACT)

This work is going to show the activities performed in the frame of my PhD studies at the University of Bologna, under the supervision of Prof. Mauro Comes Franchini, at the Department of Industrial Chemistry "Toso Montanari". The main topic of this dissertation will be the study of organic-inorganic hybrid nanostructures and materials for advanced applications in different fields of materials technology and development such as theranostics, organic electronics and additive manufacturing, also known as 3D printing.
This work is therefore divided into three chapters, that recall the fundamentals of each subject and to recap the state-of-the-art of scientific research around each topic. In each chapter, the published works and preliminary results obtained during my PhD career will be discussed in detail.

1) *Nano-theranostics*

In this first chapter, I describe the synthesis and surface modification of gold nanorods (GNRs) for applications as theranostic agents able to combine the diagnostic properties of photoacoustic imaging applied to near-infrared absorbing plasmonic nanostructures with the therapeutic effects of chemotherapy and photothermal therapy. In a first example (performed in the frame of an EU H2020 project) I show the preparation of chitosan-coated GNRs and their functionalization with active targeting ligands using different conjugation approaches for applications in bladder cancer theranostics. In a second work, lipophilic GNRs together with

a chemotherapeutic drug are encapsulated in polymeric micelles functionalized with cancer-targeting antibodies, with the aim of hepatocellular carcinoma theranostics. Besides, an application of chemometrics based on multivariate analysis is showed on photoacoustic imaging data obtained with PEGylated gold nanorods as contrast agents.

2) Flexible electronics

Not only plasmonic but also ceramic nanoparticles can undergo surface modification reactions to achieve tuneable solubility and better colloidal dispersion. In particular, I present herein how highly piezoelectric tetragonal barium titanate ($BaTiO_3$) nanoparticles could be synthesized with a simple sol-gel approach at relatively low temperature. In a first work, the prepared ceramic nanoparticles are firstly coated with a hydrophilic organic ligand and formulated in piezoionic gels to produce a pressure sensor. In a further work (still in preparation) a synthetic lipophilic ligand is attached to $BaTiO_3$ nanoparticles, allowing for its homogeneous dispersion in PDMS matrices to study the piezoelectric behaviour of the nanocomposites. Finally, I describe the possibility to employ surface stabilized ultrathin gold nanowires (AuNWs) dispersed in low concentration in thin PDMS film as capacitive strain sensors.

3) Additive manufacturing

The combination of organic and inorganic materials can have an impact also in the field of additive manufacturing. In a first work, I describe the synthesis and formulation of a novel and biobased photocurable resin for stereolithography which is functionalized with phosphorescent iridium complexes able to provide efficient light emission even at very low concentrations. Then, I present the preliminary results of the work performed as a visiting graduate student at the Johns Hopkins University in Baltimore (MD, USA), under the supervision of Prof. David Gracias. In this context, I the preliminary results obtained so far towards the development of a 3D printable polysaccharide-based thermoresponsive self-healing hydrogel are presented.

CHAPTER 1

NANO-THERANOSTICS

1.1 Introduction

1.1.1 Nano-theranostics

Theranostics represent the combination of therapeutic and diagnostic properties in a single material, as defined by Funkhouser who coined the term in 2002. [1] Practically, theranostics allows for a single drug to have effects both as contrast agents for imaging applications and as a therapeutic agent able to treat diseases or to deliver pharmaceutical components, mostly in the field of cancer research. [2,3] Such an approach reduces problems of selectivity and biodistribution of separate components, enabling the possibility to use imaging to monitor sick tissues and to follow the therapy kinetics at the same time. [4]

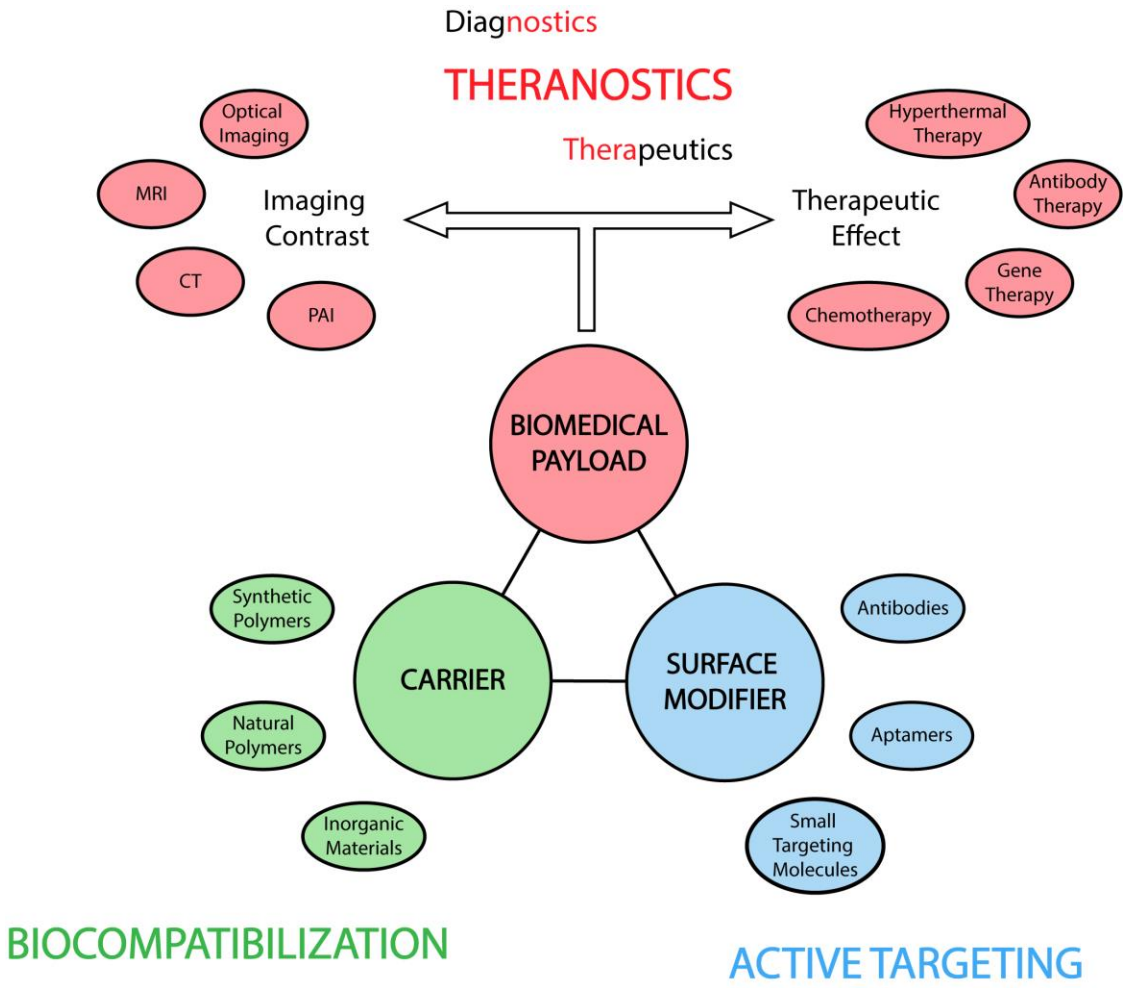

Figure 1.1.1 – Schematic representation of the main components of a theranostic nanoplatform. The biomedical payload gives the actual theranostic properties, but a careful selection of a carrier and an active targeting species is very important when designing new theranostic approaches to cancer treatment.

In the last 20 years, the scientific community rapidly gain interest in nanomaterials as theranostic platforms by their unique contrast and therapeutic properties and their potential to specifically target diseased cells. [5] Nanostructured materials are compatible with different kinds of drugs or display multiple anticancer properties. They can be also loaded with imaging contrast agents, and their accurate formulation allows for the monitoring of the evolution of diseases and to improve the efficacy of carried pharmaceutical components. [6] By adopting the classification given by Ferrari in 2005 [7], a theranostic nanoplatform can be represented as composed of three distinct elements (**Figure 1.1.1**): i) a biomedical payload, including imaging contrast agents and therapeutic agents, ii) a carrier that provides structural protection for the payload during its transportation to the active site and iii) a surface modifier, that provides to the platform additional properties such as prolonged circulation times and active targeting abilities (**Figure 1.1.2**). The most common varieties of each of the three elements of a theranostic platform are going to be discussed in the following paragraphs.

Biomedical payloads

As anticipated before, biological payloads represent the active components for the theranostic platform, the ones that give to the nanomaterial the therapeutic and diagnostic capabilities. The most common biological imaging modalities are:

- Optical imaging: with this technique, visible-light luminescent material is irradiated with UV-VIS light, and the light emitted is collected by a 2D detector that can spatially confine the source of fluorescence and thus the localization of the contrast agent. [8] Organic dyes

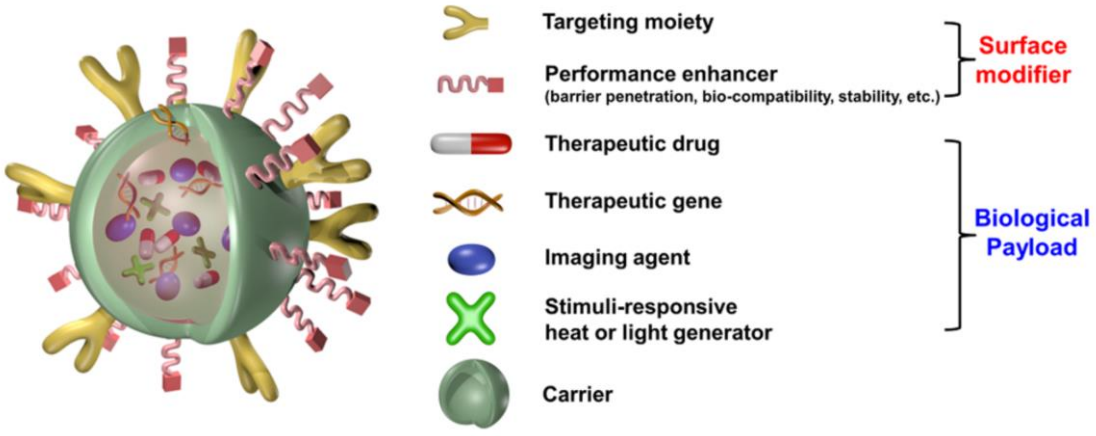

Figure 1.1.2– Different possible components of multifunctional nanocomposites for applications in theranostics. Reproduced from ref. [6]

such as cyanine 5.5 (Cy5.5) and fluorescein isothiocyanate (FITC) have been widely used for the purpose, but they are usually unstable under UV irradiation and toxic in high concentrations. Besides, biological tissues are poorly transparent to UV light, hence confining the applicability of optical imaging mostly to *in vitro* studies on cells.

- Magnetic Resonance Imaging (MRI): the interesting properties of magnetic nanomaterials such as iron-based metal oxides, rare-earth metal oxides, and alloy systems such as FePt have been widely exploited for theranostic applications. [9,10] Most of them offer efficient MRI contrast to be employed for diagnostics; however, the resolution offered by clinically available MRI machines is still quite low.
- Photoacoustic Imaging (PAI): the details of photoacoustic imaging principles and contrast agents will be reported in detail in the next chapters, as it represents one of the most promising high-resolution and non-invasive imaging techniques for the localization of near-infrared (NIR) light-absorbing contrast agents in biological tissues. [11,12] Nanosecond-pulsed NIR light is absorbed by the chromophore, which releases the absorbed energy by thermoelastic expansion generating mechanical waves that can be detected and transduced by an echograph.
- Computed Tomography (CT): as it exploits the X-ray absorbing properties of heavy elements such as gold or iodine. The use of ionizing radiations is still a concern, but the technique is widely implemented in hospitals and clinics. [13,14]

In a published work from our group, we reported a triple-modality imaging probe that was able to efficiently serve as optical imaging contrast in biological tissues thanks to the conjugation of FITC to the surface of silica-coated magnetic nanoparticles. [15] The magnetic core could act as a contrast agent for MRI while chemically conjugated gold nanorods (GNRs) could serve as contrast agents for photoacoustic imaging.

On the other hand, the most outstanding therapeutic functionalities are:

- Chemotherapy: the main difference between cancer cells and a normal cell is defined by the fast and uncontrolled growth that characterize the malignant behaviour of cancer cells. This can be eventually related to the fast synthesis of DNA that characterizes cancer cells. Therefore, chemotherapeutic drugs are designed to stop this process by interfering with the synthesis of DNA, hopefully leading to the inhibition of the growth and the spreading of the disease. Chemotherapeutic drugs can act following two different mechanisms of action: i) by inhibiting the synthesis of new DNA strands during the replication of diseased cells or ii) by stopping the mitosis of cancer cells. [16–18] For each different tumour type, several different chemotherapeutic drugs have been developed to maximize the therapeutic

effect. Amongst these, for example, the most employed drugs such as cisplatin and doxorubicin disrupt the replication of DNA in cancer cells, leading to the formation of nonsense strands that do not allow for the effective replication of cancer cells. However, chemotherapeutic approaches often suffer from a lack of selectivity and thus toxicity to healthy tissues, but these limitations have often been overcome by carefully designing specific carriers able to limit to the tumour site the area of effect of the drug. [19]

- Antibody therapy: antibodies have widely found application in cancer therapy. By exploiting the interaction between the antibody and the receptors on the surface of cancer cells, it is possible to trigger biochemical pathways that usually block some vital functions of the diseased cells. For example, growth factors inhibitors can bind to cancer cell receptors, preventing growth factors to bind to diseased cells promoting cell division and tumour proliferation. [20]
- Gene therapy: it involves the application of nucleic acids as active pharmaceutical ingredients since a therapeutic or working gene copy is transferred into malignant cells to promote the repair of gene defects due to mutations. [21] Amongst these, siRNA (short interfering RNA) represents valuable candidates since they can bind to the RNA-induced silencing complex allowing for gene-specific silencing. [22]
- Hyperthermal therapy: hyperthermia-based approaches involve the heating of diseased tissues to temperatures of about 45°C causing variations in cellular functions by damaging proteins related to cell proliferation. [23] Here, nanoparticles play a distinctive role, since they can locally generate heat by applying different non-damaging stimuli such as low energy electromagnetic radiation. For example, magnetic nanoparticles produce heat when exposed to an oscillating magnetic field (*magnetothermal therapy*) [24] while plasmonic nanoparticles such as gold nanoparticles and gold nanorods increase their local temperature when exposed to visible or NIR laser light [25,26].

Natural and synthetic materials as carriers

Several different organic and inorganic materials have been explored as valuable candidates for acting as carriers for the biological payload through biological tissues to the tumour site (**Figure 1.1.3**). Organic materials are mostly composed of synthetic polymers (PLA, PLGA, …) or biopolymers (chitosan, collagen, …) and they can encapsulate imaging or therapeutic agents by exploiting surface chemical interactions or by physically confining the active ingredient in the lipophilic polymeric core of nanomicelles. On the other hand, porous or hollow inorganic materials (such as mesoporous SiO_2 [27,28] and hollow gold nanostructures

[29–31]) have been studied in details for carrying payloads in biological systems, often suffering from problems related to aggregation and surface destabilization that are much less common when dealing with biocompatible polymers. For example, amphiphilic PLGA-b-PEG nanomicelles have demonstrated to efficiently carry lipophilic gold nanorods and doxorubicin to hepatocellular carcinoma stem cells in living mice, as published by us in 2019 and reported in details in Chapter 1.3 [32,33].

The carrier is then required to display on its surface reactive functional groups that can be further exploited for the surface conjugation of biocompatibilizing species or active targeting agents.

Biomolecular surface modifiers

A surface modification of the nanosystem is generally required to achieve active targeting and thus to direct the theranostic platform to the site of interest. Useful targeting species include antibodies or fragments of them, aptamers, peptides, vitamins, and carbohydrates. [34]

However, active targeting agents can be avoided to exploit passive targeting, enabled by the *enhanced permeability and retention* (EPR) effect, that causes tumour blood vessels to display higher pore sizes, which can be used to achieve passive targeting and the delivery of the theranostic platform to the tumour site. [35,36]

Finally, surface modification with polysaccharides allows for additional interactions with the active site, since they can widely interact with molecules found on the surface of cancer cells. [37,38]

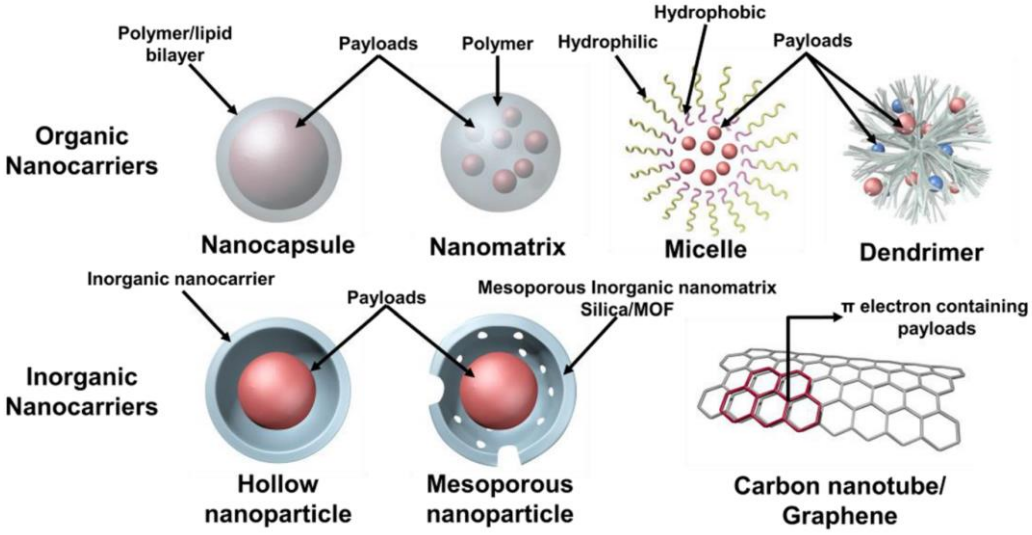

Figure 1.1.3 – Organic vs. inorganic carriers for theranostic applications. Reproduced from ref. [6]

1.1.2 Photoacoustic Effect and Photoacoustic Imaging

The photoacoustic effect (or optoacoustic effect) has been discovered in 1880 by Alexander Graham Bell, while he was experimenting with long-distance sound transmission. He spent several years trying to build a device he called "photophone", able to use reflected sunlight from a mirror to a selenium solar cell receiver for transmitting voice signals.[39] While studying how to build such a device, he observed that when a solid sample was exposed to a chopped (or pulsed) light beam, sound waves were directly produced by the bulk sample. The observed acoustic signal was noticed to be dependent on the sample material, suggesting the involvement of light absorption processes which subsequently heat the sample generating a piston-like pressure wave in the surrounding gas. A few months later, Bell found out that sound could also be generated by materials exposed to ultraviolet (UV) or near-infrared (NIR) light: he invented a second device he called "spectrophone", able to apply the photoacoustic effect for spectral characterization of light-absorbing compounds.[40] Bell, Tyndall, and Röntgen expanded independently the study to liquids and solids, but ear detection of emitted sound waves strongly limited the possibility of investigation of such phenomena: the application of the photoacoustic effect in chemistry needed to wait for the development of more powerful light sources and more sensitive sound detectors.[40–42] Different mechanisms have been developed in order to explain the generation of acoustic waves upon light absorption. The most diffused and accepted one involves *thermoelastic expansion* phenomena: light absorbed by the responsive material causes a sudden heating of the photoabsorber generating sound waves that propagate in the surrounding medium.[43] According to this mechanism, photons are absorbed by the material, their energy (or part of it) being converted to heat energy by collision of the high energy excited molecules with the surrounding environment. Then, the temperature increases drastically a few picoseconds after the absorption of the photon, but it plummets back to the initial temperature when the light is stopped and the system cools down. These oscillations result in alternated expansions and contractions of the system due to temperature variation: this induces local pressure changes that propagates throughout the sample and can be sensed with an appropriate sound-to-voltage transducer. On the basis of this model, the photoacoustic effect can be exploited to build photoacoustic spectrometers equipped with sound-responding detectors: these instruments are able to generate photoacoustic response spectra similar to extinction spectra, but rather than measuring the amount of absorbed light *per wavelength*, the intensity of the emitted acoustic wave is measured for each excitation wavelength. Photoacoustic

spectrometry allows also for the investigation of spectroscopic behaviour of opaque samples, where absorption is essentially complete.[44]

The ability of photoacoustic detection to be performed on non-transparent samples makes it possible to exploit it for spectral characterization of biologic tissues, for which the traditional optical spectroscopic tools cannot be generally applied. However, these applications have been generally exploited in the indirect gas-phase photoacoustic detection for many years, it was not until the mid-1990s that it began to be investigated for biomedical imaging. From this point onwards, the field of optoacoustics has rapidly grown in terms of the development of instrumentation, image processing algorithms, *in vivo* application of the technique in clinical medicine, and basic biologic research.[45] In *photoacoustic imaging* (PAI), ultrasound waves are generated by irradiating tissues with modulated or pulsed laser light; for applications in biology and biomedicine, optical wavelengths in the near-infrared (NIR, 700 – 1500 nm) are applied due to the high transparency of tissues in this range, achieving penetration depths up to several centimetres. Absorption of photons by the chromophores in the sample results in the generation of an acoustic wave, which is then processed to form an image. Thanks to acoustic detection, it has been possible to couple PAI to ultrasound (US) echographic systems: ultrasounds (in a different range of frequency from that involving photoacoustic effect) are directed to the sample together with the laser, scattered and diffused in the tissues and detected back by a separated US detector.[46] Although PA and US image formation and the factors that affect spatial resolution and fidelity are mostly the same, the contrasts that generate the images are essentially different. A US image provides a description of the *acoustic impedance mismatch* between different tissues: US contrast, therefore, depends on morphological features of the tissues, whilst PA represents the initial pressure distribution produced by the absorption of a pulse of laser light. With this configuration, it is possible to obtain two overlapped images: an explorative US trace and a PA contrast image, to make easier localization of the contrast into the sample. The "emitted" ultrasound can be approximated to a 1D plane wave, which propagates in a homogeneous medium, generated by absorption in a chromophore (**Equation 1.1.1**).

$$P_0 = \frac{\beta v_s^2}{c_p} \mu_a F_0 e^{-\mu_{eff} z} = \Gamma \mu_a F_0 e^{-\mu_{eff} z} \qquad \textbf{Equation 1.1.1}$$

Where P_0 is the maximum pressure generated by thermoelastic expansion of the chromophore, β is the thermal expansion coefficient, μ_a is the optical absorption coefficient of the photoabsorber and F_0 is the laser fluence at $z = 0$. Γ is defined as the Grüneisen

parameter of the tissue and μ_{eff} is the effective extinction coefficient, which contains μ_a but it also includes scattering phenomena.

Thanks to its massive potential, PAI has been developed in several different implementations. Some of them allow for high resolution at the expense of penetration depth (like dark-field confocal photoacoustic microscopy) for applications in cells and enabling live-cells experiments. Others (like photoacoustic tomography), achieve high penetration depth with low resolution but effective for tumour detection. Currently, the three major applications of PAI in biomedicine are engineered and optimized for different specific applications (**Figure 1.1.4**): photoacoustic microscopy (PAM), photoacoustic computed tomography (PACT), and photoacoustic endoscopy (PAE).[47]

Photoacoustic Microscopy, PAM

In PAM, both optical excitation and ultrasonic detection are focused, with the two foci usually confocally configured to maximize sensitivity. Each laser pulse produces a depth-resolved image without mechanical scanning, a 2D transverse scanning generates a 3D image. Depending on which focus is finer, optical or acoustic, PAM is classified into *optical-resolution PAM* (OR-PAM) and *acoustic-resolution PAM* (AR-PAM). OR-PAM provides images with resolutions as low as few micrometres but with much smaller penetration depths, while AR-PAM takes advantage of the reduced acoustic scattering at depths beyond the optical diffusion limit to produce images with high resolution.

Photoacoustic Endoscopy, PAE

In a representative PAE design, light from a nanosecond pulsed laser is delivered by a multimodal optical fibre in the central hole of a ring transducer. An optoacoustically reflective mirror rotates both light and sound waves for circumferential cross-sectional scanning, generating the image. In contrast to conventional optical endoscopy, which has an imaging depth within the optical diffusion limit, PAE exhibits a 7-mm imaging depth *ex-vivo* in the rat colon dorsal region.[48]

Photoacoustic Computed Tomography, PACT

In PACT, a large diameter pulsed laser beam irradiates the tissue surface causing impulsive heating of the absorbing chromophores that generates a broadband ultrasonic wave that propagates throughout the tissue and is detected by an array of receivers. Two detection geometries are commonly used: linear and circular (**Figure 1.1.4c-d**). Circular detection geometry requires access to the target from all directions, while linear geometry is more versatile, giving access to a great range of anatomical targets. PAI instruments that employ

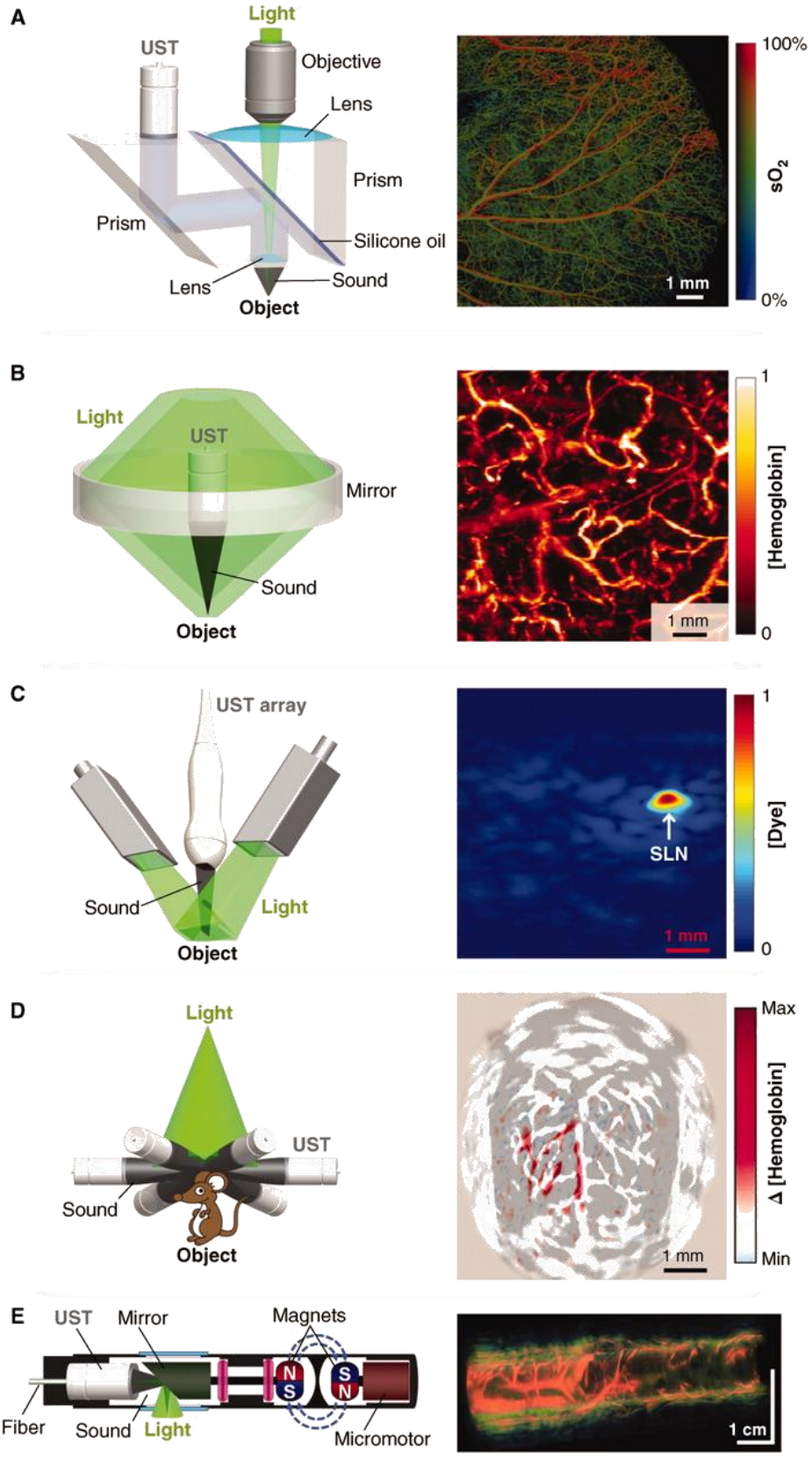

Figure 1.1.4 - Major implementations of PAI, with representative *in-vivo* images. (A) OR-PAM of sO_2 in a mouse ear, (B) AR-PAM on normalized haemoglobin concentration in a human palm, (C) Linear – array PACT of methylene blue in rat sentinel lymph node (SLN), (D) Circular-array PACT for cerebral hemodynamic changes, (E) PAE of rabbit oesophagus, UST = ultrasound transducer.[49]

linear detection geometry started to resemble common diagnostic clinical US scanners, including a hand-held probe acoustically coupled to the skin and moved around giving images in real-time. The absorption-based contrast provided by the PA signal is then coupled to a co-registered US map of the sample. However, the limited detection aperture of the probe reduces the resolution of the obtained image compared to the resolutions achievable with circular arrays of detectors. The vertical resolution, on the other hand, does not depend much on the detection aperture but it is strongly limited by acoustic attenuation. A specific apparatus, which is commercially available, contains a diagnostic linear array probe and a pair of fibre wisps are integrated to form a hand-held dual-mode US-PA imaging head. As one of the most promising implementations, the VisualSonics small-animal US scanner has been adapted to provide US-PA images in currently available instruments. For circular detection, the instrument usually includes a hemispherical detector bowl with an aperture in the bottom for the delivery of laser light. 128 unfocused 5 MHz 3-mm diameter piezoelectric elements are spirally distributed over the hemisphere.

1.1.3 Multivariate Spectral Imaging Analysis [50–52]

Photoacoustic imaging implementations often allow for the recording of a photoacoustic signal per each excitation wavelength: if the detector is able to spot a region of the sample of size ($x \times y$) pixels, it would record an image for each available excitation wavelength generating a 3D matrix ($x \times y \times \lambda$) where λ is the number of scanned wavelengths. Practically, this matrix is called *hyperspectral cube* (or *hypercube*), and it is composed of images in which for every pixel the entire photoacoustic emission spectrum is recorded (**Figure 1.1.5**); the approach of recording spectra per pixel in 3D matrices, defined as *hyperspectral imaging*, enables the use of powerful statistical tools to discriminate whether the signal is originated from one species or one other, to make quantitative analysis and to reduce the signal-to-noise ratio. [53] Each image represents the regions of the sample in which the corresponding wavelength has a big influence on the total spectrum. The hypercube ($x \times y \times \lambda$) is firstly unfolded to a 2D data matrix ($\boldsymbol{D}$) of size ($(x \times y) \times \lambda$) in which the rows are spectra of the different pixels. A bilinear model is used to fit the data, producing three matrices, **C** and $\mathbf{S}^{\mathbf{T}}$ and **E**, expressed in **Equation 1.1.2**.

$$\boldsymbol{D} = \boldsymbol{C}\,\boldsymbol{S}^{\boldsymbol{T}} + \boldsymbol{E} \qquad \textbf{Equation 1.1.2}$$

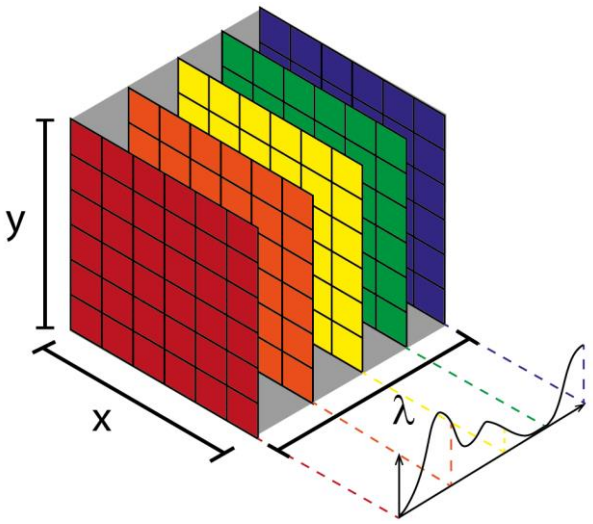

Figure 1.1.5 – Schematic representation of a hypercube. Two dimensions represent the x-y position of the spotted point (spatial information), the third dimension represents the excitation wavelength (spectral information). Each vertical slice of the cube is an image, while each pixel is a spectrum in the third dimension.

$\boldsymbol{C}$ is the obtained *concentration matrix* of size $((x \times y) \times q)$ which, once refolded, contains one image for each component q in the spectroscopic system representing the concentration profile of that component; $\boldsymbol{S^T}$, the *spectra matrix* has the size of $(q \times \lambda)$ and it carries the corresponding spectra of the spotted components while $\boldsymbol{E}$, the *error matrix* which contains the deviation of the model from the experimental data, is minimized by an iterative least-square algorithm which uses various constraints, to reduce ambiguity (**Figure 1.1.6**). It should be noticed that **Equation 1.1.2** is nothing but the multiwavelength expression of the Beer-Lambert law. The algorithm solves iteratively the equation by optimally fitting $\boldsymbol{C}$ and $\boldsymbol{S^T}$ by the alternating least-squares algorithm, using initial estimates of the spectral profiles of the mixture components. [54] These inputs can be spectra obtained from reference experiments or can be extracted from the original data set by evolving factor analysis. [55] During the optimization process, several constraints can be applied to model the shapes of the obtained profiles and to limit the number of possible equivalent solutions for the matrix problem. The result is formulated when convergence is achieved in two consecutive iterative cycles, with deviations of the residuals between experimental and ALS data is less than 0.05%.

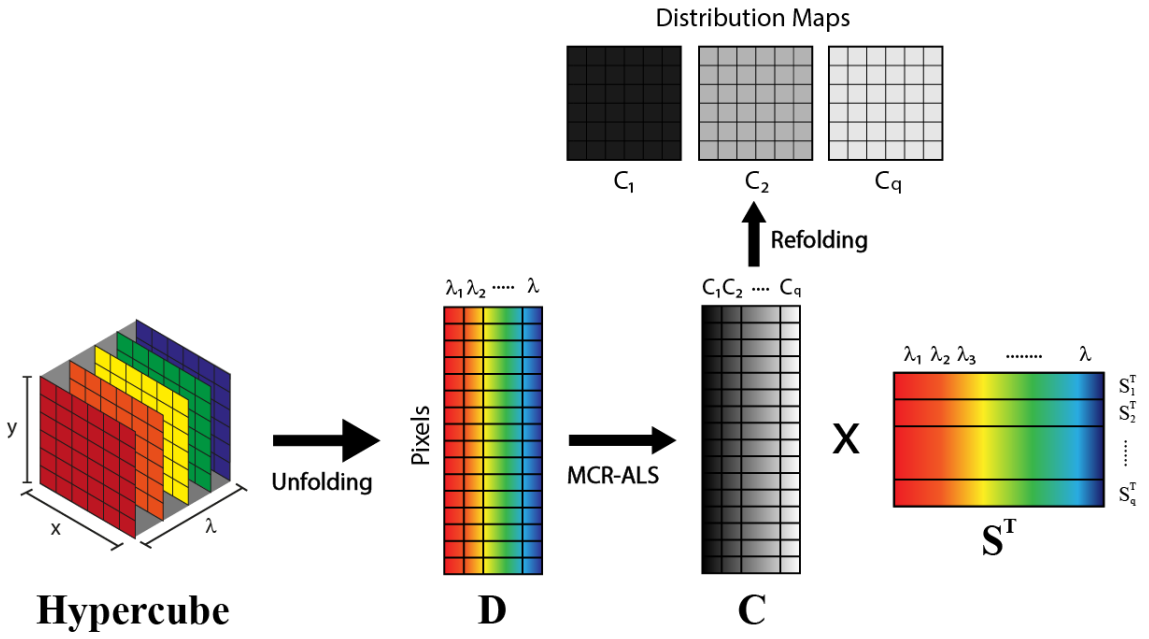

Figure 1.1.6 – Schematic representation of the action of MCR-ALS on hyperspectral data. The hypercube is firstly unfolded, then the algorithm is applied. It generates a matrix $\boldsymbol{C}$ which represents, once refolded, the distribution maps of each of the modelled components, and a matrix $\boldsymbol{S^T}$ containing the fitted spectrum for each modelled component.

Figures of merit

Three parameters are important in the evaluation of the efficacy of the optimization algorithm: per cent of lack of fit, the amount of variance explained by the model, and the standard deviation of residuals with respect to the experimental data. The first, defined in **Equation 1.1.3**, represents the difference between the input data ($\boldsymbol{D}$) and the ones obtained by the model ($\boldsymbol{CS^T}$).

$$Lack\ of\ fit\ (\%) = \sqrt{\frac{\sum_{i,j} e_{i,j}^2}{\sum_{i,j} d_{i,j}^2}} \cdot 100 \qquad \textbf{Equation 1.1.3}$$

where $d_{i,j}$ indicates the element of $\boldsymbol{D}$ (i^{th} row and j^{th} column) and $e_{i,j}$ is referred to matrix elements of $\boldsymbol{E}$. The software calculates two lacks of fit based on the initial definition of the input matrix $\boldsymbol{D}$. It can be calculated with respect to the raw experimental data matrix or the PCA reproduced data matrix, using the same number of components as MCR-ALS. These two figures of merit are evaluated after each iterative cycle, after the application of the selected constraints. These values are really important, they explain how good the experimental data have been fitted and if ALS optimization approaches PCA fit. Percentage of variance explained (R^2) and the standard deviation of residuals (σ) are calculated as shown in **Equation 1.1.4** and **Equation 1.1.5**, respectively:

$$R^2 = \frac{\sum_{i,j} d_{i,j}^2 - \sum_{i,j} e_{i,j}^2}{\sum_{i,j} d_{i,j}^2} \qquad \textbf{Equation 1.1.4}$$

$$\sigma = \sqrt{\frac{\sum_{i,j} e_{i,j}^2}{n_{rows} n_{columns}}} \qquad \textbf{Equation 1.1.5}$$

where $d_{i,j}$ and $e_{i,j}$ are the same as above, while n_{rows} and $n_{columns}$ are the number of rows and columns, respectively, for matrix $\boldsymbol{D}$.

Data augmentation

MCR-ALS can be simultaneously performed on multiple independent data sets that have been acquired with the same spectroscopic technique. This approach can achieve better species resolutions, particularly in situations of rank-deficiency. However, this can massively increase the computing time required for PCA in imaging studies, where each independent hypercube contains several hundred thousand spectra.

Constraints [50]

While performing MCR-ALS, the toolbox requires to specify which constraints should be applied to the fitting model (**Figure 1.1.7**). In hyperspectral imaging, the most applied are:

- *Non-negativity*. It can be applied to both concentrations and spectra. It forces to zero (or normalizes) the obtained matrices in order to be non-negative everywhere.
- *Closure.* By applying this constraint, the total concentration (the sum of the concentrations of each component) is constant throughout all the samples, acting as a mass balance of the system.
- *Unimodality*. Applied to the concentration profiles, allows for the existence of only one or no local maxima.
- *Hard modelling*. Concentration data are modelled according to rigid models built from mathematical expressions describing a specific physicochemical behaviour.

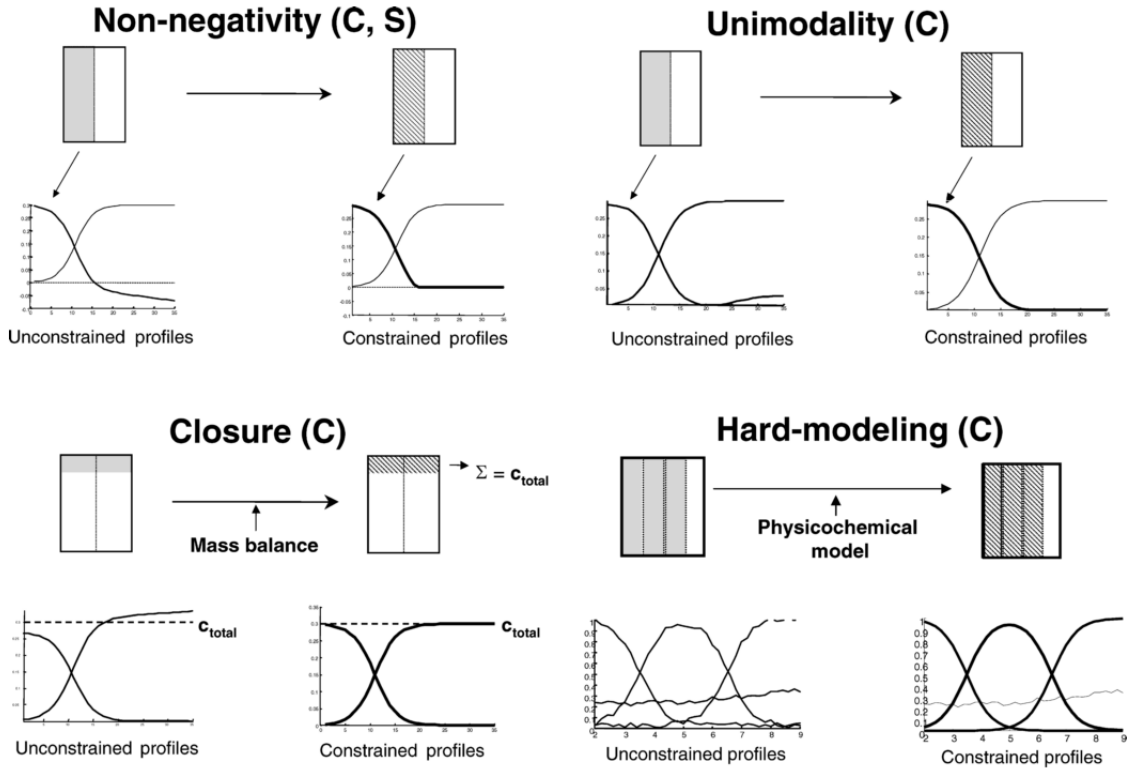

Figure 1.1.7 – Commonly employed constraints for MCR-ALS. Reproduced from ref. [50]

1.1.4 Contrast Agents in Preclinical Photoacoustic Imaging [12]

Photoacoustic Imaging (PAI) is growing quickly as a molecular imaging technique, being rapidly adopted for a wide range of applications in preclinical *in vivo* imaging of small animals. Its principal applications are directed towards cancer research, where PAI can be exploited for primary tumour identification, molecular characterization, and detection of metastatic lymph nodes. [56] The photoacoustic signal can be originated by both endogenous and exogenous sources in a living system usually the latter being the one investigated by research and development, while the former generates the background that needs to be overwhelmed by the much more intense and specific exogenous contrast.

Endogenous contrast

Endogenous PAI allows for retrieving structural and functional information of light absorption-based systems, such as haemoglobin, lipids, water, and melanin (**Figure 1.1.8**). Haemoglobin is an iron-based metalloprotein responsible for the delivery of molecular oxygen throughout the body: it undergoes structural and electronic modifications upon O_2 binding, which result in a modification of its absorption spectrum. This makes it possible to measure total haemoglobin concentration and oxygen saturation, which are helpful information for the

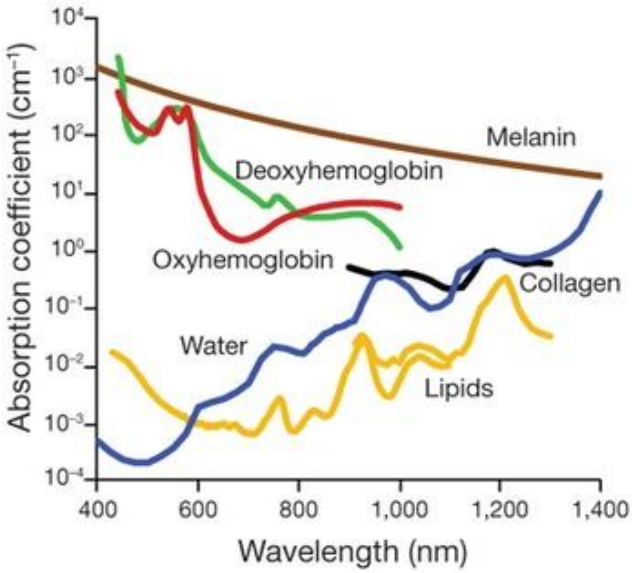

Figure 1.1.8 - Absorption spectra of the main endogenous chromophores. At long wavelengths, the contribution of oxy- and deoxy-haemoglobin is negligible but the interference of water and fat is increasing. Melanin covers the whole spectral range, strongly reducing the optical penetration depth in melanin-rich regions. Reproduced from ref. [57]

study of tumour angiogenesis.[58] It is also worthwhile to exploit the absorption behaviour of lipids at long wavelengths (930 and 1210 nm), related to the second overtone of the C-H stretching which is abundant in fatty acid chains.[59] Water can be identified by excitation at 975 nm, whereas melanin absorption allows for the detection and characterization of primary melanoma and metastatic melanoma cells.[60] Anyways, intrinsic chromophores only give access to a limited number of applications in biological processes. In molecular PAI these absorptions represent the background that must be overcome by designing efficient contrast agents able to highlight specific features of the investigated biological system.

Exogenous contrast

The ideal exogenous signalling structure has to own a very intense, narrow, and characteristic absorption behaviour (in terms of absorption wavelengths), to allow for unambiguous contrast even at low molar concentrations. Moreover, its absorption must be located in the NIR window of the electromagnetic spectrum, to ensure high tissue penetration, but avoiding the wavelength ranges in which the endogenous chromophores have their absorption maxima. This limits the exploitable NIR energy range to wavelengths higher than 800 nm, for the purpose of avoiding interferences with the intense signal originated from the two forms of haemoglobin. Moreover, it is required that the light-absorbing system shows high photostability (it needs to be stable under prolonged light irradiation), low fluorescence quantum yield (to maximize the amount of absorbed energy converted to heat), and efficient conversion of energy to acoustic waves.

Metallic or semiconducting nanoparticles are characterized by high flexibility from the chemical, physical, and biological point of view, together with very high extinction coefficients compared with the ones of NIR dyes. They are nowadays the widest class of PAI contrast agents and they can be made of a great variety of materials, shapes, and sizes, with tuneable surface and optical properties. They are mainly represented by gold and carbon nanosystems, able to absorb NIR light and to convert it into acoustic waves.

1.1.5 Optical Properties of Gold Nanostructures

Nanostructured metals have shown interesting optical, electronic, and catalytic behaviours, when compared to their bulk counterparts, since the early 5th century BC. Gold, platinum, and silver, when finely ground into nanocrystals, are able to be dispersed in aqueous media showing characteristic and very intense colours: gold nanocrystals, for example, show a strong absorption band in the blue which moves towards the red as the size of the crystals increases. Furthermore, when the size is reduced below 3 nm, the incredibly high surface-to-volume ratio makes the gold lose the inertness that made it be called "noble metal", and it acts as a catalyst for reactions on its surface. These chemical and optical features arise from the fact that the particles are so small that they mostly behave as quantic systems with well-defined energy levels, whose gaps correspond to the wavelengths of the visible light. Let's consider a spherical gold nanoparticle of radius r irradiated by z-polarized light of wavelength λ. If the dimension of the particle is much smaller than the wavelength of light, i.e. $\lambda/r > 10$, the electric field appears to be static to the nanoparticle (**Figure 1.1.9**). Because of this phenomenon, Maxwell's equations can be solved using a quasi-static approximation, leading to the final expression for the intensity of the electromagnetic field outside the particle, E_{out}, given in **Equation 1.1.6**.

$$E_{out}(x,y,z) = E_0\hat{\boldsymbol{z}} - \left[\frac{\varepsilon_{in}-\varepsilon_{out}}{\varepsilon_{in}+2\varepsilon_{out}}\right] r^3 E_0 \left[\frac{\hat{\boldsymbol{z}}}{r^3} - \frac{3z}{r^5}(x\hat{\boldsymbol{x}} + y\hat{\boldsymbol{y}} + z\hat{\boldsymbol{z}})\right] \qquad \textbf{Equation 1.1.6}$$

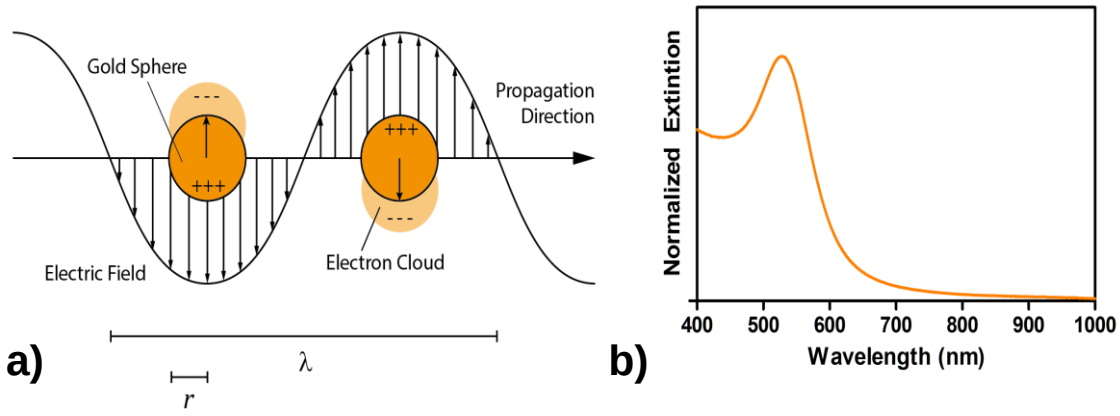

Figure 1.1.9 - (a) Schematic representation of the localized surface plasmon resonance phenomenon and (b) the typical extinction spectrum for AuNPs.

Where ε_{in} is the electric permittivity of the nanoparticle and ε_{out} is the one of the dispersant medium. ε_{in} is strongly dependent on the wavelength of the incoming radiation: the term containing permittivity mostly determines the resonance condition, that is the resonant wavelength, which clearly depends on the material. For gold and silver, this is accomplished in the visible region of the electromagnetic spectrum, explaining the differences in optoelectronic properties compared to the bulk material. Also, the size of the particle and the permittivity of the solvent (r e ε_{out}) contribute to the LSPR position, making it possible to tune the macroscopic optical properties along the visible spectrum. It is possible, then, to derive an expression for the extinction spectrum of a metal nanosphere as a function of its size and dielectric constant, together with the one of the dispersant medium (**Equation 1.1.7**):

$$E(\lambda) = \frac{24\pi^2 N a^3 \varepsilon_{out}^{3/2}}{\lambda \ln(10)} \frac{\varepsilon_i(\lambda)}{(\varepsilon_r(\lambda)+\chi\varepsilon_{out})^2+\varepsilon_i(\lambda)^2} \qquad \textbf{Equation 1.1.7}$$

Where $\varepsilon_r$and ε_i are real and imaginary parts of the electric permittivity, respectively. χ is a constant that depends on the shape of the particle: for a sphere $\chi = 2$, but it can reach much higher values (up to $\chi = 20$) for particles with elongated geometry like ellipsoids or rods. In 1912, Gans calculated the χ value for an ellipsoid, predicting that for metallic nanorods, in a good approximation, the LSPR band would split into two distinct bands, due to the anisotropy of the structure (**Figure 1.1.10** and **Equation 1.1.8**).[61] An analytical solution cannot be obtained for the actual shape of synthesizable nanorods, which is more likely to be a doubly half-sphere-capped cylinders than actual ellipsoids.

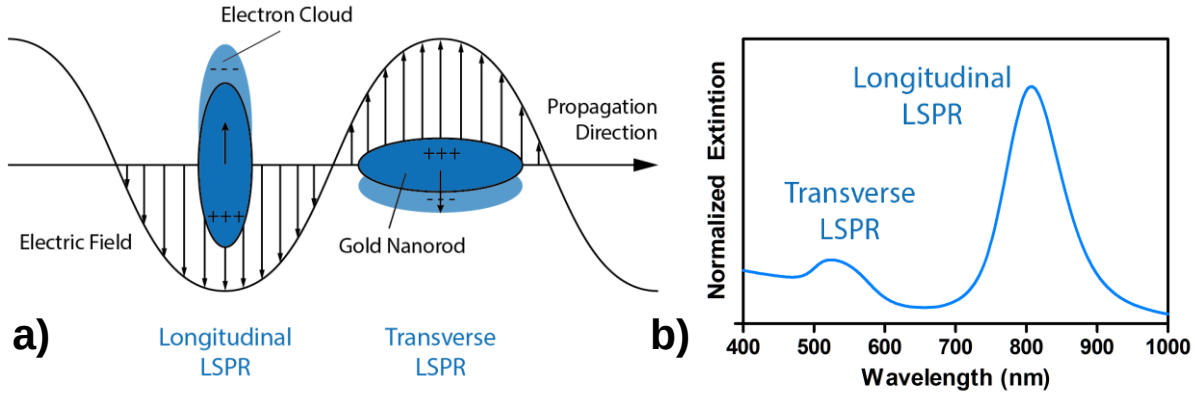

Figure 1.1.10- (a) Schematic representation of the localized surface plasmon resonance phenomenon for a metallic rod and (b) the typical extinction spectrum for GNRs

$$E(\lambda) = \frac{2\pi V N \varepsilon_{out}^{3/2}}{3\lambda} \sum_j \frac{\varepsilon_i (1/P_j^2)}{(\varepsilon_r + ((1/P_j)/P_j)\varepsilon_{out})^2 + \varepsilon_i^2}$$ **Equation 1.1.8**

Where V is the volume of the particle. P_j, is defined as the *depolarization factor*; it can assume two different values: one related to the length and one to the width of the rod. One of the two – the *longitudinal* one – is a function of the *ellipticity* of the particle, e, a geometrical parameter strictly related to the *aspect ratio* of the rod, AR, defined as the ratio between its length and width (**Equation 1.1.9**).

$$e^2 = 1 - \frac{1}{AR^2}$$ **Equation 1.1.9**

Many years later, in 2005, Murphy et al. verified these equations by measuring the position of the longitudinal LSPR peak for different preparations of gold nanorods (GNRs) with different aspect ratios.[62] They showed how the low energy band was moving towards the NIR by increasing the rod's aspect ratio, quite confirming Gans's predictions and revealing the applicability of the ellipsoid approximation to GNRs (**Figure 1.1.11**). LSPR greater than 800 nm, well suitable for PAI, has been obtained for GNRs with an aspect ratio of around 4. As it is shown in **Equation 1.1.8**, not only the shape of the particle influences the longitudinal LSPR position: the dependence on ε_{out} conceal a variation of the peaks position in relation with the dielectric constant of the surrounding medium. This it is strictly connected to the

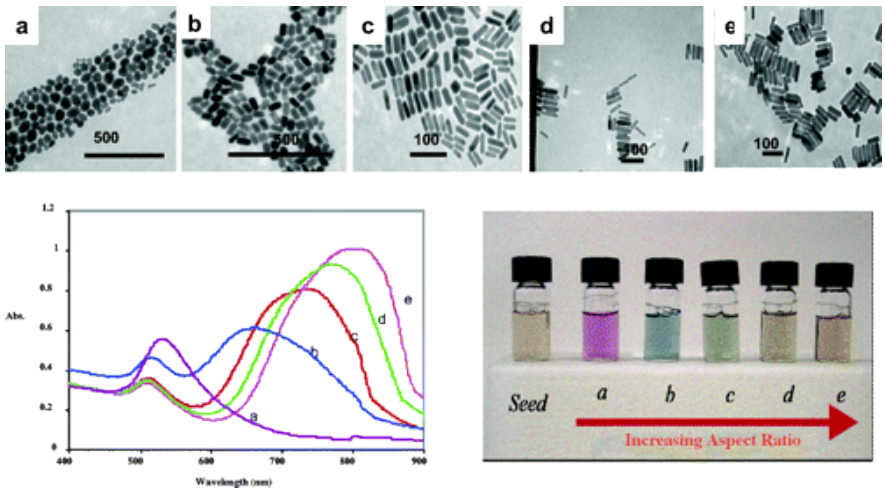

Figure 1.1.11 - Transmission electron micrographs (top), optical spectra (left), and photographs of (right) aqueous solutions of gold nanorods of various aspect ratios. a) aspect ratio 1.35; b) aspect ratio 1.95; c) aspect ratio 3.06; d) aspect ratio 3.50; e) aspect ratio 4.42 [62]

refractive index (being $\varepsilon = n^2$), therefore changes in the local environment, which modifies how fast light, travels in the proximity of the particle (like molecules adsorbed on its surface) cause a shift in the absorption maximum, following **Equation 1.1.10**.

$$\Delta\lambda_{max} = m\Delta n[1 - \exp(-2d/l_d)] \qquad \textbf{Equation 1.1.10}$$

Where m is the sensitivity upon refraction index variation; Δn is the variation in refractive index induced by the adsorbate; d is the adsorbate layer thickness and l_d is the penetration depth of the electromagnetic field, characteristic for the material (for gold it is of the order of few nanometers). It has moreover been observed that the actual refractive index felt by the nanostructure in water is slightly higher than the one of pure water: El-Sayed and co-workers propose that this is originated from the fact that the water layer around the rod is polarized by the plasmon and therefore it substantially shows higher refractive index than pure water.[63]

1.1.6 Synthesis of Gold Nanorods

The first reported procedure for growing colloidal gold dates back to 1857 when Michael Faraday found that gold chloride could be reduced by phosphorus forming a ruby suspension of gold nanoparticles.[64] Since then, a great number of methods have been developed for the fabrication of gold nanocrystals: chemical, electrochemical or photochemical reduction and different physical methods. These allow for the production of nanostructures with various architectures: nanospheres, nanorods, nanoplates, nanocubes, nanoshells and anisotropic nanostructures with protrusions can be obtained. For gold nanorods (GNRs) there are mainly two synthesis approaches, which are defined as *bottom-up* and *top-down*: the bottom-up approach is based on the nucleation and growth of the rods from salt precursors, while in the top-down one GNRs are obtained by a combination of Au deposition with different physical lithographic processes.

Bottom-up methods

In these methods, aqueous solvated Au(III) salts are reduced by various reducing agents (like citric acid, ascorbic acid, sodium borohydride, or small Au clusters) under different external stimuli. In order to break the anisotropy of the system to form a rod-like particle, a template is needed to confine the growth of the rod along one direction only during the reduction: the most widely used *hard template* for synthesis of one-dimensional nanostructures is anodic aluminium oxide, which displays randomly oriented cylindrical pores with high density and controllable size.[65] Although this approach leads to monodisperse nanorods with high yield, it needs complex techniques to release the nanorods from the alumina template for further applications. Besides, the rods have a very large diameter (> 100 nm), which abates their optical properties due to retardation of the plasmon wave. A second approach has been developed to overcome the problems with the hard-templating methods: the use of surfactants that are able to form micelles to direct the longitudinal growth of GNRs in solution. These surfactants are also known as *soft templates*; amongst them, the most commonly used is CTAB (cetyltrimethylammonium bromide) which acts both as a stabilizer for the growing rods and as a face-specific capping agent allowing for anisotropic growth of gold in solution. The most promising method which applies the use of soft templates in the seed-mediated growth approach, developed independently by Murphy and El-Sayed in the early 2000s.[62,66] In a typical procedure, small Au seeds of around 3.5 nm in size are prepared by reduction of diluted Au(III)-Br complexes in CTAB aqueous solution with a strong reducing agent such as $NaBH_4$. An aliquot of this solution is then added into a growth solution prepared

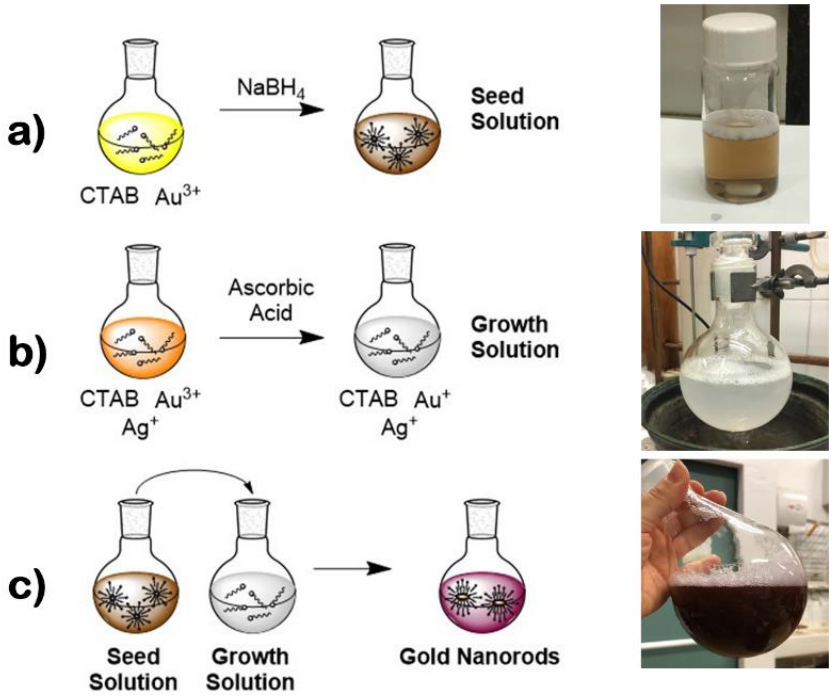

Figure 1.1.12 - Schematic representation of the main steps in the seed-mediated growth of GNRs

by reduction of Au(III) complex ions to Au(I) with ascorbic acid or other mild reducing agents in an aqueous CTAB solution (**Figure 1.1.12**). The added seeds catalyze the disproportion of Au(I) to metal gold and Au(III), the first adsorbed onto their surface, resulting in the growth of the seed to a rod. Au(III) is then converted back to Au(I) by the unreacted ascorbic acid in solution, generating a cycle that is stopped only when gold ions or ascorbic acid molecules are depleted. Silver ions play an important role in the improvement of shape selectivity (lesser production of other shapes like cubes or spheres) and reaction yield. Moreover, the presence of Ag^+ allows for fine control of the optical properties due to its influence on the aspect ratio of the rod. While the role of silver in the anisotropic growth is not clearly understood yet, two mechanisms have been proposed for explaining the symmetry breaking phenomenon. El Sayed proposed a first mechanism by which the surfactant forms a soft-templating micelle formed by a double layer of CTAB molecules, with a size that depends on CTAB concentration and ionic strength of the solution.[66] When ascorbic acid is added to the growth solution gold ions are reduced, but since silver can be reduced by ascorbic acid only at basic pH values, it is not reduced here; silver ions are located between neighbouring head groups of the templating surfactant (CTAB) generating Ag-Br pairs, decreasing charge density on the bromine atoms and thus reducing repulsion forces between CTAB head-groups,

leading to micelle elongation. This is supported by the strong affinity of CTAB for the high-energy {100} side facets compared to the low energy {111} end facets of the growing Au crystal. The second mechanism involves a rigid structure of CTAB monomers that maintains a one-dimensional shape and serves to control the reduction rate of Au(I). Silver ions will not be reduced by ascorbic acid but will rather form solid silver bromide. Murphy proposed a model in which silver bromide is absorbed on the {100} side facets of the nanocrystal surface, slowing down gold reduction on the sides and inducing single-crystalline growth along the{111} end facets (**Figure 1.1.13**).[62] In any case, the effects of the amount of silver ions in the growth solution allow for regulation of the longitudinal LSPR band from 650 nm to 850 nm. Longer GNRs (with aspect ratio > 5) can be obtained by adding a second surfactant, BDAC (benzyl cetyl dimethylammonium chloride). BDA^+ ions intercalate CTAB in the anisotropic growth, stabilizing higher aspect ratio micelles by π-stacking of the intercalating benzyl groups.[66] With this approach, it is possible to synthesize GNRs with plasmon absorption wavelengths up to 1400 nm. The bottom-up methods can allow for the production of nearly monodisperse GNRs with small diameter and high uniformity, but some disadvantages hamper their potential device applications: the shape and size of GNRs vary among different batches, it is really difficult to finely reproduce it, even following the exact same procedure.

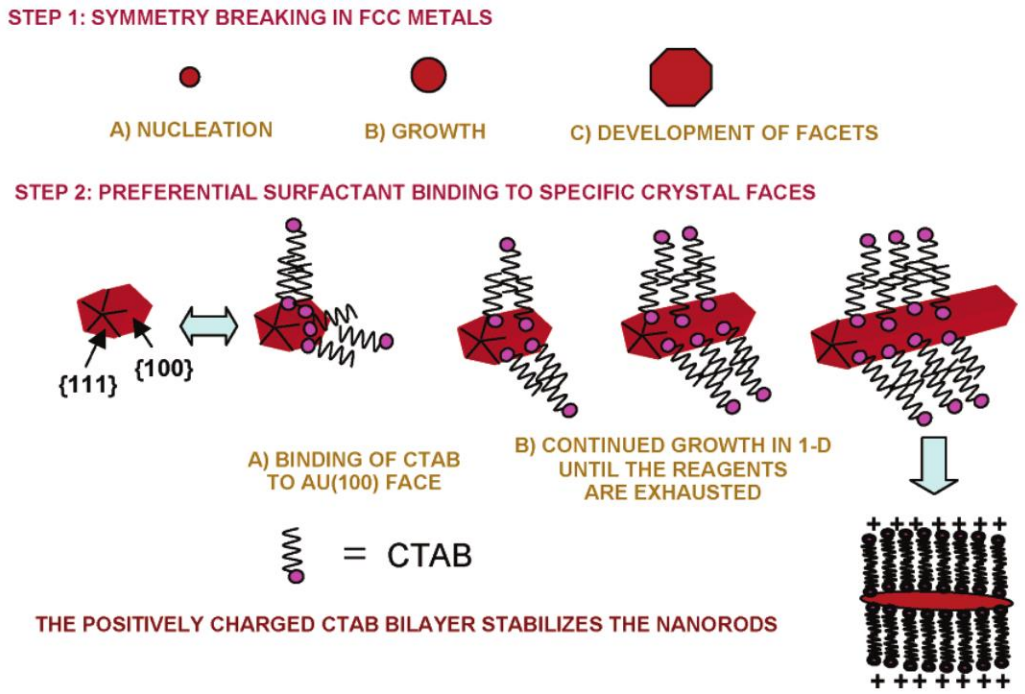

Figure 1.1.13- Mechanism for surfactant-directed metal growth proposed by Murphy et al. [62]

Top-down methods

Two types of top-down methods have been developed, mostly: the first involves the removal of gold from pre-deposited films according to specifically designed patterns using focused ion beams or other etching techniques, the second employs lithographic techniques to make masks on which gold is deposited.[67,68] The size of these structures is often limited by the resolution of the lithography, but GNRs with small size can be obtained by electron-beam lithography, down to 10 nm. Nevertheless, top-down approaches are generally time-consuming and expensive. Nanorods obtained by vapour deposition techniques are usually composed of polycrystalline nanoparticles: this causes the degradation of the optical properties of the nanorods because of electron scattering at the grain boundaries.

1.1.7 Aim of the work

This chapter recaps the main achievements of the first year of my PhD studies related to the applications of gold nanorods (GNRs) for tumour theranostics. As widely discussed in this introduction, theranostics represent the frontiers of nanomedicine, and gold nanorods can serve as biomedical payload for the purpose under several aspects.

In particular, this thesis will firstly describe the project EDIT (Chapter 1.2), funded by the European Commission, that involves the implementation of active-targeted chitosan-coated GNRs for diagnosis and therapy of bladder cancer in its earliest stages.

Successively, a gold nanorods- and adriamycin-loaded polymeric nanomicelle targeted with an antibody (*anti-epidermal cell adhesion molecule*, anti-EpCAM) able to perform active targeting towards hepatocellular carcinoma (liver cancer) stem cells (Chapter 1.3). In both cases, theranostics is achieved by exploiting the diagnostic capabilities related to the photoacoustic imaging contrast properties of NIR-light absorbing GNRs, while the therapeutic effect is obtained by the photothermal effect (combined with the presence of adriamycin as a therapeutic agent in the case of hepatocellular carcinoma). In both cases, GNRs are embedded in a polymeric carrier, but while the EDIT study involves the application of mucoadhesive water-soluble chitosan as a carrier, we developed stabilized and functionalized PLGA-*b*-PEG nanomicelles for applications against liver cancer.

Finally, in Chapter 1.4, a Matlab-supported chemometric tool will be employed to perform spectral unmixing on photoacoustic imaging to separate the spectral contribution of different populations of PEGylated GNRs in biological tissues. The nanosystem will be studied in terms of its diagnostic potential by photoacoustic imaging, but the focus of the work will be directed towards the multivariate data analysis that will allow for unambiguous spatial separation of PA signals coming from different chromophores.

1.1.8 Other publications in the field

During my PhD career, I had the chance to widely explore other possible nanoplatforms for applications in nanomedicine. These works will not be discussed in detail since they mostly focus on the applications in diagnostics, without investigations towards the possible therapeutic properties.
This is the case for ref. [15] and [69], where we developed several different diagnostic nanosystems as summarized in the abstracts here reported:

Smart assembly of Mn-ferrites/silica core-shell with fluorescein and gold nanorods: robust and stable nanomicelles for in vivo triple modality imaging
Monaco I., Armanetti P., Locatelli E., Flori A., **Maturi M.**, Del Turco S., Menichetti L. and Comes Franchini, M.* *J. Mat. Chem. B* **2018**, *6* (19), doi: 10.1039/c8tb00453f

Abstract:
Herein we report the synthesis of a resilient nanosystem based on silica-coated magnetic $MnFe_2O_3$ nanoparticles conjugated to fluorescein and PEGylated gold nanorods embedded in polymeric micelles ($MnFe_2O_4$@SiO_2@GNRs@PMs), for magnetic–photoacoustic–optical triple-modality imaging. The magnetic relaxivity of the nanosystem has been evaluated, revealing high r_2/r_1 ratios that suggest the effectiveness of the nanosystem as the T_2-contrast agent. In addition, contrast-based fluorescence imaging has been tested both in vitro and ex vivo, showing that the nanosystem exhibits the suitable optical properties of fluorescein, with contrast intensities comparable with previously reported results. Finally, photoacoustic, due to gold nanorods, performances of the nanosystem have been evaluated, revealing good linearity between concentration and photoacoustic response in the 25–250 nM concentration under irradiation at 690 nm. The results showed a contrast-to-noise ratio (CNR) as high as 60 in a mouse leg subcutaneously injected with the nanosystem. Biocompatibility studies revealed no hemolytic effect induced by the nanoconstruct, revealing the applicability of the studied diagnostic tool for medical studies.

Phosphorescent iridium-containing nanomicelles: synthesis, characterization and preliminary applications in nanomedical imaging

Monaco I., **Maturi M.**, Matteucci E., Locatelli E., Baschieri A., Zani P., Armanetti P., Menichetti L., Sambri L. and Comes Franchini M.*; *RSC Adv.* **2018**, *8* (59), 34162–34167, doi: 10.1039/C8RA05368E

Abstract:

Diagnostic nanomedicine constantly requires the development of novel contrast agents with intrinsic imaging capabilities. Phosphorescent Ir(III)-complexes represent good candidates when delivered through polymeric nanoparticles. In this work, we propose a biocompatible nanoparticle made from an intrinsically phosphorescent copolymer, synthesized directly with an imaging tag present on its backbone. Polymeric nanoparticles can be obtained with the exact amount of phosphorescent moieties needed to maximize their output signal. Complete characterization and ex vivo studies confirmed that this nanosystem is suitable as a future diagnostic tool.

Photoluminescent decoration of iron oxide magnetic nanoparticles for dual-imaging applications

Piccionello A. P., Menichetti L., Armanetti P., Flori A., **Maturi M.**, Pace A., and Locatelli E.*; Photoluminescent Decoration of Iron Oxide Magnetic Nanoparticles for Dual-Imaging Applications. *J. Nanoparticle Res.* **2018**, *20* (259), 1–7, DOI: 10.1007/s11051-018-4365-5

Abstract:

Diagnostic nanomedicine constantly requires the development of novel contrast agents with intrinsic imaging capabilities. Phosphorescent Ir(III)-complexes represent good candidates when delivered through polymeric nanoparticles. In this work, we propose a biocompatible nanoparticle made from an intrinsically phosphorescent copolymer, synthesized directly with an imaging tag present on its backbone. Polymeric nanoparticles can be obtained with the exact amount of phosphorescent moieties needed to maximize their output signal. Complete characterization and ex vivo studies confirmed that this nanosystem is suitable as a future diagnostic tool.

Finally, our research group focuses its attention on nanocellulose, as a versatile material for biomedical applications. In this field, we published a first work followed by a review paper on surface modification of nanocellulose for applications in nanomedicine: [70,71]

Surface modification of nanocellulose through carbamate link for a selective release of chemotherapeutics

Tortorella S., **Maturi M.**, Dapporto F., Spanu C., Sambri L., Comes Franchini M., Chiariello M. and Locatelli E.*. Cellulose, **2020**, *27*, 8503–8511, doi: 10.1007/s10570-020-03390-5

Abstract:

Herein we report the synthesis of cellulose nanocrystals covalently bound to a model chemotherapeutic drug (DOXO) via a novel spacer arm, which acts both as linker and as selective releasing agent. The carbamate linkage present in the linker, shows stability in aqueous environments for a wide range of conditions and can only be hydrolyzed in the presence of cells, freeing the active drug, with unmodified chemotherapeutic properties.

Surface-Modified Nanocellulose for Application in Biomedical Engineering and Nanomedicine: A Review

Tortorella S., Vetri Buratti V., **Maturi M.**, Sambri L., Comes Franchini M. and Locatelli E.*. Int. J. Nanomed, **2020**, *15*, 9909-9937, doi: 10.2147/IJN.S266103

Abstract:

Presently, plenty of concerns related to the environment are due to the overuse of petroleum-based chemicals and products; the synthesis of functional materials, starting from natural sources, is the current trend in research. The interest in nanocellulose has recently increased in a huge range of fields, from material science to biomedical engineering. Nanocellulose gained this leading role because of several reasons: its natural abundance on this planet, the excellent mechanical and optical features, the good biocompatibility, and the attractive capability of undergoing surface chemical modifications. Nanocellulose surface tuning techniques are adopted by the high reactivity of the hydroxyl groups available; the chemical modifications are mainly performed to introduce either charged or hydrophobic moieties that include amination, esterification, oxidation, silylation, carboxymethylation, epoxidation, sulfonation, thiol- and azido-functional capability. Despite the several already published papers regarding nanocellulose, the aim of this review involves discussing the surface chemical functional capability of nanocellulose and the subsequent applications in the main areas of nanocellulose research, such as drug delivery, biosensing/ bioimaging, tissue regeneration and bioprinting, according to these modifications. The final goal of this review is to provide a novel and unusual overview on this topic that is continuously under expansion for its intrinsic sophisticated properties.

1.2 Novel precision technologies for nanomedicine approach to promote non-invasive early diagnosis, eradication and prevention of cancer relapse: proof of concept in the bladder carcinoma

H2020 FET-OPEN project number 801126

Start date: October 1st 2018

End date: September 30th 2022

Project partners:
- Ospedale San Raffaele, Italy (OSR, Leader)
- Università Degli Studi di Milano, Italy (UNIMI)
- Alma Mater Studiorum Università di Bologna, Italy (UNIBO)
- Fujifilm Sonosite, Netherlands (FFSS)
- Weizmann Institute of Science, Israel (WIS)
- Lime Technologies, Greece (LIME)
- Ascend Technologies Ltd, United Kingdom (AT)
- OSM-DAN Ltd, Israel (OSM)

Project website: https://www.edit-h2020.eu

1) A manuscript is under preparation together with co-workers of San Raffaele Hospital, but before that, the two affiliations (UNIBO and OSR) are making an agreement for a common patent application.
2) During the first year our group in Bologna prepared the below-reported review:

Current concepts in nanostructured contrast media development for in vivo photoacoustic imaging

Maturi M., Locatelli E., Monaco I., and Comes Franchini M.*. *Biomaterials Science*, **2019**, *7*, 1746–1775 DOI: 10.1039/c8bm01444b

Abstract:

Photoacoustic (PA) imaging is indeed one of the most promising bioimaging techniques for theranostics applications in humans, allowing for the visualization of blood vessels and melanomas with high spatial resolution. However, in order to overcome the endogenous contrast arising from interfering endogenous species such as haemoglobin and melanin, specific contrast agents need to be developed, allowing PAI to successfully identify targeted contrast in the range of wavelengths in which interference from the biomatrix is minimized. This has been first performed by small-molecule dyes, which, however, suffer from some important limitations such as low hydrophilicity and short circulation times. For this reason, scientific research has recently directed its efforts towards the development of nanostructured contrast agents capable of providing efficient PA contrast at low concentrations with low toxicity and high biocompatibility. The principal nanostructures are based on (1) metal and semiconducting nanoparticles, amongst which variously shaped nano-gold plays the main role, (2) carbon nanomaterials, such as carbon nanotubes and graphene, and (3) conjugated polymer nanoparticles. In this review, the principal characteristics of this class of materials are reported and greater focus is directed towards in vivo studies. A detailed analysis is performed on various physical-chemical parameters that define the PA response of reported contrast agents, like absorption coefficients and photoacoustic efficiencies. By comparing the experimental data, this review provides a comprehensive tool for the evaluation of new nanostructured contrast agents for PA imaging.

1.2.1 Introduction

EDIT project aims to develop a novel technological platform for the early detection of pre-neoplastic modifications and early treatment of solid cancers by exploiting the acoustic and heat-releasing properties of gold in the form of targeted nanorods. Proof of concept of the EDIT platform will be first validated on bladder cancer. Identifying and treating developing lesions at an early stage is critical for improving therapeutic outcomes. A novel modality for detecting such changes through visualizing nanosized contrast agents is photoacoustic ultrasound (PAUS) imaging. So far PAUS is a research modality. EDIT is aiming to implement and utilize this non-invasive, non-ionizing technology as an everyday clinical practice.

PAUS imaging relies on the combination of optical and acoustic imaging where a pulsed laser light penetrates tissue and causes a thermoelastic expansion of an absorber. This expansion results in acoustic waves that are detected by the ultrasound transducer. Gold nanorods (GNRs) have emerged in recent years as specific and customizable agents detectable by PAUS. The combination of targeted GNRs and PAUS allows for detecting the anatomical details with high spatial resolution. In preclinical cancer research, progress has been made to monitor tumour oxygenation and response to therapy [72] and tracking of cells [73] by PAUS imaging. Worldwide prevalence of bladder cancer (BCa) is reported to be 2.7 million with an incidence of 350,000. [74] BCa is characterized by high unmet medical need due to a lack of effective clinical and therapeutical approaches, dating back to the early '70s. The main problem in the management of BCa is the incapacity to prevent the relapse and progression of the non-infiltrating aggressive form that is the bladder *Carcinoma in situ* (Cis/Tis, **Figure 1.2.1**). Current diagnosis and methods of an oncologic outcome evaluation of bladder Cis of less than 1 mm are limited by the flat appearance of the tumour and by the presence of few neoplastic cells that are not recognized by means of either photodynamic diagnosis (performed using blue light after preoperative intravesical instillation of 6-aminolaevulinic acid) or echography. Most patients with detectable Cis undergo repeated surgeries, each time followed by weekly bladder instillation of adjuvant therapy (failing in ca 50% of the patients). In patients with multiple Cis or where Cis is progressing and invading the muscle bladder (muscle-invasive bladder cancer, MIBC; T2-T4 in **Figure 1.2.1**) radical cystectomy is the only option. As a consequence of technological limitations, patients undergo frequent and endless follow-up and weekly treatments, or radical cystectomy, with a consequent poor quality of life and the highest cost per patient among all cancers. To overcome clinical and therapeutic limitations in the management of Cis, the approaches, technologies, and visualization platform proposed in this study for detecting pre-neoplastic areas and eradication of only a few cells with high sensitivity

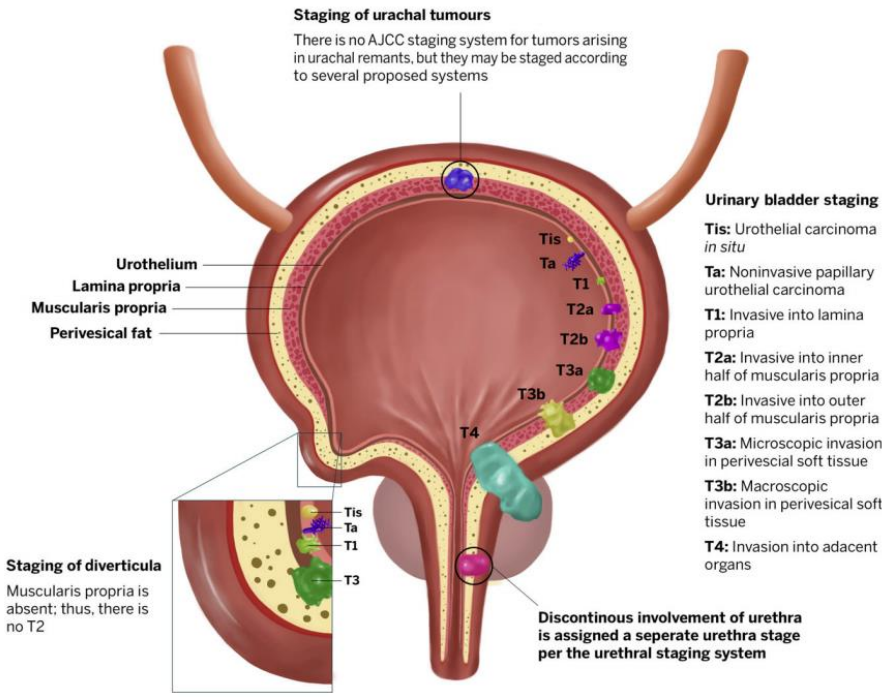

Figure 1.2.1. Overview of the staging of tumours arising from the urinary bladder, diverticulum, and urachal remnants. Reproduced from reference [75]

and specificity have not been attempted so far. Combining high-frequency ultrasound spectroscopy and photoacoustic principles on the bladder instilled with gold nanorods, EDIT will provide fast, non-invasive, and non-ionizing novel technologies for early prognosis, diagnosis, and treatment of the aggressive form of bladder Cis, by recognizing fibrotic tissue areas with a lateral resolution down to 30 μm. With an estimated 2.7 million people over the world having a history of BCa, and a cost of tens of thousands Euro/year per patient, [76] the outcomes of the project will improve the quality of life of millions of people while reducing social costs. The targeted breakthrough of the project is to provide preclinical platforms (**Figure 1.2.2**) and proof of principle of a novel and never previously attempted theranostic nanomedicine approach for early diagnosis and eradication of the aggressive bladder Cis, that is not detected/eradicated by the current technologies, by developing and applying engineered gold nanorods ligands (GNRs@Chit-Lig), further used as a nanoantenna network for high lateral resolution imaging of pathophysiological bladder ECM by ultrasound spectroscopy. These nanorods will be also used for the eradication of the tumour cells. Furthermore, the localized photothermal therapy a) will reduce side-effects related to standard and repeated mechanical removal of the malignant tissue or complications during/following surgery, b) drug-resistance is not expected with the proposed approach, as observed in 50% of individuals

treated with intravesical chemotherapy, [74] c) drug toxicity is not expected as the GNR will remain on the outer bladder wall and will be eliminated in the urine.

Long-term vision stands in the innovative strategies, technologies, and visualization platform that will allow unprecedented early diagnosis and eradication of malignant cells, i.e. in Cis. EDIT aims to revolutionize the management of BCa patients, where ongoing clinical guidelines and therapies are old and still not efficient. Tumour thermoablation will overcome

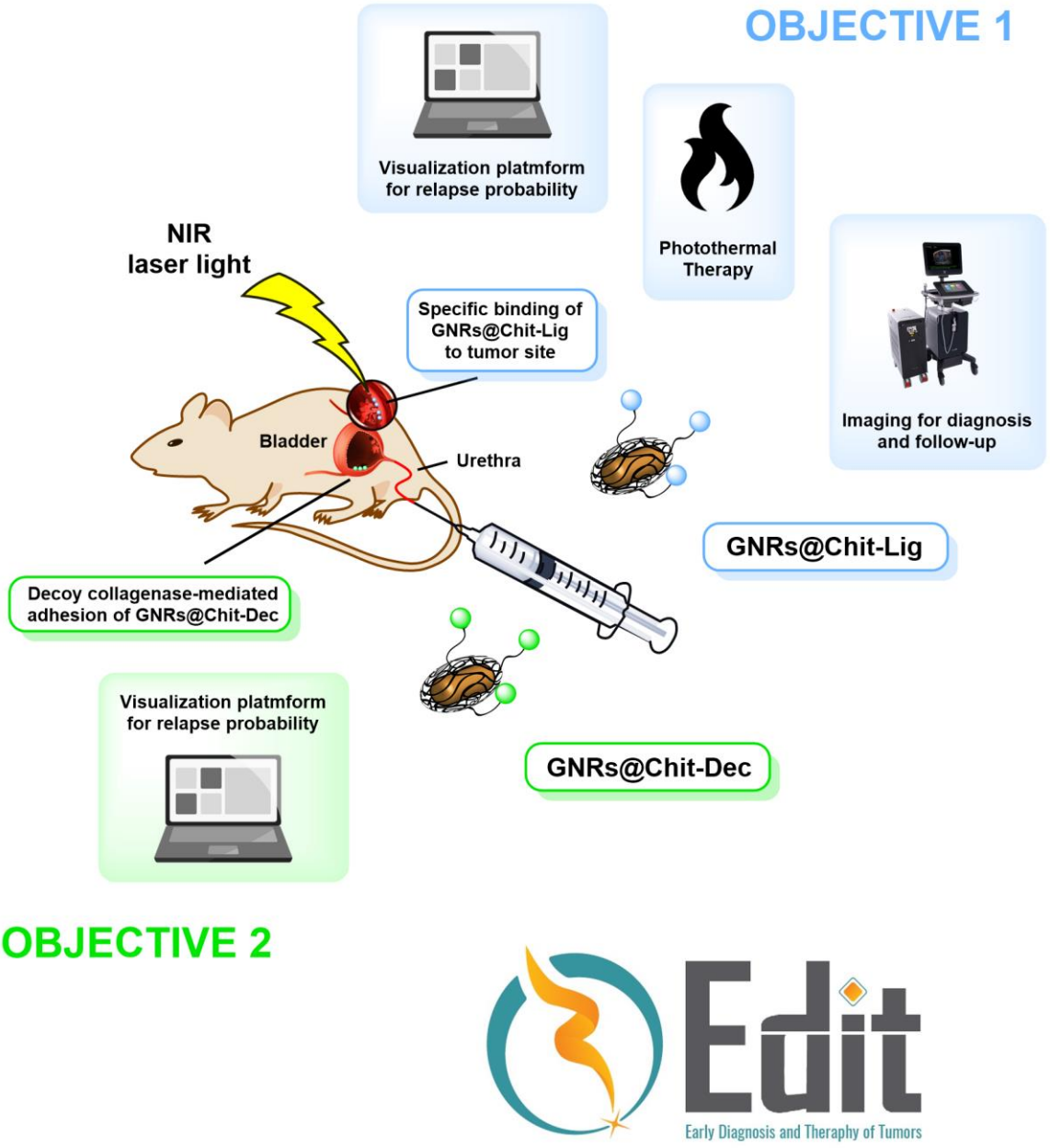

Figure 1.2.2. Schematic representation of the preclinical platform of the EDIT study.

chemoresistance, weekly adjuvant therapy, and multiple cycles of adjuvant(s), thus the theranostic approach together with early prognosis will i) reduce the occurrence of tumour invasion and relapse of chemorefractory neoplasia and ii) increase patients' survival and quality of life while reducing health care costs. The genesis of EDIT is based on unmet needs related to early prognosis, diagnosis, and treatment of bladder Cis. The project will deliver the proof of principle and preclinical validation of novel technologies for early prognosis, diagnosis, and treatment of the aggressive form of bladder Cis. Not only against bladder Cis but will our theranostic approach also be exploitable against chemoresistant relapsing bladder tumour Ta and T1. Clinical translation of our findings will revolutionize the management of bladder cancer, with its outcomes lasting for the many decades to come. In 2016 it has been reported linearization of the texture of collagen fibres pattern (vs random orientation in non-neoplastic tissue) and increased stiffness in colorectal cancer and bladder tumour (partners OSR, UniMi and Weizmann [77–79]), recently confirmed for the invasive phenotype of prostate cancer.[80] The strategies and platforms established in EDIT against BCa and the non-ionizing nature of the proposed approach will set the ground for a novel, non-invasive and earlier diagnosis and treatment of other diseases affecting organs such as colon, prostate, and brain, contributing to strengthening the long-term vision of the study.

Objective 1: Early eradication

Early eradication will exploit the superior targeting properties of locally delivered GNRs able to target and eliminate cancer cells in Cis. Diagnosis will be performed upon bladder instillation of GNRs functionalized with ligand (Lig) selectively recognized by BCa, thus resulting in the new complex named GNRs©Chit-Lig; ligands are RGD and isoDGR peptides with different integrin selectivity, already used by the partner OSR for delivering cytokine-loaded gold nanoparticles to tumours.[81,82] The GNRs will be used as sources of ultrasounds generated by resonant laser light irradiation (photoacoustic effect). Pulsed laser light will allow for the detection and diagnosis of malignant cells. The same nanorods can be used for the eradication of tumour cells since they can act as a very powerful nano-heater: excitation by continuous laser light will induce the metal to release energy (heat) thus giving selective thermo-ablation of the cancerous cells, as we reported in the preclinical model of Barret Oesophagus. [83] Heat transfer model will be employed to estimate the required concentration of GNRs on the interior bladder wall, which will enable the diagnostics and therapy while reducing the negative impact on the surrounding healthy tissue.

Objective 2: Early prognosis

Early prognosis is based on the leading hypothesis that pre-conditioning of the extracellular matrix (ECM) predisposes a soil (in the form of a fibrillary collagen-rich matrix) needed for the onset/progression/relapse of bladder cancer. Increased stiffness of ECM associates with the progression of breast cancer and correlates with poor survival of breast cancer individuals. [84] High resolution (down to 30 μm) of high-frequency ultrasounds are used to record stiffness of breast tumour, however spatial resolution with the same approach applied to the human bladder is not sufficient to image the bladder cancer in the early stage. [85,86] EDIT will pursue an innovative application of novel functionalized GNRs, to be employed as an intravesical source of ultrasound through photoacoustic effect. An innovative strategy is designed in order to enhance the ultrasound signal in the bladder wall, by exploiting intravesical GNRs for their applications as a photoacoustic antenna. We will assess the structural and mechanical modification of pathological collagen build-up within the bladder ECM as a unique biomarker of the early onset/progression/relapse of carcinoma, monitoring for the increased stiffness in pre-neoplastic areas, by taking advantage of sound beam attenuation and backscatter power spectrum of the tissue. The data obtained from the backscattered power spectrum of the radio frequency echoes and sound beam attenuation will be used with machine learning algorithms to identify the tissue changes related to Cis, and calibrated against measurements evaluated by means of state-of-the-art atomic force microscopy. High spatial resolution topographic maps of collagen rich ECM stiffness will be obtained by the use of engineered GNRs topically delivered to decorate the bladder inner surface. We will use GNRs for their original application as photoacoustic antenna to visualize the entire bladder mucosa, upon intra-vesical delivery of GNRs functionalized with highly specific evolutionary derived ECM decoy (GNRs@Chit-Dec). We will engineer and utilise enzymatically inactive matrix-metalloprotease 1 (MMP1, Decoy; partner Weizmann [87]) retaining high affinity and specificity for binding to collagen, used to anchoring the GNRs to specific dense/linearized collagen-rich sites within the pre-neoplastic tissue. With spectral unmixing photoacoustic signals will be used for monitoring tissue stiffness (GNRs as nanoantenna) and oxygenation (haemoglobin is the main natural photoacoustic chromophore in the tissues), coupled with 3D mapping of the bladder anatomy by high-frequency ultrasound providing up to 30 μm spatial resolution (partner FFSS [88]).

A platform will be developed to manage, visualize, and interpret 3D maps of the bladder stiffness, and to highlight pre-neoplastic and neoplastic areas with increased stiffness index. The innovative aspect of the visualization platform relies on its ability to overlay images

acquired at follow-up. The outcome of this specific aim is being able to apply innovative strategies and technologies for monitoring changes of bladder stiffness over time, either as i) preventive measures in healthy individuals or as a follow-up for detecting; ii) tumour relapse; and, iii) tumour progression toward the invasive phenotype. The bladder in three-dimensional space has been reproduced by using MRI, CT, and WLC videos [89–91], but the visualization platform proposed by the EDIT will be able to overlay the three-dimensional objects in follow-up visits as well, with a colour map of the stiffness index of the three-dimensional objects.

Objective 3: Biomarkers

i) characterization of markers that identify pre-conditioning of the ECM allowing the seed of cancer cells (onset, relapse, and tumour progression), ii) novel targets for the identification of Cis cells (specific integrins and cellular markers), and iii) new ligands for expanding the armamentarium for targeted delivery of gold nanorods. Findings from these sub-aims will increase the opportunities for the "bench to bedside" translational approach of the EDIT study.

1.2.2 Research methodologies

Objective 1: Early prognosis of the onset/progression/relapse of bladder cancer

Our protocol for GNR production [83,92] is compatible with Good Manufacturing Practice and scale-up production. Urine-stable GNRs capped with Chitosan (GNRs@Chit) will be functionalized with recombinant high-affinity catalytically inactive metalloprotease-1 variant retaining ability to specifically bind to fibrillar collagen (decoy matrix metalloproteinase-1) [93] (GNRs@Chit-Dec) expressed in the bladder mucosa, thus to recognize and decorate the entire luminal area of the bladder. The function of GNRs@Chit-Dec is to anchor the GNRs to collagen-rich tissue. This aim will be pursued in two animal models currently in use at OSR; i) a murine model of orthotopic bladder tumour established after intravesical instillation of an aggressive tumour cell line (developing Cis 4 days after instillation and progressing to MIBC very rapidly) and ii) rat model of spontaneous bladder carcinoma mimicking the human situation in which chronic inflammation sets the soil (e.g., tissue stiffness) for the onset, progression, and relapse of Cis. This model uses radiation-induced chronic inflammation and sub-optimal concentration of organ-specific bladder carcinogen nitrosamine.

An external probe is used to generate laser light in the biological window (near-infrared light at wavelengths of 680-970 nm), with an energy level of $\leq$ 20 mJ/cm^2 of skin, approved for clinical practice by the American National Standards Institute (ANSI). After instillation of GNRs@Chit-Dec in the bladder of the two animal models, a pulsed laser light will be used to generate ultrasounds from GNRs, thus monitoring for bladder stiffness. Setup of the photoacoustic imaging platform VevoLAZR is composed of a tunable laser unit and the photoacoustic transducers LZ550 (40 MHz central frequency) and LZ400 (30 MHz central frequency) and the beta version of the latest software under development; laser wavelength-specific ultrasound responses and signal processing bandwidth will be used to discriminate echo signal of GNR-generated ultrasound from the tissue-generated ultrasounds. Research efforts have focused on the ultrasound tissue backscatter analysis of power spectra of the radiofrequency echoes in order to obtain information on the characteristic size of the tissue microstructure, which can be used to assess the pathology of the imaged region. [94]

The EDIT approach is expected to provide visualization of the bladder with a spatial resolution never achieved before because i) urine inside the bladder is acoustically clear, ii) ultrasounds from laser pulses exciting GNRs are unmixed from tissue-generated ultrasounds because a time difference in the two ultrasounds and iii) echo-signal from GNR will be used as a contrast agent in order to normalize tissue stiffness to the amount of GNRs bound to the different bladder luminal areas.

The outcome of Objective 1 is the preparation of an innovative prognostic tool for the identification of pre-neoplastic regions, to predict tumour onset, tumour relapse, and progression based on the overlay of normalized 3D maps of the stiffness index over time, taking into account the bladder volume and the echo-signal of GNR in the algorithm. This strategy will also bypass the semi-quantitative nature of measurements, allowing to evaluating variations of stiffness within the same tissue over time.

Objective 2: Theranostic nanomedicine against bladder carcinoma in situ (Cis)

This aim takes advantage of very high absorption of energy and efficient photothermal conversion of GNRs, exploitable for application in photothermal therapy. GNRs@Chit will be functionalized with ligand (Lig; GNRs@Chit-Lig) discovered by OSR, containing Arg-Gly-Asp (RGD) or the related isoAsp-Gly-Arg (isoDGR) motif capable of binding to RGD-binding site of integrins αvβ3, α5β1, and αvβ6 overexpressed by urothelial cell lines derived from human BCa patients (**Figure 1.2.3**). In particular, GNRs@Chit-Lig will be tagged with a) n GD-containing peptide derived from human chromogranin A (CgA38-63) [95] capable of binding αvβ6 on bladder cancer cells with high affinity and selectivity (1.6 nM), b) a head-to-tail cyclized isoDGR hexapeptides [81] capable of binding αvβ3 (5 nM, called isoDGR1) or α5β1 (15 nM, called isoDGR4) with good selectivity, and c) a non-selective isoDGR peptide capable of recognizing αvβ3, αvβ5, αvβ6, and α5β1 will be also included (called isoDGR3). In addition to divalent metal ions (Mn^{2+}, $Mg^{2+,}$ and Ca^{2+}), acidic extracellular pH promotes activation of integrins,[96] suggesting that the urinary environment will be the ideal condition

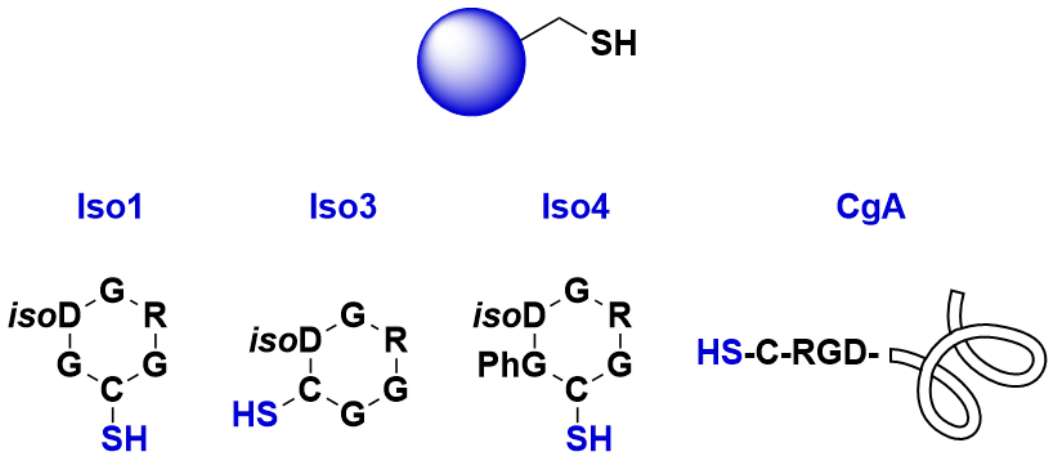

Figure 1.2.3. Structures of the isoDGR cyclic peptides and RGD-tagged CgA that are employed in this study. All compounds bear a thiol group from cysteine amino acids, which will be exploited for chemical conjugation with GNRs@Chit.

for RGD/isoDGR mediated delivery of GNRs@Chit-Lig. GNRs@Chit-Lig nanoparticles administered in the animal bladder are recognized upon pulsed laser light, and by switching the laser source to a continuous laser the excited GNRs produce heat, thereby allowing for targeted thermo-ablation of cancer cells. The outcome of Objective 2 is the superior targeting properties of single instillation of locally delivered GNRs@Chit-Lig able to target and eradicate the few bladder cancer cells forming the aggressive Cis. Combining all the above findings the study will provide information i) on the light energy required to detect the Cis, ii) the heat generated from the GNR and iii) the ultrasound frequencies needed to provide reliable and reproducible PAUS images. Together the information can be used for designing a clinical PAUS transducer for an effective theranostic approach.

1.2.3 Synthesis and characterization of GNRs@Chit-based nanoplatforms

CTAB-coated GNRs (GNRs@CTAB)

CTAB-coated Gold Nanorods (GNRs@CTAB) have been prepared following two very similar procedures in order to produce two populations of GNRs: one displaying the absorption band at around 800 nm ($GNRs_{800}$@CTAB), and another with maximum absorption band at around 950 nm ($GNRs_{950}$@CTAB). Both syntheses imply the preparation of a solution of small CTAB-capped Au nanoparticles (the seed solution), a portion of which is injected into a growth solution, in which the seeds are allowed to anisotropically grow forming rods. Firstly, the growth solution is prepared by dissolving 5.19 g of cetyltrimethylammonium bromide (CTAB) and 713 mg of sodium oleate in 300 mL of warm water (~ 50°C) in a 500-mL round-bottomed flask. This solution is then allowed to cool down by placing the flask into a thermostatically controlled bath set at 30°C. When thermal equilibrium is reached, 135 μL of a 0.4 M solution of $AgNO_3$ are injected. The solution is left unstirred for 15 min, then 1.442 mL $HAuCl_4$ 0.1 M are added with continuous stirring at 700 rpm. Au(III) is allowed to be reduced to Au(I) by sodium oleate for 90 min, after which 593 μL (for $GNRs_{800}$) or 1.2 mL (for $GNRs_{950}$) of HCl 37%w/w and 600 μL of ascorbic acid 0.079 M are added to adjust pH and to ensure complete reduction of gold precursor, respectively. By varying the pH of the growth solution, the redox potential of ascorbic acid is modified, allowing for tunability of the aspect ratio of the growing nanostructures. Later, the seed solution is prepared by dissolving 364 mg of CTAB in 10 mL of warm water in a 50-mL round-bottomed flask. After it cools down to room temperature, 25 μL of $HAuCl_4$ are added under stirring conditions. The seeds are formed by quickly injecting into this solution 600 μL of an ice-cold 0.01 M sodium borohydride ($NaBH_4$) aqueous solution. The solution turns immediately from yellow to brown suggesting the formation of ultra-small gold seeds. Finally, after 30 minutes from the addition of the reductant to the seed solution, 115 μL of it are added to the growth solution, which is vigorously stirred for 30 s then left undisturbed overnight at 30°C to allow GNRs growth. After establishing this consolidated protocol for GNRs synthesis, the process has been scaled up to fill a 2.5 L reactor, using the same experimental conditions but increasing all the relative amounts of reagents by a factor of 6. This allowed for the preparation of uniform batches of $GNRs_{800}$@CTAB and $GNRs_{950}$@CTAB, suitable for PA imaging. There are no more differences in the experimental procedures leading to $GNRs_{800}$@Chit and $GNRs_{950}$@Chit since only the position of the absorption band is influenced by the aspect ratio of the particles. To avoid any contamination and ensure the lowest level of endotoxins, all the procedures have been conducted under a sterile hood using

sterile glassware and plastics. All aqueous solutions have been prepared with sterile water for molecular biology.

After purification of the synthesized GNRs@CTAB, the concentration of atomic gold has been determined by flame atomic absorption spectroscopy (FAAS). Good linearity is obtained for the detected atomic line, allowing for efficient quantitative analysis. The small-scale synthesis produced 30 mL of 2.51 mM $GNRs_{800}$@CTAB, (Yield = 53%) and 30 mL of 2.34 mM $GNRs_{950}$@CTAB (Yield = 49%), while the scale-up produced 200 mL of 2.09 mM $GNRs_{800}$@CTAB (Yield = 49%) and 200 mL of 1.99 mM $GNRs_{950}$@CTAB (Yield = 47%). In addition, the total dry matter has been measured to be equal to 0.8 mg/mL for all preparations, which reveals that gold content is around 60% of the nanosystem mass. That is not surprising, since the organic portion (mostly CTAB) completely covers the gold core with a double bilayer, and an excess of surfactant in solution is required to keep the nanosystem stable. In fact, if CTAB concentration is reduced below its CMC (critical micellar concentration, which is around 0.9 mM for CTAB) [97], assemblies are no longer stabilized and the nanoparticles aggregate irreversibly. Moreover, surface zeta potential has been measured to be equal to + 29.8 mV, in agreement with the model of CTAB-capped gold nanosystems. [98] Primary evaluation of the geometrical anisotropy of the synthesized nanostructure has been performed by UV-VIS spectroscopy, measuring light absorption properties of the GNRs solution from 400 to 1100 nm (**Figure 1.2.4**). The presence of two distinct absorption bands proves the success of the synthesis, revealing that GNRs have been obtained with a longitudinal-LSPR peak at 798 and 945 nm, which corresponds to the

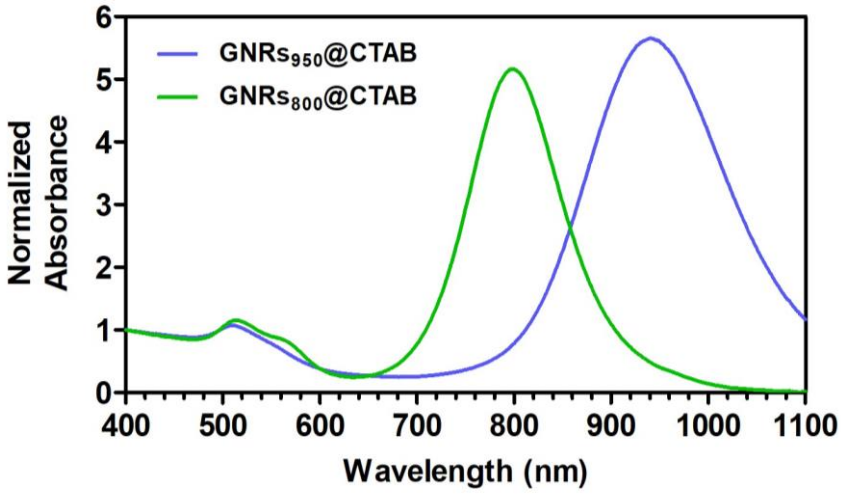

Figure 1.2.4 – Overlap of normalized UV-VIS spectrum of the synthesized $GNRs_{800}$@CTAB and NRs_{950}@CTAB.

longitudinal coherent electron oscillation of gold nanorods with an aspect ratio of around 3.5 and 5, respectively.

The obtained GNRs@CTAB have been studied by transmission electron microscopy to extract information on the morphology of nanoparticles and the shape selectivity of the syntheses (**Figure 1.2.5a,d**). TEM analysis confirmed the expected features of the nanosystem: the size of a total of 300 nanorods have been measured, leading to length and width distributions centred at 90.2 and 24.9 nm respectively, revealing an average aspect ratio of 3.6 for $GNRs_{800}$@CTAB (**Figure 1.2.5b,c**) and 75.0 and 14.9 nm respectively for $GNRs_{950}$@CTAB, leading to an aspect ratio of 5 (**Figure 1.2.5e,f**). This result is coherent with the previously observed optical behaviour of the systems. **Figure 1.2.5g** shows the EDX spectrum (energy-dispersive X-ray spectroscopy) which reveals gold as the principal component of the identified structures. Then, SAED (selected area electron diffraction) allowed for cross-validation of the expected crystalline structure of the particles (**Figure 1.2.5h**). Two diffraction spots are present: by calculating the corresponding interplanar distances in GNRs electron diffraction, of 2.04 and 1.19 Å have been determined. These correspond to distances between specific planes in gold FCC crystal structure (space group Fm3m), the [200] and [222] sets of planes, respectively. The overall TEM experiments allow stating the efficient synthesis of single-crystalline gold nanorods of the appropriate aspect ratio.

Thermogravimetric analysis (TGA) has been performed on CTAB and freeze-dried GNRs@CTAB in nitrogen atmosphere: the experiment on CTAB alone showed that between 160°C and 220°C it undergoes complete gasification due to thermal decomposition. Similar results are observed for GNRs@CTAB, which lost 25.6% of the mass in the same temperature range, followed by a further loss of 5.1% reaching 440°C. At 600°C, the residual non-volatile material is then quantified as 67.6%, comparable with the percentage of gold determined by the dry matter measurement.

Thiolated Chitosan (Chitosan-TGA)

The insertion of a thiol group on chitosan monomers have been performed by carbodiimide-assisted coupling between amino groups on chitosan and the carboxylic acid moiety on thioglycolic acid, TGA (**Figure 1.2.7**). Both reactant and product of the reaction have been studied by mean of proton nuclear magnetic resonance, with the aim of assessing the outcome of chitosan thiolation (**Figure 1.2.6**). Full assignment of spectral features has been performed by evaluating peak positions and intensities. Multiplicities are not resolved because each glucosamine monomer is magnetically different from the others to a really small extent, giving

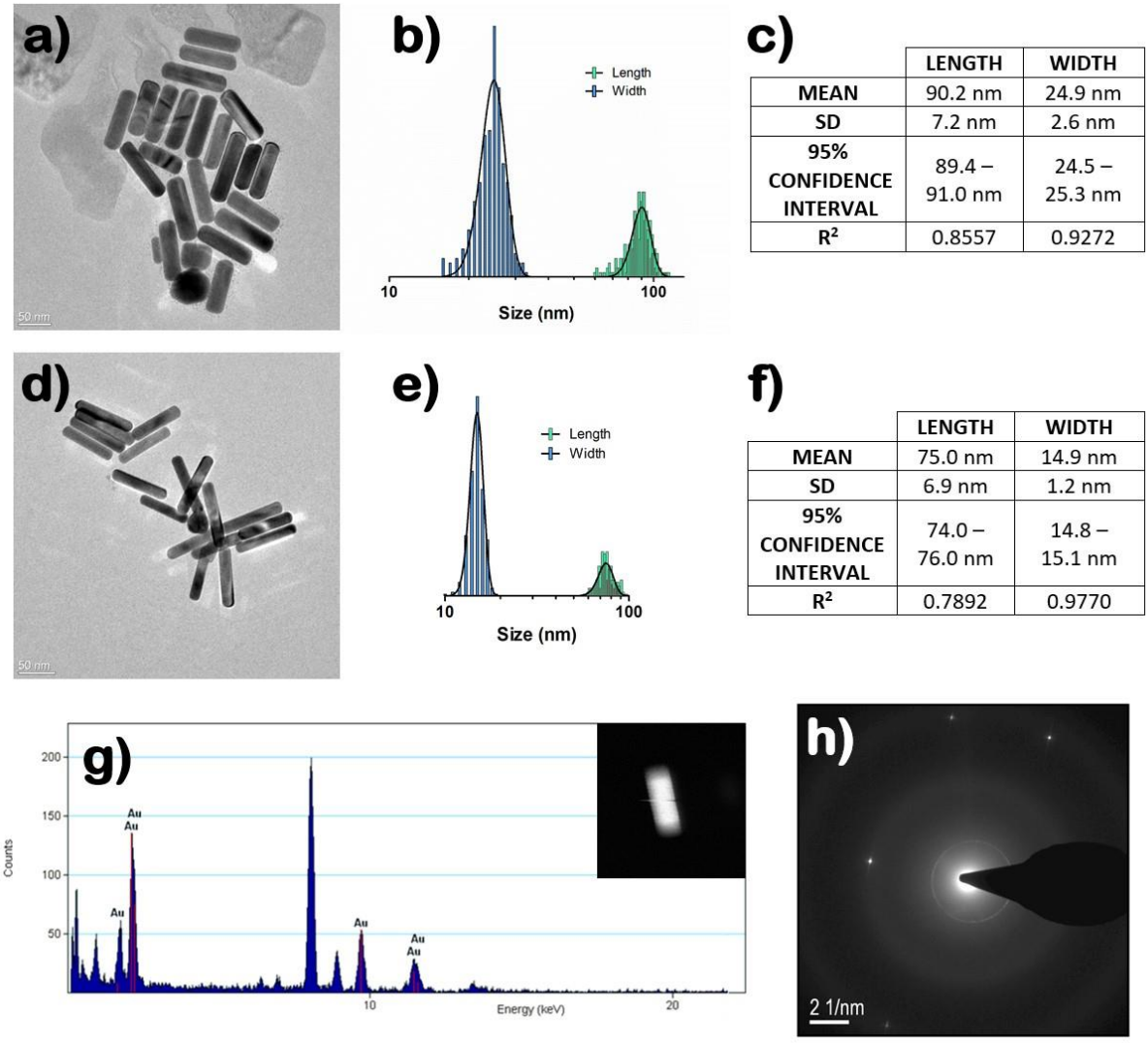

	LENGTH	WIDTH
MEAN	90.2 nm	24.9 nm
SD	7.2 nm	2.6 nm
95% CONFIDENCE INTERVAL	89.4 – 91.0 nm	24.5 – 25.3 nm
R^2	0.8557	0.9272

	LENGTH	WIDTH
MEAN	75.0 nm	14.9 nm
SD	6.9 nm	1.2 nm
95% CONFIDENCE INTERVAL	74.0 – 76.0 nm	14.8 – 15.1 nm
R^2	0.7892	0.9770

Figure 1.2.5 – TEM experiments. (a) Representative TEM images of $GNRs_{800}$@CTAB, with (b) the corresponding size distribution (n = 300) and (c) the corresponding Gaussian fit. (d) Representative TEM images of $GNRs_{950}$@CTAB, with (e) the corresponding size distribution (n = 300) and (f) the corresponding Gaussian fit. (g) EDX of the selected $GNRs_{800}$. Unassigned peaks are related to the emission from copper atoms composing the sample grid. (h) SAED diffraction pattern.

rise to broad unresolved peaks. By comparison, the obtained spectrum with the ones reported in the literature, the unambiguous assignment of peaks is possible.[99] A broad peak from 3.5 to 4 ppm has been assigned to protons in positions 3, 4, 5, and 6 of chitosan monomers, while a peak at 3.0 ppm has been related to proton 2, more upfield than the others due to lower electronegativity of nitrogen compared to oxygen. Chitosan proton 1 is not observed: it should appear as the most deshielded signal due to the presence of two oxygen atoms on the anomeric carbon. We concluded that its resonant peak is hidden under the extensively more intense signal of monodeuterated water (DOH) at 4.8 ppm. The most upfield signal has been then

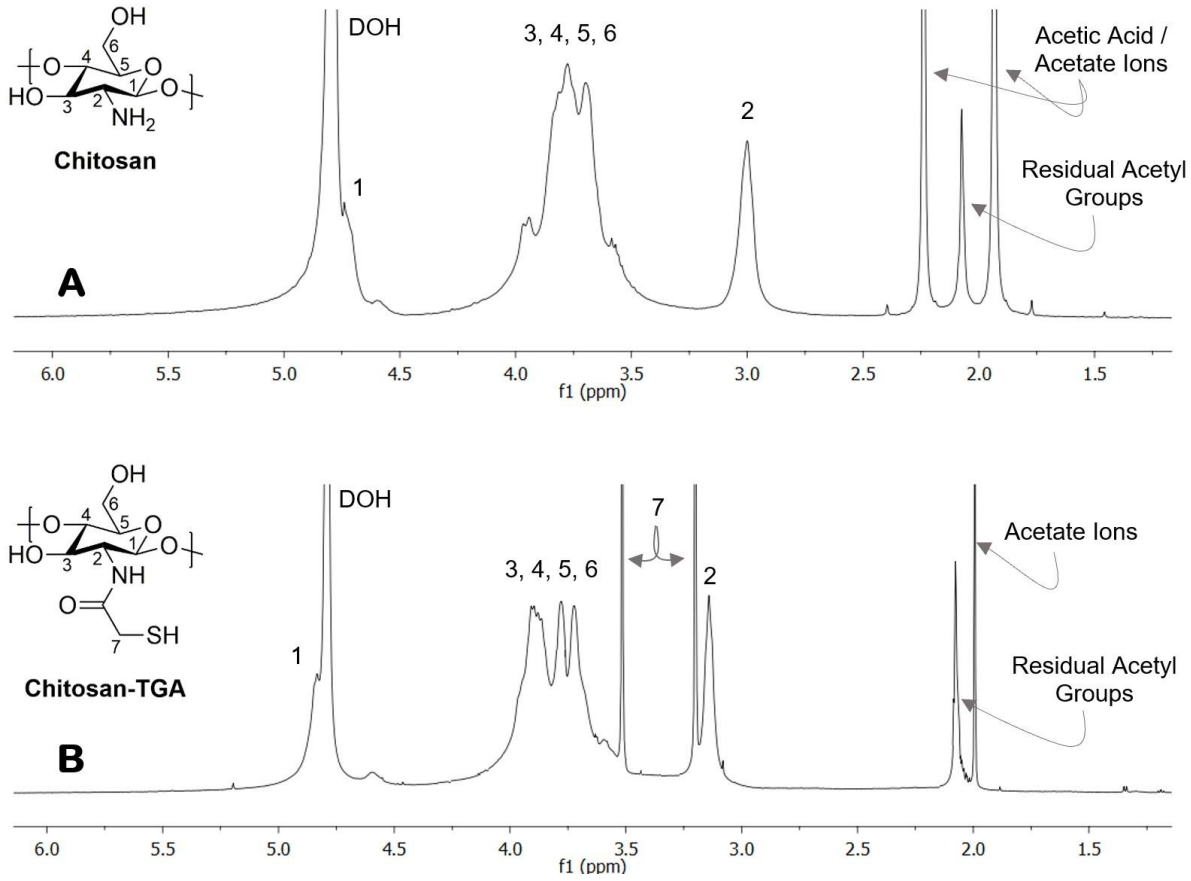

Figure 1.2.6 – ^{1}H-NMR analysis of Chitosan and Chitosan-TGA. (A) ^{1}H-NMR (600 MHz, CH_3COOH 1% in D_2O) of chitosan before the reaction. (B) ^{1}H-NMR (600 MHz, D_2O) of the obtained thiolated chitosan. The peaks corresponding to bound thioglycolic residues (7) are located at 3.2 and 3.5 ppm.

assigned to the CH_3 of the acetyl moieties, residuals of incomplete deacetylation of chitin. After conjugation with thioglycolic acid, sharp singlet peaks appear at 3.20 and 3.50 ppm. this has been related to the CH_2 residue of the thioglycolic moiety attached to the chitosan amino group, which splits upon partial deprotonation of the thiol group in a neutral aqueous environment. Moreover, by the integration of the NMR signals, it has been possible to determine the substitution degree of Chitosan-TGA, revealing that 9% of the monomers are N-acetylated, 71% are N-thioglycolate and 20% display the free amino group.

The thiolated product underwent thermogravimetric analysis (TGA) after freeze-drying in order to study its thermal behaviour. Firstly, a small weight loss in the range 20-130°C has been attributed to the loss of physisorbed water, strongly attached to the macromolecules via hydrogen bonding with the abundant -OH groups of the polysaccharide. A second loss of about 11.9% of the total mass is observed between 130°C and 220°C. This is most probably

related to the loss of acetic acid and thioglycolic acid bound to the amino groups on chitosan monomers, which requires higher temperatures. Then, reaching 600°C, further weight loss of 48.6% is observed and attributed to the overall degradation of the polymer matrix. Residual 30% of the mass is expected to represent the carbonaceous residue that cannot be gasified in the absence of oxidizing species such as O_2.

Chitosan-coated GNRs (GNRs@Chit)

Ligand exchange reaction has been performed as reported: due to the strong affinity of gold for thiol groups, the reaction takes place just by dropping GNRs-CTAB solution into a diluted solution of chitosan-TGA in water (**Figure 1.2.7**). After purification, nanoparticle surface potential has been measured to be ranging from + 35 to + 45 mV. The increase in zeta potential suggests a good replacement of CTAB: residual non-functionalized amino groups of chitosan preserve their cationic nature in water, leading to a high positive surface charge. UV-VIS spectrophotometry has been applied to assess the extent of conservation of the optical properties of the nanostructure after ligand exchange reaction. As it is shown in **Figure 1.2.8**, the position of the longitudinal-LSPR peak only slightly moved from 798 to 802 nm for

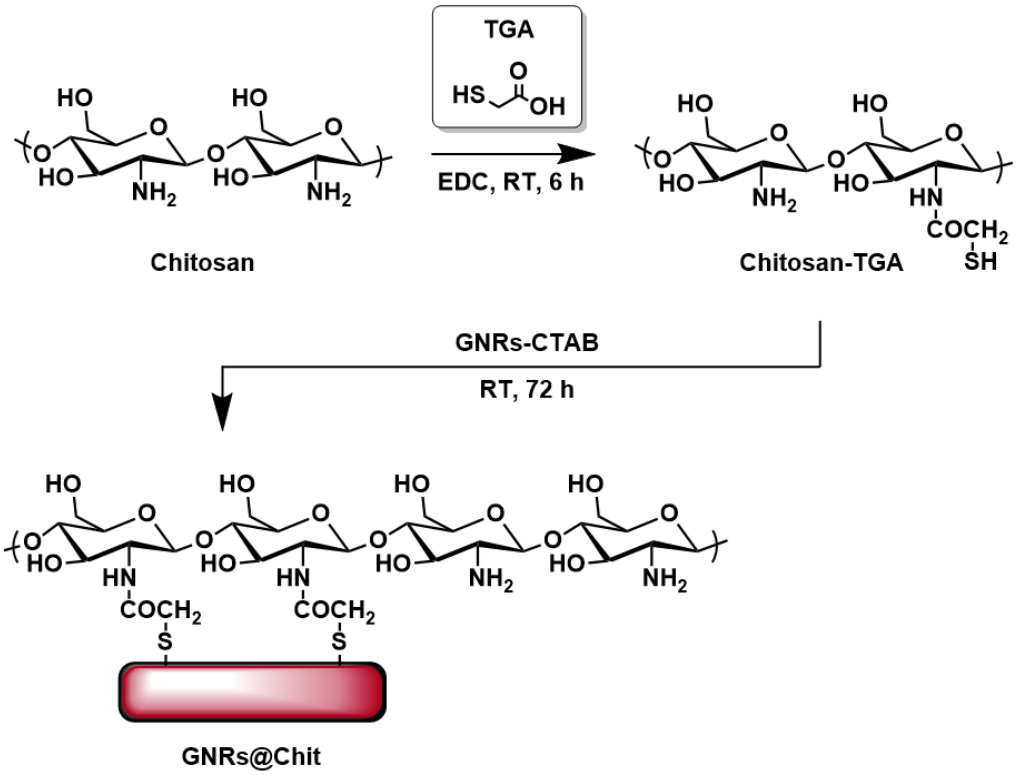

Figure 1.2.7 – Schematic representation of the synthesis of thiolated chitosan and its conjugation onto GNRs surface by the interaction of the free thiol groups with the gold surface.

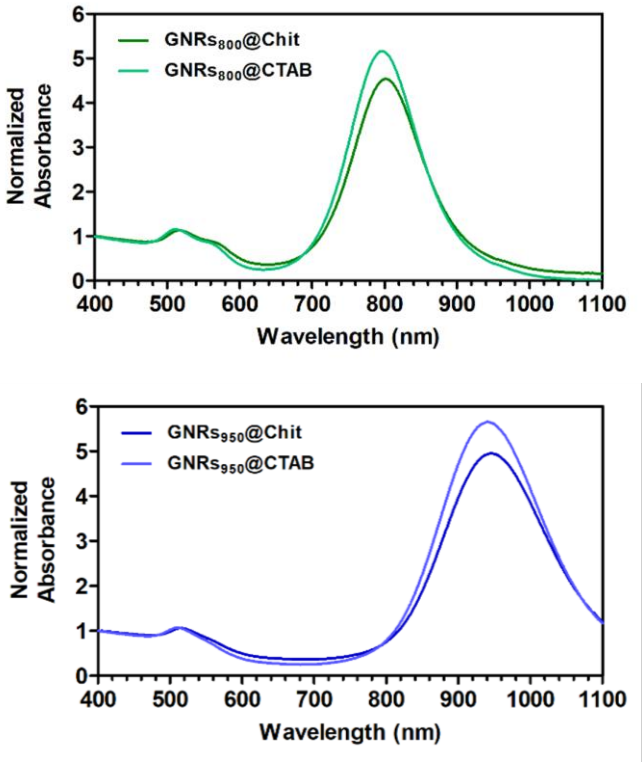

Figure 1.2.8 – UV-VIS spectra of GNRs@Chit compared to GNRs@CTAB for $GNRs_{800}$ (top) and $GNRs_{950}$ (bottom).

$GNRs_{800}$@Chit and from 945 to 949 for $GNRs_{950}$@Chit, sign of a small variation of the nanoparticle chemical environment. Reduction of the intensity of the main LSPR band is observed after replacement of CTAB with thiolated chitosan, probably due to little aggregation phenomena.

Transmission electron microscopy has been exploited to assess the conservation of the particle shape and dispersion, revealing no significant differences between CTAB- and chitosan-coated gold nanostructures (**Figure 1.2.9a,b**). Chitosan is not observed in TEM images because light atoms like C, N, O, and H which have too few electrons do not appreciably scatter accelerated electrons, therefore generating little or no contrast. Complete removal of CTAB from GNRs surface has been successfully assessed by ^{1}H nuclear magnetic resonance. The obtained spectrum resembles all the features of the chitosan spectrum (**Figure 1.2.9c**). The absence of signals coming from CTAB allows to state the success of the ligand exchange reaction. Moreover, it is clearly noticeable that the sharp peak corresponding to the CH_2 on thioglycolic moieties does not display splitting due to thiol deprotonation equilibrium. This can be directly connected with the efficient attachment of chitosan on GNRs surface since the thiol group is now bound to gold atoms and protonation equilibrium is not allowed.

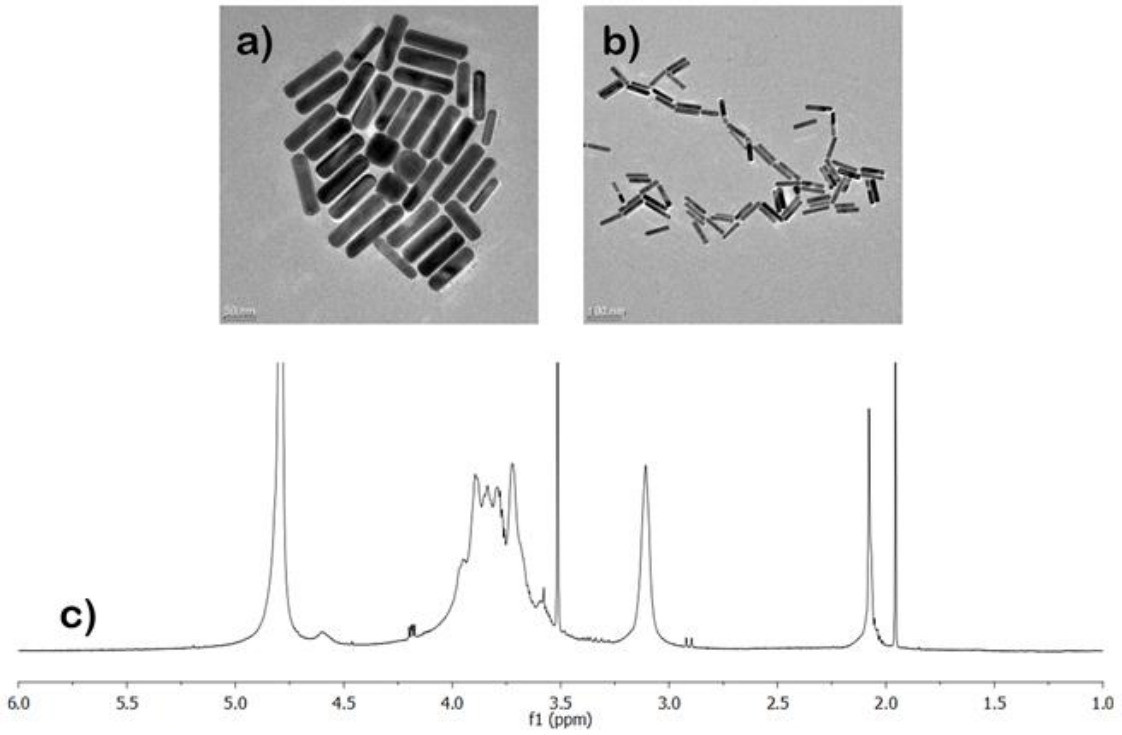

Figure 1.2.9 – TEM and ^{1}H-NMR analyses. TEM images of (a) $GNRs_{800}$@Chit and (b) $GNRs_{950}$@Chit. (c) ^{1}H-NMR spectrum of the synthesized GNRs@Chit (D_2O, 600 MHz).

Besides, the freeze-dried product underwent thermogravimetric analysis to study its thermal behaviour. The TGA profile mostly resembles the one of thiolated chitosan: 8.8% loss due to water desorption at low temperature and further 10.2% loss for detachment of acetyl and thioglycolic groups, with a residual mass at 600°C of around 33%.

Binding of tumour-targeting cyclic peptides

By integration of the ^{1}H-NMR spectrum of thiolated chitosan, it is possible to calculate that around 20% of the amino groups on chitosan have not reacted with thioglycolic acid, therefore the nucleophilic functionality is still available. In order to perform the conjugation of cyclic peptides on the GNRs@Chit nanosystem, we decided to exploit the reactivity of a synthetic PEG linker composed of 12 ethylene glycol units which shows at its ends an N-hydroxysuccinimidyl (NHS) carboxylic ester and an N-maleimide functionality (1-maleimide-3 - oxo - 7,10,13,16,19,22,25,28,31,34,37,40 - dodecaoxa- 4 - azatritetracontan - 43 - oic acid succinimidyl ester, named NHS-PEG_{12}-maleimide, MW = 865.9 g/mol). The NHS ester terminus reacts with free amino groups on chitosan ensuring the binding of the linker to chitosan, while the maleimide group is available to react with the cysteine residues on the cyclic peptides (**Figure 1.2.3**). The conjugation is performed as follows (**Figure 1.2.10**):

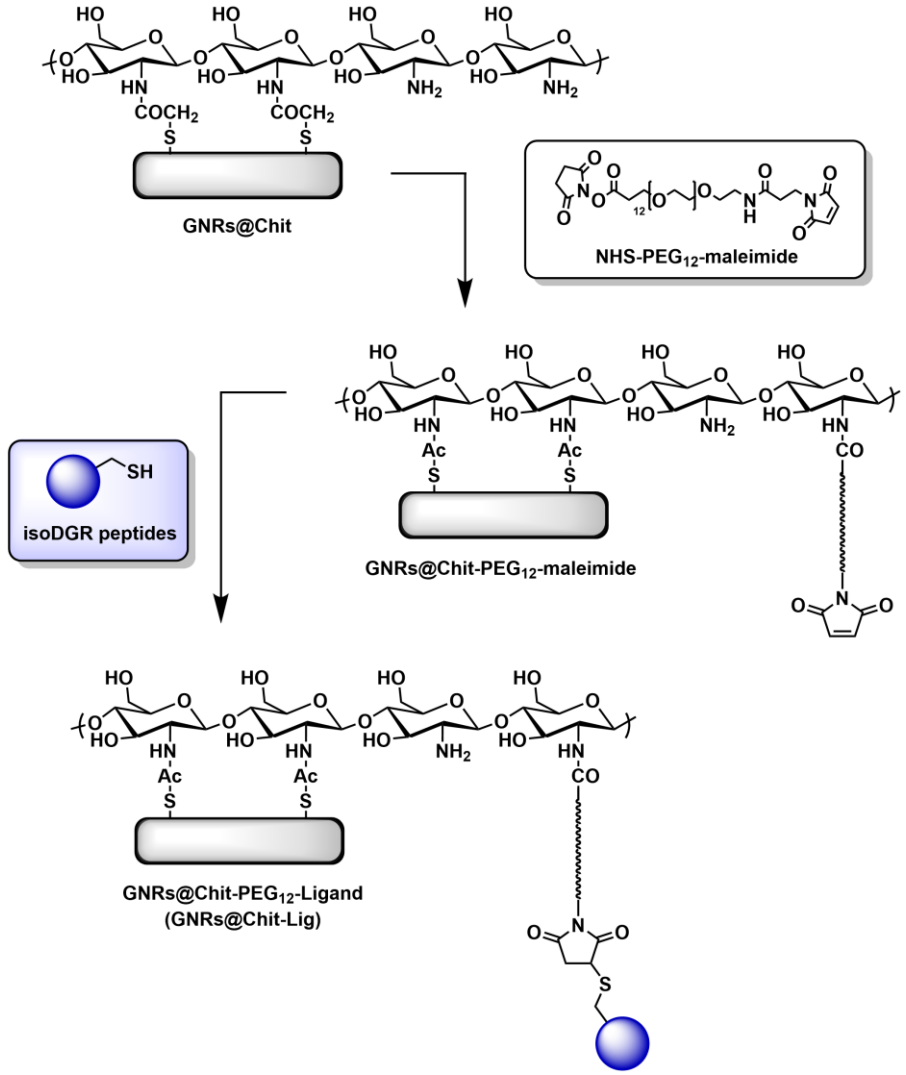

Figure 1.2.10 – Reaction scheme for the attachment of targeting peptides on GNRs@Chit. Firstly, the residual non-thiolated amino groups on chitosan have been reacted with NHS-PEG_{12}-maleimide to afford GNRs@Chit-PEG_{12}-maleimide, which is then purified and further conjugated to integrin-targeting peptides at the maleimido terminus of the PEG_{12} linker leading to the final GNRs@Chit-Lig nanoplatform.

a. Freeze-dried GNR@Chit, prepared as described in the previous paragraphs, is dissolved in water to achieve a final gold concentration of 500 μM, then the NHS-PEG_{12}-maleimide is added as an aqueous solution under stirring. The binding of the linker is allowed to take place by stirring overnight at room temperature. Before proceeding with the next conjugation step, the nanosystem (GNRs@Chit-PEG_{12}-maleimide) is purified by dialysis to remove any unreacted linker molecule.

b. The so obtained GNRs@Chit-PEG_{12}-maleimide is then reacted with the targeting ligands via thiol-ene click chemistry. After reacting at room temperature for 24 h, all unreacted

Parameter	Acceptability Range	Characterization Technique
$GNRs_{800}$ λ_{max} (nm)	770-830	UV-Vis
$GNRs_{800}$ aspect ratio	3.7-4.3	TEM
Gold concentration (mM)	0.95-1.05	FAAS
Thiolation efficiency of Chitosan (% SH/NH_2)	65-85	^{1}H-NMR
Gold content in freeze-dried samples (wt%)	2-4	Gravimetric analysis

Table 1.2.1 – Acceptability ranges for the parameters that describe different batch properties of $GNRs_{800}$@Chit-Lig.

maleimide groups are quenched by adding an excess of cysteine. The final nanosystem is then purified by dialysis, chemically characterized, and freeze-dried in order to obtain single-use vials containing the right amount of nanomaterial to achieve 1 mM gold concentration when dissolved in 0.5 mL of water.

After the synthesis, the nanosystem is characterized to assess the integrity of the plasmonic properties of GNRs and the reproducibility of the preparations. **Table 1.2.1** shows the several physical-chemical parameters evaluated for each batch and, for each parameter, the range of values for which the batch is accepted for the successive tests. If the batch is accepted, it is then shipped to OSR partners for *in vitro* binding assays on tumour-expressed integrins and for *in vivo* theranostic studies on tumour-bearing mice.

As already anticipated in the previous sections, the EDIT project involves the study of four different targeting peptides: Iso1, Iso3, Iso4, and CgA, leading to four different biopolymer nanocomposites named, respectively, GNRs@Chit-Iso1, GNRs@Chit-Iso3, GNRs@Chit-Iso4, and GNRs@Chit-CgA. Parallelly, as a negative control, GNRs@Chit loaded with non-targeting in place of the targeting peptide (called GNRs@Chit-Cys) are prepared.

Attachment of MMP1 decoys

The strategy involved for the conjugation of isoDGR and RGD cyclic peptides could not be applied to matrix metalloproteinase 1 decoys since they do not display any cysteine residue to be exploited for maleimide-based linkers. Therefore we identified possible alternative proteins and enzymes with Ni(II)-nitrilotriacetic acid in water (the so-called *His tag*) [100,101]. With this approach, engineered MMP1 decoys bearing the His-tag (H-H-H-H-H-H) motif are able to strongly interact with GNRs@Chit bound to an appositely selected linker. In this case, the employed linker is N-[5-(4-Isothiocyanatobenzyl)amido-1-carboxypentyl] iminodiacetic acid (Isothiocyanobenzyl-NTA), which is able to bind to chitosan by amine-isothiocyanate

click chemistry forming stable thiourea bonds. At the other end of the linker, the nitrilotriacetic acid (NTA) residue can chelate Ni^{2+} ions in water forming the $Ni[NTA(H_2O)_2]$ complex. This species is then able to bind adjacent histidine residues on polypeptides by the interaction between the Ni-NTA complex with imidazole residues on histidine (**Figure 1.2.11**). Each conjugation step is followed by extensive purification and lyophilization.
We tested the NTA-mediated conjugation protocol on His-tagged green fluorescent protein (GFP) as a model substrate. We selected GFP since it displays intense green fluorescence that allows for easy assessment of the reaction outcome. We performed the conjugation in the exact conditions planned for the binding of MMP1, for which it was estimated the effective dose of the decoy as 6000 decoy molecules per GNR:

a. GNRs@Chit are dissolved in sterile H_2O to a final gold concentration of 0.25 mM;
b. 1 mg of Isothiocyanobenzyl-NTA is dissolved in 50 µl of DMSO;
c. The two solutions are mixed in a 10:1 volume ratio and incubated at 37°C for 1 h;
d. The GNRs@Chit-NTA nanosystem is purified by centrifugation over membranes with molecular weight cut-off (MWCO) of 300 KDa;
e. GNRs@Chit-NTA are added to 2 mM $NiCl_2$ solution in 1:5 volume ratio and incubated at room temperature for 90 min;
f. After purification by centrifugation over membranes with MWCO of 300 KDa, the nickel-activated GNRs@Chit-NTA-Ni is freeze-dried;
g. GNRs@Chit-NTA-Ni are dissolved in the required amount of water to achieve a gold concentration of 0.25 mM, then a solution containing the His-tagged protein is slowly added;
h. After incubation at +4°C for 60 min, unbound protein is removed by centrifugation over membranes with MWCO of 300 kDa. The final nanosystem GNRs@Chit-Dec is then freeze-dried and shipped to EDIT partners at the WIS for *in silico* and *in vivo* experiments to assess the binding efficiency of the nanosystem towards specific linearized collagen-rich sites within the pre-neoplastic tissue.

When testing the protocol using GFP as a model protein, the waste solution from step *h* (that should contain unbound protein) was analyzed by fluorescence spectroscopy compared to the synthesized GNRs@Chit-GFP. The analysis revealed the absence of fluorescence signals on the waste solution a strong green emission from the GNRs solution (**Figure 1.2.12**). These results suggest that the His-tagged protein was quantitatively conjugated on the nanosystem

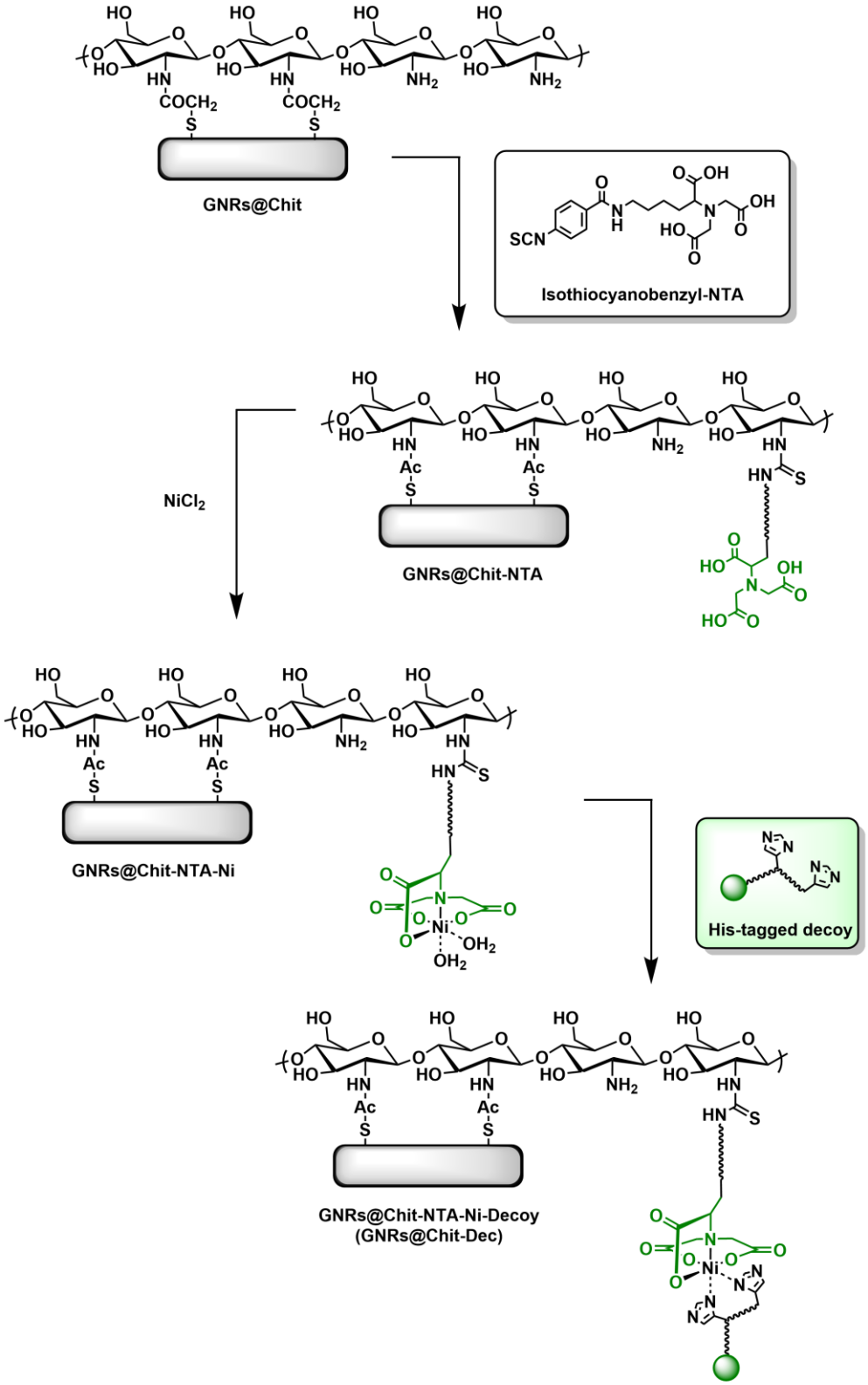

Figure 1.2.11 – Reaction scheme for the attachment of His-tagged MMP1 decoys on GNRs@Chit. The isothiocyanobenzyl linker is firstly coupled to free amino groups on chitosan forming thiourea linkages, then Ni(II) is chelated by the NTA end of the linker. The NTA-Ni complex is now reactive towards histidine-tagged proteins and allows for the conjugation of MMP1 decoys to form GNRs@Chit-Dec.

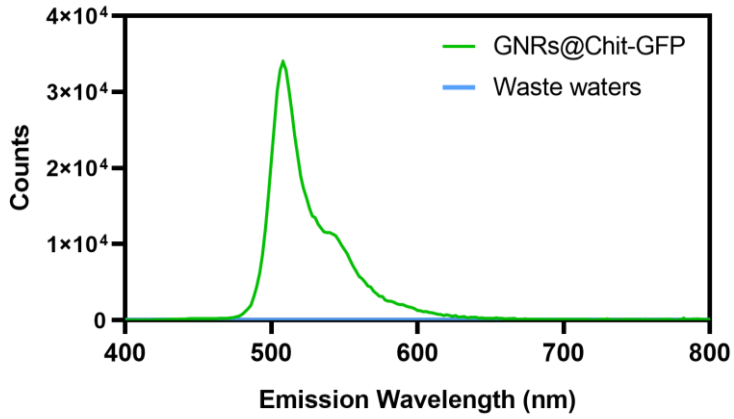

Figure 1.2.12 – Fluorescence emission spectra of GNRs@Chit-GFP (green line) compared to the spectrum of wastewaters (blue line), which reveals the absence of unbound GFP and therefore the quantitative yield of the performed His-tag-mediated protein conjugation. The excitation wavelength was 395 nm.

since simple aqueous solutions of GFP can pass the centrifugal membranes in the absence of GNRs@Chit-NTA-Ni. The protocol is then validated and ready to be applied for the binding of MMP1 decoys before being employed for pre-clinical tests.

Stability of GNRs@Chit in human urine

Stability tests have been conducted by placing a defined amount of $GNRs_{950}$@Chit and $GNRs_{950}$@Chit in mixed urine samples and incubating them at 37°C for 2 hours. At predetermined time steps, portions of the mixtures are withdrawn, quenched in cold water, and underwent UV-VIS and SEM analysis. Any variation in the spectral features or the morphology of the nanosystem would suggest some kind of destabilization of the structures. For $GNRs_{950}$@Chit, VIS-NIR analysis (**Figure 1.2.13**) revealed a 13% reduction in the intensity of the absorption maximum at t = 0 for samples diluted in urine compared to samples diluted in water. This is probably due to a partial destabilization of the nanostructure upon mixing with urine, due to pH variations that can reduce the particles' surface potential and induce little aggregation. At the end of the experiment, a maximum reduction by around 20% of the absorption maximum is observed: therefore, the plasmonic properties of $GNRs_{950}$@Chit have been shown to be mostly preserved in urine environment for 2 h, as well as for $GNRs_{800}$@Chit. In fact, in the case of $GNRs_{800}$@Chit, after 2 h of incubation in urine environment, the main absorption peak intensity decreased by 18%, but more slowly than for $GNRs_{950}$@Chit. The stability of the nanosystem in urine environment is also confirmed by SEM analysis (**Figure 1.2.13a-c**), which displays no modification whatsoever in the particle's morphology or degree of aggregation over time.

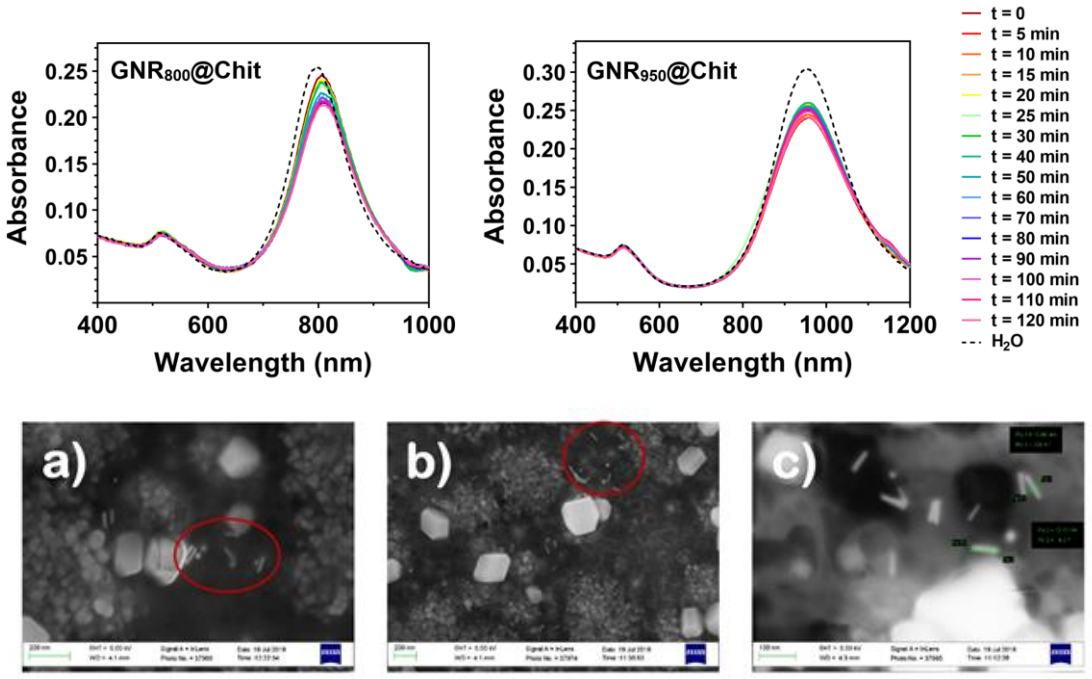

Figure 1.2.13 – Top: GNR@Chit stability in human urine. VIS-NIR spectra have been recorded to evaluate the integrity of the GNRs plasmonic properties in urine environment over a period of 2 h. Bottom: Scanning Electron Microscopy analysis of GNRs stability in urine. GNRs@Chit maintain their morphological characteristics as well as their dispersibility from (a) t = 0 through (b) t = 60 min to (c) t = 120 min.

1.2.4 Future Perspectives

In the first two years of the EDIT project (2018-2020) we developed a stable, robust, and reproducible sequence to perform the synthesis and chemical modification of ready-to-use freeze-dried targeted chitosan-coated gold nanorods represented in **Figure 1.2.14**.

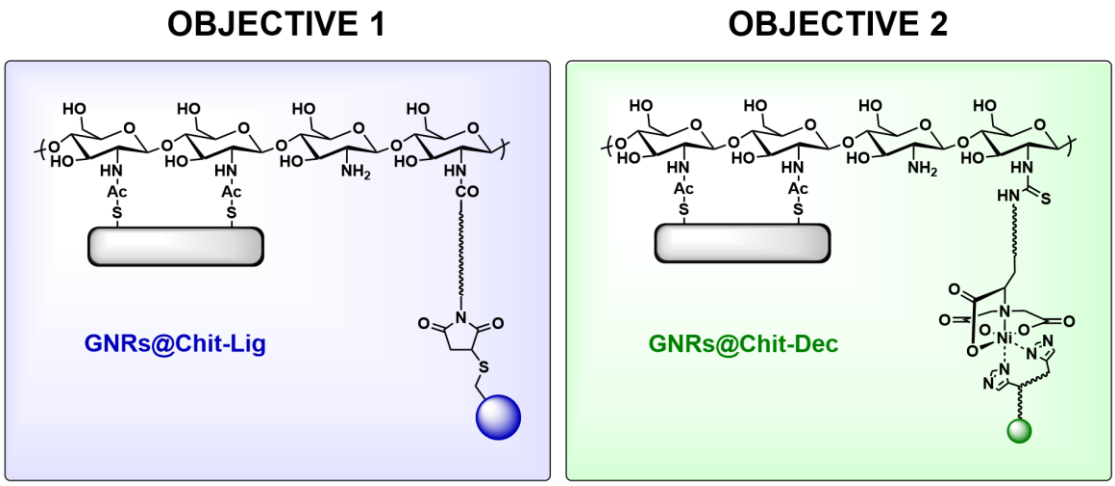

Figure 1.2.14 – Structure of the final targeted nanosystems employed in the EDIT study.

Presently, the EDIT project is still ongoing and it will end by September 2022. Currently, GNRs@Chit-Lig is under evaluation by the partners at San Raffaele Hospital (OSR) for *in vitro* and *in vivo* binding to integrins overexpress in bladder cancer. Parallelly, GNRs @Chit-Dec binding to stiffer collagen regions in the pre-neoplastic areas is being evaluated at the Weizmann Institute of Science (WIS).

The main tasks of the project partners are:

- In vitro and ex-vivo approaches for establishing the binding of GNRs@Chit-Dec and GNRs@Chit-Lig in presence of urine. (OSR and UNIBO). Binding of GNRs@Chit-Dec and GNRs@Chit-Lig will be evaluated in vitro using purified receptors immobilized to microtiter-plates and nitrocellulose filters and ex-vivo on fresh explanted mouse bladder (healthy or tumoural tissues) in presence of various amounts of urine in the binding buffer (mimicking the instillation process occurring in vivo). Optimization of buffer composition for delivering the nanoparticles, such as ionic strength, divalent ions, and pH, will be carried out in order to optimize for the presence of urine. The binding of GNRs@Chit-Dec and

GNRs@Chit-Lig will be quantified exploiting the physical-chemical properties of the gold such as total content of metal in the tissue/cells after metal extraction and/or by dark-field microscopy for nanoparticles visualization.

- Establish the minimal amount of GNRs@Chit-Lig and photoacoustic parameters necessary for the diagnosis of Cis. (OSR, UNIMI, and FFSS). We will combine the histological determination of healthy tissue and tumour with ultrasound detection of GNRs@Chit-Lig.
- Specificity, efficacy, and safety of the theranostic approach. (OSR and UNIMI). In the orthotopic animal model of Cis, the specificity of thermoablation will be assessed using the bioluminescent tumour model (intravesical instillation of cancer cells stably transfected with firefly luciferase reporter gene). Detection of in vivo bioluminescence will be before and once a week for 6 weeks after thermoablation. Efficacy of the theranostic approach will be further implemented by histological analysis at the end of the follow-up. The efficacy of the theranostic approach (single treatment) will be compared with the effect of 6 weekly instillations of BCG, which is the typical intravesical therapy for high-risk Cis. Safety of the thermo-ablation (i.e., the extension of the ablated area) will be estimated by immunohistochemistry. To identify if GNRs@Chit-Lig instilled in the bladder of healthy animals (mimicking patients testing negative for the presence of tumour at follow-up) can spread in the surrounding tissues; urine, urogenital tissues, liver, and blood will be analyzed at first.
- Identification of clinical PAUS set-up (OSR). Pigs share with humans similar anatomic and physiologic characteristics, including bladder thickness, bladder volume, and the urinary apparatus. Swine will be used to adapt the size of the probe, the size of optic fibre laser parameters, and the amount of GNRs for future clinical application, by performing thermoablation and 3D visualization platform in human-like bladder instilled with. Six adult female swine of 30-40 kg will be exposed to PAUS before and after 1 hour of GNRs@Chit-Dec instillation. Second, in the same animal localized thermoablation will be produced, to induce and to monitor tissue changes (i.e., stiffness) by PAUS at 1 and 3 months of follow-up; urine collected for 7 days following GNRs instillation, blood/bladder/liver collected at sacrifice monitoring for GNRs bio-distribution. Bladder collected at sacrifice will be used for 3D visualization of the stiffness of the entire organ.

1.3 A novel theranostic gold nanorods- and Adriamycin-loaded micelle for EpCAM targeting, laser ablation, and photoacoustic imaging of cancer stem cells in hepatocellular carcinoma

Locatelli, E.; Li, Y.; Monaco, I.; Guo, W.; Maturi, M.; Menichetti, L.; Armanetti, P.; Martin, R. C.; Comes Franchini M., *Int. J. Nanomedicine* **2019**, 14, 1877–1892.

1.3.1 Introduction

About 90% of therapeutic failures in cancer patients are attributed to chemoresistance. Conventional therapeutic strategies, such as chemo-agents killing rapidly growing cancer cells, may exhibit an initial success, but the eventual relapse of the tumour, due to the greater resistance of some cells is a critical point. A certain type of cancer cells, such as progenitor cells/cancer stem cells (CSCs), renders the capability to this subset of cancer cells to evade slaughter from a variety of structural and functional chemo-agents, thus accounting for nearly all therapeutic failures. However, most chemotherapeutic agents aim to destroy rapidly dividing cancer cells other than undifferentiated CSCs. New types of therapeutic strategies for targeted drug delivery to cancer cells, especially to the CSCs, could be promising as a radical treatment for cancer. Finding the agents for CSC killing could be the key to eliminate these cancer-initiator / progenitor cell CSCs, thereby radically abolishing the tumours. Unlike the cancer cells that were rapidly dividing and differentiating, CSCs underwent continuous self-renewal to avoid insult and chemo-killing. Targeting the CSCs would provide a novel therapeutic strategy, a shift away from traditional chemotherapy. To test this hypothesis, we first performed an in vitro study using a sphere-formation assay to enrich the CSCs. This sphere-formation assay was originally established as an in vitro culture system to enrich nervous stem cells[102] and was used latterly to enrich CSCs.[103] In this *in-vitro* culture system, two important growth factors used were the epidermal growth factor (EGF) and basic fibroblast growth factor (bFGF). The use of bFGF was critical to regulate the proliferative fate of unipotent and bipotent EGF-generated progenitor cells.[104]

Hepatocellular carcinoma (HCC) is the fifth most common cancer and the third leading cause of cancer-related deaths worldwide.[105] HCC is often resistant to chemotherapeutic drugs, with only a few drugs eliciting a therapeutic effect in HCC patients.[106]

The treatment results obtained with chemotherapeutic agents in advanced HCC have been disappointing. Adriamycin (Adr) has been commonly used for the comprehensive treatment of various cancers including HCC. Adr was one of the first chemotherapeutic drugs used for

HCC and showed interesting results;[107] however, the chemoresistance that developed its efficacy, with a marginal role in the treatment of HCC patients. The interest in Adr is growing again due to the technological advancements that now allows targeted release of the drug. In our previous study,[108] we demonstrated that Adr can decrease the expression of epithelial cell adhesion molecule (EpCAM). Recent finding demonstrated that EpCAM, an important CSCs surface marker, is overexpressed in the cancer cells contributing to chemoresistance.[106] Therefore, a targeted release of Adr could be a potential strategy to improve its chemotherapeutic efficacy.

Gold nanorods (GNRs) have shown promising applications in imaging, therapy, and biological sensing, thanks to their peculiar geometry.[109] Significant biomedical applications based on targeted heat delivery, such as killing localized cancer cells by hyperthermia after optical excitation, become possible when GNR resonance is tuned to near-infrared (NIR), rays to which tissues are relatively transparent. Besides, under nanosecond-pulsed NIR laser irradiation, GNRs act as perfect contrast agents for photoacoustic (PA) imaging, a powerful diagnostic, non-invasive technique, which could be used for early cancer diagnosis.[110,111] Moreover, by employing continuous-wave NIR laser tuned in the region of GNR plasmonic absorption, they can increase the temperature of their surroundings up to several tens of degrees, enabling their employment for photothermal therapy (PTT) of cancer.[112,113] Many other nanostructured materials have been recently developed to efficiently convert NIR light into heat, but GNRs display higher photothermal conversion efficiencies and improved biocompatibility.[114,115]

Recently, a simultaneous loading of lipophilic GNRs and curcumin into polymeric nanomicelles (GNRs-**1**/curc@PMs) made of biocompatible PLGA-b-PEG copolymer has been developed and used for in vivo treatment of premalignant oesophageal adenocarcinoma.[83]

A similar strategy is exploited in the present work to create a drug delivery carrier able to host two different therapeutic agents, Adr and GNRs, simultaneously and to deliver them to the site of action, thanks to decoration with the EpCAM antibody on the surface of the nanosystem. When decorated with EpCAM antibodies, Adr/GNRs@ PMs-antiEpCAM could specifically target CSCs and enhance the concentration of drugs in the tumour site, thereby killing, especially under laser irradiation, the CSCs completely.[116] Moreover, the enhanced localization of GNRs on the tumour region could be efficiently detected by using photoacoustic imaging, thus allowing diagnosis and therapy by using a single drug.

1.3.2 Results

Synthesis of Adr/GNRs@PMs-antiEpCAM

GNRs were coated on their surface with ethyl 11-mercaptoundecanoate **1**, obtained as previously reported[117] in order to make them lipophilic and stable in organic solvents, thus allowing their entrapment into the polymeric micelles. After incubation of GNRs coated with cetyltrimethylammonium bromide with ligand **1**, lipophilic GNRs-**1** were easily redispersed in DCM. Next, GNRs-**1** were entrapped along with Adr into polymeric nanomicelles (PMs) using water-in-oil-in-water (W/O/W) double emulsion solvent evaporation technique: the amphiphilic PLGA-*b*-PEG-COOH and PLGA-*b*-PEG-NH_2 copolymers were selected to create biocompatible, biodegradable, and water-soluble micelles able to circulate for long periods of time in the bloodstream.[32] Therefore, the organic solution composed of GNRs-**1** and copolymers was emulsified with a small amount of water phase containing Adr, and the so-obtained pre-micelles were stabilized by second emulsification with a larger amount of

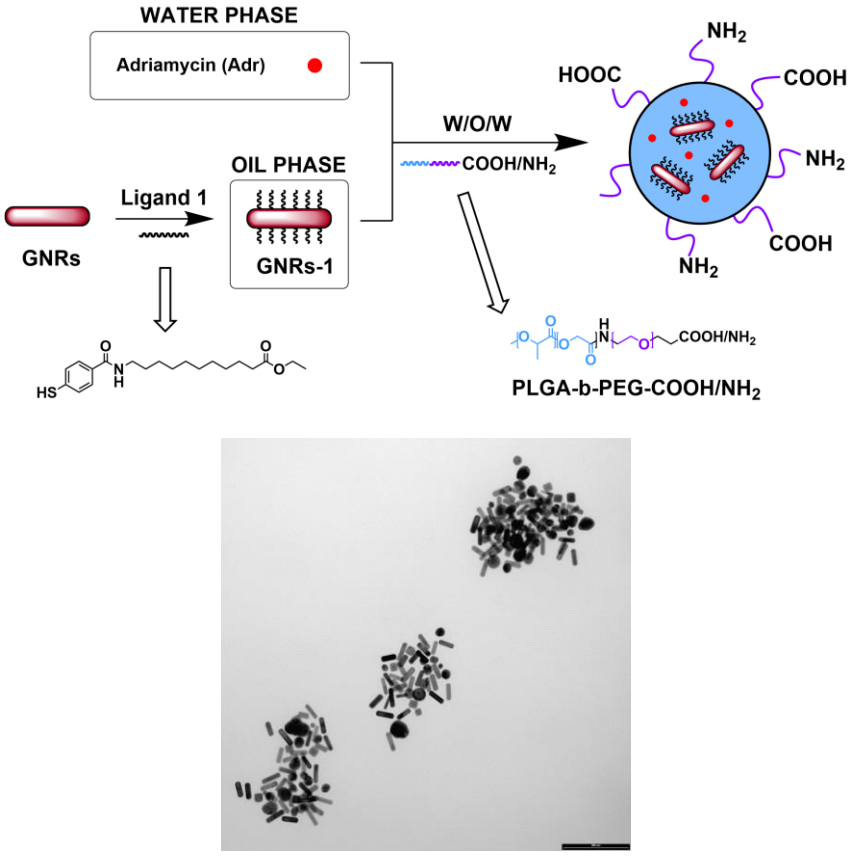

Figure 1.3.1 - Representative procedure for the synthesis of Adr/GNRs@PMs-antiEpCAM and TEM image of the final nanosystem.

	Adr/GNRs@PMs	Adr/GNRs@PMs-antiEpCAM
Size (nm, mean ± SD)	110.0 ± 0.7	117.1 ± 1.3
PDI (nm, mean ± SD)	0.258 ± 0.04	0.270 ± 0.03
ζ_{pot} (mV)	- 30.8	- 27.4
[Au] (mM)	1.2	1.1
λ_{max} (nm)	820	820
[Adr] (μg mL^{-1})	62	55
[anti-EpCAM] (μg mL^{-1})	-	4

Table 1.3.1 - Characterization of Adr/GNRs@PMs and Adr/GNRs@PMs-antiEpCAM.
Abbreviations: λ_{max}, maximum absorption wavelength; Adr, Adriamycin; EpCAM, epithelial cell adhesion molecule; GNRs, gold nanorods; PDI, polydispersity index; PM, polymeric nanomicelles; ζ_{pot}, Zeta-potential.

an aqueous solution containing sodium cholate hydrate as a stabilizing agent (**Figure 1.3.1**). The resulting Adr/GNRs@PMs were partially kept as negative control and partially conjugated with the A complete characterization of the final micelles, before and after conjugation with antiEpCAM antibody, was carried out and reported in **Table 1.3.1**. Micelles showed a suitable size and polydispersity index for in vivo applications and excellent stability even after the conjugation procedure. Similarly, GNRs remained unaltered during the entire process as demonstrated by the maintenance of λ_{max}.

Identification of binary bomb-EpCAM in Hepa1-6 cell spheroids

To determine if the synthesized Adr/GNRs@PMs-antiEpCAM can bind to HCC cell spheres, immunofluorescence staining was performed to identify the antiEpCAM in the micelles using donkey anti-mouse IgG1 PE-conjugated antibody. Positive staining (red spots in **Figure 1.3.2**) was found in the Adr/GNRs@PM-antiEpCAM-treated Hepa1-6 cell spheroids but not with Adr/GNRs@PMs-treated Hepa1-6 cell spheroids, thus confirming the importance of the targeting EpCAM on the surface of micelles to increase their binding affinity for the CSCs which are enriched in the Hepa1-6 cell spheroids.

Cell viability

Significant cell viability reduction was found in both cells and spheroids treated with Adr/GNRs@PMs-antiEpCAM. In particular, laser exposure produces a drastic decrease in the viability of cancer cells treated with the final nanosystems, thus demonstrating the advantages in terms of the binary bomb for releasing Adr in addition to thermal ablation properties

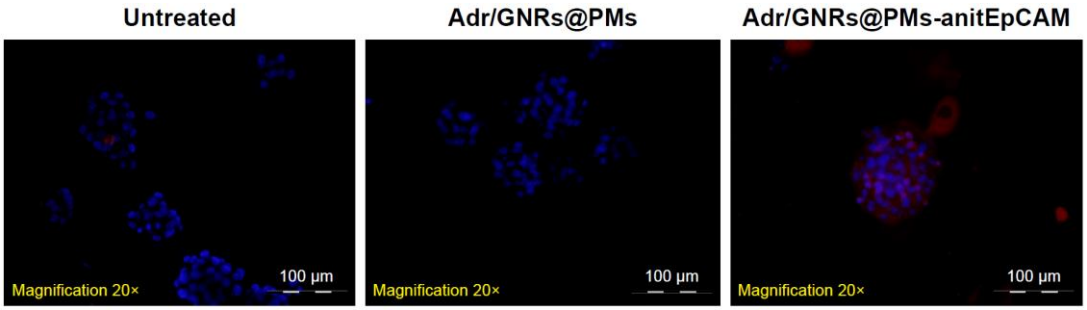

Figure 1.3.2 - Identification of Adr/GNRs@PM-antiEpCAM in Hepa1-6 cell spheroids.
Notes: Blue: DAPI positive staining of nuclei in the spheroid. Red: positive staining of antiEpCAM which were labelled Adr/GNRs@PMs.

derived from GNR particles (Figure 1.3.2). To determine whether the photothermal effect of the GNRs could affect cell viability, the temperature was determined in the Hepa1-6 cells with treatments of three GNR-based micelles (GNRs@PM, GNRs@ PMs-antiEpCAM, and Adr/GNRs@PMs-antiEpCAM). The temperature was significantly increased with laser exposure at 40 and 60 seconds, compared to the 0-second laser exposure. The cytotoxicity of GNRs@PMs and GNRs@PM-antiEpCAM was also determined by MTT assay. The result indicated that about 10% growth inhibition of Hepa1-6 cells was induced by the two micelles (GNRs@PMs and GNRs@PMs-antiEpCAM) with laser exposure, indicating that GNR-derived thermal effect could also contribute to the cell death which was consistent with our previous report (**Figure 1.3.3**). [116]

Orthotropic tumour model

An orthotropic tumour model was established for further study. The animal surgery procedure was reported by our group previously.[118] Ultrasound imaging was performed weekly to measure the tumour size. The tumour size was measured as 2.2 mm in length and 1.5 mm in width. Then the animals were further treated with Adr/GNRs@PM-antiEpCAM.

Identification of Adr/GNRs@PM-antiEpCAM in HCC tissues

As described in the Experimental section, the tumour burden in the animals was treated with Adr/GNRs@PMs-antiEpCAM and laser. Three days after the treatments, the animals were sacrificed and the tumour tissues were harvested. In the frozen tissue, Adr/GNRs@PMs-antiEpCAM binding to the tumour tissue was determined using immunofluorescence staining. Positive staining (green spots in **Figure 1.3.4**) identified antiEpCAM in the micelles using anti-mouse IgG1 FITC-conjugated antibody. This result provided evidence that Adr/ GNRs@PMs-antiEpCAM also had a high binding affinity with tumour tissue in vivo.

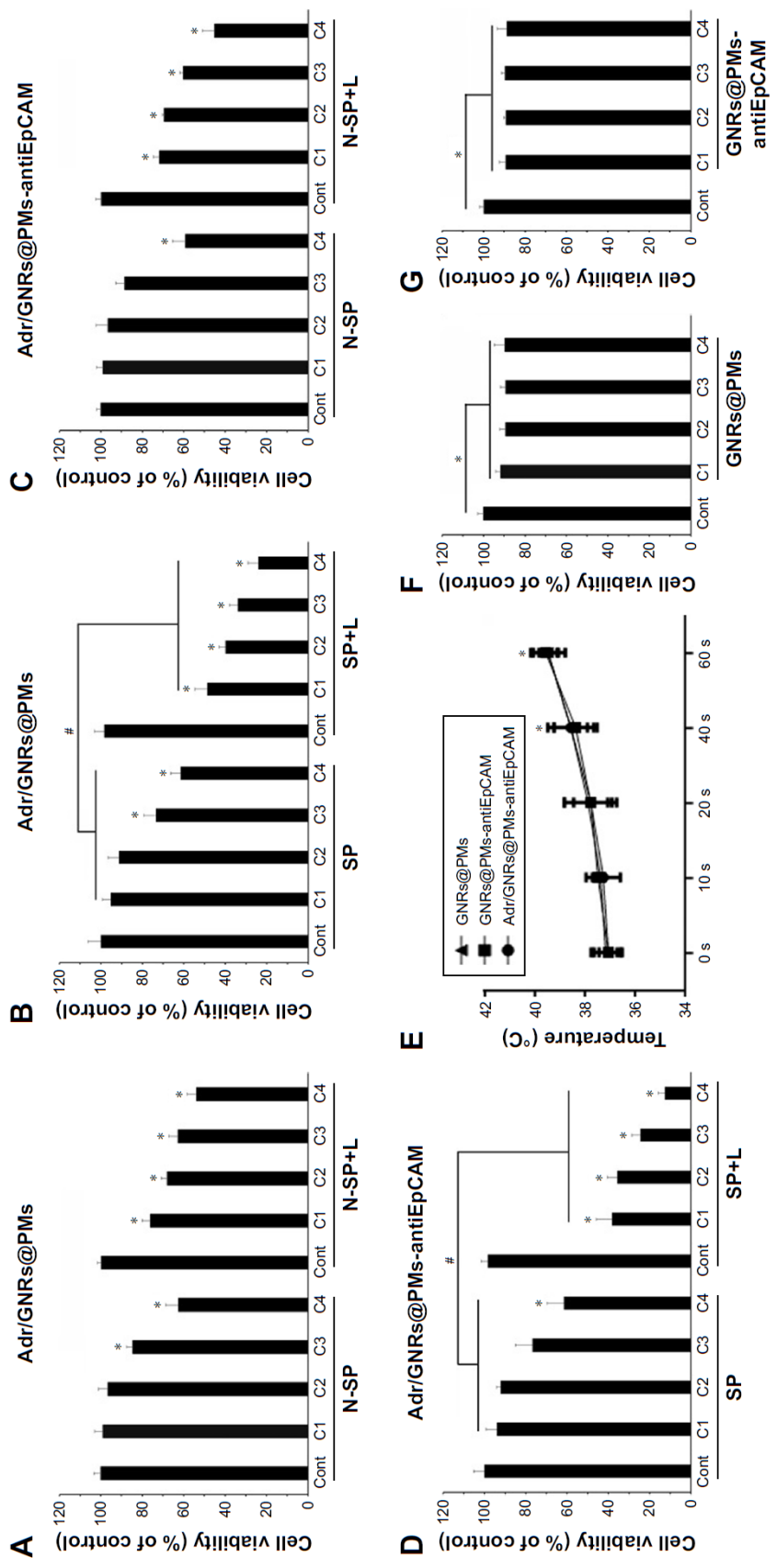

Figure 1.3.3 - Cell viability by MTT assay.
Notes: (**A**, **B**) Adr/GNRs@PMs-treated Hepa1-6 cells and Hepa1-6 spheroids. (**C**, **D**) Adr/GNRs@PMs-antiEpCAM-treated Hepa1-6 cells and Hepa1-6 spheroids. (**E**) Temperature determined in the medium of epa1-6 cells with the treatments of three micelles and laser exposure. (**F**) Cell viability of GNRs@PMs at 4 different concentrations. (**G**) Cell viability of GNRs@PMs-antiEpCAM at 4 different concentrations. **P*,0.05 vs control, #*P*,0.05.
Abbreviations: Adr, Adriamycin; C1, concentrations of 12.5 μg; C2, concentrations of 25 μg; C3, concentrations of 50 μg; C4, concentrations of 100 μg; Cont, untreated control; EpCAM, epithelial cell adhesion molecule; N, gold nanorod; L, laser exposure; N-SP, non-spheroids; PM, polymeric nanomicelles; s, second; SP, spheroids.

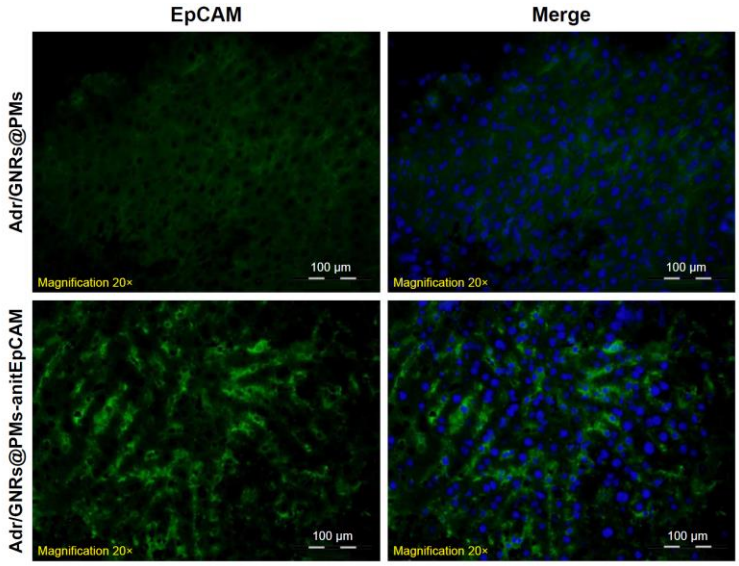

Figure 1.3.4 - Identification of binary bomb-EpCAM tumour tissues of mice.
Notes: Blue: DAPI-positive staining of nuclei in the spheroid. Green: positive staining of antiEpCAM which were labelled Adr/GNRs@PMs.

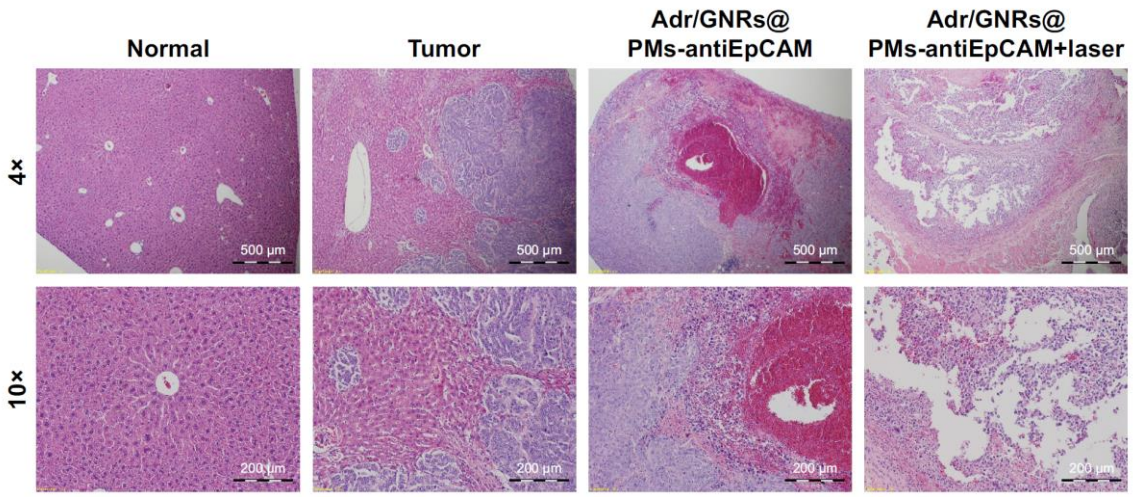

Figure 1.3.5 - Histology of Adr/GNRs@PMs-antiEpCAM treatment and Adr/GNRs@PMs-antiEpCAM treatment with laser exposure.
Notes: Left: normal liver tissue and HCC cell inoculation; Right: Adr/GNRs@PMs-antiEpCAM treatment only and Adr/GNRs@PMs-antiEpCAM treatment after laser exposure. Adr/GNRs@PMs-antiEpCAM with laser exposure caused significant cell death in the tumour tissue.
Abbreviations: Adr, Adriamycin; EpCAM, epithelial cell adhesion molecule; GNR, gold nanorod; PM, polymeric nanomicelles.

Histopathology

Histology showed that the inoculated HCC tumour grew and invaded the hepatic parenchyma. Three days after treatments, it was observed that Adr/GNRs@PMs-antiEpCAM treatment caused tumour cell death and lymphocyte infiltration as well as haemorrhage in local regions. However, Adr/GNRs@ PMs-antiEpCAM treatment with laser exposure caused extensive tumour cell death, implying that most tumour cells were killed by the binary bomb by the release of Adr in addition to thermal ablation properties deriving from GNRs (**Figure 1.3.5**).

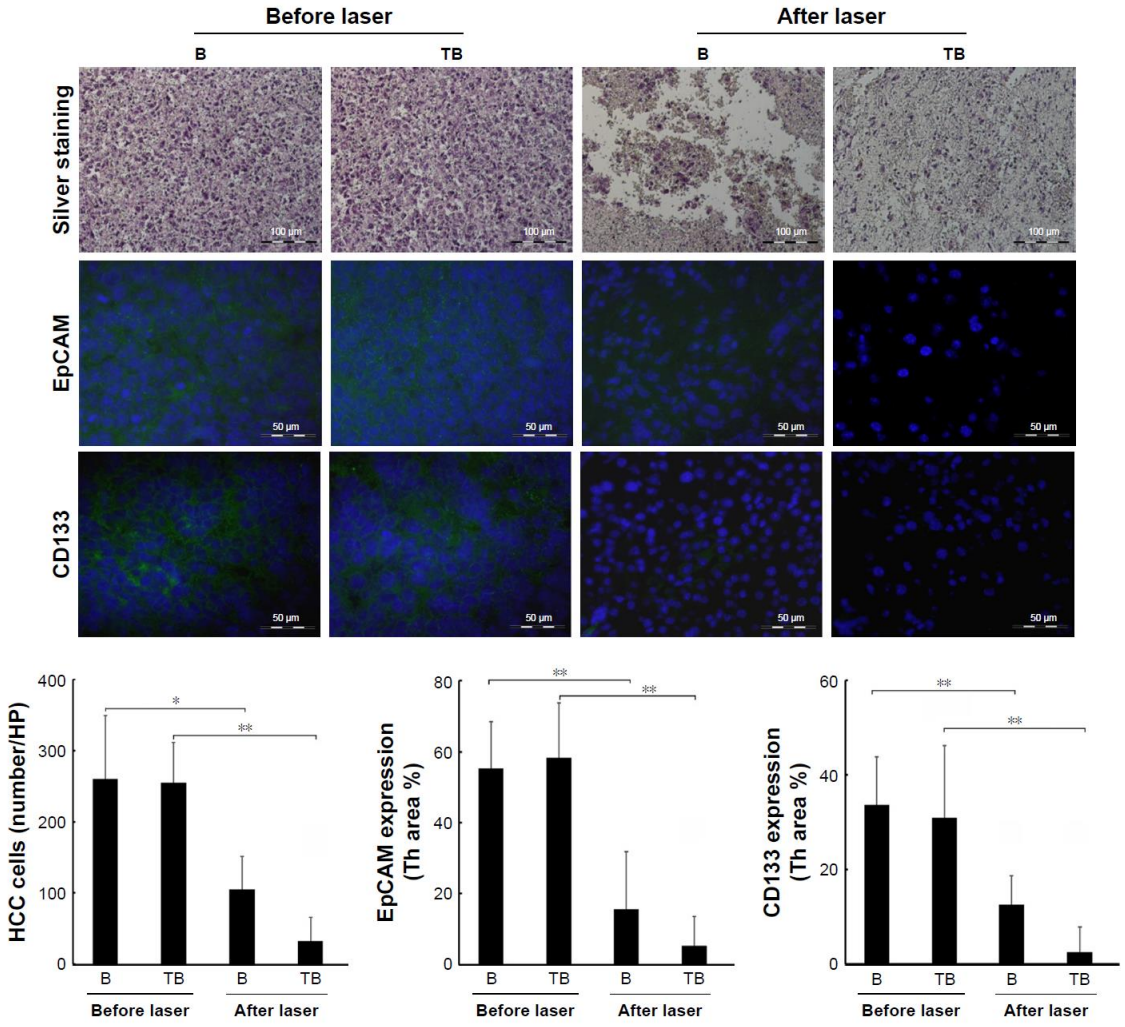

Figure 1.3.6 - Upper: Quantification of HCC cell-killing in the tumour tissue by silver staining. Middle and lower: Identification and quantification of cancer stem cell surface markers EpCAM and CD133 by immunofluorescence staining. Blue: DAPI-positive staining of nuclei in the tumour tissue. Green: positive staining of EpCAM and CD133. B (bomb): Adr/GNRs@PMs; TB (targeting bomb): Adr/GNRs@PMs-antiEpCAM. *P,0.05, **P,0.01.

Evaluation of HCC cell killing and CSC surface markers

To evaluate the tumour cell-killing effect in vivo, a silver staining assay was performed to determine the tumour cell-killing efficacy of Adr/GNRs@PMs-antiEpCAM and Adr/GNRs@PMs. As shown in **Figure 1.3.6**, both of the two micelles showed excellent tumour cell-killing effects after laser exposure. Adr/GNRs@PMs-antiEpCAM with laser exposure showed a significant effect of tumour cell-killing compared with Adr/GNRs@PMs. To evaluate whether the binary bomb targeted the CSC, two CSC markers were determined in the tumour tissues. Both the micelles showed a significant effect for destroying the CSC markers in the tumour tissues.

PA results

We report the patterns and the PA images acquired on different slices in **Figure 1.3.7A–C**. The typical PA spectra show two peaks around 700 and 800 nm over an increasing trend (PA intensity was between 0.05 and 0.15 a.u.) with respect to the increase of the wavelengths. 3D PA-US reconstruction of the whole healthy liver is shown in **Figure 1.3.7D**.

The assessment of PA readouts in different slices of liver samples with the tumour injected

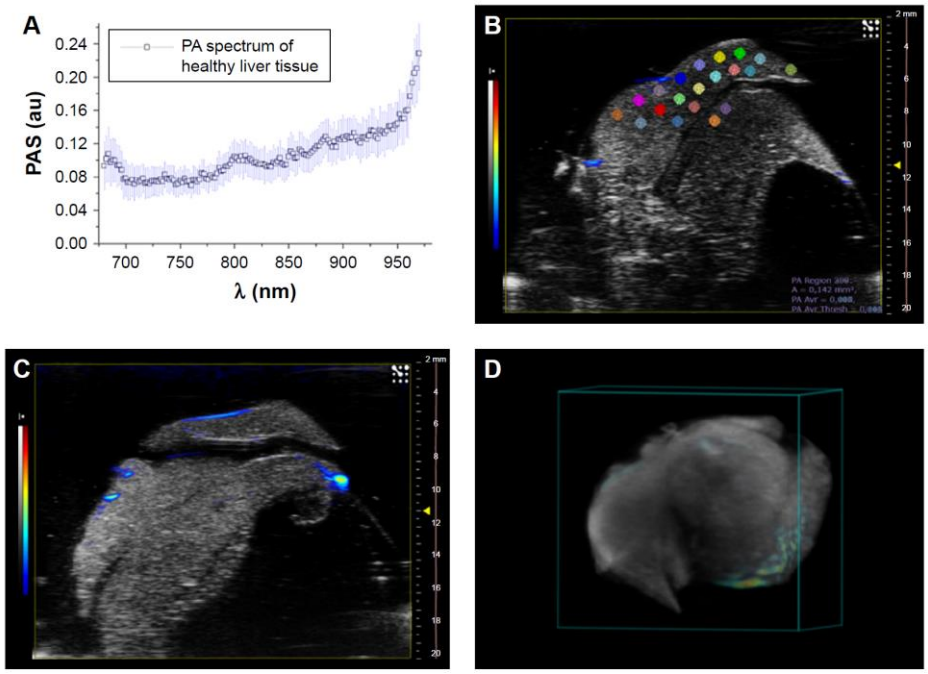

Figure 1.3.7 - (A) PA spectrum of healthy liver tissue; (B and D) two different PA-US slice images acquired from the healthy liver, where some ROIs (0.334 mm^2) in which the PA signal was calculated are shown in (B); (C) the 3D PA-US render of healthy liver reconstructed from 176 slices of around 150 μm, the intensity of ultrasound signal in grayscale and PA records in coloured bars.
Abbreviations: PA, photoacoustic; PAS, photoacoustic signal; ROI, region of interest; US, ultrasound

with the functionalized nanoparticles, showed different PA spectral patterns and intensity, compared with healthy liver tissues. The mean PA spectrum calculated on the EpCAM samples presented a Gaussian trend with a peak at around 860 nm. The plot also reported the mean normalized signal of GNRs (non-functionalized nanoparticles) found in *in-vitro* characterization. The spectral shift in corresponding phantoms (test object been used) could be explained by the interaction of the functionalized GNRs and the biological environment in which the nanoparticles are distributed after the injection, which modifies the original GNR spectrum in terms of peak shift and shape (wideness).

By unmixing processing, we obtained a spatial distribution map of different spectral distributions that revealed the presence of PA signal of nanoparticles in the livers analyzed. **Figure 1.3.8A–H** reports two PA-US acquisition series of EpCAM1 (A–D) and EpCAM2 (E–H) liver samples in which the PA signal distribution (A and E) and their related result after spectral unmixing processing (B and F) were shown. The PA unmixed images (**Figure 1.3.8B,F**) showed the PA spectral contribution of deoxy-haemoglobin in blue colour, the PA spectral contribution of oxy-haemoglobin in red colour, and the PA distribution due to the nanoparticles in green colour. The 3D PA-US renders of the whole liver sample (**Figure 1.3.8D,G**) were reported so as to better clarify the PA distribution inside the liver lobes.

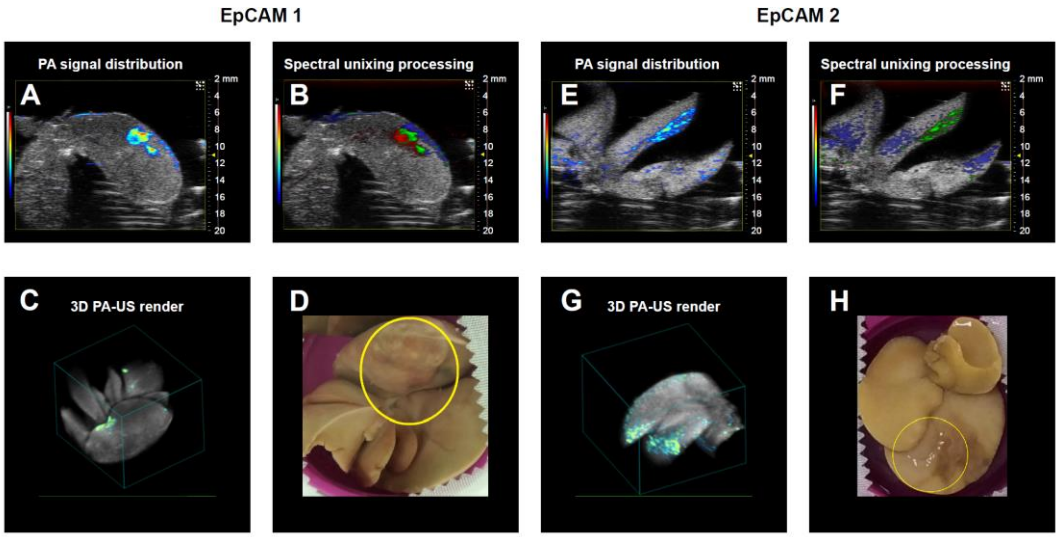

Figure 1.3.8 - PA signal distribution (**A**, **E**), spectral unmixed algorithm processing (**B**, **F**), and 3D PA-US render reconstructed by 145 slices of 150 μm thickness (**C**, **G**), and the photos of samples (**D**, **H**), for EpCAM 1 and EpCAM 2, respectively. The yellow circles were placed on the tumour regions where the signal was acquired. In the PA unmixed images (**B**, **F**), the spatial distribution of nanoparticles is represented in green colour, deoxy-haemoglobin chromophores in blue colour, and oxy-haemoglobin chromophores in red colour; grey scalebar for ultrasound signal intensity; coloured scalebar for PA signal intensity.

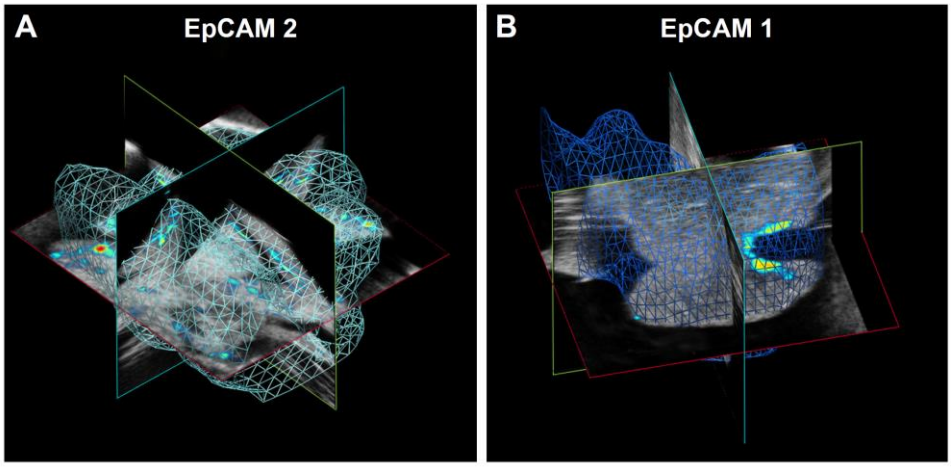

Figure 1.3.9 - Volumes of calculation of averaged PA signal in (**A**) EpCAM 2 and (**B**) EpCAM 1 liver samples.

Figure 1.3.8D and H show the photos of liver samples, where the yellow circle represents the region of PA and US acquisition.

We examined the whole 3D PA-US acquisitions (**Figure 1.3.9**): the PA signal average on a 3D volume representation of EpCAM 1 and EpCAM 2 found to be 0.132 and 0.534 au confirmed a similar trend with the ratio of the equivalent Au content found by ICP-MS assay. Although the number of samples was low, we tried to analyze the texture of the images to find a parameter that could describe the pattern of tumour tissue. The texture analysis, already tested in our previous work, was based on the study of 122 parameters. In this work, we applied the analysis on ten different slices of healthy, EpCAM 1, and EpCAM 2 liver samples.

1.3.3 Discussion

An ideal chemo-drug would not be toxic to normal cells but able to kill the cancer cells at the local tumour site. In this study, the Adr/GNRs@PMs-antiEpCAM was designed to release the Adr drug and GNRs under the control of NIR light exposure.

In the literature, several studies describe the photothermal effect generated by the light irradiation of gold nanoparticles in tumours.[112,119,120] Indeed, the production of plasmonic resonances can be stimulated and used to increase the local temperature drastically to provide heating capabilities to the nanoparticles to kill the cancer cells, without damage to

the healthy tissue. This effect was extensively studied and demonstrated in different ways. In particular, Norouzi et al.[121] in 2018 reviewed the past studies of PTT using gold nanoparticles, underlining the efficacy of the methodology and how it is possible to apply PTT by manipulating the physical characteristics of gold nanoparticles, in terms of size, synthesis, and other reported parameters. The GNRs used in the present work, that is, Adr/GNRs@PM-antiEpCAM, have similar physical-chemical characteristics and optimized aspect ratio to those reported in the literature, leading to a comparable heating performances vs quantum yield.

The important features of this nanosystem were biocompatibility and controlled release of the drug on to target CSCs leading to their elimination. Our in vitro data indicated that Adr/GNRs@PMs-antiEpCAM was effective to kill the CSCs which were enriched by the spheroid assay. When administrated locally into the tumour, this Adr/GNRs@ PMs-antiEpCAM also showed a tumour-killing effect, evidenced by extensive cell death in the tumour. Adr/GNRs@ PMs-antiEpCAM could be more efficient to kill the CSCs via antiEpCAM targeting because EpCAM has been identified as a surface marker, which is associated with aggressive clinicopathological features and indicates poor prognosis in patients with HCC.[122] Furthermore, the increase of local concentration of Adr by Adr/GNRs@PMs-antiEpCAM would increase the efficacy in tumour cell-killing. Unlike traditional administration of chemo-agents, the unique aspect of Adr/GNRs@PM-antiEpCAM could be the reduced toxicity to benign cells because it is targeted to the EpCAM-positive tumour cells, other than those EpCAM-negative hepatocytes.[123] In addition, the GNRs in Adr/GNRs@PMs-antiEpCAM coupled with NIR light exposure could enable thermal-based ablation targeted specifically at the tumour site. Evidence has shown that cancer cells are more vulnerable to elevated temperatures (42°C–49°C) compared with healthy cells, due to the hypoxic environment and higher metabolic rates, which is supported by a previous report.[124,125] Taken together, our study shows that the combination of Adr/GNRs@PMs-antiEpCAM with NIR exposure to treat liver cancer is technically feasible. Drug targeting using gold nanoparticles exhibit potential for use in the HCC patients who are not candidates for surgery and considerable study on this strategy remains to be carried out in the future.

1.4 An Application of Multivariate Data Analysis to Photoacoustic Imaging for the Spectral Unmixing of Gold Nanorods in Biological Tissues

Maturi, M.*; Armanetti, P.; Menichetti, L.; Comes Franchini M.. *Nanomaterials* **2021**, *11*, 142

1.4.1 Introduction

Nowadays, hyperspectral photoacoustic (PA) imaging of endogenous contrast in biological systems shows good potential as it is exploitable for the study of tumour angiogenesis and melanoma.[72,126] A relevant number of contrast agents for photoacoustic imaging (PAI) has been developed[12,127,128], and among them, plasmonic nanoparticles have gained considerable interest over the past few decades due to their tunable surface plasmon resonances, relative biological stability/biocompatibility, and easy functionalization. Indeed, GNRs represent an ideal contrast agent for PA since they can provide an enhanced optical absorption contrast against background tissue.[15,33,129] Their tuneable longitudinal surface plasmon resonance (LSPR) properties allow for the preparation of tissue-specific theranostic platforms exploiting the contrast they provide in photoacoustic imaging and their photothermal properties, which can be exploited for laser ablation-based therapeutic techniques. [130–132] The use of hyperspectral imaging coupled with multivariate resolution analysis techniques could represent a powerful approach in studying the biological variation of samples and developing new biomedical applications. Hyperspectral images combine the spatial information of optical microscopy and the biochemical information provided by a spectroscopic technique. In the case of biological samples, contributions of many different molecules (i.e. oxy- deoxy-haemoglobin), the variability of the biological components *in-vivo*, and the limited PA signal amplitude are often very critical to the interpretation of the PA spectra and the multivariate resolution image. To resolve this issue, the use of image resolution/unmixing methods can aid in recovering the single component of the spectra and defining the image constituents of the biological sample. Due to the high variability of *in vivo* micro-environment, the definition of the association between molecular absorption and image constituent is not straightforward as this heavily depends on the within-tissue compositional and molecular variability.

To extract the spectral information of biological samples, multivariate solution analysis techniques represent a powerful solution that can perform the spectral unmixing.[133] Several methods have been reported in the literature for multivariate analysis of hyperspectral data (*principal component analysis*, PCA, and *principal component regression*, PCR), which are mostly coupled to spectroscopic imaging techniques like fluorescence microscopy, NIR, and Raman imaging.[134–138] Among them, *multivariate curve resolution – alternating least squares,* MCR-ALS, became a popular chemometric tool for the resolution of multiple-component responses in complex mixtures when dealing with hyperspectral imaging data.[139–141] Up to date, the application of multivariate analysis in the PA field is still in the infancy and limited so far to the resolution of the different sources of endogenous contrast, even though its potential for discriminating between exogenous contrast agents is promising. [142–144] Recently, additional complex mathematical approaches were implemented for the study of PA imaging data (such as deep learning and neural networks) that apply non-linear models to perform spectral unmixing.[145–147] However, these approaches appear less versatile than linear models since they include much more information of the system, such as the modelling of the propagation of light inside the tissue, and are strongly dependent on the type of tissue and the instrumental parameters selected for the experiment.

This work aims to report the performances of MCR-ALS analysis to PA real images: three distinct PEGylated synthetic GNRs with LSPR absorption peak ranging from 700 to 950 nm underwent PA imaging analysis *ex vivo*, and the multivariate approach was applied on the raw PA data to separate the spectral contributions arising from the different chromophores (**Figure 1.4.1a,b**). As a case study, MCR-ALS was used to analyze *ex vivo* imaging data recently published by our groups on active-targeted GNRs in mice liver.[33] The selection of biological test objects and real biological tissues ex vivo allowed us to validate the methodology and verify the performance of the method. In this case, the unmixing algorithm allowed for the separation of the spectral contribution of GNRs, related to the presence of hepatocellular carcinoma, to the contribution of blood, which represents the main interference when dealing with the PA imaging of living tissues (**Figure 1.4.1c**). Finally, the MCR-ALS results were semi-quantitatively compared with the PA built-in unmixing tool to evaluate their performances.

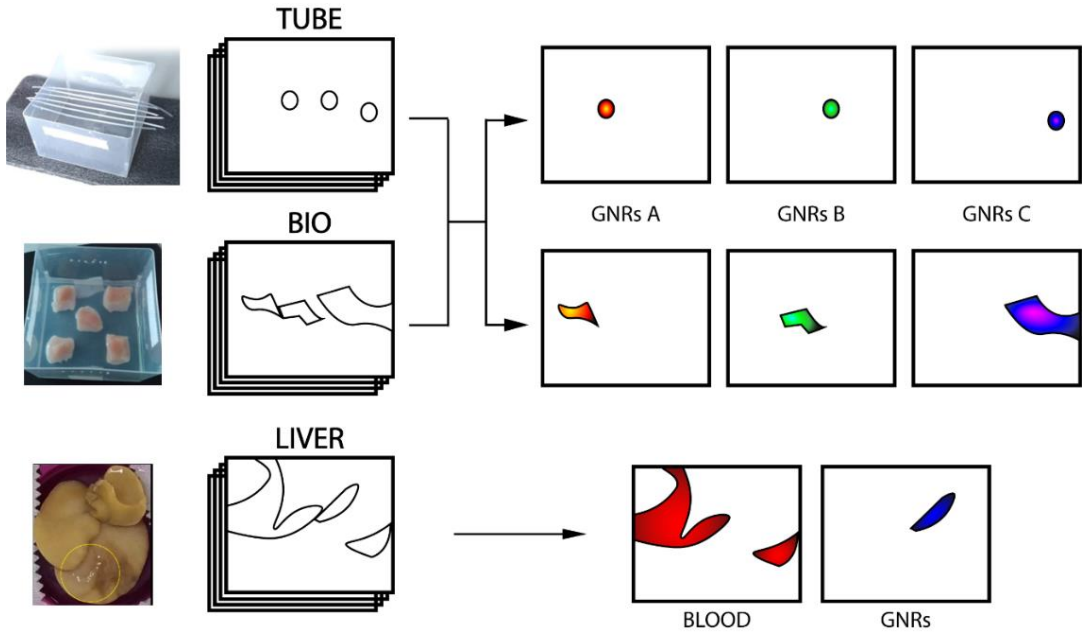

Figure 1.4.1 - Schematic representation of the approach described in this work. GNRs with different absorption properties underwent multispectral PA imaging in polyethylene (PE) tubes and chicken breasts generating "TUBE" and "BIO" multispectral datasets (**a, b**). Then, the multivariate analysis was applied to the combined datasets generating spatial distributions of the different contrast agents in the imaged section. Then, as a case study, the algorithm was applied to the multispectral PA imaging data of GNRs in tumour-bearing mice liver, the "LIVER" data set (**c**).

1.4.2 Methods

PA in a standard sample ("TUBE" data set)

The PA tests were performed analyzing the PA multispectral signal amplitude of GNRs at different longitudinal surface plasmon resonances (LSPR) in the optical windows of near-infrared I (NIR I), corresponding at the wavelength range between 680 and 970 nm. The GNRs were loaded in a coplanar net of polyethylene tubes inserted in a polypropylene box (PA panel I), then the PA probe was coupled to the samples by water to prevent possible artefacts. To avoid reshaping of GNRs under PA excitation, a homogeneous thin layer of biological tissue (chicken breast) was put on top of the tubes. The PA characteristics of GNRs were studied using PA multispectral analysis (**Figure S3b-d)** to find their specific spectral fingerprint and, under prolonged laser stimulation at their LPRS peaks, to assess the photostability of the PA signal over time (around 40 seconds, corresponding at over 200 laser shots). The data set produced with these acquisitions will be referred to as the "TUBE" data set.

***Ex-vivo* PA evaluation in chicken breast**

As reported[148], a chicken breast sample injected with a standard solution of GNRs was produced (for simplicity, identified as "BIO" data set). A bolus of the order of 100 μL was prepared and injected *ex-vivo* in a chicken breast specimen. Then, the spectral distributions of the PA signals generated inside the chicken breast volume by laser stimulation were evaluated. Images were acquired using PA multispectral analysis between 680 nm and 970 nm at 2 nm steps, generating 146 images per analyzed specimen. Since each image had a size of 503x647 pixels, the total data set contained 325441 spectra for each acquisition. From the image size and the corresponding number of pixels, the pixel size was estimated to be around 36 μm.

***Ex-vivo* PA evaluation in mice liver**

The PA images contained in this data set were acquired in *ex-vivo* samples obtained as reported previously. [6] Employed GNRs displayed a maximum absorption wavelength of 820 nm. PA images were acquired in the range 680-970 nm at 2 nm steps, generating 146 images per analyzed section. Since each image had a size of 505x648 pixels, the total data set contained 327240 spectra for each acquisition.

Multivariate Analysis

The data post-processing was conducted on the Matlab R2018a platform, exploiting the MCR-ALS toolbox developed by Jaumot et al. in 2005 and optimized in 2015.[149,150] An overview of the theory involving the MCR-ALS approach can be found in the Supplementary Materials.

Briefly, it involves an iterative calculation that employs least-squares approaches to solve **Equation 1.1.2** under the obligation to comply with some mathematical constraint, generating the optimal results for **C** and $\mathbf{S^T}$ and minimizing the matrix of residuals, **E**.

$$\boldsymbol{D = C\,S^T + E} \qquad \textbf{Equation 1.1.2}$$

where **D** is the raw data set, **C** contains the distributions profiles of the modelled chemical species, $\mathbf{S^T}$ is their corresponding PA spectra and **E** represents the residual, the portion of data that is not included in the model. Non-negativity of both concentration profiles and spectra was set as a constraint for the multivariate analysis.

The result is formulated when convergence is achieved in two consecutive iterative cycles, with deviations of the residuals between experimental and ALS data less than 0.05%. The overall computing time required to run the algorithm on the input data set was lower than 5 min employing an Intel®Core™ i7-7700 processor with CPU@3.60 GHz and 32 GB of RAM.

1.4.3 Results and Discussion

Synthesis of PEGylated GNRs

CTAB-coated Gold Nanorods (GNRs) have been synthesized according to the previously reported seed-mediated growth method. [24,25] After ligand exchange with thiolated PEGs and purification, the three samples underwent VIS-NIR absorption analysis to assess the outcome of the syntheses in terms of their optical properties. The absorption analysis revealed the presence of high-intensity LSPR bands for GNRs A, B and C centred at 688, 820, and 940 nm, respectively (**Figure 1.4.2a**).

By adjusting the concentrations of surfactants, silver ions, and reducing agents, the aspect ratio of the prepared GNRs was 2.8, 4.2, and 5.5 for GNRs A, B, and C, respectively. These values were obtained from the wavelength of the longitudinal surface plasmon resonance (LSPR) peak according to the formula developed by Link et al [31] and showed herein as **Equation 1.4.1**:

$$\boldsymbol{AR = \frac{\lambda_{max} - 495.14}{53.71 \cdot \varepsilon_m} + 0.79} \qquad \textbf{Equation 1.4.1}$$

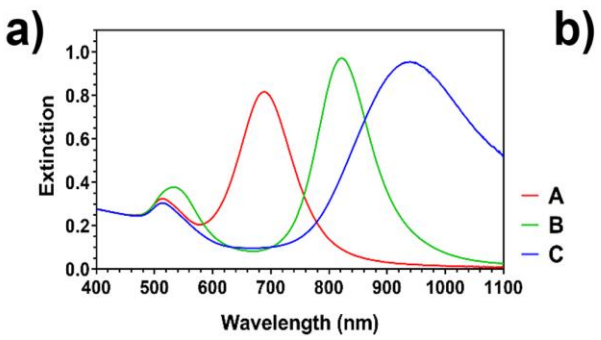

b)

	GNRs A	GNRs B	GNRs C
λ_{max}	688 nm	820 nm	940 nm
Aspect Ratio	2.8	4.2	5.5
Average width (TEM)	22 nm	23 nm	15 nm
Average length (TEM)	57 nm	91 nm	90 nm
Size (DLS)	85 ± 2 nm	104 ± 3 nm	105 ± 2 nm
ζ_{pot}	+19.8 mV	+17.4 mV	+18.1 mV

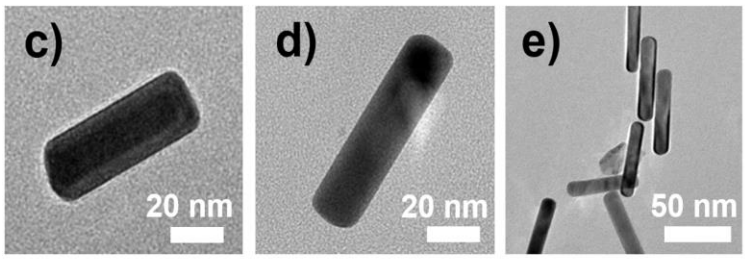

Figure 1.4.2. - Characterization of PEGylated GNRs. a) VIS-NIR extinction spectra of GNRs in water. Gold concentration was 100 μM for the three specimens. b) Summary of GNRs characterization parameters. Average TEM size has been obtained by measuring n=50 different GNRs for each synthetic batch. c-e) Representative TEM images of GNRs A, B, and C, respectively.

Where $\boldsymbol{AR}$ is the aspect ratio of the GNRs sample, $\boldsymbol{\lambda_{max}}$ is the wavelength corresponding to their LSPR peak and $\boldsymbol{\varepsilon_m}$ is the refractive index of the medium (for water $\boldsymbol{\varepsilon_m}$=1.77). These results were also confirmed by electron microscopy (**Figure 1.4.2c-e**) from which aspect ratios were calculated by measuring different GNRs (n=50) as 2.6, 4.0, and 6 for GNRs A, B, and C respectively. The nanosystem size determined by DLS is in agreement with the size determined by TEM, with no signs of aggregation phenomena in solution. Finally, dynamic light scattering was used to determine the hydrodynamic radius of the nanosystem and surface zeta potential measurements were performed to assess the stability of GNRs due to electrostatic repulsion between different nanoparticles. Results are summarized in **Figure 1.4.2b**, and they are compatible with the GNRs size determined by TEM and the presence of cationic amino groups on their surface.

Photoacoustic Imaging analysis

The PA signal of GNRs was stable during prolonged laser illumination at the LPSR peak wavelengths, with variation coefficients and signal-to-noise ratios ranging from 3.2% to 4.2% and 24 to 31, respectively.

Raw photoacoustic data were extracted from the Vevo platform as *.*dicom* files, containing the hypercubes for each selected projection in arbitrary units, co-registered with the US image. Multivariate analysis was performed twice:

- TUBE and BIO data sets have been combined into a single matrix $\mathbf{D}_1$, in order for them to be modelled simultaneously. This can be performed since the source of contrast (i.e. GNRs) has the exact same spectroscopic properties amongst the two experiments;
- For the LIVER data set, instead, the analysis was performed on a single data set, unfolded in the matrix $\mathbf{D}_2$.

The MCR-ALS algorithm requires an estimate of the spectra of the pure components to proceed with the data compression. Since in the TUBE data set the three GNRs solutions were physically separated and distinguishable, their uncontaminated PA spectra were employed for such purpose. This was performed by extracting the average PA spectrum of representative regions (50 x 50 pixels) of the "TUBE" data sets containing the PA response

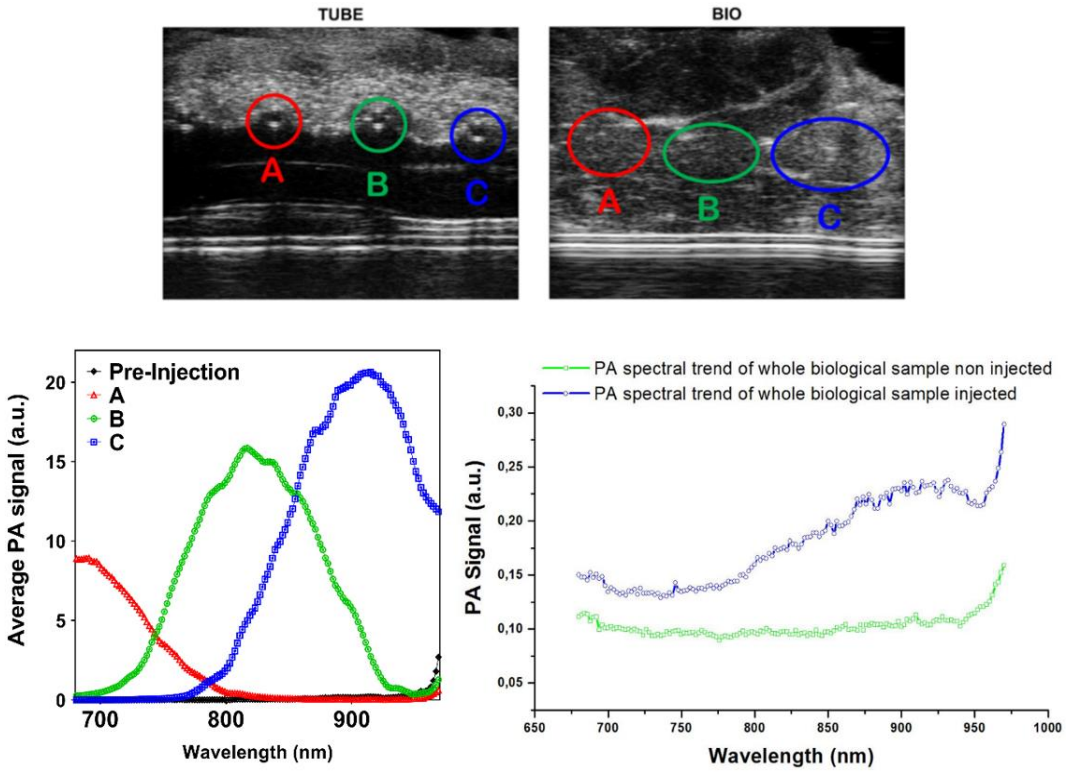

Figure 1.4.3 - Top: ultrasound images of the analysed specimens showing the regions in which the three contrast agents (GNRs A, B and C) were injected. Bottom left: comparison between PA spectra of PEGylated GNRs before and after injection of the three solutions in PE tubes. The PA spectra were obtained by averaging the spectra recorded in 50x50 pixel regions. Bottom right: plot of PA spectral trends of the biological sample before and after the injection of the different GNRs. This plot underlines the important role of unmixing algorithm and reveals the specific spectral trend of each one colloidal solution inside the biological tissue

of the separated GNRs solutions and compared to the PA spectrum of the biological tissue recorded prior to injection (**Figure 1.4.3**) revealing strong contrast from the nanostructured materials with partial overlap between different contrast agents but a negligible contribution from the background. These were compared with the VIS-NIR absorbance spectra of GNRs, showing perfect similarity (**Figure 1.4.3**). The input spectra were firstly normalized, then collected in the second input matrix, $\mathbf{x}_{0\_1}$, with size 146x3.

Multivariate Analysis of TUBE and BIO data sets

MCR-ALS was applied to the multivariate analysis of the sample as reported in **Figure 1.4.4a**. Since TUBE and BIO data sets were acquired by imaging identical sets of GNRs solutions, they were merged in order to model the two experiments simultaneously. The only applicable constraint of MCR-ALS to PA imaging was found to be the non-negativity of both concentration profiles and spectra. The unimodality constraint could not be applied since it forces the refined spectra to display only one local maximum, and this is misleading in the case of noisy spectra.[151,152] Besides, the closure constraint could not be applied: it acts as a mass balance and implies that the sum of the modelled concentration for all the modelled components is the same everywhere in the image. This is not applicable in multispectral imaging, whereas it finds useful applications in modelling chemical equilibria and reaction kinetics.[153] The intrinsic noise of the experimental technique does not allow for the implementation of unimodality constraints and the closure constraint had to be discarded because during the acquisition time, GNRs have the time to diffuse in and out from the sampled 2D section of the specimen, and a strict mass balance could not be applied. The output of the spectral unmixing was a 650882x3 matrix containing the whole distribution profiles of the three different GNRs in three separate images, $\mathbf{C}_1$. In addition, the algorithm generates the modified spectral profiles for the three contrast media, $\mathbf{S}^T_1$ such as to satisfy **Equation 1.4.1** while minimizing the error matrix $\mathbf{E}_1$. The $\mathbf{C}_1$ matrix was then separated and reshaped to obtain the pure distribution profiles, which were simultaneously overlapped with the original US traces of the original data sets (**Figure 1.4.4b, c**). Moreover, the output spectra contained in $\mathbf{S}^T_1$ resemble the input ones (**Figure 1.4.4d, e, f**).

This approach permitted a significant reduction of the size of the data set and was able to compress 650882 spectra into the combination of three spectra and six distribution images (corresponding to a total reduction of the number of data points from more than 95 million to less than 2 million). The most common approach for analyzing multispectral PA imaging involves the isolation from the hypercube of the images corresponding to the maximum absorption wavelengths of the identified chromophores and therefore relating those PA

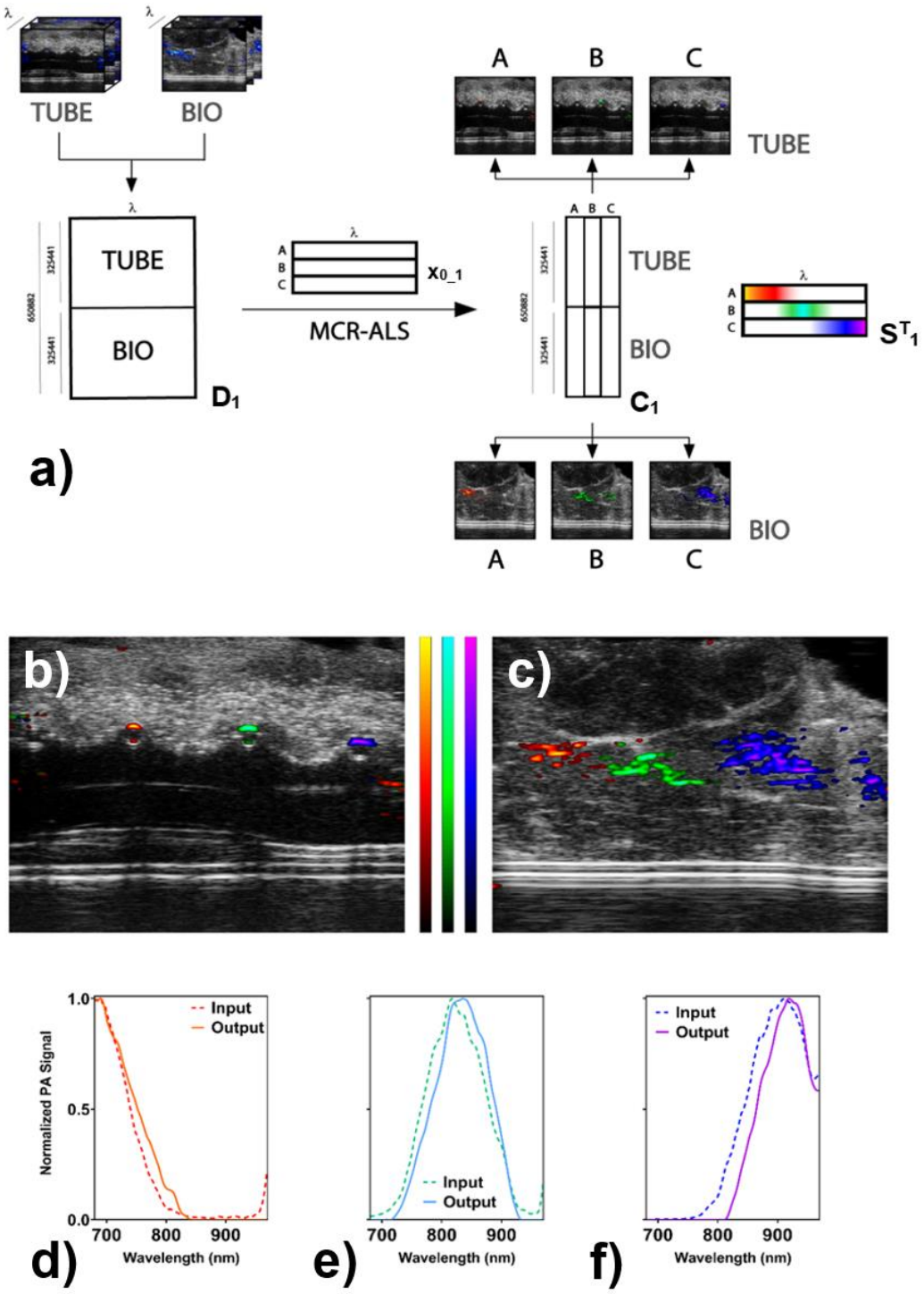

Figure 1.4.4 - a) Schematic representation of the applied algorithm on TUBE and BIO data sets. Firstly, the hyperspectral data cubes containing the PA images recorded at different wavelengths are reshaped to bidimensional matrices and merged into the input matrix $\mathbf{D_1}$. Then, by using the pure PA spectra of isolated GNRs A, B, and C in PE tubes (collected in the matrix $\mathbf{x_{0\_1}}$) the MCR-ALS analysis is applied, leading to the obtaining of a reduced matrix $\mathbf{C_1}$ containing the distribution profiles of the different GNRs in both data sets and the refined PA spectra of GNRs in the matrix S^T. Matrices sizes are: 503x647x146 for the hyperspectral data cubes, 650882x146 for matrix $\mathbf{D_1}$, 3x146 for $\mathbf{x_{0\_1}}$ and $\mathbf{S^T_1}$ and 650882x3 for matrix $\mathbf{C_1}$. b,c) Distribution profiles of GNRs obtained by applying the MCR-ALS algorithm to the TUBE and BIO data sets. Colour bars are in arbitrary units and are referred to as GNRs A (red to yellow), GNRs B (green to light blue), and GNRs C (blue to purple). d-f) Normalized input and output spectra for the three components are displayed.

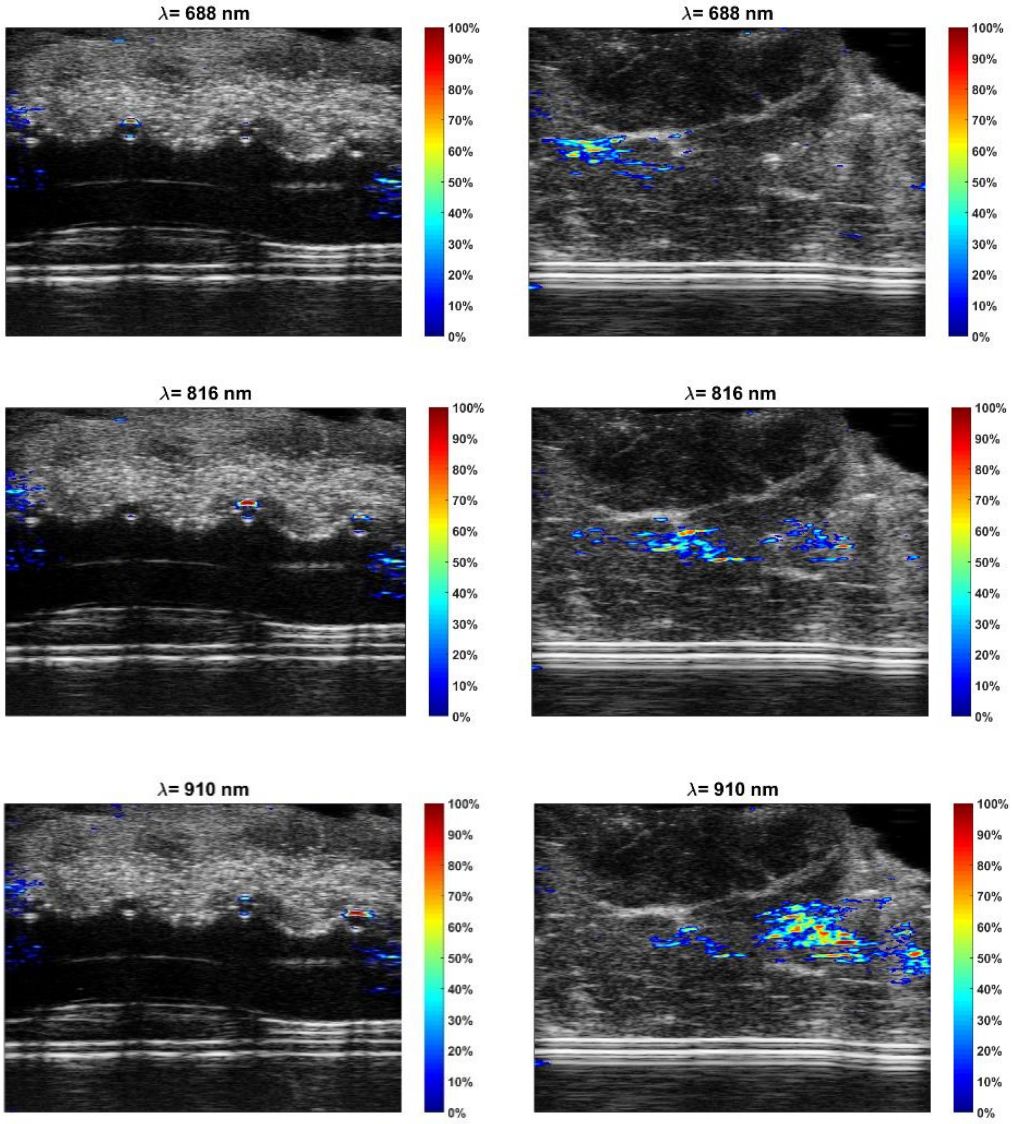

Figure 1.4.5 - Raw PA images (colour scale) overlapped with the co-recorded US trace (greyscale) for both TUBE (left) and BIO (right) data sets at the wavelengths of maximum PA emission for the three explored contrast agents.

emission maps to the spatial distribution of the corresponding chromophore (as it is reported in **Figure 1.4.5**). A limitation of this approach is represented by an incorrect balance between intensity and concentration. That is, a recorded low-intensity PA signal could suggest both a low concentration of one chromophore and a much higher concentration of another species that responds poorly to the excitation wavelength in question. For each overlapping region, it is necessary to extract the whole PA spectrum and to assess which is the dominant component. A multivariate approach was applied to process the massive amount of PA data contained in

the hypercube (146 images), giving only three images spatially encoded. Here, in the case of overlapping distributions, a strong signal in the unmixed distribution maps corresponds to an intense unresolved signal of the related species. With the presented multivariate approach, the images represent the distributions of the whole spectral features related to the present chromophores, thus allowing for fast and unambiguous discrimination between signals arising from competing molecular species. In the case of overlapping responses, a strong signal in the unmixed distribution maps corresponds to a considerable overall contribution of the related species. Due to the partial overlap between the spectra of GNRs B with GNRs A and C, few

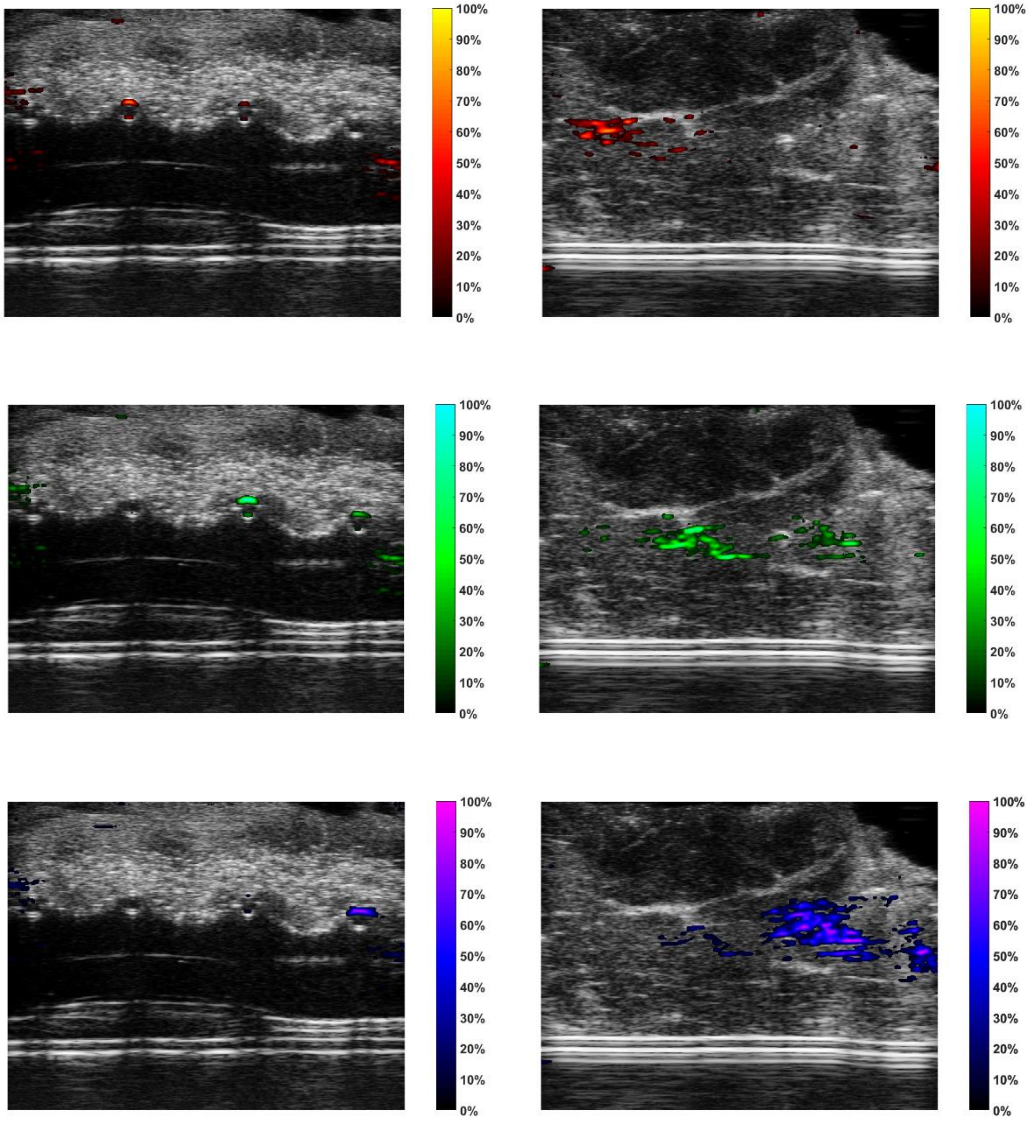

Figure 1.4.6 - Unmixed PA images (colour scale) overlapped with the co-recorded US trace (greyscale) for both TUBE (top) and BIO (bottom) data sets. Colour bars are in arbitrary units and are referred to GNRs A (red to yellow), GNRs B (green to light blue), and GNRs C (blue to purple).

pixels show non-zero concentration at the same time for more than a single contrast agent (A and B or B and C). However, by comparing the ratio between the intensity of the modelled signal of the two competing species, it was noticed that in all overlapping spots, one was at least 10 times stronger than the other (**Figure 1.4.6**). Therefore, it was chosen to display for each pixel only the contrast species that gave rise to the highest modelled concentration, which led to a distinct separation of the different contributions. Finally, the matrix of residuals ($\mathbf{E}_1$) was evaluated with respect to the corresponding original PA data set, revealing that all the deviations of the modelled data from the raw ones are less than 3% of the maximum amplitude for both data sets (**Figure 1.4.7**).

Multivariate Analysis of the LIVER data set

The PA response of the liver tissue is strongly influenced by the presence of blood; depending on whether it is oxygenated or deoxygenated, haemoglobin displays a distinct spectral profile in the NIR. For setting up the MCR-ALS spectral unmixing of GNRs, no reference material was available for the ex vivo sample. To extract the input spectra of blood and GNRs, the entire organ was analyzed and the following assumptions were made. Starting from the unmixed PA data, different profiles were detected in proximal organ regions: the first and third lobes respond mostly in the first part of the NIR I range (680-720 nm, peaked at 684 nm), while the central lobe was shifted to 800-840 nm region, peaked at 862 nm. The difference was sufficiently marked to perform an assignment of the different components, 1)

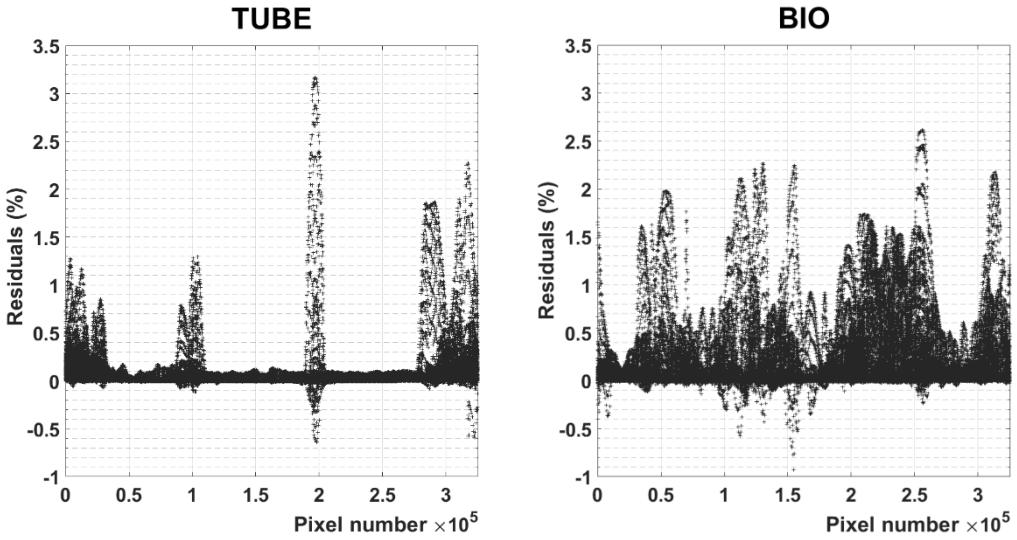

Figure 1.4.7 - Plot of the maximum residuals for each pixel across all wavelengths, representing the percentage of the maximum PA signal recorded for each data set that is not included in the model.

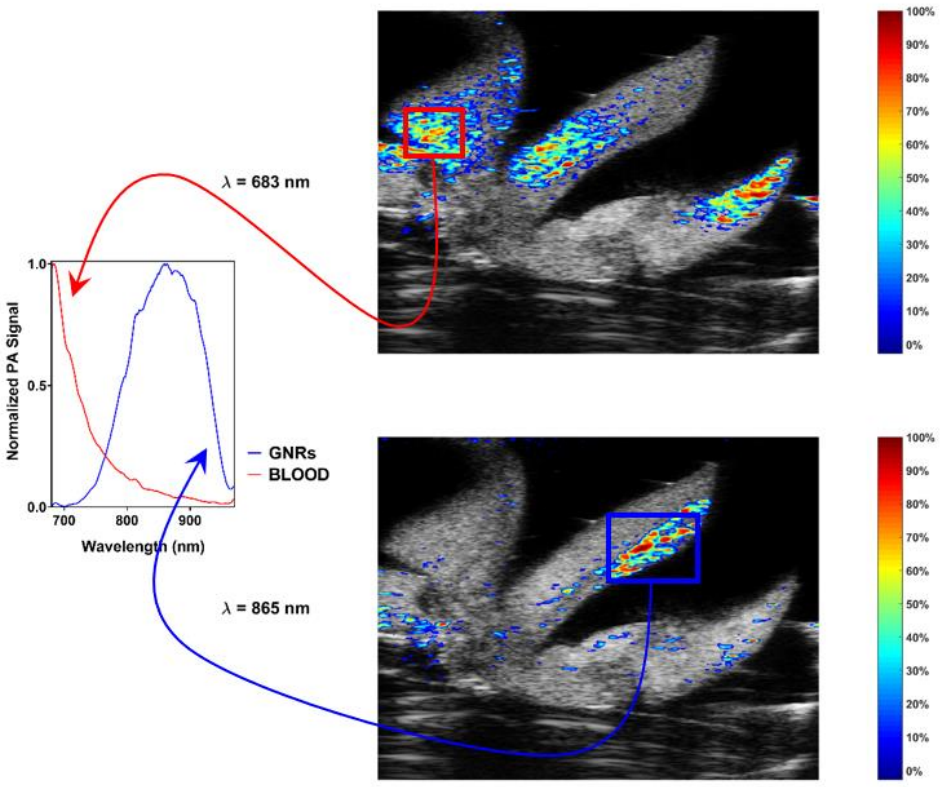

Figure 1.4.8 - Raw PA images (colour scale) overlapped with the co-recorded US trace (greyscale) for the LIVER data set at the wavelengths of maximum PA emission of the two main chromophores. Red and blue boxes identify the regions whose spectra have been averaged to obtain the input matrix $\mathbf{x}_{0\_2}$ for the MCR-ALS analysis, as highlighted in the plot at the left.

in the middle lobe to GNRs component, while 2) the signal in the lateral lobes to mainly blood. This was confirmed by the ratios between the PA signals of the two regions at the two selected wavelengths: at 684 nm the PA signal of the central lobe was only 1.3% of the signal at 862 nm, and the lateral lobes displayed at 862 nm 5% of the signal recorded at 684 nm. The input spectra for MCR-ALS were collected, averaging a relevant number of PA spectra in those two regions (**Figure 1.4.8**). At this level, the algorithm was fed with the new arrays (contained in the matrix $\mathbf{D}_2$ with size 327240x145) together with the normalized input spectra (**Figure 1.4.9a**).

A simple and fast unmixing of the PA imaging data into the matrix $\mathbf{C}_2$, containing the separated spectral contributions of GNRs and blood (**Figure 1.4.9b**), and the matrix $\mathbf{S}^T_2$ carrying the refined PA spectra of the two components (**Figure 1.4.9c, d**) was obtained. The capacity of separation of the two main chromophoric components in the analyzed organ provided a precise separation of the distribution profiles of the endogenous and exogenous contribution, with minimal overlapping (**Figure 1.4.10**).

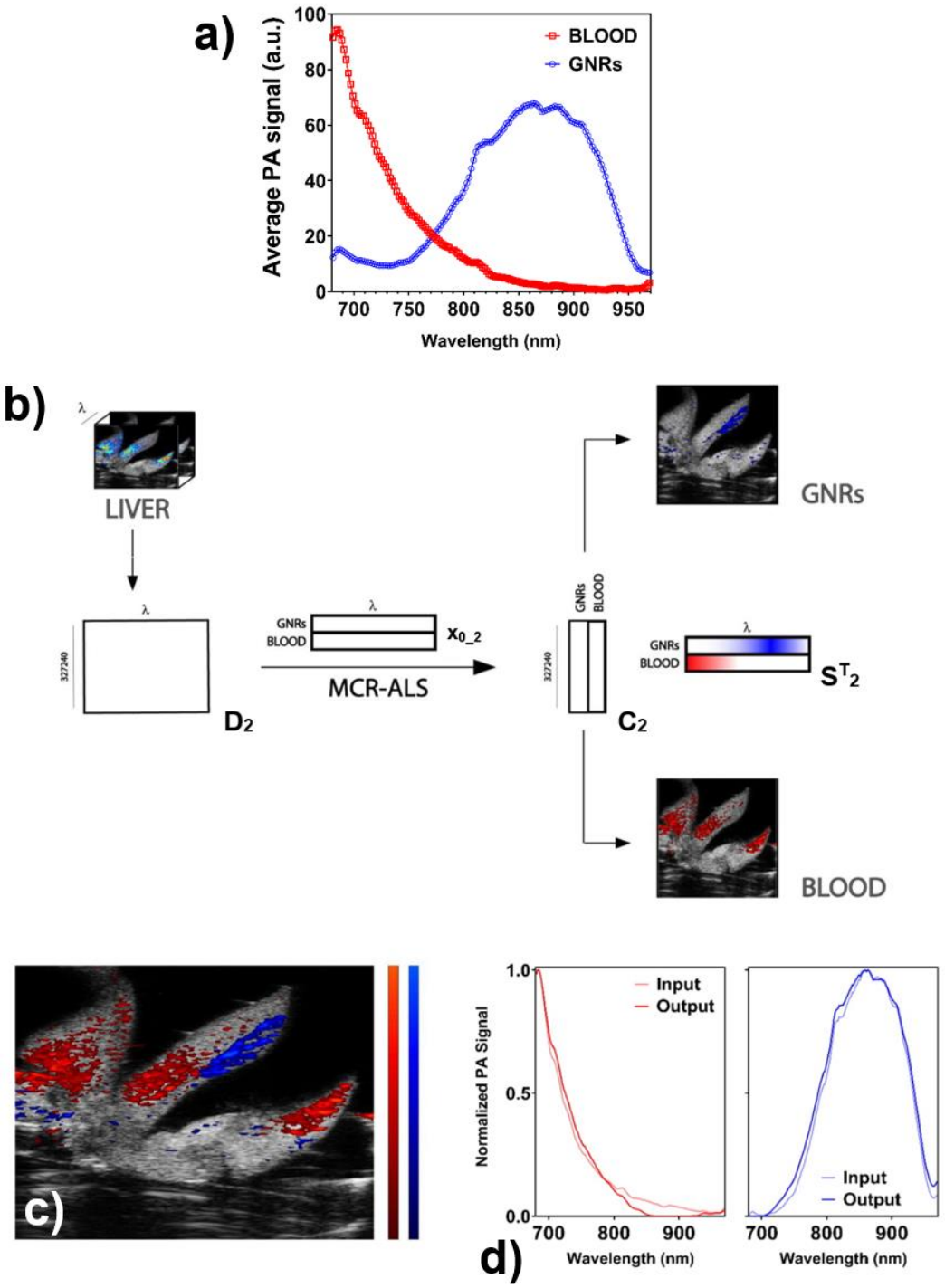

Figure 1.4.9 - a) Recorded non-normalized PA spectra averaged in a region of 50 x 50 pixels in the lateral lobes (blood, red line) and middle lobe (GNRs, blue line) revealing partial overlap between the spectral profiles and comparable signal intensities. b) Schematic representation of the applied algorithm on the LIVER data set. Firstly, the hyperspectral data cube containing the PA images recorded at different wavelengths is reshaped to the bi-dimensional matrix $\mathbf{D_2}$. Then, by extracting the PA spectra of blood and GNRs from different regions of the image, the matrix $\mathbf{x_{0\_1}}$ was built and fed to the MCR-ALS analysis. This lead to the obtaining of a reduced matrix $\mathbf{C_2}$ containing the separate distribution profiles of GNRs and blood and their refined PA spectra in the matrix S^T. Matrices sizes are: 505x648x146 for the hyperspectral data cubes, 327240x146 for matrix $\mathbf{D_2}$, 2x146 for $\mathbf{x_{0\_2}}$ and $\mathbf{S^T}$ and 327240x2 for matrix $\mathbf{C_2}$. c) Distribution profiles of GNRs obtained by applying the MCR-ALS algorithm to the LIVER data set. Colour bars are in arbitrary units and are referred to GNRs (red) and blood (blue) d). Normalized input and output spectra for the two components displayed.

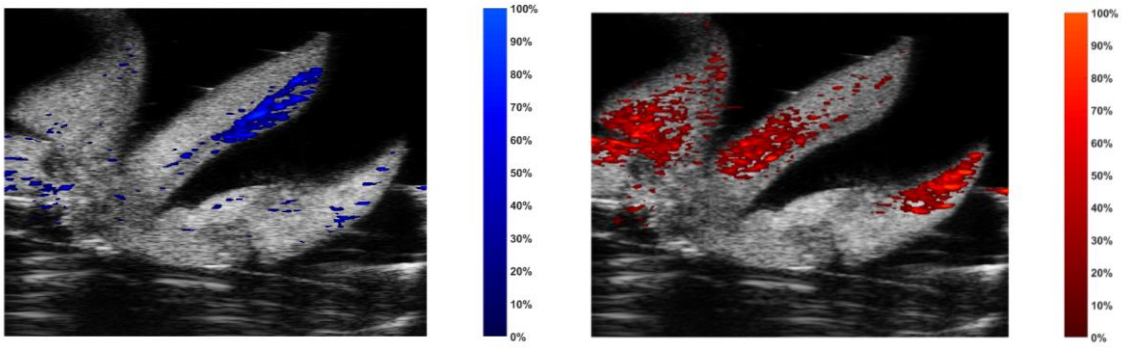

Figure 1.4.10 - Unmixed PA images (colour scale) overlapped with the co-recorded US trace (greyscale) for LIVER data sets. Colour bars are in arbitrary units and are referred to GNRs (blue, top) and blood (red, bottom).

The multivariate analysis was permitted to compress 327240 spectra into two spectra and two images that are still able to represent more than 95% of the total variance contained in the initial data set. In this case, the residuals hardly reach 1% of the maximum PA amplitude recorded for these acquisitions (**Figure 1.4.11**). Additional information about the statistical analysis of the datasets was reported and commented on in the Supplementary Materials. With this approach, good results were obtained without any prior knowledge, i.e. without recording the PA behaviour in separate *ex vivo* experiments.

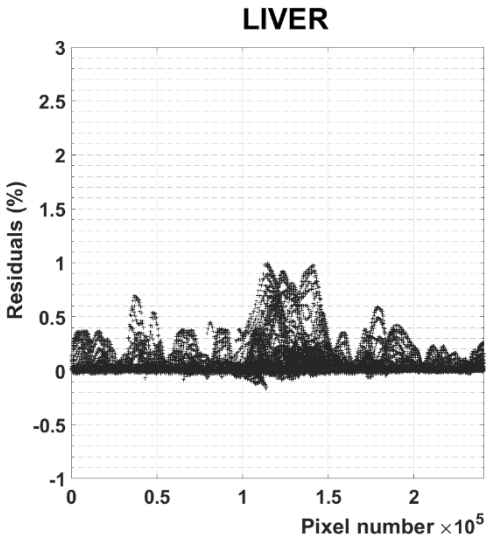

Figure 1.4.11 - Plot of the maximum residuals for each pixel across all wavelengths, representing the percent of the maximum PA signal recorded for the LIVER data set that is not included in the model.

Semi-quantitative comparison with "commercial unmixing tool"

Most PA imaging platforms allow the manipulation of raw data using proprietary software. This is the case for the VEVO Lazr 2100, which is supported by the VEVOLAB software that contains a built-in unmixing tool. This data visualization algorithm requires the spectra of the pure components (pre-recorded or available in a recordable repository/library) and spatially separates them, allowing only limited data manipulation from the operator.

To evaluate the performances of the presented MCR-ALS approach, with respect to VEVO, the performances of these tools were compared to the BIO data set. Three regions of interest (ROI of 2.212 mm^2) were selected around the injection points of three contrast agents. Then, separately for each region, the unmixed distribution of each contrast agent was averaged throughout the selected region and plotted in **Figure 1.4.12** by setting the highest average contribution equal to 100% and calculating the other two accordingly. Ideally, a perfect unmixing would let us expect a value of 0 for each species that is not the one present in the analysed region, but in a real system, this is not always the case. The analysis of this mismatch allowed us to assess whether the two unmixing methods deliver comparable results.

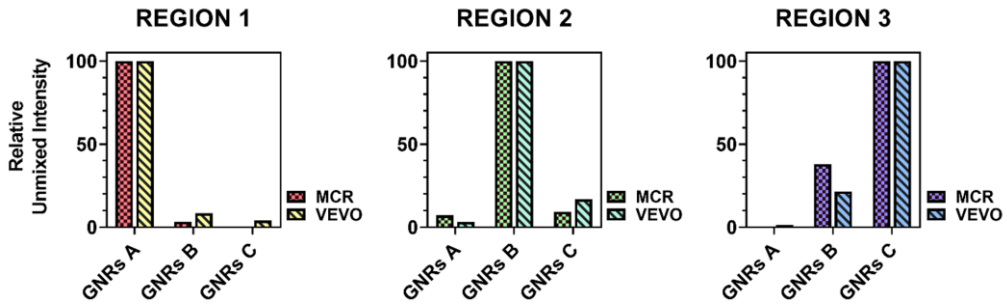

Figure 1.4.12 - Quantitative comparison of the mismatch in the two unmixing processes for the three responsive components. Relative unmixed intensity has been calculated by setting it at 100% for the main species in each distribution map and by averaging the mismatched signals in the same region accordingly.

CHAPTER 2

FLEXIBLE ELECTRONICS

2.1 Introduction

2.1.1 Organic Electronics

Organic electronic is the branch of electronic that deals with the implementation of flexible organic materials in the field of electronics, which is dominated by silicon-based semiconductors since the discovery of its fundamental properties. [154] Even though the possibility of implementing organic materials in electronics was firstly theorized more than 50 years ago, the interest of the scientific community towards organic electronics has exponentially grown in the last two decades. In the year 2000 only 41 papers were published with the keyword "organic electronics", but this number increased to more than 600 in the 2010s (**Figure 2.1.1**). Several companies are nowadays participating in the process of bringing organic electronics devices into the market, exploiting amongst others the OLED (organic light-emitting diodes) technology. Even though this is still achieved with traditional Si-based backplanes, but they represent a first step towards the implementation of new soft devices in the everyday life. [155–157]

In this chapter, we will give some examples of the main classes of materials employed in organic electronics applications.

Semiconductors

The active ingredient of electronic devices is indeed the semiconductor, which is the basics component of most electronic devices. Amongst the wide class of organic semiconductors (that display small band gaps due to extensive π delocalization), the most widely employed

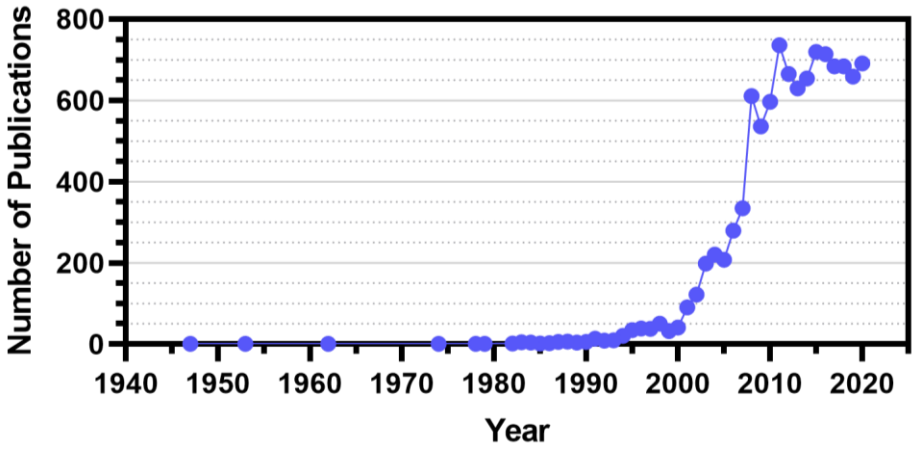

Figure 2.1.1 – Number of publications with the keyword "organic electronics" in the recent literature. Source: Scopus (December 2020)

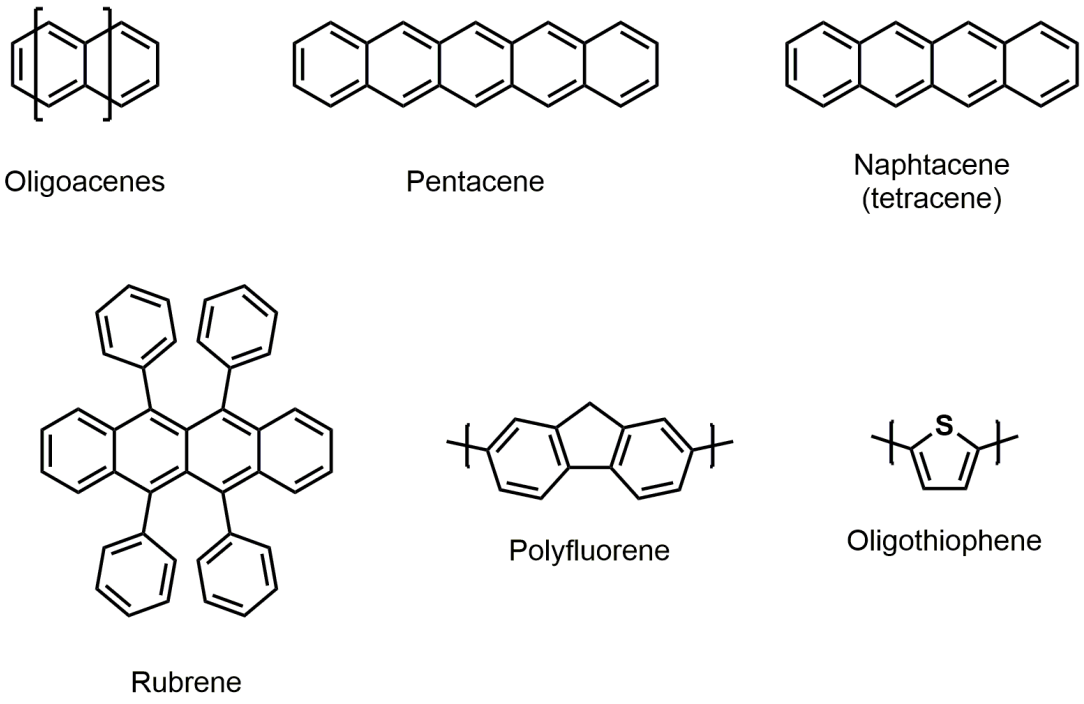

Figure 2.1.2 – Chemical structure of the most common organic semiconducting materials.

and studies small molecule semiconductor is indeed pentacene. [158] It remains the most reliable benchmark material for preparing vapour-deposited thin-film transistors (TFTs) with a hole mobility of around 1 cm^2/Vs. Recently, several other materials have been employed for these applications, including naphtacene, rubrene, oligoacenes, oligothiophenes and polyfluorenes (**Figure 2.1.2**). [159–163] However, organic n-type semiconductors still suffer from rapid degradation in mobility and on/off ratios, but recently great efforts have been made to improve the oxidative stability of such semiconductors. Due to its limited solubility, solution-processed routes are very limited, and implementations exploit its tendency to sublimate to employ evaporation-based manufacturing techniques. Nevertheless, it has been reported by Philips the preparation of TFTs from pentacene precursor solutions, allowing for the implementation of organic semiconductors to traditional manufacturing techniques such as spin-coating and photolithography. [164]

Electrodes

In the production of organic-based electronics, insulators and electrodes materials should also be considered. Inexpensive and stable conductive electrodes have been prepared using thin metallic films such as Al, Cr, Cu and Ni, with peculiar surface modifications that altered their electron injection properties. [165] Recently, the scientific community-directed most of its

efforts toward the replacement of mechanically unstable metal junctions with more versatile and flexible conductive polymers such as poly(3,4-ethylenedioxythiophene) polystyrene sulfonate (PEDOT:PSS) and conductive particle-based inks. [166–168] Polymeric and particle-based systems need to be carefully selected on the basis of their compatibility with the polymeric substrate and the fabrication methods (usually involving temperature above 150°C), often replacing the substrate with temperature-resistant materials such as polyimides, PIs and poly (ethylene naphtalates), PENs.

As an additional problem to be solved, some materials that show outstanding electrical properties present some issues during the manufacturing of the device, such as throughput, equipment cost, temperature limitations, reproducibility, and sensitivity of previously deposited layers. The interfaces between different layers are also extremely important, but the fine control of these interfaces is often accompanied by additional preparation steps that increase the complexity of the device manufacturing.

Conductive nanocomposites

When the electronic properties given by semiconducting organic small molecules or polymers are not enough to ensure applicability in organic electronics, nanofillers can play an important role in improving the quality of manufactured devices. Polymer-based nanocomposites can combine the good mechanical properties of inert polymers that act as a matrix with the peculiar and outstanding properties (conductivity, piezoelectricity, fluorescence, …) of nanostructured materials. [169]

Amongst these, graphene and carbon nanotubes are indeed the most widely used. [170–172] In particular, graphene has proven outstanding thermal, optical, mechanical and electrical properties, with carrier mobility at room temperature as high as 15000 cm^2/Vs. [173–175] It is worth mentioning the work performed by Wang et al., who described a healable multifunctional electronic tattoo (E-tattoo) thanks to the interaction of graphene with silk fibroin (**Figure 2.1.3**). [176] After the dissolution of silk fibroin in the presence of Ca^{2+} ions, graphene is homogeneously dispersed into the aqueous matrix and deposited via mask printing or direct ink writing on a substrate. Graphene allows for the formation of electrically conductive paths that can sensitively respond to changes in temperature and humidity of the surrounding environment. Therefore, the deposition of the developed nanocomposite on the skin is expected to allow for employing such electronic tattoos as on-skin sensors for wearable electronics applications. The E-tattoo can be damaged by water, but it is able to completely self-heal in a fraction of a second, resulting in the efficient reformation of broken bonds at the fractured interface.

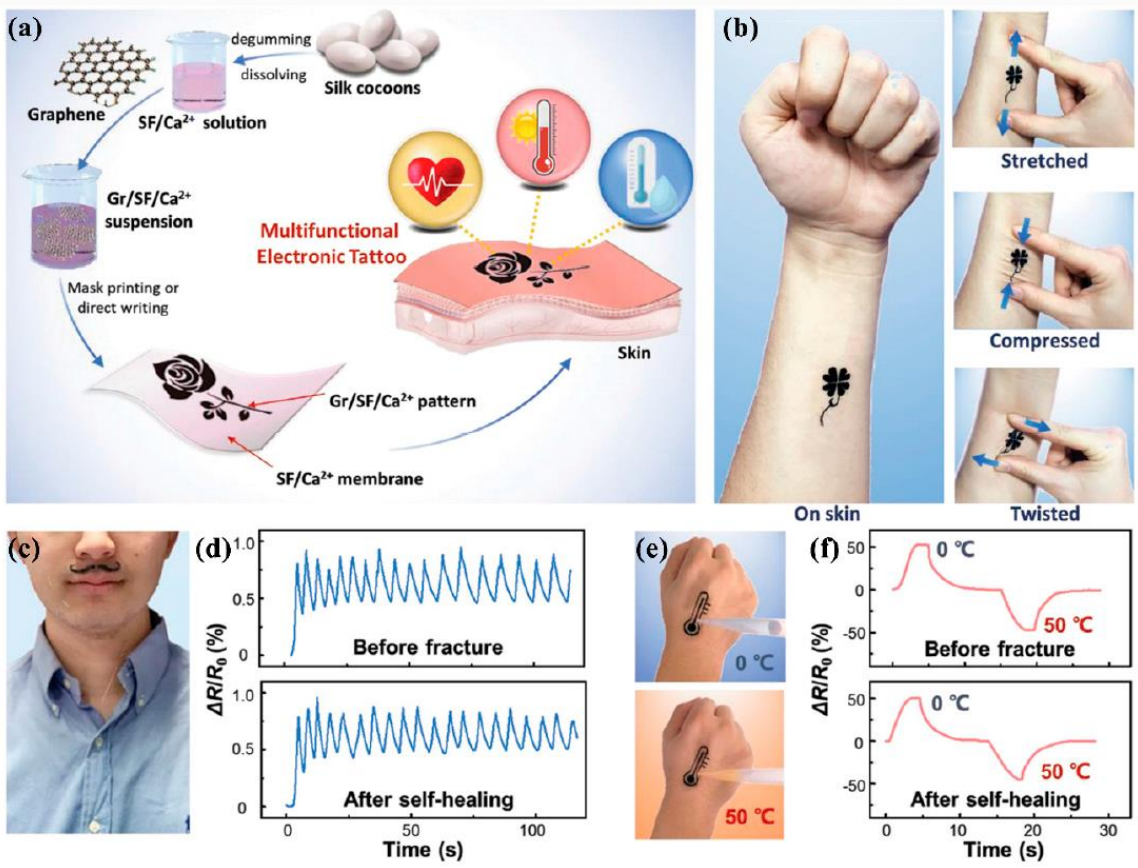

Figure 2.1.3 – a) Fabrication of a silk fibroin/graphene E-tattoo. b) Representation of on-skin tattoo in relaxed, stretched, compressed and twisted positions. c) Tattooed moustache that allows for monitoring respiration. d) comparison between the response of unbroken and healed humidity sensors. e) E-tattoo on-skin for temperature sensing. f) comparison between the response of unbroken and healed temperature sensors. Reproduced from ref. [176]

As well as carbon nanomaterials, conductive metal nanowires (mainly silver, gold and copper) have found extensive applications for the preparation of conductive nanocomposites in organic electronics. In this field, outstanding results have been firstly obtained by Cheng and co-workers in 2014. [177] In their work, the authors report the preparation of highly sensitive wearable pressure sensors based on ultrathin gold nanowires (AuNWs). Such gold nanostructure showed great mechanical stability and flexibility and it was previously employed for building flexible transparent electrodes. AuNWs-impregnated tissue paper was sandwiched between two layers of PDMS: a blank substrate sheet that acts as a support and a patterned layer with interdigitated electrode arrays, leading to a flexible strip that can sense pressure thanks to the increase in the density of conductive junctions in the interdigitated electrode cause by application of external forces on the electrode (**Figure 2.1.4**).

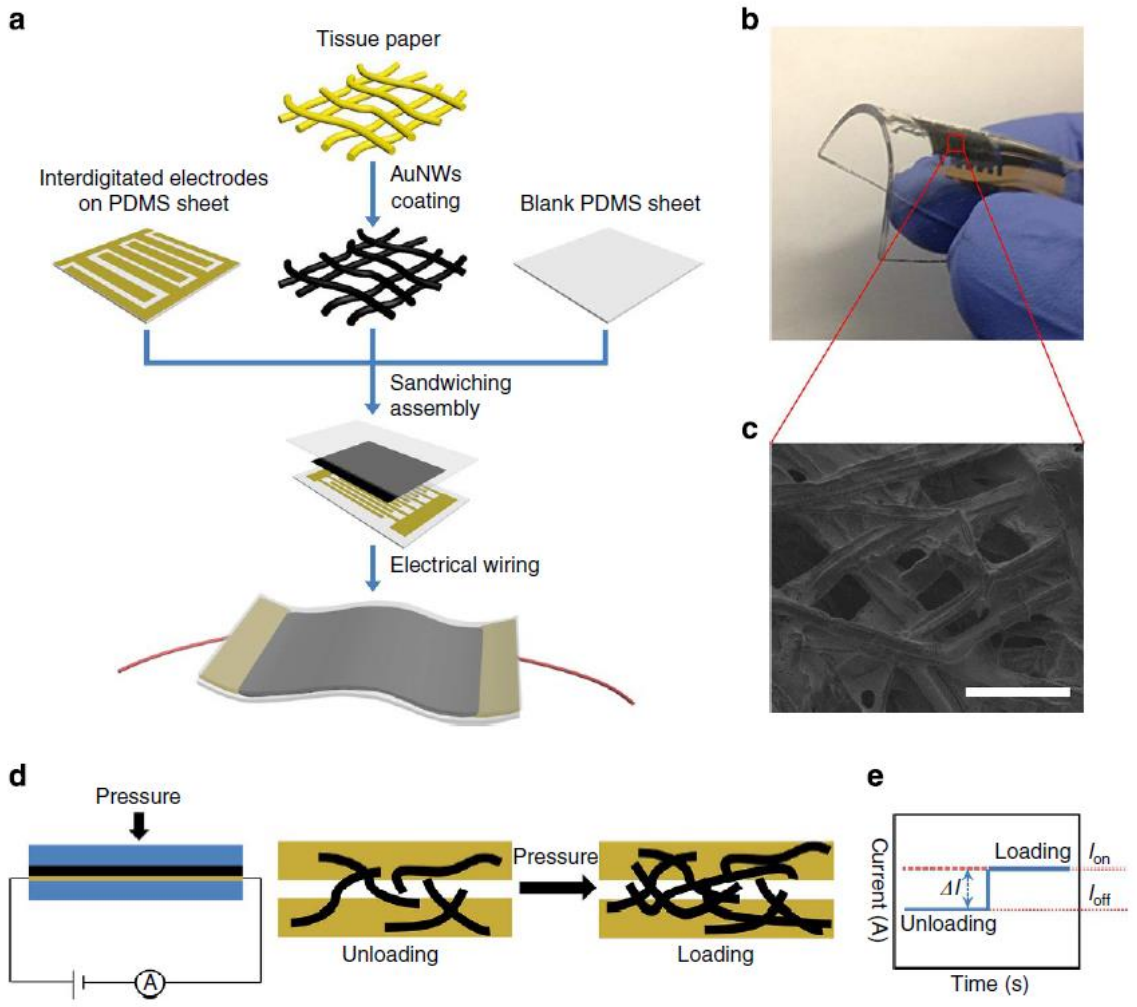

Figure 2.1.4 – Pressure sensor based on ultrathin AuNWs. a) schematic representation of the fabrication of the layered flexible sensors; b) optical camera photograph of the sensor; c) SEM image of nanowire-impregnated tissue paper (scale bar is 100 μm); d) schematic illustration of the principle of pressure sensing in such device; e) modifications in the measured electron current before and after the application of a load on the sensor. Reproduced from ref. [177]

The proposed sensor allowed for the manufacturing of pressure sensors with sensitivities up to 1.14 kPa^{-1}, with response rates of the order of 0.05 s at frequencies of around 5.5 Hz. Also, AuNWs-based pressure sensors have demonstrated to be able to efficiently detect pressing, bending, and twisting of the flexible device, enabling its employment as wrist motion and vibration sensor that requires low input powers (< 30 μW) at low operating voltages (1.5 V). However, although the synthetic approach described for the formation of such nanowires is easy and easily scalable, a great effort still needs to be directed towards the stabilization and manipulation of ultrathin AuNWs in more sophisticated manufacturing techniques.

Piezoelectric nanocomposites

The piezoelectric effect has attracted increasing interest from the scientific community thanks to its possible implementation for piezoelectric energy harvesting (PEH). Such systems are characterized by simple configuration, high conversion proficiency and integrability in complex systems [REF]. PEH composites are associated with three principal vital phases:

1) Mechanical-mechanical energy conversion, that allows for the PEH to react to external stimuli with vibrations and deformations at the molecular scale;
2) Mechanical-electrical energy conversion, in which the mechanical vibration or deformation caused by the external stimuli is converted into electronic transitions inside the PEH materials;
3) Electrical-electrical energy transfer, leading to an output signal that leaves the PEH and is read by a transducer or stored in an accumulator.

More than 200 piezoelectric materials have been discovered to this date for such applications, amongst which ferroelectric ceramics are still the best candidates since they offer higher piezoelectric coefficients when compared to piezoelectric polymers (such as PVDF or PLA). A comparison between the main parameters describing the piezoelectric behaviour of ceramic and polymeric piezoelectrics is summarized in **Table 2.1.1**. The table clearly shows that piezo ceramics display much better piezoelectric properties when compared to most organic piezoelectric polymers, but they often suffer from high density, rigidity and fragility. To overcome the intrinsic limitations of pure piezoelectric ceramic materials, nanocomposites can be formulated to exploit both the interesting piezoelectric properties of ceramic nanomaterials combined with the mechanical flexibility and elasticity of inert polymeric matrices. [178]
However, the type of selected polymer can influence the piezoelectric response of the ceramic nanofiller in different ways. In addition, the fabrication methods, the degree of alignment of the crystalline domains both in the ceramic and in the polymer and the poling conditions strongly affect the performances of the prepared devices. [179]
It has been reported in a review paper from Annamalai et al. the description of various piezoelectric nanocomposites in terms of the main parameters used for their characterization: the piezoelectric strain coefficient (d_{33}) and voltage coefficient (g_{33}). The voltage coefficient g_{33} is proportional to piezoelectric strain coefficient d_{33} but it is inversely proportional to the permittivity. It was also described how the d_{33} values are functions of the volume fraction of the ceramic particles in the nanocomposite and the direction of the polarization matrix.

Properties / Parameters	Ferroelectric ceramics (PZT)	Piezoelectric polymers (PVDF)
Piezoelectricity	High	Low
Acoustic impedance (10^6 kg m^{-2} s^{-1})	High (30)	Low (2.7)
Density (10^3 kg m^{-3})	7.5	1.78
Relative Permittivity ($\varepsilon/\varepsilon_0$)	1200	12
Piezo-strain constant (10^{-12} C N^{-1})	d_{31} = 110 d_{33} = 225-590	d_{31} = 23 d_{33} = -33
Piezo-stress constant (10^{-3} V m N^{-1})	g_{31} = 10 g_{33} = 26	g_{31} = 216 g_{33} = -330
Electromechanical coupling factor (% at 1 kHz)	k_{31} = 30	k_{31} = 12
Dielectric constant	1180	10-15
Mechanical flexibility	Poor	Outstanding
Curie temperature (°C)	386	80

Table 2.1.1 – Comparison of quantitative parameters that describe the piezoelectric properties of PZT (as an example of ceramic material) and PVDF (as an example of polymeric material). Reproduced from ref. [180]

For example, it has been reported by Cui et al. in 2019 the implementation of piezoelectric nanoparticles for photopolymerization-based 3D printing to produce directionally responding sensors (**Figure 2.1.5**). [181] The authors of this work describe the preparation of lead zirconate titanate (PZT) colloids covalently bound to photoactive monomers such as trimethoxysilylpropyl methacrylate via siloxide bonds. The methacrylate-functionalized colloid is then hardened into arbitrary 3D structures exploiting high-resolution additive manufacturing techniques. It was observed that the designed piezoelectric patterns could be assembled into smart structures that can display a variety of functions, including force magnitude and directionality sensing, impact absorption and self-monitoring, and location mapping, without any additional sensing component. The prepared piezoelectric nanocomposites are able to achieve high piezoelectric performances at low volume fractions, together with high flexibility ensured by the printed architecture.

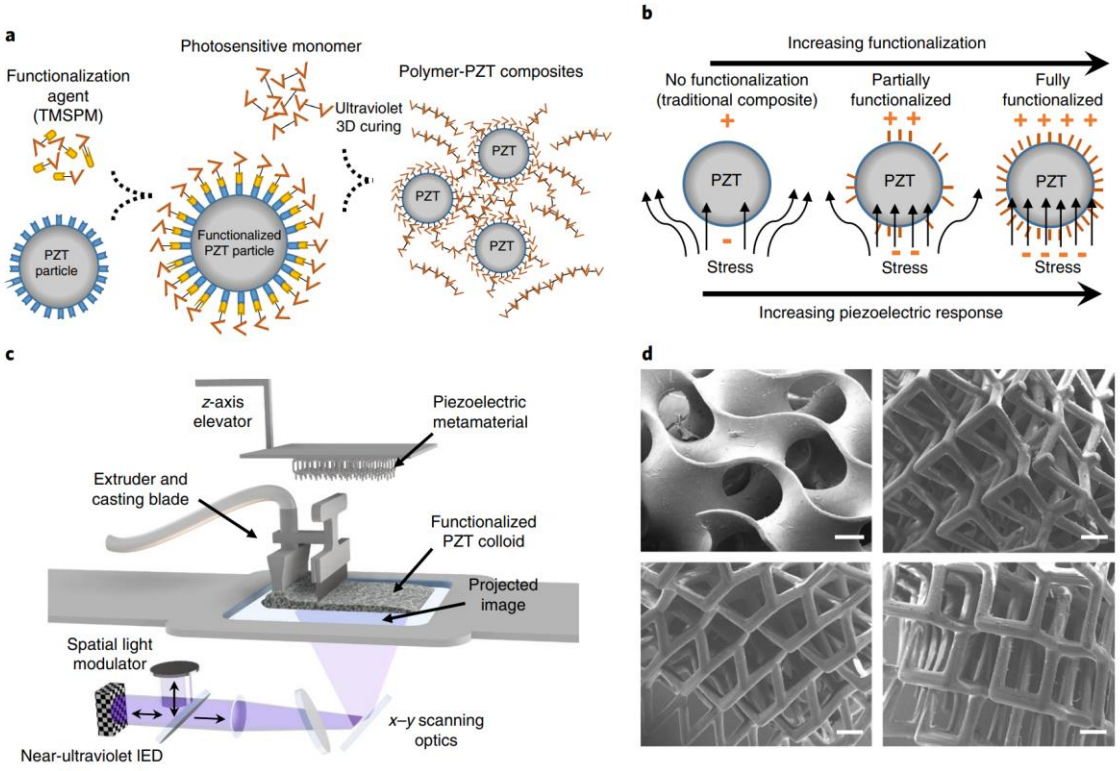

Figure 2.1.5 – Surface functionalization of PZT with photosensitive monomers and 3D printing of piezoelectric metamaterials with complex microarchitectures. a) Schematic illustration of surface functionalization method and strong bonds between the nanoparticles and the polymer matrix after the ultraviolet curing process. b) Schematic illustration of the relationship between the surface functionalization level and the piezoelectric response. The piezoelectric response increases with the surface functionalization level as a result of increasing stress transfer. c) Schematic illustration of the high-resolution additive manufacturing system. d) Scanning electron microscope images of 3D-printed piezoelectric micro lattices. Scale bars are 300 μm. Reproduced from ref. [181].

2.1.2 Perovskite materials and their properties

Perovskites

In inorganic chemistry, perovskites are a class of crystalline inorganic materials with the general formula ABX_3 (where A and B are cations and X are anions) that adapt the crystal cell typical for calcium titanium oxide ($CaTiO_3$), simply referred to as perovskite. The ideal cubic structure of perovskite has 8 A ions at the vertices of a cube, one B ion at the centre, surrounded by an octahedron of X atoms that occupy the centre of the cube faces. Most often, the X atom is oxygen, but other anions such as fluoride (F^-) and chloride (Cl^-) can be found. Compared to other ternary crystal structures, the perovskite structure is able to produce a wide range of different phases that display completely different properties, with applications of these ceramic materials from capacitors to conductors, insulators, magnetoresistors, catalysts, etc. (**Figure 2.1.6**). The ideal cubic phase is however uncommon since many effects are able to distort the symmetry of perovskite crystal cells. The first example of a detailed study on crystalline perovskites was published by Goldschmidt in the 1920s, laying the foundations for the structural analysis of this interesting class of compounds. [182] The most common distortions in the cubic structures are related to deformations of the $[BO_6]$ octahedra

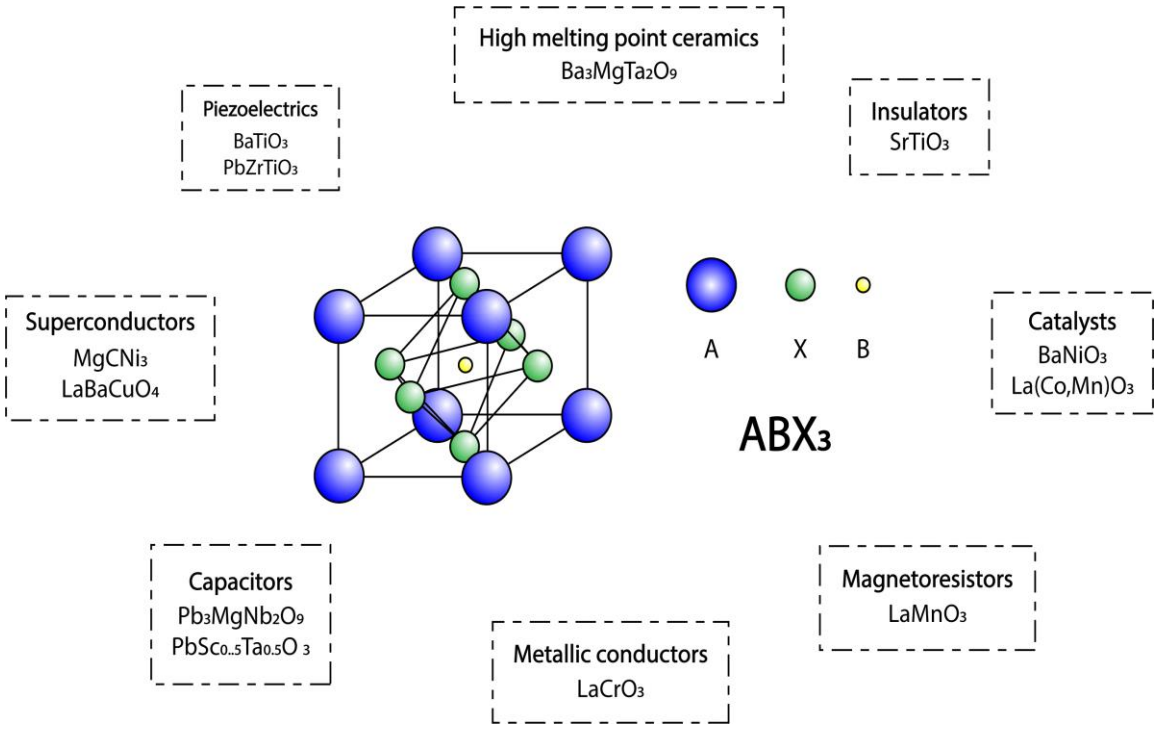

Figure 2.1.6 – General perovskite crystal structure and unit cell. Examples of the various properties observed for different perovskite materials are also reported.

that generates tetragonal, rhombohedral or orthorhombic variants of the ideal cubic structure. The perovskite structure has a wide range of possible substitution of cations and anions. The ion replacement must preserve the charge balance and keep the ion radii within the range for each particular coordination number. Variations in the ion size and composition result in the distortion of the structure and the reduction of symmetry with tremendous effects on the physical properties of the perovskite material. The lack of symmetry caused by these deformations is often responsible for peculiar magnetic and electric properties displayed by perovskites. [183]

Several factors are responsible for the occurrence of distortions in the crystal structure, but the most important are here summarized:

1) Size effect of atoms

In idea cubic systems, it is possible to derive from simple geometry that the length of the cell unit a is related to the ionic radii of the ions that build up the perovskite structure as recalled in **Equation 2.1.1**:

$$a = \sqrt{2} \cdot (r_A + r_O) = 2 \cdot (r_B + r_O) \qquad \textbf{Equation 2.1.1}$$

Where r_A, r_B, and r_O are the ionic radii of A, B and oxygen, respectively. The two identities are equal only for perfect cubic structure and their ratio, defined as the Goldschmidt's tolerance factor (t) can be used to express the degree of distortion of perovskite structures (**Equation 2.1.2**):

$$t = \frac{r_A + r_O}{\sqrt{2} \cdot (r_B + r_O)} \qquad \textbf{Equation 2.1.2}$$

In fact, for perfectly cubic systems $t = 1$ since **Equation 2.1.1** is satisfied. This is the case, for example, for $SrTiO_3$, for which $r_A = 1.44$ Å, $r_B = 0.605$ Å, and $r_O = 1.40$ Å. [184] However, if A ions are smaller than the ideal value, the Goldschmidt's tolerance factor will be smaller than 1 and as a result, the $[BO_6]$ octahedra deforms to fill more empty space. For example, $GdFeO_3$ with t = 0.81 adopts the orthorhombic structure as well as perovskite mineral itself ($CaTiO_3$) with a Goldschmidt's tolerance factor less than 0.8 that leads to the higher stability of the rhombohedral deformed structure. [185,186] Oppositely, $t > 1$ is observed with large A ions or small B ions and the perovskite adopts the hexagonal structure like $BaNiO_3$ (t = 1.13), in which the $[NiO_6]$ octahedra are forced to share an edge. [187,188]

2) Presence of impurities and doping

The perovskite structure is able to accommodate a great variety of atoms, depending on their size and valence. In addition, it can tolerate ion vacancies in allow extent. [189,190] Because of its packing density, the perovskite structure is more likely to display A-site vacancies, but B-site vacancies are not tolerated by the perovskite which undergoes a crystal phase transition to more stable geometries. [191,192] Also, oxygen vacancies are tolerated in limited extent: for example, for the family of compounds with the formula $SrFeO_x$ ($2.5 < x < 3$). Since iron ions can be easily oxidized or reduced by heating the sample in an oxidizing or reducing environment, the oxygen content of the crystals can be tuned in the range reported. For some stoichiometries, FeO_5 square pyramidal domains are formed. [193]

3) Jahn-Teller distortions

Jahn-Teller distortions are referred to the geometrical deformations of molecular structures due to peculiarities in their electron configuration. The related Jahn-Teller theorem states that any non-linear molecule with a spatially degenerate electronic ground state will undergo a geometrical distortion that removes that degeneracy because the distortion lowers the overall energy of the species. [194] An interesting implication of the Jahn-Teller theorem is that is some molecules there must be some degenerate electronic state interacting with one or more normal vibration modes, which leads to symmetry-breaking interactions in which molecular distortion is associated with the loss of the electron degeneracy. In perovskite, the Jahn-Teller effect acts mostly on the ions in the B position. In the case of $XMnO_3$ (X = La, Pr, or Nb) compounds, the $3d^4$ electrons of Mn^{3+} ions are described by the crystal field theory to be split between t_{2g} (3 electrons) and e_g (1 electron) orbitals. The electron in the e_g orbital is in degenerate states, thus for the Jahn-Teller theorem the octahedra distort along the z-axis causing the splitting of the e_g orbital; the highest energy electron now occupies the orbital a_{1g}, more stable than the e_g orbital of the symmetric octahedron (**Figure 2.1.7**). [195]

Ferroelectricity and ferroelectric perovskites [196]

Ferroelectric materials are defined as materials that display a spontaneous dipole moment, whose orientation can be switched by applying an external electrical field. Cubic perovskite structure only displays induced polarization, which drops to zero when the applied electrical field is turned off. However, a slight distortion of the perfect cubic lattice caused by a variation in the position of B atoms can cause the structure to shift to the tetragonal phase, which is able to reveal a net and persistent dipole moment, associated with ferroelectric properties. The higher the distortion from the cubic centrosymmetric system, the stronger will be the

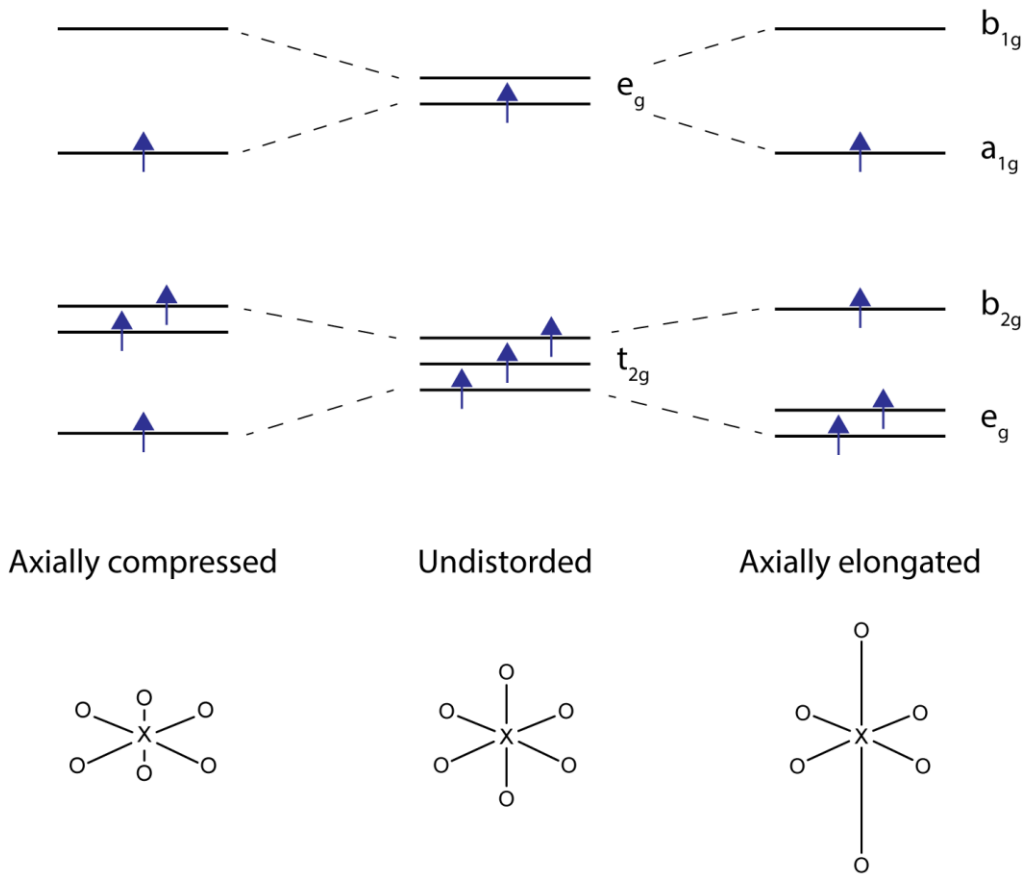

Figure 2.1.7 – Jahn-Teller effects applied on crystal field theory for octahedral coordination of d^4 metal ions.

associated net dipole moment. In typical ferroelectric perovskite oxides, the cubic phase is more stable at a higher temperature but a transition temperature exists, below which the most stable conformation is given by the tetragonal structure. This transition temperature is defined as Curie temperature (T_c) and **Table 2.1.1** shows the T_c values for some common ferroelectric perovskite oxides. It can be noticed from the polarization values that lead-containing perovskite offer the best performance of this class of materials. However, problems related to toxicity and high density of PZT ceramics are moving the attention towards the implementation of less toxic ferroelectric materials such as barium titanate ($BaTiO_3$), which will be described om details in the next chapter as a cheap and easy-to-produce perovskite ferroelectric material. Another interesting property of ferroelectric perovskites is their incredible dielectric constant at their Curie temperature, discovered first by von Hippel in the 1940s and exploited to produce dielectric-based capacitors. [197]

Compound	Chemical Formula	Year Discovered	Curie Temperature (K)	Remanent Polarization ($\mu K\ cm^{-2}$)	Crystal Structure
Rochelle salt (Potassium sodium tartrate tetrahydrate)	$KNaC_4H_4O_6 \cdot 4H_2O$	1921	255 and 297	0.25	Monoclinic between the T_c Orthorhombic otherwise
Potassium dihydrogen phosphate	KH_2PO_4	1935	123	6.1	Orthorhombic
Barium titanate	$BaTiO_3$	1945	398	25	Tetragonal
Lithium niobate	$LiNbO_3$	1949	1415	10 – 30	Trigonal
Potassium niobate	$KNbO_3$	1949	400	20 – 40	Orthorhombic
Lead zirconate titanate (PZT)	$PbZr_{1-x}Ti_xO_3$	1949	Depends on composition	20 – 97	Tetragonal for Ti-rich Rhombohedral for Zr-rich
Lead titanate	$PbTiO_3$	1950	763	20 – 96.5	Tetragonal
Lead zirconate	$PbZrO_3$	1951	503	20 – 50	Orthorhombic
Guanidine aluminium sulphite hexahydrate	$C(NH_2)_3Al(SO_4)_2 \cdot 6H_2O$	1955	473	0.5	Trigonal
Lead bismuth niobate	$PbBi_2Nb_2O_9$	1959	833	≈ 3	Pesudo-tetragonal
Strontium bismuth tantalate	$SrBi_2Ta_2O_9$	1960	600	30 – 70	Orthorhombic
Barium strontium titanate	$Ba_{0.73}Sr_{0.27}TiO_3$	1960	298	10 – 30	Tetragonal
Bismuth titanate	$Bi_4Ti_3O_{12}$	1961	983	10 – 30	Orthorhombic

Table 2.1.1 – Most common piezoelectric ceramics materials with the corresponding chemical formula, year of discovery, Curie temperature, remanent polarization and stable crystal structure at room temperature. Except for the first two, all of the entries are perovskite materials. Data from ref. [198]

2.1.3 Barium Titanate nanomaterials and preparation methods [199]

Barium titanate ($BaTiO_3$) is employed in a great variety of applications due to its ferroelectric properties, accompanied by its high dielectric constant and low dielectric loss. Moreover, it is a cheap material that is easy to produce in large scale and it does not contain heavy atoms that could induce toxic effects on human health. [200] It was the first discovered ferroelectric oxide, with a simple crystallographic structure and well-consolidated applications in electronics, optics and communications. It has demonstrated to be one of the best lead-free alternatives to the most efficient lead zirconate-titanate (PZT) ceramics for applications in microelectronics. [201]

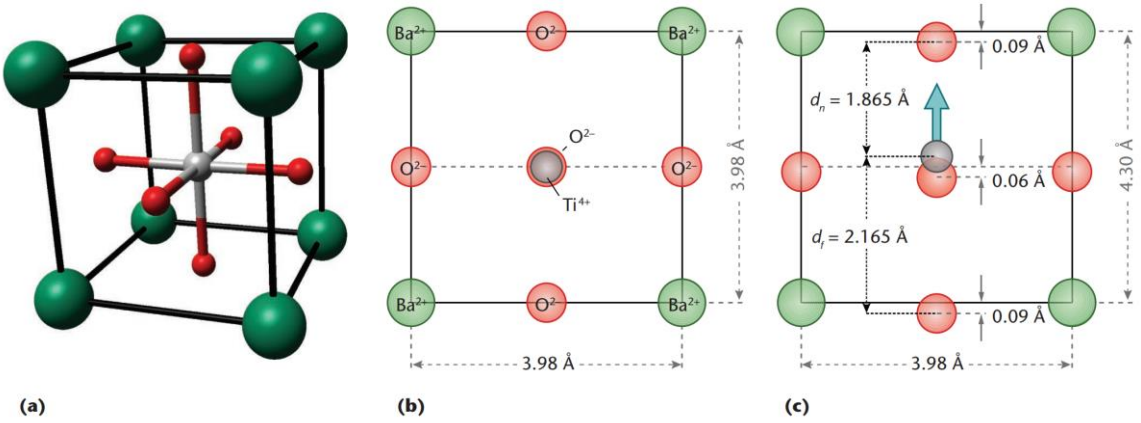

Figure 2.1.8 – a) Single unit cell of $BaTiO_3$ in the b) cubic and c) tetragonal crystal structures. As the transition between the two phases occurs, Ti and O atoms move in opposite directions along one of the three major axes, resulting in the elongation of the unit cell along the same major axis. Reproduced from ref. [202]

Crystal structure and phase transitions [203]

Barium titanate adopts the typical perovskite structure ABO_3 represented in **Figure 2.1.8**, and it displays interesting crystal phase transitions upon cooling (**Figure 2.1.9** and **Figure 2.1.10**). The ideal cubic structure can be obtained only above the Curie temperature of the material, with large Ba^{2+} ions (158 pm) at the 8 corner sites, small Ti^{4+} ions (60 pm) in the middle of the cube and oxygen anions at the face centres. This phase is characterized by the cubic ***Pm3m*** space group with a unit cell length a = 4.009 Å.

At the Curie temperature (T_c = 133°C) the cubic structure undergoes displacement phase transition caused by the displacement of the Ti^{4+} ions that move upwards, leading to the

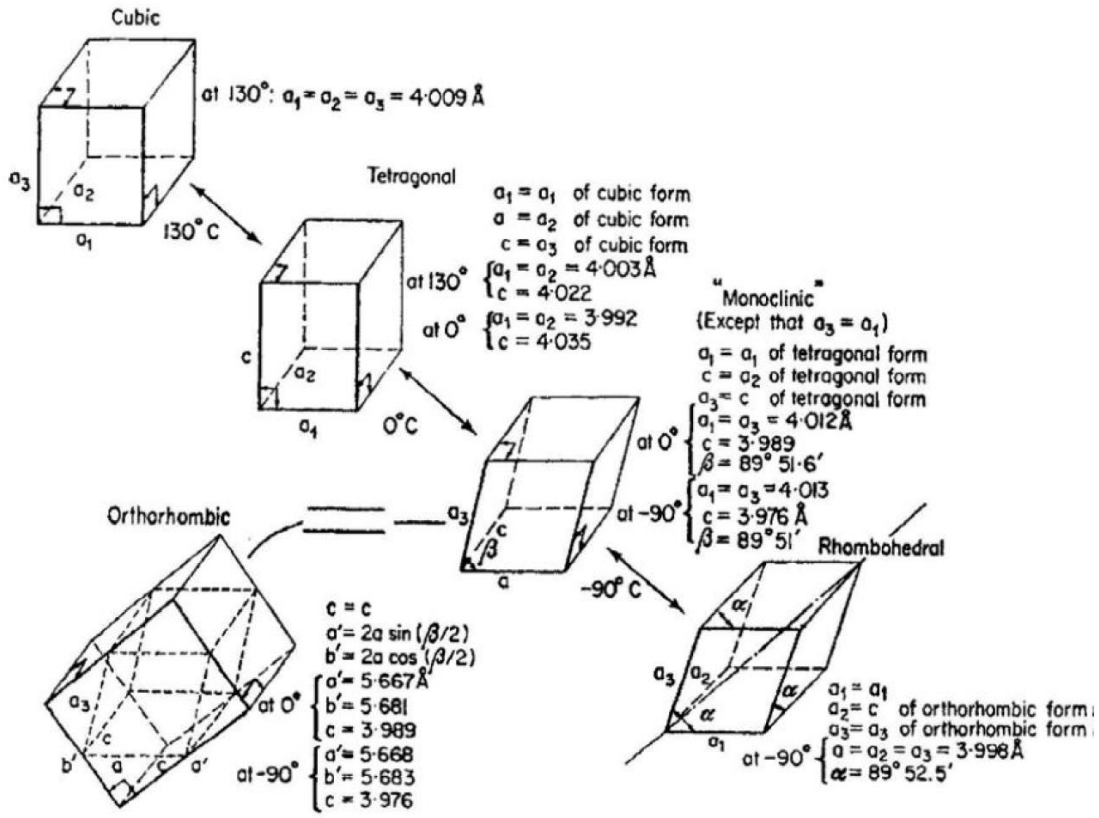

Figure 2.1.9 – Crystal phase transitions of $BaTiO_3$ when cooled below its Curie temperature. Reproduced from ref. [203]

tetragonal crystal structure (***P4mm***, a = 3.992 Å and c = 4.035 Å). The formation of the tetragonal phase causes the permanent and spontaneous polarization of the crystal cell along the z-axis. Since the cubic phase has six equivalent <100> axes along which the Ti^{4+} ions can displace, the polarization vector can arise along with any one of them. Therefore, polycrystalline samples of tetragonal $BaTiO_3$ display randomly oriented dipole moment which sums up to zero hiding the ferroelectric potential of the material. However, by applying an external electrical field it is possible to orientate parallelly the polarization of the crystallites allowing for the obtainment of a macroscopically polarized material since the polarization vectors now sum up constructively. This treatment is referred to as poling and it is required to produce polarized materials that can act as piezoelectric sensors and actuators. [204]

Upon further cooling of $BaTiO_3$ crystals below 0°C, the distortions increases and by elongating along the face diagonals, the material transitions from the tetragonal structure to the orthorhombic (sometimes defined "pseudo-monoclinic") one. Since there are 12 equivalent <110> directions in the original phase, 12 possible polarization directions can be

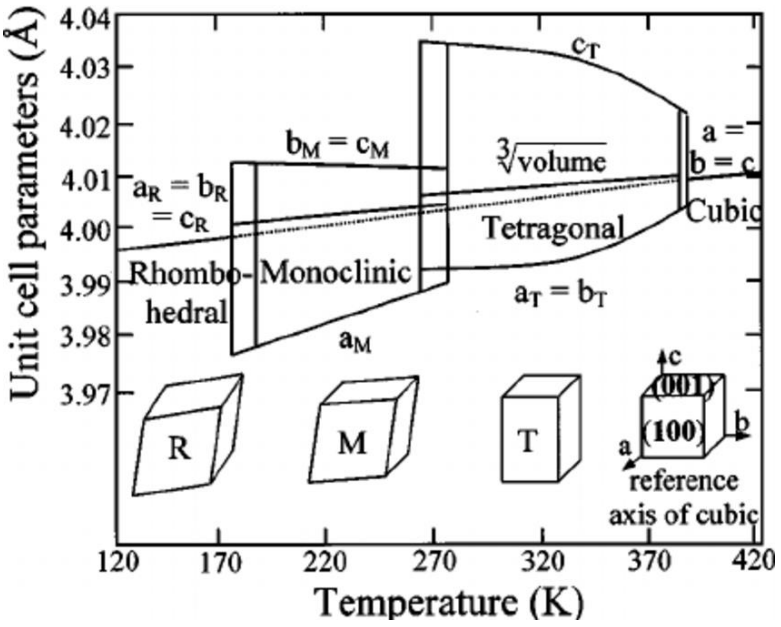

Figure 2.1.10 – Lattice constant a of $BaTiO_3$ lattice as a function of temperature. R = rhombohedral, M = monoclinic, T = tetragonal. Reproduced from ref. [205]

obtained with this crystal phase transition. This phase is considered stable in the 0°C to -90°C temperature range, below which further distortions cause the rhombohedral (***R3m***) structure to be formed, with 8 possible different polarization directions. [206]

The transition temperatures can be widely modified by the presence of dopants and impurities, but also on residual stress built up if too fast cooling rates are applied. At room temperature, the ratio between the a and c unit length is 1.01, suggesting that the spontaneous deformation of $BaTiO_3$ crystal cell is limited at 1% at room temperature.

$BaTiO_3$ nanocrystals

Like most other kinds of nanostructured materials, also ceramic nanocrystals display unique properties when employed at the nanoscale. Effects related to microstructure, composition, stress and surface composition are able to strongly enhance the type and intensity of the permanent ferroelectric dipoles in $BaTiO_3$ nanocrystals. [207] Two factors play an important role in affecting the behaviour of these ceramics at the nanoscale:

- *Size and shape*

As particle size decreases in the micrometre scale, the dielectric constant of the material increases significantly until reaching a maximum value after which the dielectric constant decreases by reducing the crystallite size. [208,209] The Curie temperature of the material is

also affected by a reduction of the grain size, therefore there is a dimensional limit after which the Curie temperature is so low that nanostructured $BaTiO_3$ is not ferroelectric at room temperature. This size limit is in the range between 1 and 100 nm but it strongly depends on how the nanopowder is prepared. [210]

- *Surface effects*

The wide range of possible preparation methods for $BaTiO_3$ allows for the obtainment of nanocrystals showing a variety of different surface functionalities like hydroxyl groups (OH), carbonaceous species or organic coatings. Surface modifications of barium titanate nanocrystals with surface ligands and coatings are often exploited to tune the solubility properties of the nanoparticles or to enhance electronic effects. For example, it has been reported the surface functionalization of barium titanate nanocrystals with n-hexyl phosphonic acid (HPA), allowing to produce ceramics with higher dielectric constants but with lower sensitivity to frequency and temperature. Typical functional groups that can be exploited to chemically coat the surface of oxide nanoparticles are catechols, silanes, phosphate esters, phosphonic and carboxylic acids. [211,212]

Organometallic syntheses

In a typical organometallic synthesis of $BaTiO_3$, an organometallic precursor (usually barium titanium ethyl hexane-isopropoxide) is injected into a heated reaction system composed of a stabilizing agent (like oleic acid) in a high-boiling organic solvent (like diphenyl ether). The high temperature causes the decomposition of the organometallic precursor and the nucleation of the perovskite nanocrystals, followed by their growth associated with the drop in the system temperature caused by the injection of the organometallic precursor. The stabilizing agent plays a fundamental role in determining the size and shape of the synthesized nanocrystals. [213] To these days, this approach has allowed for the preparation of a great variety of metal oxide nanoparticles and it is considered the best approach for controlling size and morphology of the prepared nanocrystals.

Solvothermal/hydrothermal syntheses

These methods have received a lot of attention recently since they are able to produce great quantities of high-purity materials in one-step processes at relatively low temperatures (**Figure 2.1.11**). [214] The thermal methods imply the heating of metal precursor salts in water or a solvent to the point that the precursors react to form nanosized metal oxide crystals. However, the reaction temperatures are usually higher than the boiling point of the solvent, therefore the synthesis needs to be conducted in pressure-resistant apparatuses.

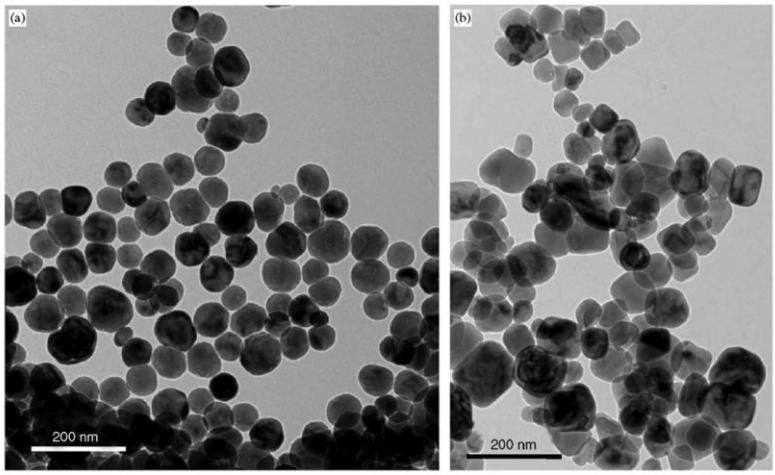

Figure 2.1.11 - TEM images of $BaTiO_3$ nanocrystal obtained by hydrothermal methods. Reproduced from ref. [215]

Template-assisted methods

In template-assisted procedures, the crystallization of the precursors into the oxide nanomaterials is allowed to happen within a specific area of a template, allowing to simply and efficiently produce nanostructures with finely controlled morphologies. [216] Depending on the type of template materials, we can distinguish between "hard templates" (like anodic alumina and titania) and "soft templates" (polymers, surfactants, biomaterials, …): these allow for the preparation of a large variety of $BaTiO_3$ nanostructures including nanodots, nanowires and nanotubes (**Figure 2.1.12**). [217,218]

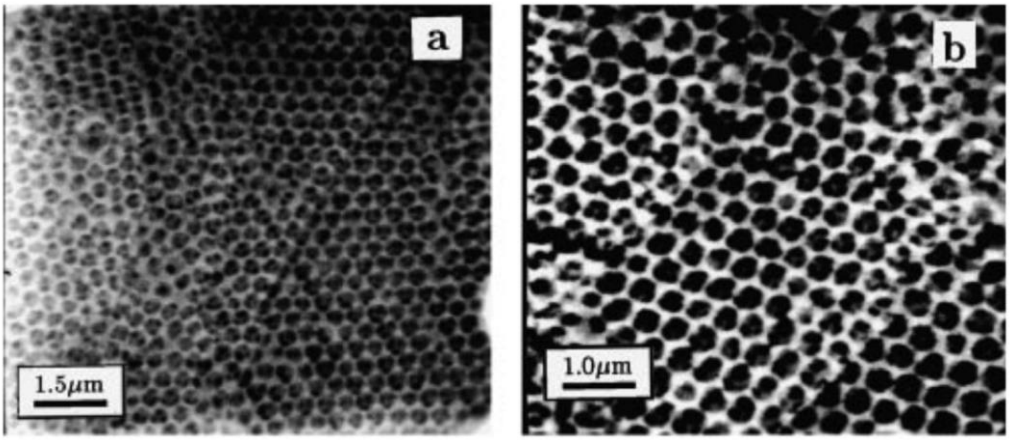

Figure 2.1.12 - SEM images of $BaTiO_3$ layers obtained by employing an ordered array of polystyrene spheres as a soft template

Molten salt methods

Solution processes allow for a great tunability over the shape and size of the obtained ceramic nanosystems, but they are produced in relatively small quantities and often involving the use of unstable and toxic precursors. However, the molten salt method employs molten ionic salts at very high temperature as the solvent for the growth of ceramic nanocrystals. [219,220] With this approach, the molten salt (usually NaCl at 820°C) dissolves the reactants and precipitates the nanocrystals (often in the presence of ionic or non-ionic surfactants), while an accurate balance between the precursor salts and the molten solvent determines the overall morphology and shape of the obtained nanoceramics (**Figure 2.1.13**). Typical precursors for $BaTiO_3$ are $BaCO_3$, BaO and TiO_2.

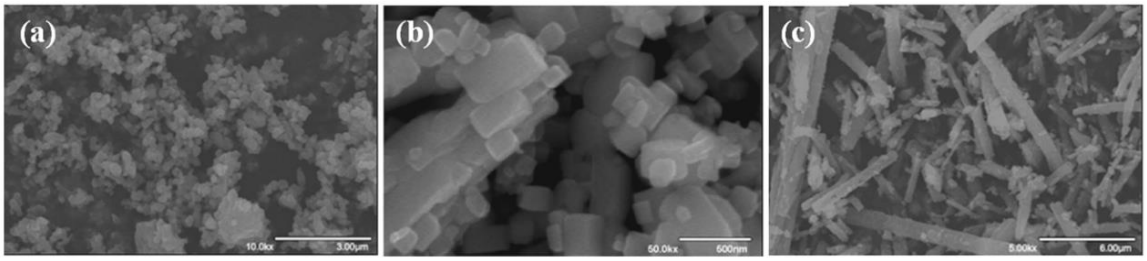

Figure 2.1.13 – SEM images of a) spherical, b) cubic and c) rods-shaped BaTiO3 nanocrystal prepared using surfactant-free molten salt methods. Reproduced from ref. [221]

Sol-gel methods

Sol-gel approaches usually involve the formation of a colloidal particle solution (the "sol") by hydrolysis and polymerization of the monomeric metal alkoxide precursors, leading to the formation of a gel-like structure containing a liquid solvent and a stable 3D network of solid nanocrystal phase. After drying of the solvent and sometimes calcination, inorganic nanoparticles are obtained. Size and morphology of the obtained nanosystem strongly depend on solvent evaporation rate, temperature, reaction conditions and solvent type. [222–224] This method is the one selected for the preparation of $BaTiO_3$ nanoparticles in this thesis, based on the work published by Yoon et al. in 2006. [225] In this work, the authors describe the hydrolysis of titanium tetraisopropoxide, $Ti(iPrO)_4$ by the crystallization water molecules of $Ba(OH)_2 \cdot 8H_2O$ in isopropanol al 80°C leading to the formation of the titanate $[TiO_6]^{2-}$ octahedra network in which Ba^{2+} ion diffuse to produce highly-tetragonal crystalline $BaTiO_3$ (**Figure 2.1.14**).

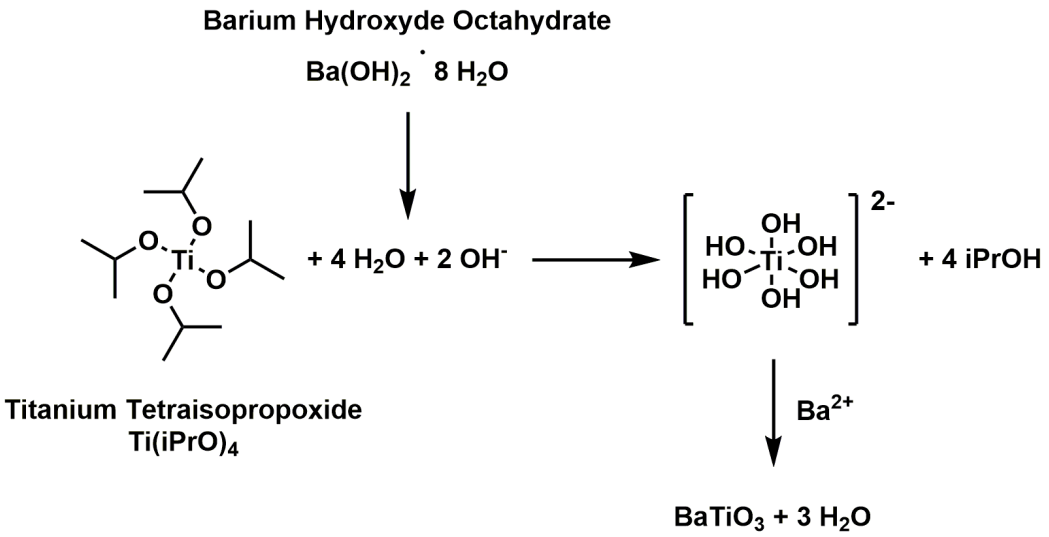

Figure 2.1.14 – Reaction scheme for the sol-gel production of BaTiO3 from titanium alkoxide precursor and barium hydroxide octahydrate as reported by Yoon et al. [225]

2.1.4 Aim of the work

This chapter recaps the main achievements of my PhD studies related to the field of organic electronics. In particular, we will describe the synthesis and surface functionalization of ferroelectric tetragonal barium titanate ($BaTiO_3$) nanoparticles with a hydrophilic commercial ligand such as hydrocaffeic acid (HCA) and with a synthetic lipophilic ligand such as dopamine dodecyl amide (DDA). After thorough chemical characterization of the synthesized nanosystem, the first hydrophilic nanocomposite ($BaTiO_3$-HCA) will be formulated in an ionic liquid-based ionogel to produce a flexible device able to directionally respond to low-frequency mechanical stimuli, to be employed as a discriminative pressure sensor. On the other hand, lipophilic $BaTiO_3$-DDA nanoparticles will be formulated with different loading in polydimethylsiloxane (PDMS) flexible matrices in order to study the piezoelectric properties of the nanocomposite in terms of its piezoelectric coefficients and stability over repeated measure cycles.

Finally, we will describe the preliminary results of a work involving the employment of ultrathin gold nanowires (AuNWs) in PDMS stretchable matrices to produce piezoresistive strain sensors.

2.2 Soft Piezoionic/Piezoelectric Nanocomposites Based on Ionogel/ $BaTiO_3$ Nanoparticles for Low Frequency and Directional Discriminative Pressure Sensing

Villa, S. M.[♪]; Mazzola, V. M.[♪]; Santaniello, T.[♪]; Locatelli, E.; Maturi, M.; Migliorini, L.[♪]; Monaco, I.; Leonardi, C.[♪]; Comes Franchini, M.; Milani, P.[♪] *ACS Macro Lett.* **2019**, *8* (4), 414–420.

[♪] Interdisciplinary Centre for Nanostructured Materials and Interfaces (CIMaINa), Università degli Studi di Milano (Italy)

2.2.1 Introduction

Piezoelectric nanocomposites are electro-mechanical transducers based on polymeric materials incorporating piezoelectric nanoparticles, such as ferroelectric perovskites (e.g., barium titanate, $BaTiO_3$), presenting a net polarization due to their non-centrosymmetric structure. The crystallites are randomly oriented so that the net polarization is averaged out, but it is possible to reorient the ferroelectric domains by subjecting the material to intense static electric fields and, thus, obtain a nonzero polarization.[226,227] This procedure is called poling. The piezoelectric response of poled perovskites determines the nanocomposite electromechanical performance and has a double contribution: a lattice contribution, due to single domains deformation, and an extrinsic contribution, due to the relative displacement of the domains. Because of these features, piezoelectric nanocomposites respond to external mechanical stimuli by generating an output voltage ranging from a few millivolts to hundreds of volts, depending primarily on the nanofiller type and amount, polymer−filler interaction, and poling conditions.[228–232] Their operational output voltages render them suitable candidates for a variety of sensing and energy harvesting applications. [233–235] They usually require high-frequency stimulation, which implies a significant power loss in the electro-mechanical conversion of low-frequency movements, like the ones typical of human motion.[236] Another limitation is the requirement of high nanofiller amounts (up to 40 wt.%) and severe poling conditions (field intensity around 100 kV/cm and high temperatures) to reach such performances. The use of large volume fractions of the filler involves a drastic decrease in compliance and flexibility of the composite with respect to the pristine polymer and often results in a nonhomogeneous dispersion of the nanostructures in the polymer matrix. [237] Piezoionic gels are an emerging class of soft smart materials constituted by a polymeric backbone filled with a fluid containing mobile ions, such as room temperature ionic

liquids or a solved salt in aqueous solution. [238] The piezoionic effect consists in the generation of an output voltage induced by the separation of ions with different mobility, stimulated by a differential pressure applied to the material. [239] The redistribution of the ionic charges inside the polymer is driven by the matrix volumetric changes at the microscopic level induced by the imposed mechanical stress, which locally alter the ions concentration. The piezoionic effect depends on the ion type, size, and mobility, as well as on the mechanical properties of the polymeric network. These gels have low output voltages (1 - 10 mV) [240,241] and respond well to low frequencies (< 1 Hz). The electro-mechanical response of piezoionic gels is isotropic, at odd with that of piezoelectric nanocomposites, where the bias of the output voltage is univocally determined by the presence of the electrically poled nanofillers.

Both piezoelectric and piezoionic materials require suitable surface electrodes and electrical contacts in order to collect and transfer the electrical generated charge. [242] The fabrication of resilient and compliant electrodes able to stably sustain repeated deformations without damage and performance loss is still a major challenge. [243] In fact, electrodes are usually constituted by thin metal layers (few microns thick) directly pasted onto the substrate, thin metallic films produced by sputtering and evaporation, [244,245] or by coatings of conductive polymers (such as poly(3,4-ethylenedioxythiophene) and polystyrenesulfonate) or polymeric blends incorporating conductive nanostructures. [246,247] The Young's modulus mismatch between the polymeric active material (fractions to hundreds of MPa) and the electrode (tenths to hundreds of GPa) is mainly responsible for the system failure and electrode deterioration along with cyclic deformations. [248] Moreover, the manufacturing and integration of electrodes physically interpenetrating with the piezo-materials are of primary importance to enhance the charge collection ability of the system, minimizing charge dispersions at the electrode/piezo-polymer interface and spurious capacitive effects.

In this work, we present the fabrication and characterization of a polymeric nanocomposite designed to merge the responsive properties of piezoelectric and piezoionic transducers. This material is constituted by a gel matrix incorporating a suitable room temperature ionic liquid (namely, an ionogel [249]) with physically embedded barium titanate ($BaTiO_3$) piezoelectric nanoparticles. This soft piezoionic/piezoelectric nanocomposite was characterized by low-frequency open-circuit voltage measurements under mechanical stimulation. We observed a response consisting in a combination between the piezoionic and the ferroelectric effect, resulting in intermediate electro-mechanical properties: the system responds to low-frequency stimulations (100 mHz to 1 Hz), with output values higher than those reported in the literature

for piezoionic gels, and it exhibits an anisotropic behaviour in the electro-mechanical conversion, typical of piezoelectric nanocomposites. [250] The system was provided with compliant cluster-assembled gold electrodes produced by Supersonic Cluster Beam Deposition (SCBD). [251] The implementation of SCBD electrodes enhanced the charge accumulation efficiency of the transducer by a factor of 10, without significant modification of the mechanical properties of the nanocomposite. [252–254]

We fabricated the ionogel/$BaTiO_3$ nanocomposite (IG/BAT-Nc) using a one-pot synthesis approach, by means of a free-radical UV photo-cross-linking reaction and a simple moulding process. The photopolymerization process is cost-effective and enables to print polymeric nanocomposite layers (1 mm thick) in a simple, controllable and reproducible fashion, with potential for future implementations in UV-assisted 3D printing technologies (e.g., digital light projection-based stereolithography [255]). The polymeric matrix was composed by polyvinylpyrrolidone (PVP, 40000 Mw), physically intertwined with a chemically cross-linked polymer network, constituted by a random copolymer of highly hydrophilic (hydroxyethyl)methacrylate (HEMA) and acrylonitrile (AN), namely, poly-HEMA-co-AN. PVP was introduced as a toughening agent for the ionogel, reinforcing the poly-(HEMA-co-AN) matrix through the formation of an interpenetrating network (IPN) between the two polymers. This network structure was engineered to allow the polymer to retain a large amount of suitable ionic liquids and to incorporate hydrophilic piezoelectric nanostructures, responsible for the piezoionic and piezoelectric effect, respectively. We used 1-(2-hydroxyethyl)-3-methylimidazolium tetrafluoroborate (HoEMIMBF_4, uptake equal to 45 wt. %) as the ionic liquid due to its good solubility in water, affinity with hydrophilic compounds, and high ionic conductivity. [256] We also added a water suspension of custom-synthesized $BaTiO_3$ nanoparticles ($BaTiO_3$ NPs, 2.5 wt.% with respect to the total polymer mass), chemically modified with hydrophilic surface moieties (3,4-dihydroxyhydrocinnamic, HCA), which make them well dispersible in aqueous solutions. After moulding, the polymeric film was dried in vacuum overnight to remove water residuals. The optimal formulation and synthesis procedure were determined empirically, by qualitatively evaluating the uniaxial stretching of the material. The soft nanocomposites exhibited elastomeric-like properties, which are beneficial to enhance their electromechanical response under low frequency stimulations in the quasi-static regime.[257]

2.2.2 Methods

Synthesis of $BaTiO_3$ nanoparticles

Barium titanate nanoparticles ($BaTiO_3$ NPs) have been synthesized according to the literature with small modifications. [225] In a typical procedure, 938 μL of titanium tetraisopropoxide (900 mg, 3.17 mmol) have been dissolved under inert atmosphere in 1.5 mL of isopropanol at room temperature in a 5 mL round-bottomed flask 2 equipped with a magnetic stirrer. Then, 1 g of $Ba(OH)_2 \cdot 8\ H_2O$ (3.17 mmol) was added, and $BaTiO_3$ NPs have been allowed to form by heating up to 80°C in 30 min and leaving the solution at 80°C for 1 h. After the reaction cooled down to room temperature, the obtained nanoparticles were centrifuged (15 min at 6000 rpm) and repeatedly washed with H_2O to remove solvent and by-products. Finally, $BaTiO_3$ NPs have been dried under vacuum to afford a fine white powder stored under inert atmosphere to avoid the formation of carbonates on the surface.

Synthesis of $BaTiO_3$-HCA

The reactive surface of $BaTiO_3$ NPs has been covered with 3,4-dihydroxyhydrocinnamic acid (hydrocaffeic acid, HCA). 0.577 g of $BaTiO_3$ NPs have been redispersed in 50 mL of absolute ethanol. In order to ensure complete disaggregation of the NPs, the suspension has been treated with tip-probe ultrasonicator (600 W, 70% amplitude) for 1 min. Then, 0.860 g of HCA have been added to the suspension, which has been further ultrasonicated for another 1 min. Hence, the mixture has been stirred at 60°C overnight to ensure the HCA attachment. Purification of the final mixture is performed by repeated centrifugation (15 min at 6000 rpm) and wash with ethanol/water mixture (1:1) until colourless supernatant is obtained.

Ionogel formulation and synthesis

The polymeric matrix was composed by polyvinylpyrolidone (PVP, MW = 40000), physically intertwined with a chemically cross-linked polymer network, constituted by a random copolymer of highly hydrophilic (hydroxyethyl)methacrylate (HEMA) and acrylonitrile (AN), namely poly-HEMA-co-AN. The relative ratio of the compounds was set as (PVP : HEMA : AN = 1 : 12.7 : 8.3 wt), while the cross-linker used was ethylene glycol dimethacrylate (EGDMA) (5.5% wt with respect to the PVP and acrylic monomers weight). After addition of the ionic liquid and BaTiO3 NPs, the photoinitiator solution (dimethoxyphenylacetophenone, DMPA, 15% wt in ethanol) was added to the mixture (3.5% wt). The pre-polymer was then poured into a simple moulding constituted by two glass slides and a silicone spacer (1 mm thick). The radical polymerization process is then activated by means of UV light, generated by a Blackray B100-AP lamp (100W, 0.15 W/cm2).

2.2.3 Results

In the present study, $BaTiO_3$ NPs were synthesized according to the literature with small modifications [225] via the sol-precipitation method at atmospheric pressure and were obtained as a fine white powder. The as-synthesized $BaTiO_3$ NPs showed poor dispersion properties in water, mostly due to aggregation induced by surface instabilities. Hence, the surface of the nanoparticles was coated with HCA, by exploiting the catechol functionality of the ligand: HCA acts both as a stabilizer and as water-dispersing agent (**Figure 2.2.1**). Indeed, after surface functionalization, the particles showed higher dispersibility in an aqueous media. The nanoparticles size and crystallinity are very important features to confer piezoelectric behaviour to polymer-based nanocomposites: [208,228,258]

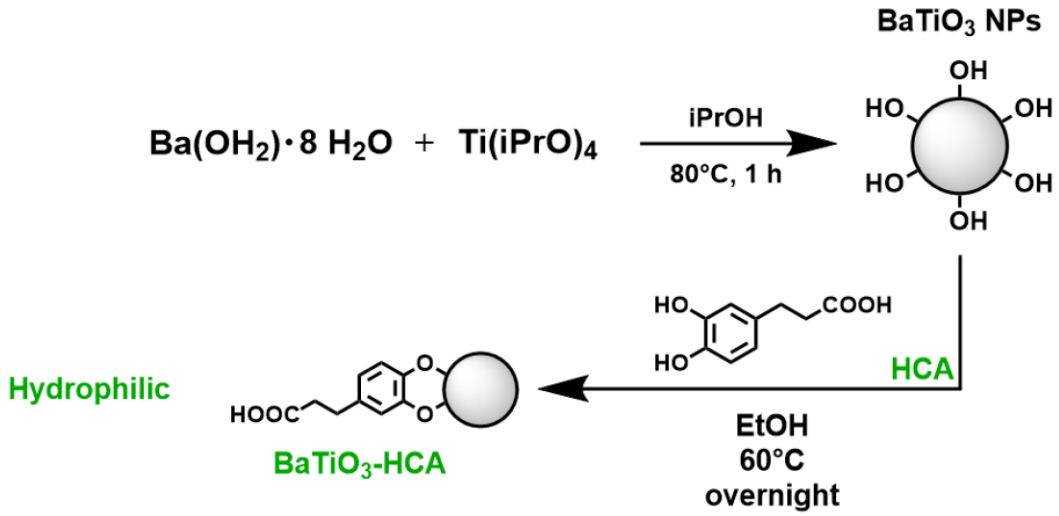

Figure 2.2.1 - Schematic representation of the synthesis of $BaTiO_3$ NPs (top) and the ligand exchange reaction with HCA (bottom).

DLS characterization

DLS analysis of $BaTiO_3$-HCA NPs revealed an average hydrodynamic radius of 296.1 ± 3.9 nm, high monodispersity (PDI = 0.112 ± 0.014) and negative surface Zeta potential (- 37 mV), confirming the presence of deprotonated carboxylic residues on the NPs surface. Transmission electron microscopy (TEM) revealed the presence of particles of 30−50 nm in size (**Figure 2.2.2a**), with the crystal planes clearly visible (**Figure 2.2.2b**).

XRD spectrum analysis

The crystalline structure of the obtained NPs was confirmed by powder X-ray diffraction (XRD) on the dried NPs (**Figure 2.2.2c**). As reported in **Table 2.2.1**, differences in the XRD reflections of cubic and tetragonal phases are only related to the peak splitting observed in the tetragonal phase due to the decrease in crystal symmetry; hence, due to the small crystallite size, XRD peak broadening does not allow for the discrimination between cubic and tetragonal phases of $BaTiO_3$ NPs. However, the cubic structure is only stable above the Curie temperature of $BaTiO_3$ (T = 133°C) and is not piezoelectric, while the synthesized $BaTiO_3$ NPs have shown good piezoelectric response at room temperature, suggesting the presence of mainly tetragonal structures [206].

Average crystallite size has been estimated as 20.2 nm by applying the Scherrer equation (**Equation 2.2.1**) on the most intense and resolved peaks:

$$D = k \cdot \lambda \cdot \beta \cdot \cos\theta \qquad \textbf{Equation 2.2.1}$$

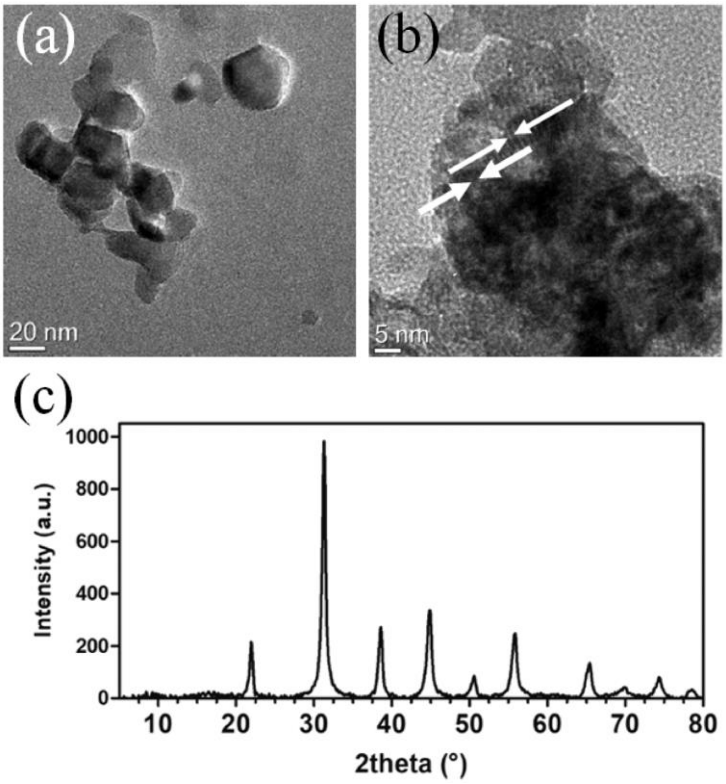

Figure 2.2.2 - TEM images of $BaTiO_3$−HCA NPs. (a) Small globular particles (30−50 nm) are grouped in bigger assemblies of 150−200 nm. (b) Detail of a particle, revealing the $BaTiO_3$ crystal planes (indicated by arrows). (c) XRD pattern of $BaTiO_3$ NPs powder. X-ray source: Cu(Kα).

2theta (°)	*d* spacing (Å)	Relative Intensity (experimental)	Relative intensity (tetragonal) [259]	Relative intensity (cubic) [259]
22.26	3.994	206.4	209.3	206.6
31.61	2.831	1000	1064.9	1057.1
38.89	2.316	265.7	263.2	259.4
45.17	2.007	342.8	345.2	344.7
50.85	1.796	78.2	88	95.9
51.17	1.785	/	10.7	/
56.1	1.639	244.2	278.6	356.4
56.4	1.631		79.5	/
65.72	1.421	138.3	118	118.5
66.03	1.415	/	39.2	59.3
66.19	1.412	/	19.8	/
74.67	1.217	79.6	69.5	89.7

Table 2.2.1 - Experimental XRD reflections with the corresponding reference parameters for cubic and tetragonal $BaTiO_3$

Where D is the mean size of crystallites (nm), k is crystallite shape factor (a good approximation is 0.9), λ is the X-ray wavelength, β is the full width at half maximum (FWHM) in radians of the X-ray diffraction peak and θ is the diffraction angle [260]. A k value of 0.94 has been chosen as it usually applies for quasi-spherical particles. This result totally agrees with TEM images, which show bigger particles but crystalline domains around 20 nm.

However, the small size of the $BaTiO_3$ crystal domains caused XRD peaks broadening, thus limiting the possibility to distinguish between the cubic and the tetragonal crystalline phase, the latter being the most stable at room temperature. After samples preparation, the nanocomposites were poled at room temperature under an electric field of 3.3 kV/cm for 7 h in a vacuum (10^{-5} Torr) by clamping the materials between a pair of anticorodal aluminium slabs. The choice of these relatively mild polarization conditions was due to the low tolerance of the ionogel matrix to high-intensity electric fields and harsh temperature conditions, which may induce the polymer backbone degradation.[261] At the same time, we expected to obtain an adequate polarization of the piezoelectric material with lower coercive fields thanks to the presence of the ionic liquid, as previously demonstrated by Fukagawa et al.[262] A schematic of the obtained poled piezoionic/piezoelectric nanocomposite is reported in **Figure 2.2.3a**, along with a photograph of a typical sample. The response to mechanical stimuli of both the

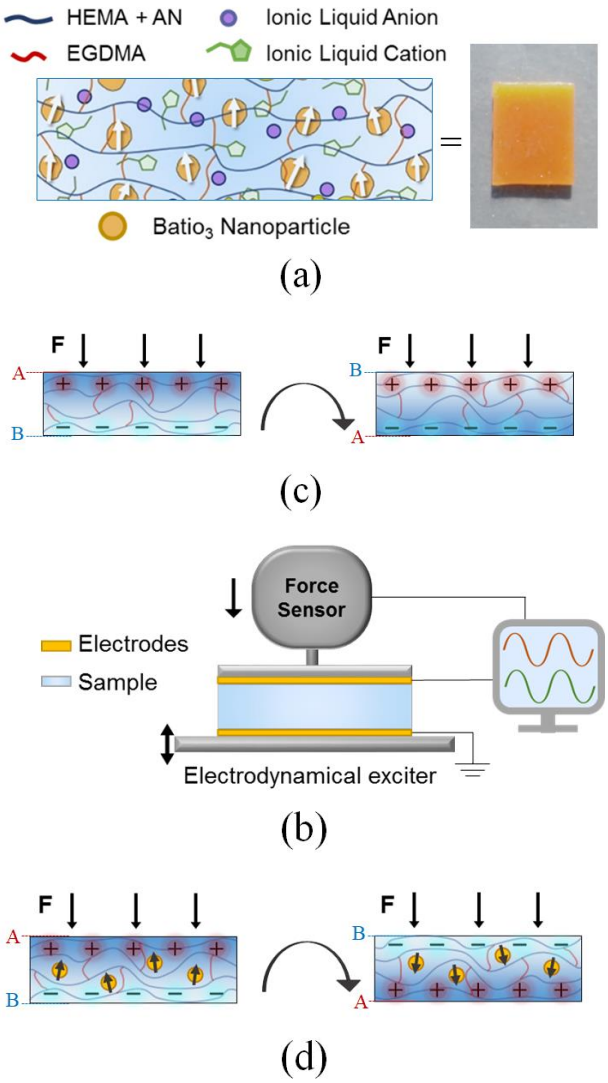

Figure 2.2.3 - (a) Schematic representation of the poled IG/BAT-Nc (white arrows indicate the nanoparticles electrical dipoles) and a picture of a typical sample. (b) Schematic of the measurement system employed for electromechanical testing. (c) Isotropic piezoionic response of a pristine ionogel. (d) Anisotropic piezoionic/piezoelectric response of a poled IG/BAT-Nc (dark grey arrows indicate the nanoparticles electrical dipoles).

pristine ionogel and the poled IG/BAT-Nc samples were assessed through open-circuit voltage measurements under a low-intensity periodical driving force, at low frequencies. A quasi-static method was used, employing a custom-designed measurement apparatus represented in **Figure 2.2.3b**. It operated by establishing a compressive static load to the sample, sandwiched between two metallic plates, and by subsequently applying an oscillating component to the applied force. The output signal generated by the materials was then recorded using a multimeter connected to the electrodes. All measurements were performed with a static load of 0.5 N, to guarantee electrical contact between the samples and the

electrodes, and a periodic force of 0.5 N. Voltage and force data were acquired in real-time at a sampling frequency of 300 Hz with a dedicated LabView program.

Both ionogel and IG/BAT-Nc were tested for comparison at the frequencies of 100 mHz, 500 mHz, and 1 Hz. In order to verify the isotropy or anisotropy of the response of the material, all groups of measurements were performed twice by flipping the orientation of the sample with respect to the direction of the normal force, as schematized in **Figure 2.2.3c,d**. Both the pristine ionogel and IG/BAT-Nc responded to low frequencies, with no frequency-dependent output voltage in the range explored. The electrical response was, for both sample types, out of phase with the mechanical stimulation, with a constant lag time corresponding to 180 ms (**Figure 2.2.4a**). This delay could be ascribed to an interplay between a material intrinsic property (i.e., the mechanical relaxation and ionic transport dynamics) and an instrumental error derived from the data acquisition and communication rates between the multimeter and load cell. As shown by the graphs (**Figure 2.2.4a**), the presence of the poled nanoparticles enhanced the electromechanical performance of the material, allowing to reach a response of 8 mV under a compressive force of 0.5 N, corresponding to a pressure of 5 kPa. This value falls into the low-pressure range (<10 kPa, 1 kPa being roughly the sensitivity of the human finger), as identified in the touch sensors framework,[263] and it is adequate to monitor a variety of biomechanical motions, such as blood pressure changes between heartbeats.[264] Moreover, the poled sample showed a typical ferroelectric hysteresis,[265] not shown by the piezoionic gel (**Figure 2.2.4b**). The maximum output values reached by the nanocomposites were systematically higher with respect to that of the pristine ionogel for all of the frequencies tested when the direction of the applied compressive force was the same as the electrical polarization of the nanoparticles (8 mV to 7 mV against 3.5 mV to 1 mV for 0.1 and 1 Hz, respectively). This effect was damped down when the preload was applied in the opposite direction, and no significant difference in the response between the samples was observed (3 mV to 1 mV for 0.1 and 1 Hz, respectively). This anisotropic response can be ascribed to the presence of the $BaTiO_3$ NPs, which confer to the ionogel the bias directionality typical of ferroelectric materials. This behaviour was probably due to a cooperation between two mechanisms: the isotropic piezoionic effect and the anisotropic ferroelectric effect. While the pristine ionogel response remained almost unvaried in both amplitude and phase under sample switching (**Figure 2.2.4c**), the IG/BAT-Nc response exhibited both an anisotropic behaviour (phase inversion) and an amplitude modulation (**Figure 2.2.4d**). The piezoionic and piezoelectric contributions showed the same phase in one configuration (the directions of preload and polarization are parallel) and an opposite phase when the sample was flipped

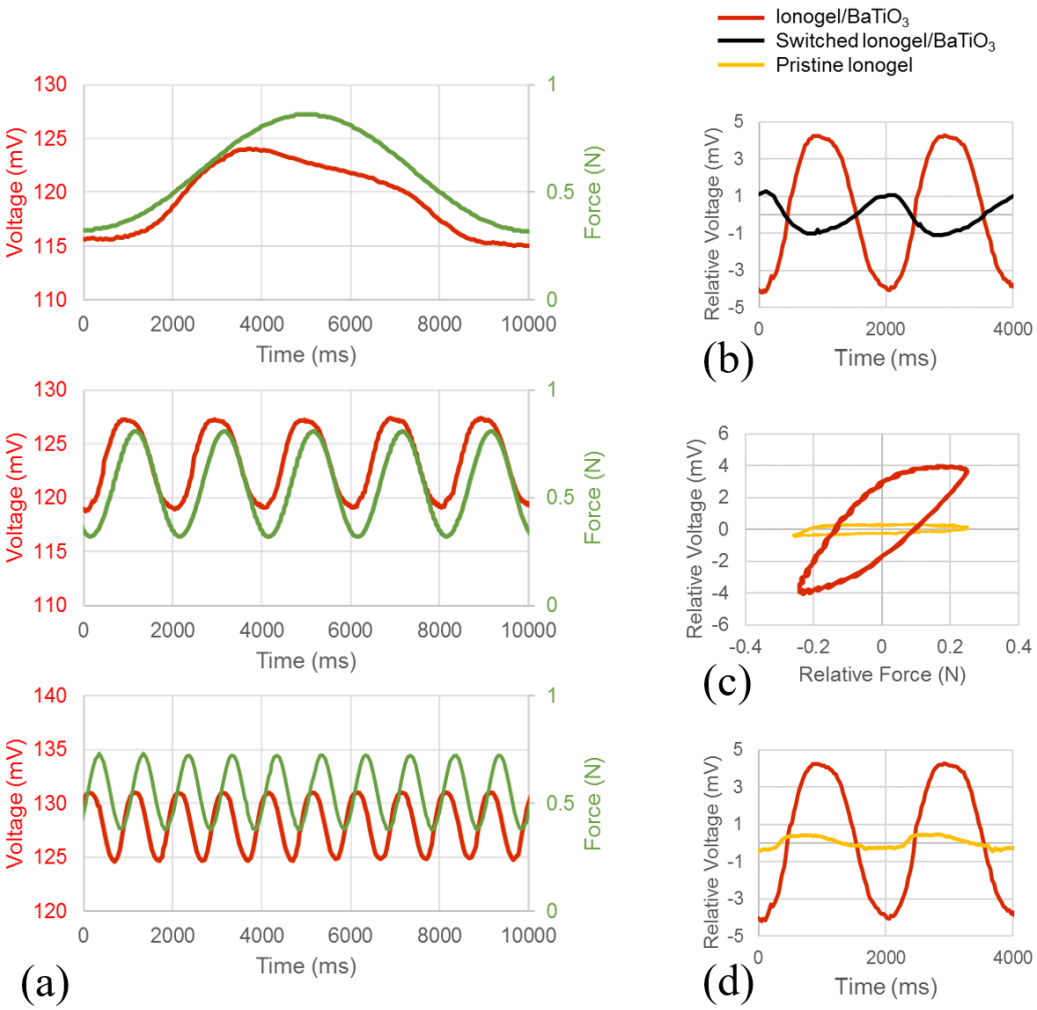

Figure 2.2.4 - (a) IG/BAT-Nc response at 0.1 (left), 0.5 (middle), and 1 Hz (right). (b) Hysteresis loop of pristine ionogel and IG/BAT-Nc, the latter showing the typical ferroelectric behaviour. (c) Pristine ionogel and IG/BAT-Nc response at 0.5 Hz. (d) Anisotropic response of the IG/BAT-Nc at 0.5 Hz, observed by flipping the sample with respect to the normal force direction.

with respect to the applied force (the directions of preload and polarization are antiparallel), causing the observed amplitude modulation. This remarkable feature is particularly interesting for applications in discriminative touch sensing and objects localization in physically unstructured environments.[266–269] In fact, ionic gels and ionogel-based materials are isotropic systems that allow to identify only the direction of the applied force by measuring the generated bias, despite the sample orientation.[240,241,270] On the other hand, the nanocomposite developed in the present work enables to discriminate the sensing element orientation with respect to the applied force, exploiting the anisotropy induced by the combination of the piezoionic and piezoelectric effect. The electromechanical stability of the materials was assessed through cyclic measurements using the same experimental apparatus.

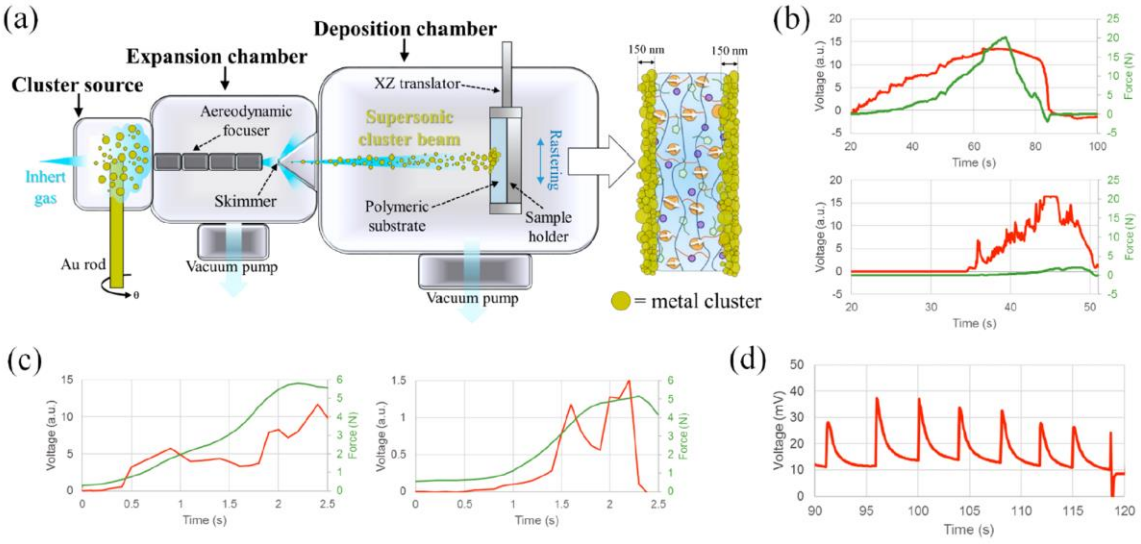

Figure 2.2.5 - (a) Schematization of a typical SCBD apparatus and nanoparticles deposition procedure to fabricated cluster-assembled thin electrodes, integrated into IG/BAT-Nc. (b) Static measurements to qualitatively evaluate the piezo-response of a bare IG/BAT-Nc (top) and an IG/BAT-Nc provided with gold nanostructured electrodes (bottom). (c) Output voltage of the IG/BAT-NC subjected to a compressive load of 5 N in with (left) and without (right) the SCBD electrodes (left). (d) Finger tapping tests performed on an IG/BAT-Nc sample provided with integrated gold electrodes.

The samples showed good signal stability for over 20000 cycles (more than 15 h of operation), preserving their responsive behaviour for several months after fabrication. In order to enhance the efficacy of the electro-mechanical conversion of the IG/BAT-Nc, the poled materials were provided with monolithically integrated nanostructured electrodes, fabricated by SCBD of gold nanoparticles (**Figure 2.2.5a**). Details on the operational principle of SCBD can be found elsewhere.[251] The use of SCBD allowed obtaining large surface area electrodes, physically interpenetrating with the polymer, which morphology (**Figure 2.2.6**) dramatically increases the electrode/piezo−polymer interface area. [254,270] This was expected in turn to significantly increase the charge collection and transportation in response to the application of compressive loads. Electrical resistance of about 100 Ohm/cm was reached at a thickness of the deposited gold layer corresponding to 150 nm. The feasibility of the approach was preliminary assessed through a static measurement, performed by manually applying compressive loads at the sample. This was sandwiched between the two planar charge collectors previously employed. The load was applied by regulating the micrometric screw controlling the dynamometer motion using the apparatus described above. For comparison, an IG/BAT-Nc without the integrated electrodes was tested in the same conditions. The output voltage was measured by using a charge amplifier, elaborating the signal acquired from

the charge collectors using a classical circuit layout such as the one reported in the literature.[255] Due to variations of the input resistance introduced by the presence of the ion-conductive ionogel, the voltage output is affected by an undetermined gain factor. Therefore, the measurements readout had merely a qualitative and comparative meaning in order to investigate on the effect of the cluster-assembled electrodes on the nanocomposite response. The static tests showed a significant difference in the response between the bare IG/BAT-Nc (**Figure 2.2.5b, top**) and the same material provided with the integrated electrodes (**Figure 2.2.5b, bottom**). In fact, the nanocomposite having gold nanostructured electrodes required the application of a compressive load equal to one tenth of that applied to the bare material in order to reach the same output response. This increased sensitivity is related to the presence of the integrated electrodes, which probably both enhanced the charge accumulation at the nanocomposite/metal interface and favoured the electrical contact between the sample and the charge collectors, decreasing the overall charge dispersion. This enhanced response was also confirmed by subjecting the samples to the same compressive load and by recording the output voltage, as shown in **Figure 2.2.5c**. A further assessment of the suitability of the SCBD approach was carried out by performing finger tapping measurements to obtain quantitative operative voltage values of the integrated electrodes conversion efficiency, which resulted up to 40 mV for compressive stresses of about 10 kPa (**Figure 2.2.5d**). In conclusion, we demonstrated the fabrication and electro-mechanical characterization of a novel piezoionic/piezoelectric polymeric nanocomposite material based on a chemically cross-linked ionogel with $BaTiO_3$ NPs. The composite responded to low frequency (0.1−1 Hz) mechanical compressive stresses in the low pressure regime (<10 kPa), generating output voltages up to 8 mV. The combination of the piezoionic and piezoelectric activity resulted in an anisotropic electrical response to quasistatic mechanical perturbations, enabling to discriminate the sample orientation with respect to the load direction by monitoring the phase and amplitude modulation of the output signal. The fabrication of cluster-assembled gold electrodes produced by SCBD was also assessed. This resulted in an enhancement of the charge accumulation efficiency by a factor of 10, compared to the bare material, as demonstrated by static electro-mechanical tests. Our results suggest that the presented piezoionic/piezoelectric nanocomposites constitute an interesting solution for the development of smart devices for discriminative touch sensing and objects localization in physically unstructured environments for soft robotics and wearable electronics applications.

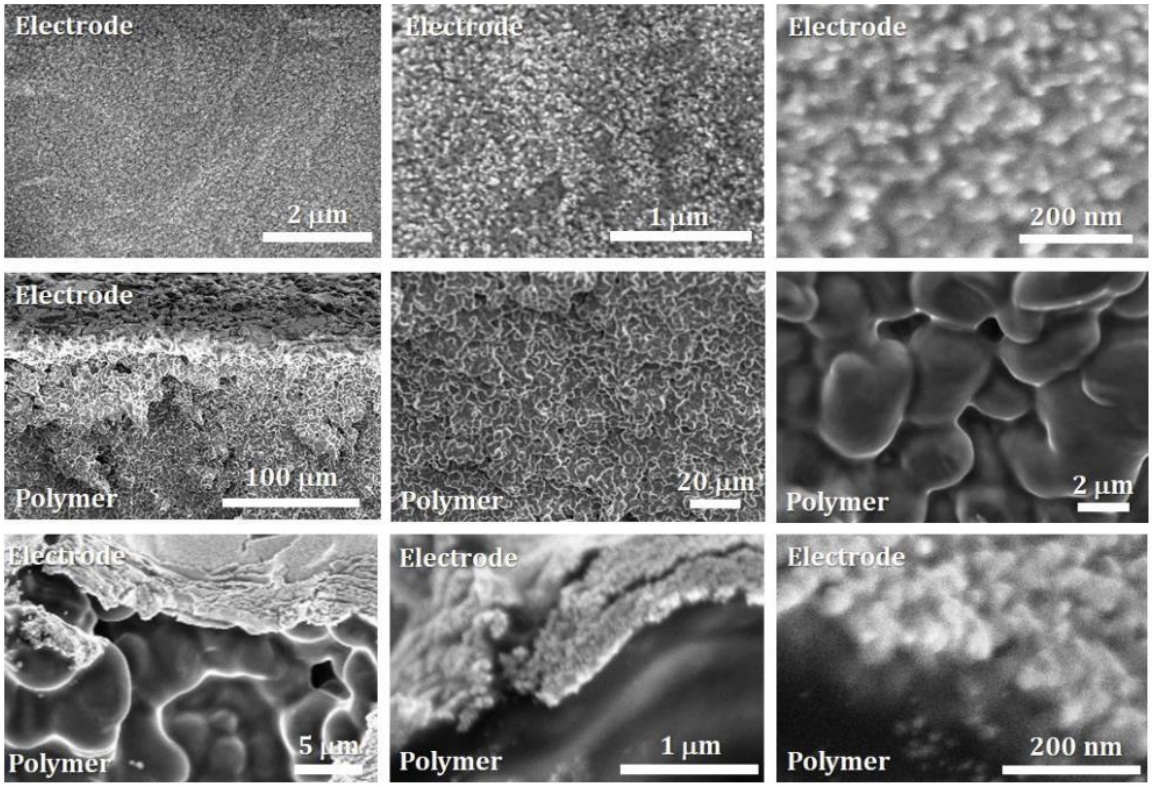

Figure 2.2.6 - SEM imaging of the ionogel/BaTiO3 nanocomposite provided with nanostructures gold electrodes produced by mean of SCBD. A top view of the electrode is reported on top, while a cross-section of the material, highlighting the morphology of the ionogel/BaTiO3 nanocomposite, is shown at the middle row of the panel. Details of the electrode morphology in the cross-sectional view are reported at the bottom.

2.3 Piezoelectric properties of lipophilic $BaTiO_3$ nanoparticles in stretchable PDMS matrix

Maturi, M.; Comes Franchini, M.; Milani, P.[♪] et al. *Manuscript in preparation*

[♪] Interdisciplinary Centre for Nanostructured Materials and Interfaces (CIMaINa), Università degli Studi di Milano (Italy)

2.3.1 Introduction

As discuss in detail in Chapter 2.2, barium titanate represents one of the best candidates for ceramic-based nanocomposites thanks to its good piezoelectric response and reduced toxicity. In this case, a simpler nanocomposite is simply prepared by dispersing lipophilic nanocrystals in PDMS matrices. The nanocomposite will be therefore fully characterized to quantitatively describe its piezoelectric behaviour. As anticipated in the previous sections, the poling procedure is to align the electrical dipoles within the ferroelectric domains of the nanoparticles and among different nanoparticles, enhancing the piezoelectric effect [271]. In order to efficiently align the dipoles and the ferroelectric domains, a common procedure is to heat the material over its Curie temperature, and let it cool down under the action of an external electrical field (field-cooling).

The measure of piezoelectricity presents many challenges and technical issues, caused mainly by the lack of a standard and universally recognized method. The lack of a standard method results in a non-uniformity in how the results are presented in literature. Most of the work presented in literature report operative values of voltage and current as the piezoelectric output effect, usually without a detailed explanation of the method used to obtain them. Only for few piezocomposites the value of the piezoelectric coefficient is presented, usually measured with a commercial system operating at a single frequency and with a single pre-load. In this work the piezoelectric performance of the nanocomposites was measured using an instrument developed in CIMaINa laboratories in order to overcome some of these problems. The instrument is designed to operate in a quasi-static or dynamic regime, in the way of the Berlincourt technique [272]. A vertical oscillating force is applied perpendicularly to the sample and measured with a force sensor while the output charge is collected and measured with a dedicated electronic circuit. The system allows to select the stimuli frequency and the dynamic force programmatically, allowing to make multiple measurements, and the pre-load can be selected manually. This allows to reproduce the measurement protocol in a very simple way by defining a measurement protocol.

2.3.2 Methods

Synthesis of dopamine dodecyl amide (DDA)

In a 500 mL round-bottomed flask equipped with a magnetic stirrer and under nitrogen flow, 2.49 g (13.2 mmol) of dopamine hydrochloride are dispersed in 100 mL of dry THF, then 4.5 mL of triethylamine (32.3 mmol) are added leading to the dissolution of dopamine. The mixture is cooled to 0°C with an ice bath and a solution of lauryl chloride (3.00 mL, 13.0 mmol) in 150 mL of dry THF is added dropwise in 3 hours. After complete addition of the acyl chloride, the mixture is stirred at room temperature for 45 minutes then 25 mL of water are added to ensure the dissolution of the precipitated triethylammonium chloride, the organic solvent is removed by rotary evaporation and the aqueous phase is extracted 3 times with ethyl acetate. The organic phase is then dried over dry Na_2SO_4 and concentrated under reduced pressure to afford DDA as a white solid. Yield = 85%. The product underwent NMR and ESI-MS analysis to assess purity and to confirm the structure (**Figure 2.3.1**).

^{1}H NMR (600 MHz, $CDCl_3$) δ = 6.77 (d, *J* = 8.0 Hz, 1H), 6.70 (d, *J* = 2.0 Hz, 1H), 6.51 (dd, *J* = 8.0, 2.0 Hz, 1H), 5.67 (t, *J* = 6.0 Hz, 1H), 3.45 (t, *J* = 7.0 Hz, 2H), 2.66 (t, *J* = 7.0 Hz, 2H), 2.13 (t, *J* = 7.0 Hz, 2H), 1.56 (m, 2H), 1.22 (bs, 16H), 0.85 (t, *J* = 7.0 Hz, 3H).

^{13}C-NMR (75 MHz, CDCl3): δ = 14.10, 22.67, 24.80 25.7, 29.18, 29.28, 29.32, 29.45, 29.59, 31.9, 34.8, 36.8, 41.0, 115.2, 115.5, 120.4, 130.4, 143.2, 144.4, 174.7.

ESI-MS [M+Na] = 358

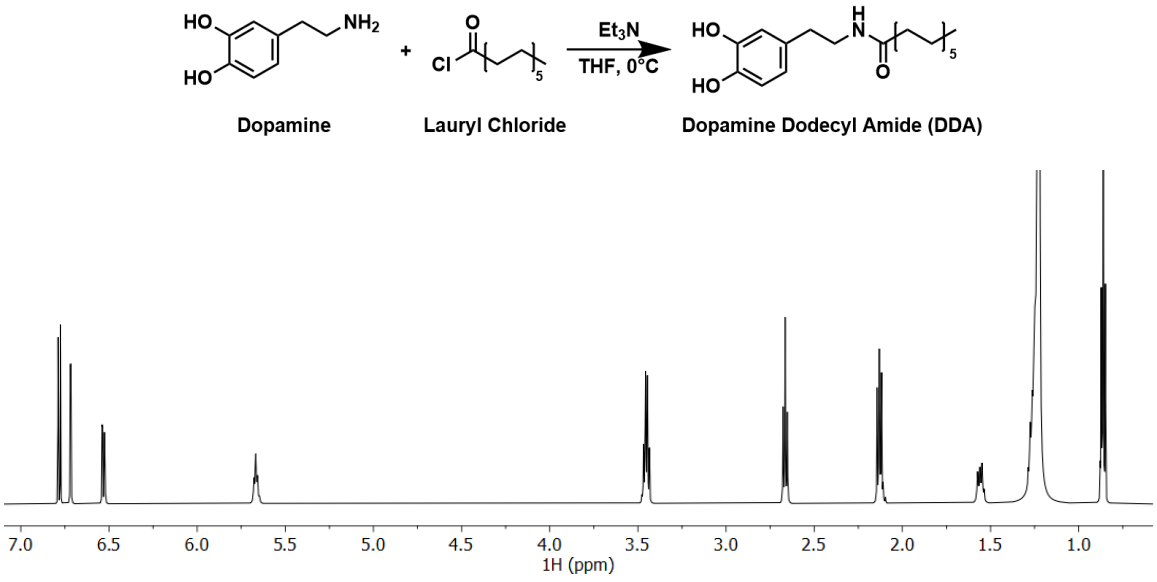

Figure 2.3.1 – Reaction scheme for the synthesis of the lipophilic DDA ligand and ^{1}H-NMR spectrum of the ligand.

Ligand exchange on $BaTiO_3$ NPs surface

The reactive surface of $BaTiO_3$ NPs has been covered with dopamine dodecylamide (DDA) by exploiting the catechol functionality of the ligand. In a 250 mL beaker, 0.577 g of $BaTiO_3$ NPs have been redispersed in 50 mL of absolute ethanol. In order to ensure complete disaggregation of the NPs, the suspension has been treated with tip-probe sonicator (70% amplitude) for 1 min. Then, 1.15 g of DDA have been added to the suspension, which has been further ultrasonicated for another 1 min. Hence, the mixture has been placed in a 100 mL round-bottomed flask and stirred at 60°C overnight to ensure the ligand exchange.
Purification of the final mixture is performed by repeated centrifugation (15 min at 6000 rpm) and wash with ethanol two times then with hexane until colourless supernatant is obtained. Finally, the obtained $BaTiO_3$-DDA NPs have been collected in 5 mL of hexane, leading to a uniform brown suspension of NPs. After ligand exchange reaction, the particles showed dispersibility in organic solvents such as chloroform, dichloromethane and THF.

Electron microscopy analysis

The solution is drop casted a perforated carbon film supported by a copper grid. The preparation was then dried at 100 °C. The Transmission Electron analyses were performed with a FEI TECNAI F20 microscope operating at 200 keV. The instrument is also equipped with a dispersion micro-analysis of energy (EDS) and the STEM accessory. The TEM image were taken in the phase contrast mode and Selected Area electron diffraction (SAED). STEM pictures were recorded using an High Angle Annular Dark Field (HAADF) detectors: in this imaging mode the intensity I is proportional to $Z^{1.7}t$, where Z is the mean atomic number and t is the thickness of the specimen

Nanocomposite synthesis

One of the most used polymeric matrixes to embed piezoelectric particles is polydimethylsiloxane (PDMS), a silicone-based organic polymer. PDMS is particularly convenient for several applications because it is hydrophobic, permeable to gases, physiologically inert and thermally stable. Moreover, it has good mechanical properties, such as high stretchability and deformability, it is optically transparent and a good dielectric [273]. Those characteristics make it suitable for a wide range of applications. PDMS' mechanical properties (e.g. stiffness) can be tuned during the fabrication process, and its piezoelectric properties are determined by the loading of piezoelectric particles and the poling process. For all of these characteristics PDMS has been widely used for piezoelectric nanocomposites development [274]. In order to achieve a uniform distribution of $BaTiO_3$-DDA nanoparticles inside the PDMS matrix, a common organic solvent was used to dissolve the elastomer base

and to disperse the nanoparticles, and the two solutions were mechanically stirred together. After the complete evaporation of the solvent, when the nanoparticles are well dispersed in the PDMS base, the curing agent is added and mechanically stirred with the PDM-nanoparticle dispersion [275]. The fabrication procedure followed is reported below:

1. The silicon elastomer base is dissolved in chloroform, and the solution is mechanically stirred for 30 minutes.
2. The chosen quantity of nanoparticles is dispersed in chloroform. The mixture is mechanically stirred for 30 minutes.
3. The solution of silicon elastomer base and the nanoparticles dispersion is mixed and stirred for 20 minutes with the help of a magnetic anchor.
4. The solution is heated at 60°C in order to speed up the solvent evaporation process. The complete evaporation of chloroform leaves the BaTiO3-DDA nanoparticles dispersed in the polymer base.
5. The curing agent is added, and the mixture is mechanically stirred for other 20 minutes.
6. The obtained mixture is degassed and poured in a prepared mould.
7. The mould is degassed in a vacuum chamber in order to eliminate air bubbles trapped in the mixture during the previous phases and other bubbles originated from the roughness of the mould.
8. The material is cured at 150°C for 2.5 hours in a pre-heated oven.

The resulting material (**Figure 2.3.2**) is a flexible and elastic solid, and it was cut into 16mm-diameter discs. **Table 2.3.1** reports the quantities of the compounds used to fabricate 70 x 60 x 0.6 mm samples at different loadings of nanoparticles.

Loading (wt.%)	Silicone elastomer base	Curing agent	$BaTiO_3$-DDA NPs	Chloroform
0%	3.2 g	320 mg	0 mg	18 mL
5%	3.2 g	320 mg	175 mg	18 mL
10%	3.2 g	320 mg	350 mg	18 mL
15%	3.2 g	320 mg	525 mg	18 mL
20%	3.2 g	320 mg	700 mg	18 mL

Table 2.3.1 - Compounds and relative quantities used in the nanocomposite fabrication process.

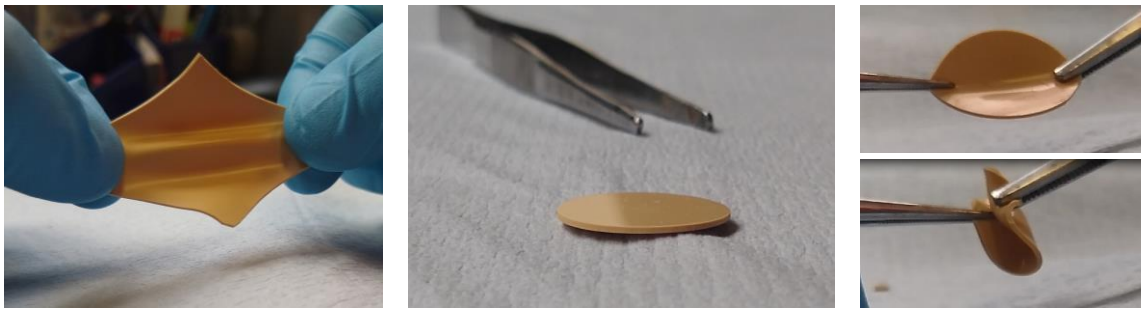

Figure 2.3.2 - The PDMS-$BaTiO_3$-DDA nanocomposite is a free-standing, flexible and elastic solid.

Poling

A schematic representation and a picture of the setup needed for the poling procedure is shown in **Figure 2.3.3**.

The poling procedure is the following:

1. The samples are placed between two metal plates, forming a plane capacitor in contact with both sides of the samples.
2. The plates are heated at 130°C through resistive heaters.
3. Once the plates reach the temperature, a voltage difference of 1.2kV is imposed between the two plates, generating an electrical field of 20kV/cm. The system is kept in this configuration for 2 hours.
4. The temperature is slowly decreased from 130°C to 110°C, under the electrical field mentioned before. This first cooling phase takes two hours.
5. The heaters are turned off, and the samples cool from 110°C to room temperature under the effect of the electrical field. This second cooling phase takes another 2 hours.
6. The electrical field is turned off.

In order to prevent ionization discharges in air the whole process is performed inside a vacuum chamber at the pressure of $3 \cdot 10^{-5} bar$.

Electrodes

For polymeric nanocomposites the choice of the electrodes is an essential aspect to be addressed during the fabrication process. Since piezoelectricity is an electro-mechanical effect, coupling adhesion and compliance between the polymeric nanocomposite and the electrode is pivotal to enhance the material response. The PDMS-$BaTiO_3$ nanocomposites were equipped with monolithically integrated nanostructured electrodes, fabricated by means of supersonic cluster beam deposition (SCBD) [251,252,276].

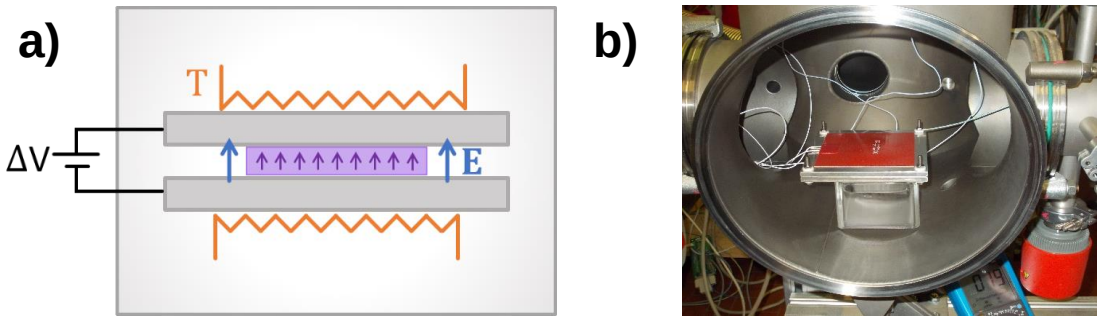

Figure 2.3.3 - Poling schematic representation (a) and experimental set-up (b).

This technique is based on the implantation of neutral metal nanoclusters, accelerated by a supersonic aerodynamical flow using a carrier gas, into the polymer matrix. The deposition takes place at room temperature and low energy. This avoids thermal or chemical damage of the samples. As a result, this leads to the formation of large surface area nanostructured electrodes with controlled morphology at the nanoscale, which is a salient feature to promote an effective charge accumulation. The electrodes deposited with this technique are excellently adherent to the polymer matrix and do not significantly alter the mechanical properties of the nanocomposite. A schematic of the apparatus is reported below (**Figure**Error! Reference source not found. **2.3.4**).

The electrical conductivity of the layer, with typical thickness from few tens to few hundreds of nanometres, is a function of the number of clusters deposited and therefore of the film

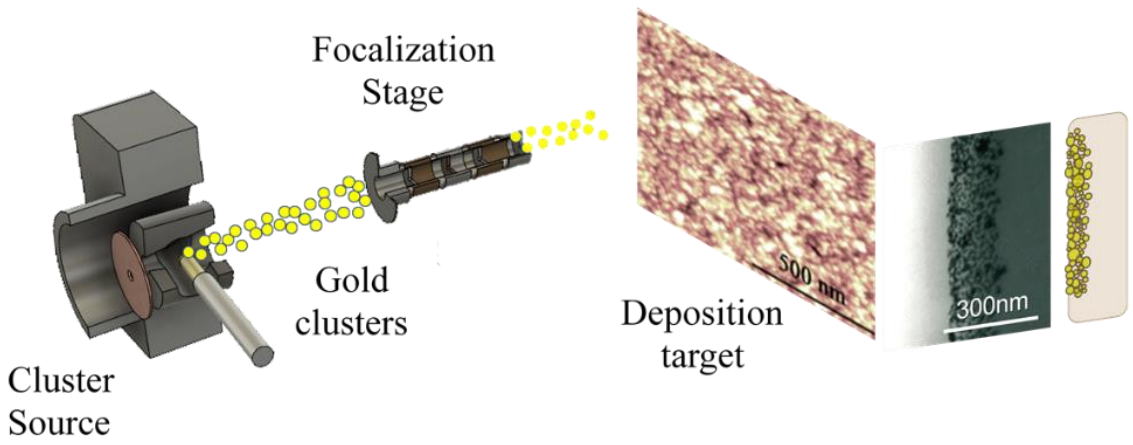

Figure 2.3.4 - Supersonic cluster beam deposition schematic. This technique allows to implant metallic neutral nanoparticles on a polymeric surface by means of a supersonically accelerated carrier gas.

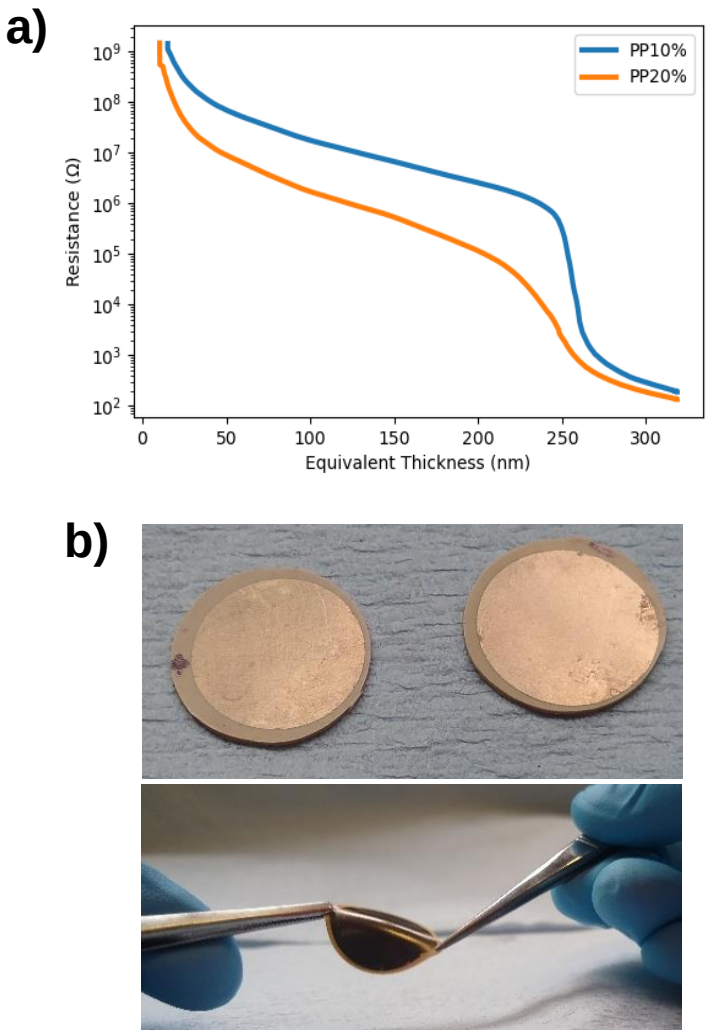

Figure 1.3.5 - a) Evolution of the gold nanocomposite sheet resistance with deposited thickness. b) The PDMS-$BaTiO_3$-DDA/Au nanocomposite is still a flexible and free-standing material. The nanostructured electrodes fabricated with this technique maintain the base material flexibility and stretchability without compromising their electrical properties.

thickness. It is possible to monitor the electrical transport properties of the metal film during the deposition process by an in-situ measure of the layer resistance versus the deposited thickness. Gold nanostructured electrodes were deposited with this technique on the PDMS/$BaTiO_3$-DDA samples A resistance of about 100 Ω was reached at a thickness of the gold layer corresponding to 320 Ω, and was maintained stable until the final thickness of 450 nm. The resistance evolution can be observed in **Figure 1.3.5**. The thickness of the gold layer was measured using as a reference the gold nanoparticles deposited on a reference sensor.

The penetration depth of SCBD-deposited gold electrodes does not strictly depend on the deposition time, but on other deposition conditions such as the deposition rate (number of clusters that impact the substrate surface at a given time) and other experimental parameters such as pressure and frequency on nanocluster production, i.e., their kinetic energy at the impact. [277] The penetration depth

Piezoelectricity assessment

Due to sensitivity issues these systems are usually employed to measure the piezoelectric coefficients of PVDF-based nanocomposites [271] or piezoelectrects, namely voided charged polymers [228], which have a high piezoelectric constant, even though they lack in thermal stability, they age at high deformations and they don't show any longitudinal piezoelectric effect [278–281]. There is only one case of a measure of d_{33} concerning a piezoelectric nanocomposite with a polymeric base different than PVDF [255], where the measure was performed applying specific loads orthogonal to the substrate, and the charge was measured using an in-home built electrical conditioning circuit.

Measurement method

For the measurements presented here the following protocol was implemented:

1. A 5 N pre-load force is imposed manually.
2. For every frequency in the selected range are imposed a sequence of oscillating stimuli with increasing dynamic force, and the charge response of the material is collected through a couple of electrodes.
3. $d_{33}(f)$ is calculated as the slope of the force-charge curve.
4. This cycle can be repeated as many times needed in order to investigate the piezoelectric effect stability.

In order to obtain quantitative results, the electronic circuit was calibrated using controlled input signals, and the whole system was validated measuring the piezoelectric coefficient spectrum of a known sample, i.e., a commercial PVDF membrane (©Precision Acoustics, thickness $110\mu m$). The system has a sensibility of 1 pC/N and can measure piezoelectric coefficients in the range 1 pC/N – 500 pC/N for frequencies between 100 Hz and 1200 Hz (**Figure 2.3.6**).

2.3.3 Results

Barium titanate nanoparticles were synthesized by the sol-gel method published by Yoon et al. and described in Chapter 2.2. [225]

The crystal structure of the prepared nanopowder was assessed by powder XRD giving identical results to the ones reported in Chapter 2.2, therefore they are not repeated here for conciseness.

Lipophilic $BaTiO_3$ nanoparticles

After ligand exchange reaction (**Figure 2.3.6**) the $BaTiO_3$-DDA nanosystem showed good dispersibility and colloidal stability in organic solvents such as hexane, chloroform and THF, revealing the effectiveness of the surface modification with the synthetic catechol ligand.

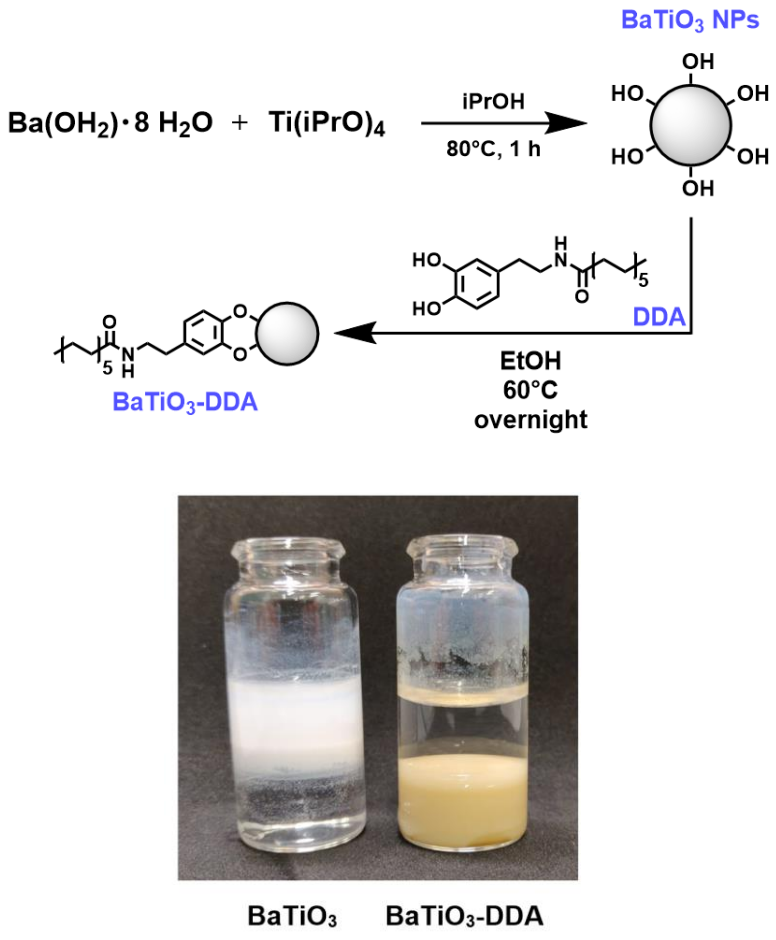

Figure 2.3.6 – Top: reaction scheme for the of lipophilic barium titanate nanoparticles by coating with dopamine dodecyl amide (DDA). Bottom: optical camera picture demonstrating the efficient stabilization of $BaTiO_3$-DDA nanoparticles in chloroform. While pristine $BaTiO_3$ nanoparticles (left) are efficiently dispersed in the upper aqueous phase and do not diffuse into the lower organic layer, lipophilic $BaTiO_3$-DDA nanoparticles show better dispersibility and inverse solubility properties.

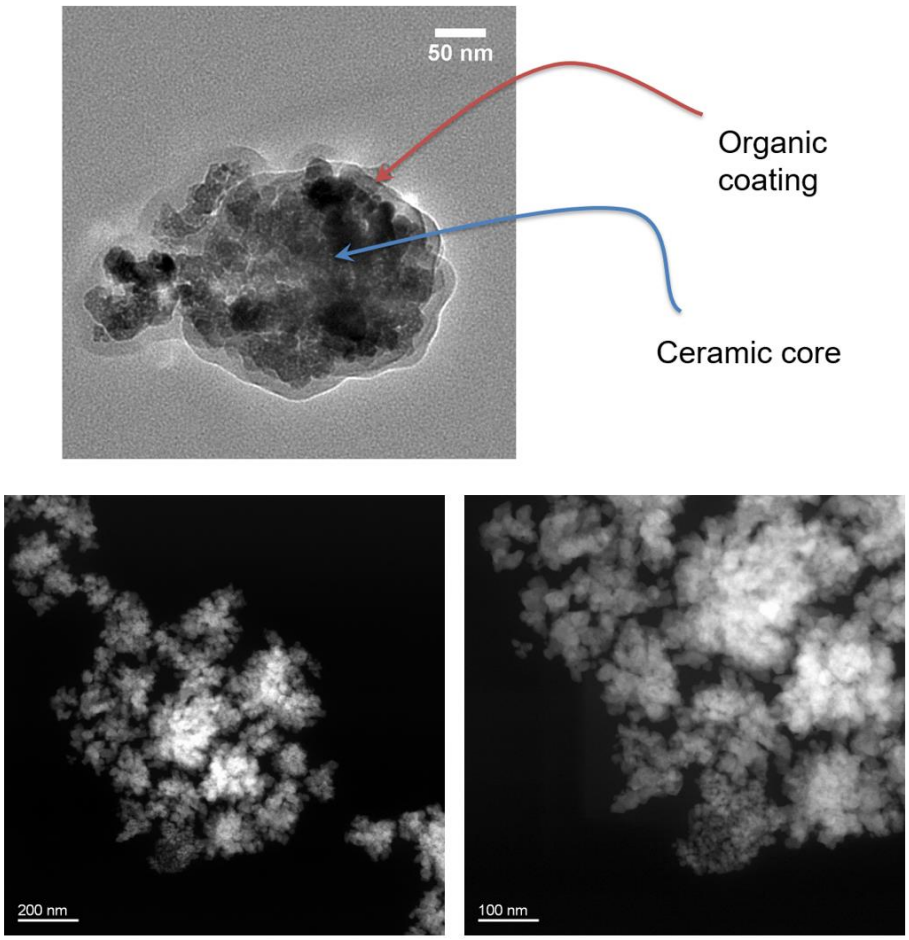

Figure 2.3.7 – TEM (top) and STEM (bottom) images of the prepared $BaTiO_3$-DDA. The organic coating is visible in TEM mode as casing the ceramic cores.

The obtained nanosystem was therefore deeply studied by TEM analysis which first revealed the presence of crystallites having a size between 20 and 50 nm (**Figure 2.3.7**). The organic coating was also visible from TEM images as a thin layer that wraps the surface of the entire nanoparticles. Moreover, selected-area electron diffraction (SAED) analysis was performed over a 200 nm^2 area of the sample, revealing some crystal plane reflections (**Figure 2.3.8**). Then, by software manipulation of the SAED pattern, it was possible to extract a pseudo-diffraction spectrum where the *x*-axis is attributed to the reciprocal of the distance between crystal planes. The contribution from the amorphous organic coating can be assigned to the diffuse light from the centre of the SAED pattern while the clear spots represent well-distinct crystal plane reflections. At this point, the position and relative intensities of the SAED diffraction peaks were extracted from the pseudo-diffractogram and compared to the literature values for tetragonal $BaTiO_3$ reflections, giving a good degree of match between the two. As expected from what was obtained in the previous Chapter in the powder XRD analysis

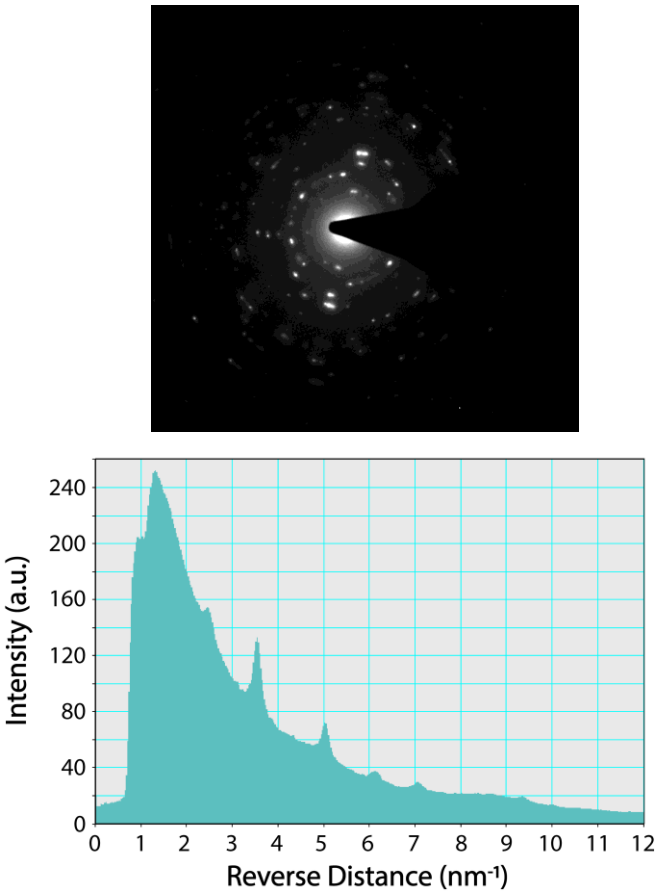

Figure 2.3.8 – TEM analysis. Top: selected-area electron diffraction (SAED) pattern of a crystalline $BaTiO_3$ nanoparticle. Bottom: integrated spectrum revealing main diffraction peaks obtained by the SAED analysis.

of lipophilic $BaTiO_3$, the small crystallite size does not allow for the analytical determination of the degree of tetragonality of the prepared nanopowder. However, the good piezoelectric properties that will be shown next reveal good piezoelectric response (and thus high tetragonality) of the nanopowder. Finally, the elementary chemical composition of the nanopowder was assessed by energy-dispersive x-ray spectroscopy (EDX) (Figure 2.3.9). The irradiation of the sample by high-energy electron cause for the formation of inner electron vacancies in the specimen atoms, which then relax emitting characteristic x-ray lines that can be unambiguously attributed to the element that generated them. The Ba and O peaks are displayed. The Ti K-peak is superimposed on the Ba L-lines, but it is possible to confirm the presence of titanium by observing the presence of the Ti L-line to the left of the oxygen peak, just above the background. The Cu characteristic line are due to the support grid.

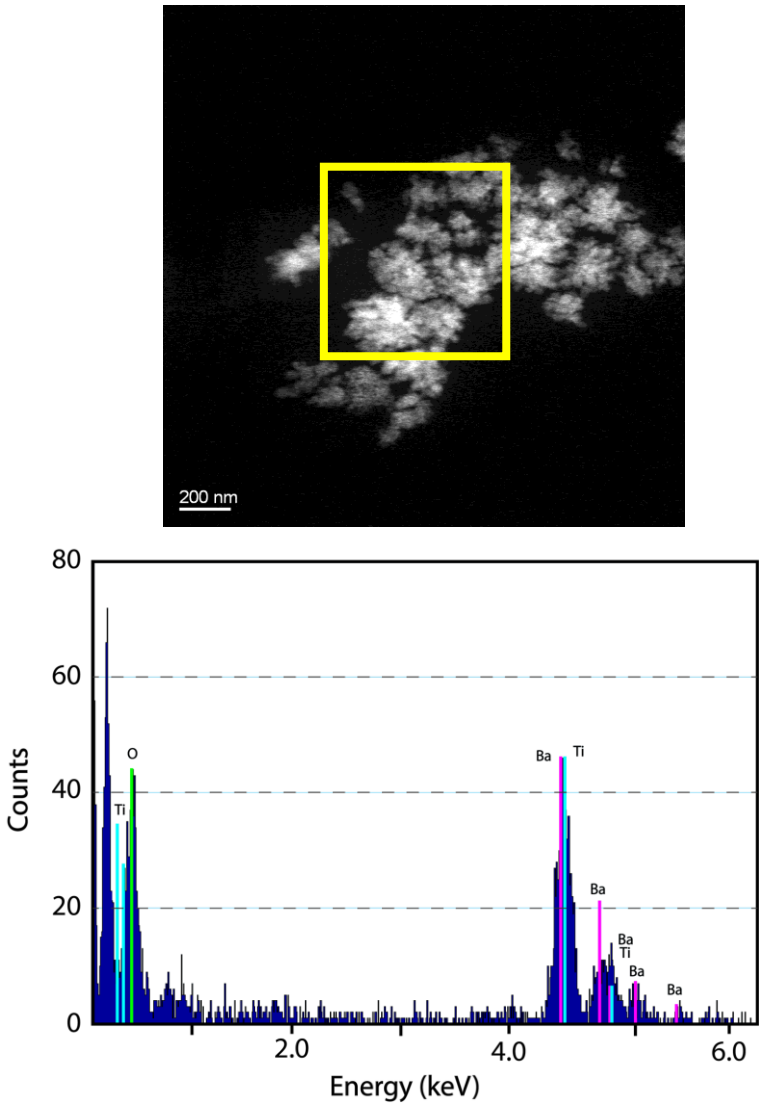

Figure 2.3.9 – Energy-dispersive x-ray spectroscopy (EDX) of the region highlighted by the yellow box in the upper STEM image. Tabulated spectral lines for barium (pink), titanium (blue) and oxygen (green) are reported for comparison.

$BaTiO_3$-DDA nanocomposites

In order to characterize the nanocomposite' piezoelectric performance samples at 4 different $BaTiO_3$-DDA loading (5%, 10%, 15% and 20% in weight) were produced and tested (**Figure 2.3.10**). A pristine PDMS sample was used as a reference, in order to recognize eventual additional contributions to the electro-mechanical effect different than the piezoelectric one [282], for example, the triboelectric effect [283], electrostriction [284] or dielectric charging [278]. All the samples were poled with the same procedure, except for control samples that were not poled in order to assess the poling effect on the piezoelectric performance of the nanocomposite.

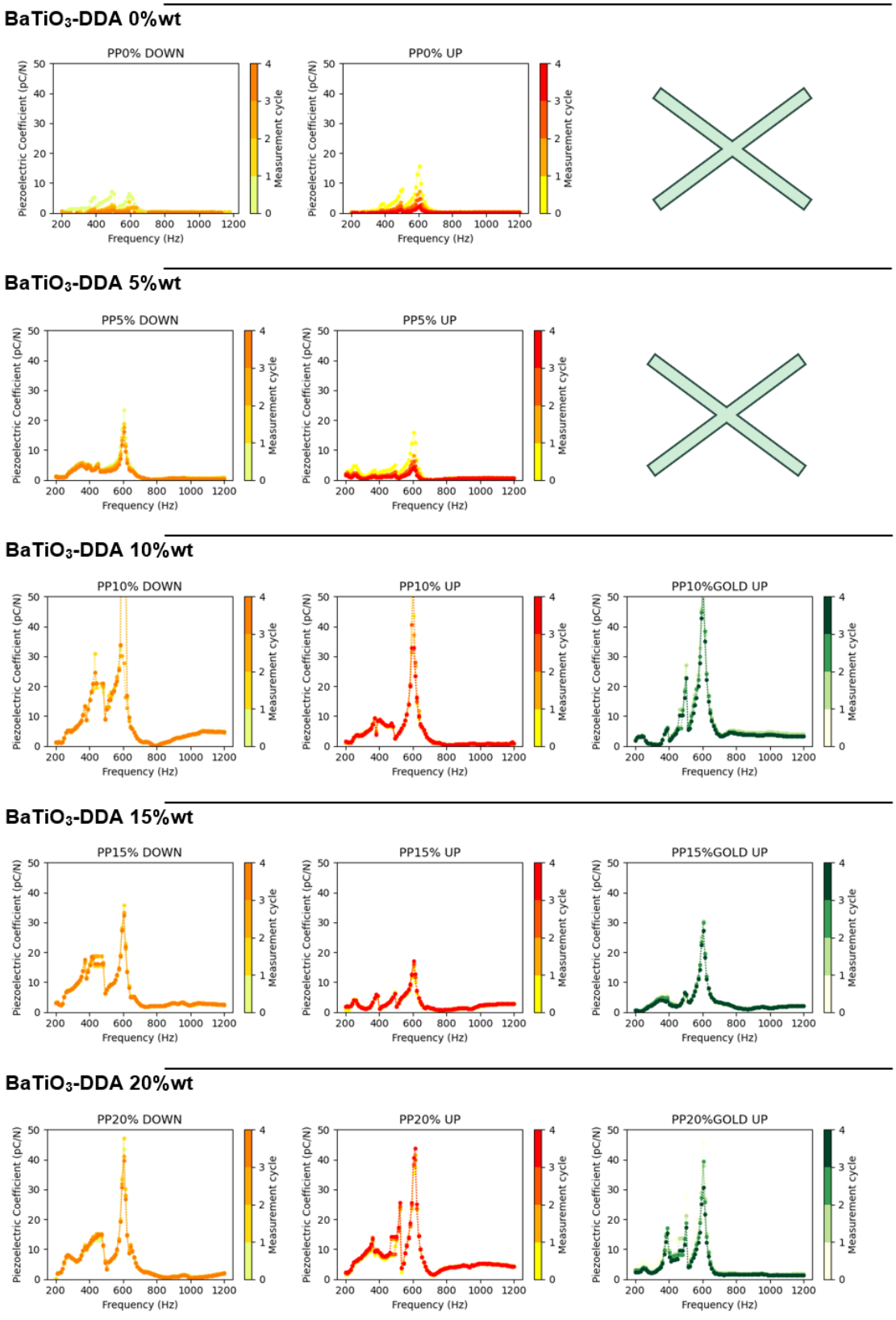

Figure 2.3.10 - Piezoelectric spectra of PDMS-$BaTiO_3$-DDA nanocomposites measured in the two configurations (same side facing up, in red, and down, in orange), and the nanocomposites with the nanostructured gold electrodes (in green). The 600 Hz peak is an instrumental resonance, it does not give information about the piezoelectric behaviour of the nanocomposites. For the lowest loadings (0% and 5%) the test with SCBD-deposited gold electrodes was not performed.

Stability

In order to investigate the long-term stability of the piezoelectric effect in these samples multiple-cycle measurements were performed. In **Figure 2.3.11** are shown 10- cycle measurements for the same sample before and after the poling procedure. As can be observed from the graphs even before the poling procedure the nanocomposite exhibits a piezoelectric behaviour, but the effect is not stable, and the piezoelectric coefficient shows a 92% loss between the 1st and the 10th cycle. On the other hand, the poled sample's response is stable over the 10 cycles, displaying a maximum d_{33} variation of ±5% , depending on the tested sample. Stability of the piezoelectric response was further assessed over 100 cycles, showing stable output values (**Figure 2.3.12**)

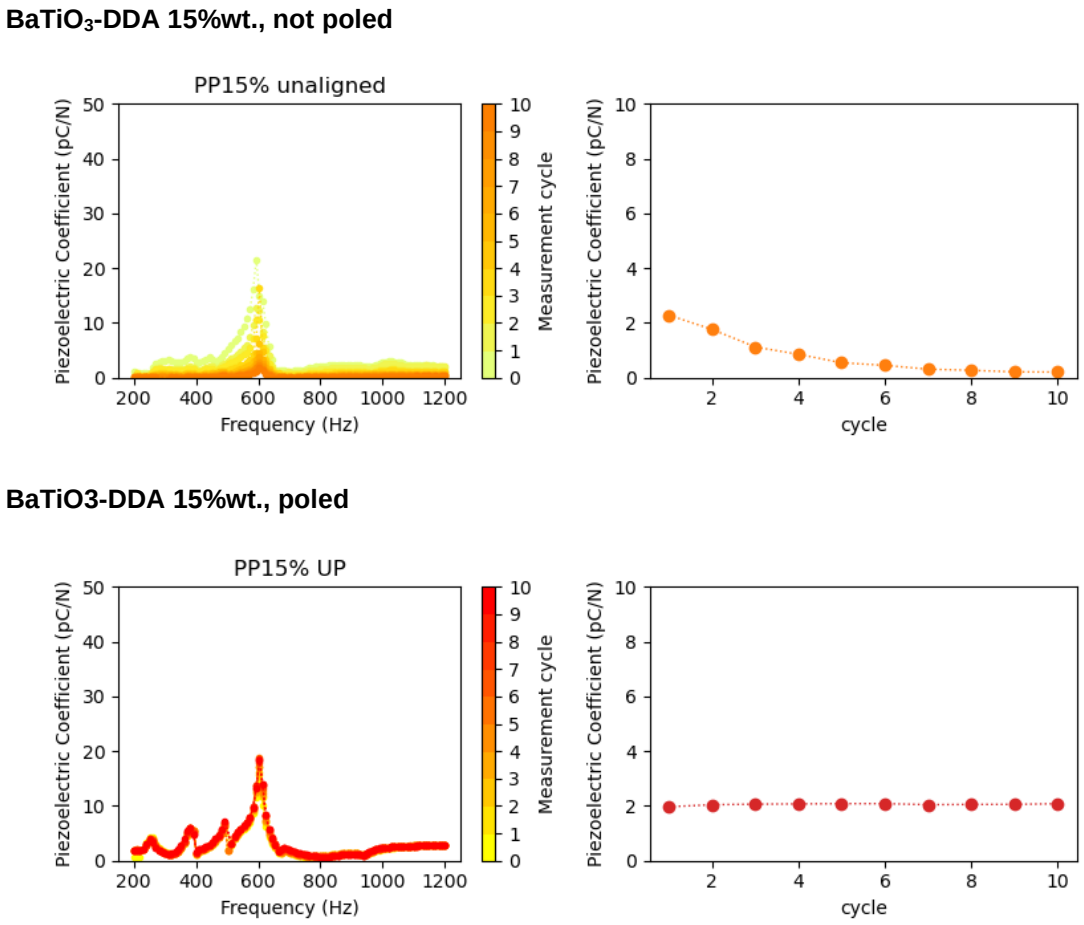

Figure 2.3.11 - Performance loss over 10 cycles for the same sample before and after poling. During these cycles there is a 92% loss of the piezoelectric coefficient averaged across the different frequencies (excluding the peak between 400 Hz and 700 Hz). The measure is compared to an identical one done on the same sample gone through the poling process.

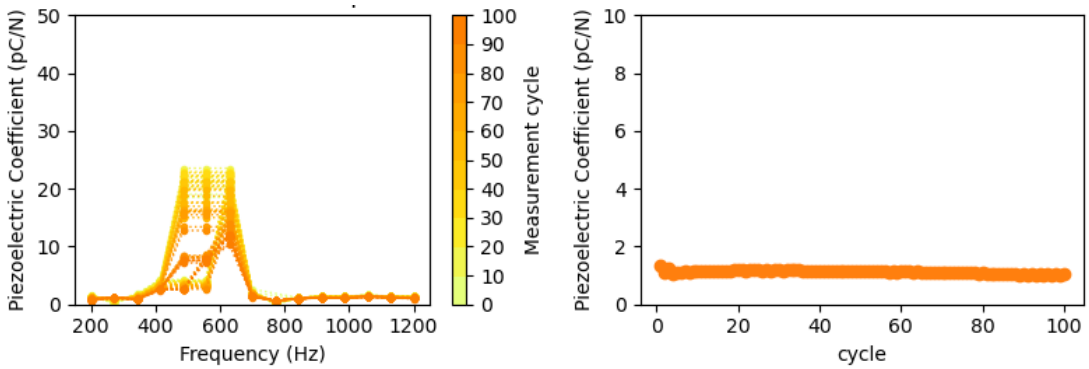

Figure 2.3.12 - A 100-cycle measurement over a poled sample. The measurement lasted more than 24 hours of uninterrupted mechanical stimulation. As can be observed in the graph on the right the piezoelectric response was not significantly reduced over this span of time.
resonances influence the measures.

Piezoelectric coefficients

In order to identify a unique piezoelectric coefficient to investigate its dependence from the nanoparticle loading and the aging or fatigue effect after a long number of cycles an average was performed between the values found at frequencies outside the interval 400Hz-700Hz, which is the frequency interval where most of the electro-mechanical crosstalk and system. **Figure 2.3.13** sums up the results of these averages over a 4-cycle measurement and reports the averaged d_{33} percentual loss from the first to the fourth cycle as a stability evaluation. Piezoelectric charge coefficients calculated averaging the piezoelectric response between the different frequencies, excluding the interval 400-700Hz where the response is highly influenced by the system resonances.

As can be observed in **Figure 2.3.13** the piezoelectric coefficient increases with the nanoparticle loading in one of the two configurations, while it has a different behaviour in the other configuration. This could be ascribed to a structural anisotropy, which could be both originated by nanoparticle dispersion inside the polymer matrix and to a non-uniform poling. The nanostructured electrodes do not significantly alter the piezoelectric performance of the nanocomposites; in fact, they diminish it by a small factor $1{,}2 \div 1{,}5$. This occurs due to the morphology of the nanostructured layer, which is compliant with the polymeric matrix: in the compression configuration of the characterization instrument the nanostructured electrode is not only compressed, but also stretched in the longitudinal direction, increasing its sheet resistance and dispersing part of the electrical charge generated by the nanocomposite. The nanostructured gold electrodes are particularly promising for free-standing applications since they allow to collect and transport the generated charges without limiting the nanocomposite flexibility and stretchability.

Loading (wt.%)	Electrode	$d_{33}\uparrow$ (pC/N)	$d_{33}\downarrow$ (pC/N)	Stability
0%	-	0.6	1.8	-80%
5%	-	1.2	1.4	-20%
10%	-	2.5	4.8	-1%
15%	-	2.0	4.0	-2%
20%	-	5.3	3.1	-1%
10%	450 nm	-	4.0	-18%
15%	450 nm	-	2.5	-18%
20%	450 nm	-	2.8	-22%

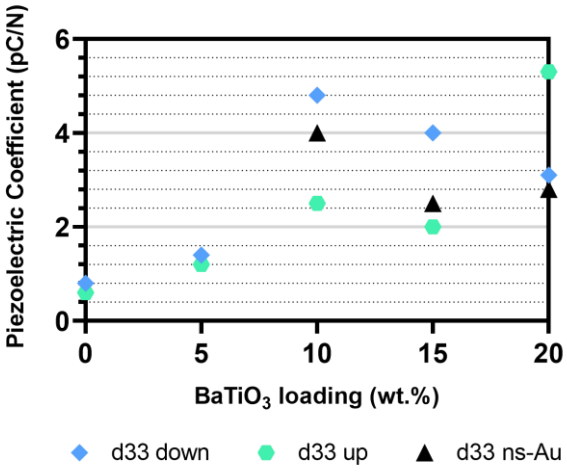

Figure 2.3.13 - Averaged piezoelectric coefficient as a function of nanoparticles' loading for both pristine nanocomposites and nanocomposites with electrodes.

In order to compare this nanocomposite with the results obtained in literature some open-circuit voltage measurements were conducted using the same experimental set-up and protocol of the previous measures, simply connecting the electrodes directly to ad ADC converter, with an input impedance of 20 MΩ. The results can be observed in **Figure 2.3.14**. Except for some mechanical resonances the samples exhibited a piezoelectric linear response between 50 and $200\ mV/N$ depending on the stimuli frequency, with higher responses at lower frequencies (20 Hz). The voltage response of the sample is not significantly influenced by the sample loading, and is comparable to the ones found in literature for similar nanocomposites [228].

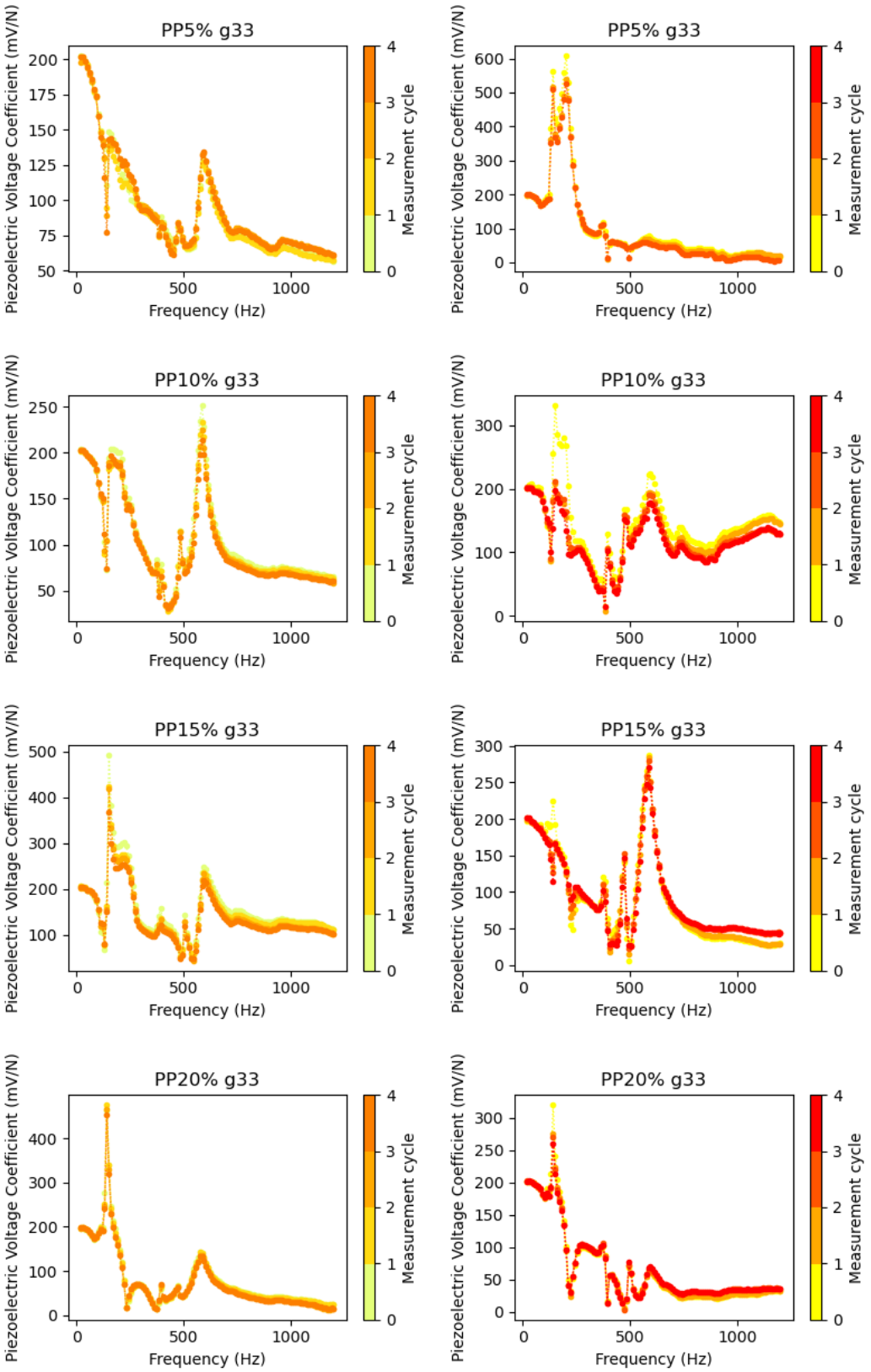

Figure 2.3.14 - Open circuit voltage measurements at different frequencies for nanocomposites at different particle loading in both orientation configurations.

The obtained maximum piezoelectric coefficient for the nanocomposites presented is 5.3 pC/N. This value is not very high when compared with pure PZT (270 – 310 pC/N, [285]) or PVDF (10-30 pC/N), but they give comparable results with other $BaTiO_3$-based ceramic nanocomposites such as gelatine-hyaluronic acid nanocomposites used for bone tissue engineering applications (0.5 – 4.5 pC/N, [286]) but much higher than other reported d_{33} values for $BaTiO_3$ nanocomposites (0.2 – 1.2 pC/N). [287]

The drawbacks of using low response piezoelectrics are often shadowed by the versatility of nanocomposites and their tuneable mechanical properties that make nanocomposite-based piezoelectrics a valuable alternative to rigid lead-based ceramics in the field of mechanical waves sensing.

2.4 Synthesis and stabilization of ultrathin gold nanowires (AuNWs) in PDMS for applications as stretchable motion sensors for wearable electronics

Maturi, M.; Comes Franchini, M.; Bonfiglio, A.[♪] et al. *Preliminary results*

[♪] Departmentof Electric and Electronic Engineering, Università di Cagliari (Italy)

2.4.1 Introduction

As already discussed in the introduction of this chapter, conductive metal nanostructures represent promising candidates for the preparation of conductive nanocomposites for organic electronics. Their very high aspect ratios (>1000) allow them to form interconnected conductive networks with very low loadings. However, such high aspect ratio also makes them extremely unstable and causing them to collapse into nanospheres quite easily.

In this preliminary work, we describe the surface stabilization of ultrathin gold nanowires (AuNWs) for the manufacturing of strain sensors when formulated in polydimethylsiloxane (PDMS) matrices. The surface-modified AuNWs demonstrated prolonged stability when compared to as-synthesized AuNWs and the formulated nanocomposites showed a good response when explored as capacitive strain sensors Preliminary results presented in this chapter will show that a preferential concentration of AuNWs will enable a linear impedance variation with the strain of spin-coated thin PDMS films, with a sensitivity of about 0.1% impedance variation per point of strain.

What we will present is a completely reversible (when strain is removed the initial impedance value is restored) and reproducible (the same impedance variation was obtained in different measurement for the same strain applied) device.

2.4.2 Methods

Synthesis of ethyl 11-(4-mercaptobenzammido) undecanoate (T11, 1)

The thiolated ligand has been prepared as previously reported. [117] Effectiveness of the chemical synthesis has been verified by ^{1}H-NMR (**Figure 2.4.2**).

Synthesis of AuNWs@Oleylamine

Oleylamine-coated ultrathin gold nanowires (AuNWs@Oleylamine) have been prepared on the basis of the procedure developed by Feng et al. in 2009, with small modifications[288]. Typically, 174 mg of hydrogen tetrachloroaurate (III) trihydrate ($HAuCl_4 \bullet 3H_2O$) were dissolved in 55 mL of hexane by addition of 10 mL of oleylamine under magnetic stirring at 30°C. Reduction of the metal precursor salt was performed by adding 8.5 mL of triisopropyl silane (TIPS) to the Au(III)-oleylamine complex. The mixture has been stirred for a few seconds then left undisturbed for 3 days at 30°C. Purification of the nanostructures was performed by precipitation with ethanol and centrifugation (6 krpm, 10 min). The obtained pellet was then dissolved in 200 mL of THF to undergo ligand exchange.

Ligand Exchange Reaction

To remove oleylamine from the surface of AuNWs and to replace with a much stronger surface stabilizing agent such as T11, AuNWs@Oleylamine in THF were added dropwise to a solution of 500 mg of T11 in 200 mL of THF. Ligand exchange was performed by stirring the mixture at room temperature for 24 h, then purified by repeated precipitation with a 1:1 H_2O/EtOH mixture, centrifugation (6 krpm, 10 min) and redissolution in the minimum amount of THF. After three purification cycles, the centrifugated pellet was dissolved in chloroform, which was then dried over anhydrous Na_2SO_4 and filtered. The solvent has been partially evaporated by rotary evaporation to achieve a final volume of 10 mL.

Manufacturing of AuNWs-PDMS nanocomposite thin films

For making elastic thin films SYLGARD-184 elastomer kit was used. It is composed of two liquid mixtures (solutions A and B) that polymerize once mixed in a 10:1 ratio and cured for a certain amount of time. A predetermined volume of AgNRopes-**1** in chloroform was added to and mixed thoroughly with a known amount of solution A, then the solvent is removed by rotary evaporation and solution B is added and mixed well. After degassing the mixtures to remove air bubbles by applying high vacuum, the mixtures have been spin-coated on 90 mm PP Petri dishes at 1000 rpm for 20 s. In this way, elastomer films containing gold as AuNWs ranging from 0.015% to 0.08% of Au have been prepared.

2.4.3 Results

Gold nanowires have been synthesized according to the procedure reported by Feng et al. but in more concentrated conditions. [288] This allowed for a reduction of the total reaction volume without any variation in the quality of the prepared nanostructure or in the yield, which was measured via atomic absorption spectroscopy (AAS) to be as high as 67%.

Oleylamine-coated AuNWs are intrinsically unstable due to their extreme surface-to-volume ratio. The weak Au-N interaction is not strong enough to prevent the rearrangement of gold atoms into rounder structures, therefore nanowires in solution hardly keep their shape over time at room temperature, even in presence of high concentrations of free oleylamine in solution. Therefore, in order to increase the surface stability of ultrathin gold nanowires, oleylamine needs to be replaced with a thiolated ligand, which is able to reduce the surface energy of AuNWs thanks to the high Au-S bond energy. For this purpose, we decided to exploit the thiolated ligand **1**, ethyl 11-(4-mercaptobenzamido) undecanoate (T11), which has demonstrated to be able to efficiently form lipophilic self-assembled monolayers (SAMs) onto gold surfaces thanks to its ability to establish hydrogen bonds, π-stacking and Van der Waals interactions (**Figure 2.4.1**). [117]

The effectiveness of the ligand exchange was confirmed by ^{1}H-NMR, which revealed complete replacement of oleylamine with T11 (**Figure 2.4.2**). No residual oleylamine peak can be noticed in the ^{1}H-NMR spectrum of AuNWs@T11, as it clearly showed only signals related to T11. The effects of the thiol binding onto the gold surface are reflected in the NMR

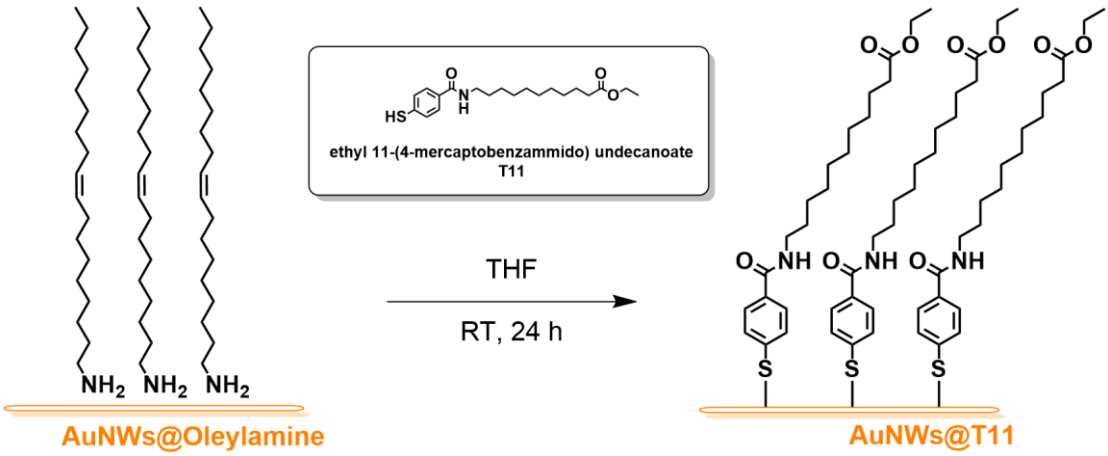

Figure 2.4.1 - Ligand exchange reaction. Since the interaction of gold with sulphur is much stronger than that with nitrogen, oleylamine is easily replaced. The SAM is formed by π-stacking interactions between the aromatic rings, H-bonding between the adjacent amide groups and Van der Waals attractive interactions between the long aliphatic chains of the ligand.

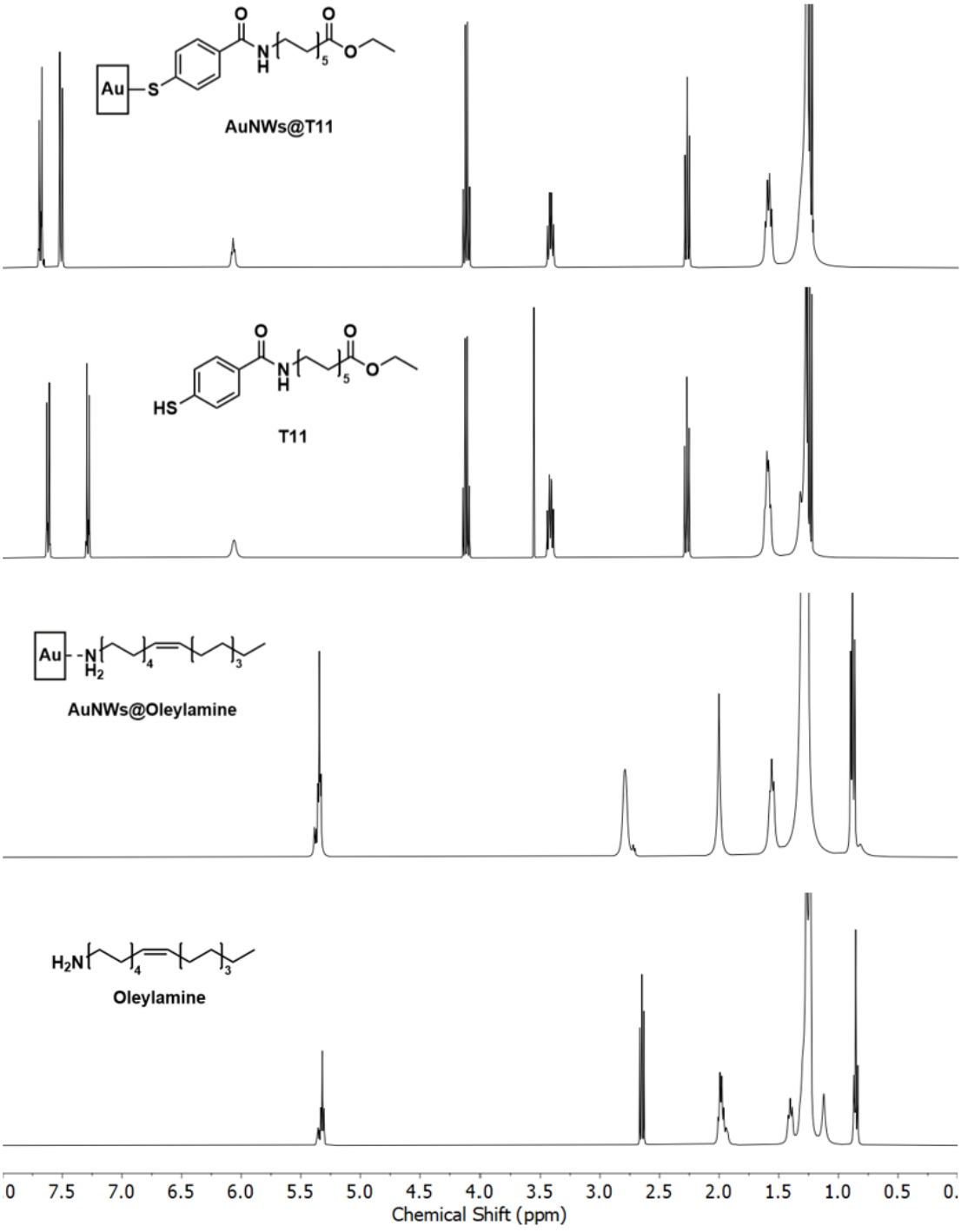

Figure 2.4.2. - ^{1}H-NMR spectra (400 MHz, $CDCl_3$) of oleylamine, AuNWs@oleylamine, T11 and AuNWs@T11.

spectrum of the bound ligand; as expected, the SH proton signal of T11 (at 3.55 ppm) disappears after ligand exchange, and the also the aromatic signals get deshielded due to the electron attracting features of the Au surface. A similar effect can also be seen by comparing free oleylamine and its monolayer on the gold surface, but in a lower extent due to the weaker interaction between gold and nitrogen.

The prepared nanostructure was characterized via TEM, which revealed the successful preparation of gold nanowires with an average diameter of 2 nm and length up to 5 μm (**Figure 2.4.3**). The nanostructure demonstrated to be unstable when exposed to the 200 keV electron beam of the microscope, which lead to a fragmentation of the nanowires over time during the analysis (**Figure 2.4.4**). For this reason, AuNWs appear to be broken in multiple locations, but we can reasonably presume that this phenomenon only happens under exposure of TEM electron beam.

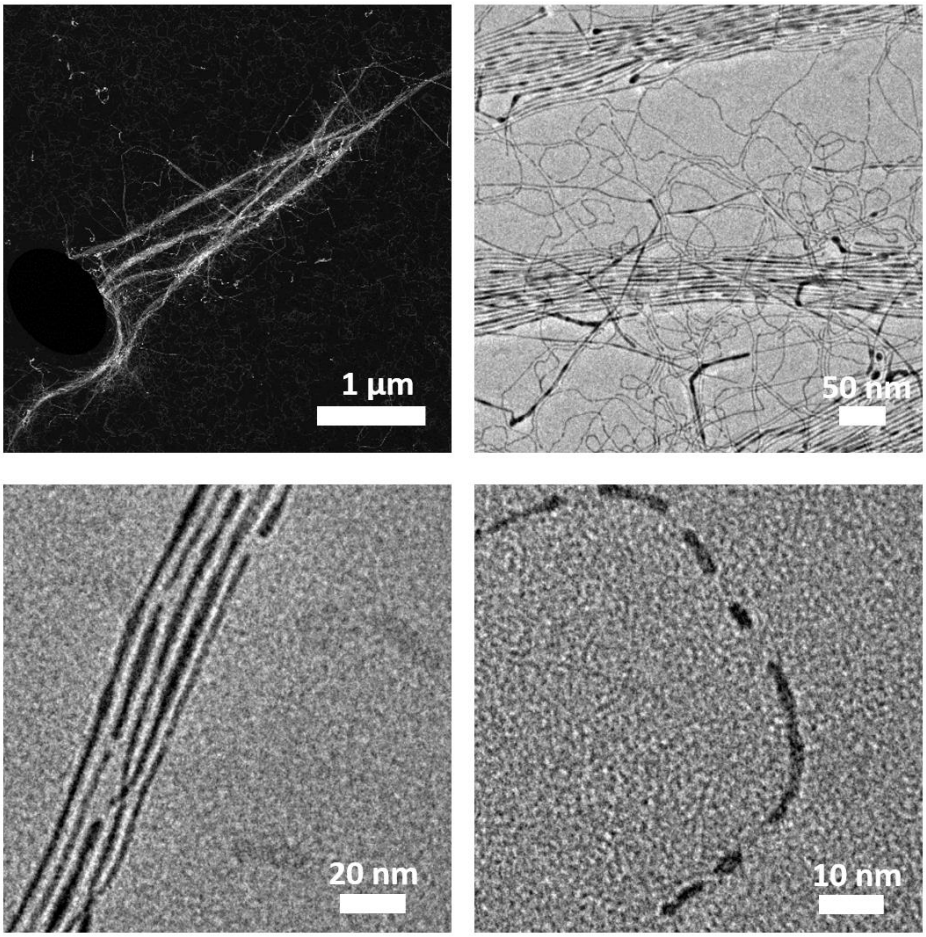

Figure 2.4.3 - TEM images of AuNWs@T11. Nanowires appear to be fragmented under high magnification, but this is due to the highly focused electron beam damaging the thin nanostructure.

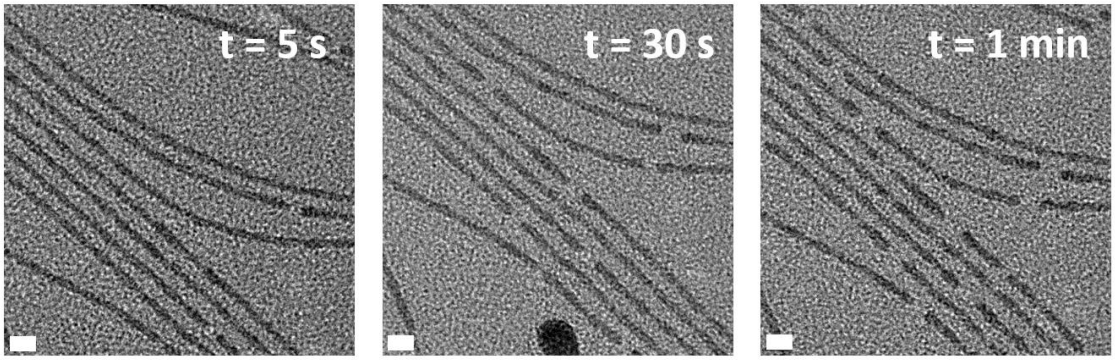

Figure 2.4.4 - Instability of AuNWs under TEM electron beam. The same region of the sample grid was imaged at high magnification repeatedly over a short period of time, clearly showing the progressive fragmentation of AuNWs over time, when exposed to the high-energy electron beam. Scale bar: 5 nm

The surface stabilization of AuNWs related to surface coating was demonstrated by recording the UV-VIS spectrum of oleylamine-coated AuNWs compared to AuNWs@T11 over a period of time. **Figure 2.4.5** clearly displays the stabilizing effect of T11 on the morphology of the nanostructure: in the absence of the thiolated ligand, an absorption maximum between 500 and 600 nm appears and gets more and more intense as time passes, suggesting the formation of round nanoparticles able of surface plasmon resonance effects in the visible range. On the other hand, T11-coated nanowires display complete stabilization and the absence of spherical impurities over a wide period of time, maintaining their UV-VIS features for several weeks of storage at room temperature.

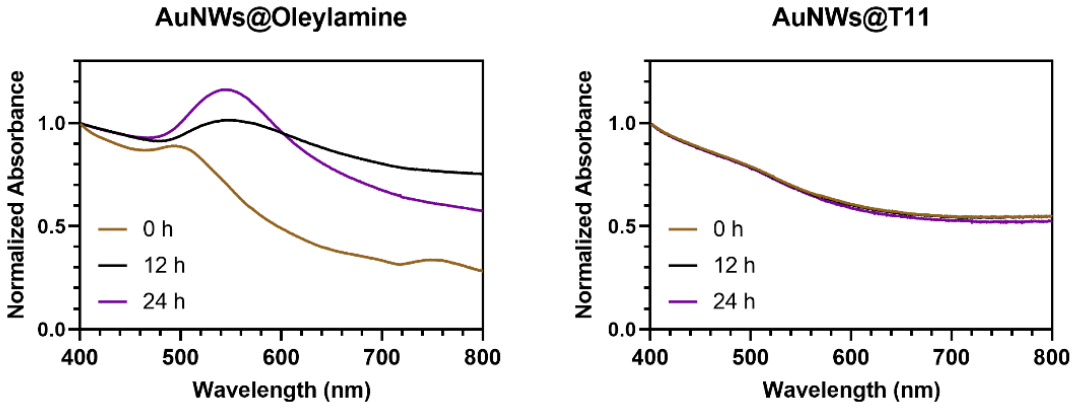

Figure 2.4.5 - Visible spectrophotometric analysis of gold nanowires solutions (THF, 25°C) recorded at different time steps after their purification.

PDMS nanocomposites

The effects of AuNWs@T11 in transparent PDMS nanocomposites have been characterized by considering the relative variation of the module of the impedance ($\Delta Z/Z$) where the value of impedance for the non-stretched device has been considered as reference (**Figure 2.4.6**). This variation has been evaluated at different frequencies, for the different extent of elongation (ΔL). (**Figure 2.4.7**). At 0.015% Au content, a trend of the variation of impedance with ΔL can be observed: impedance increases with stretch. However, impedance variation is not constant in frequency. At 0.03% Au content, a trend with ΔL was still observed: the more the device was stretched, the more the impedance increases. The impedance variation is almost constant with frequency, but some problems can be observed at certain frequency due to set up problems near the full scale of the LCR meter employed for the measurements. At 0.08% Au content, the trend of $\Delta Z/Z$ with ΔL was confirmed, showing a linear correlation between impedance and elongation. The impedance variation is now almost constant in frequency.

On the basis of these results, we plotted the variation of impedance recorded for each sample as a function of the elongation at the frequency of 66 kHz (**Figure 2.4.8**).

For gold content of 0.015%, we could not notice good linearity of the response in the case

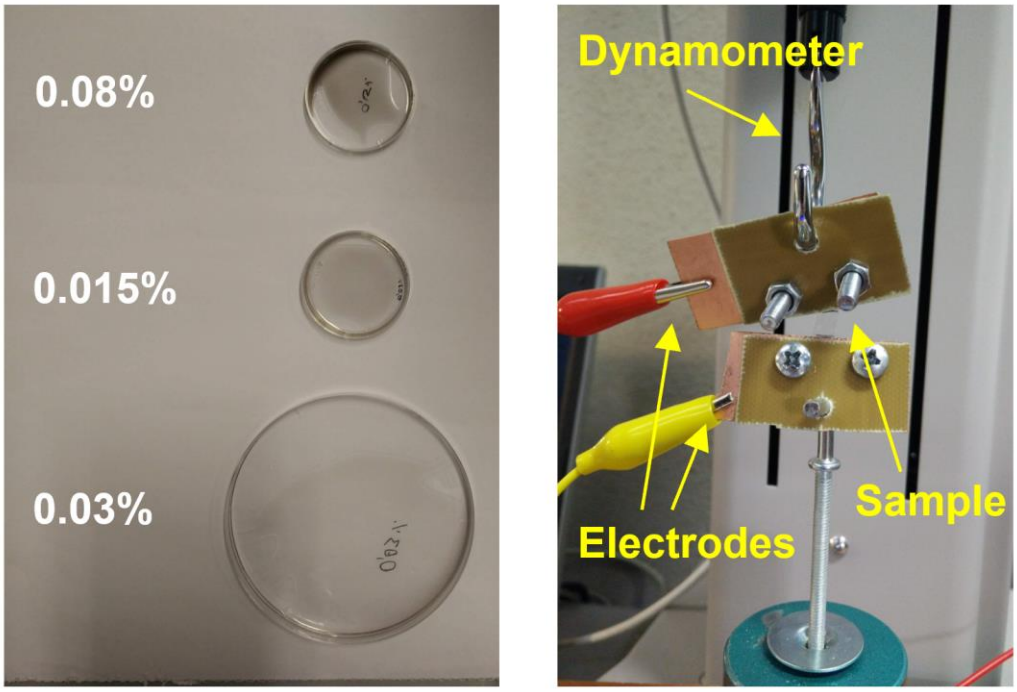

Figure 2.4.6 – Optical camera picture of spin-coated PDMS-AuNWs nanocomposites at different AuNWs loadings (left) and of the impendence measure set-up (right).

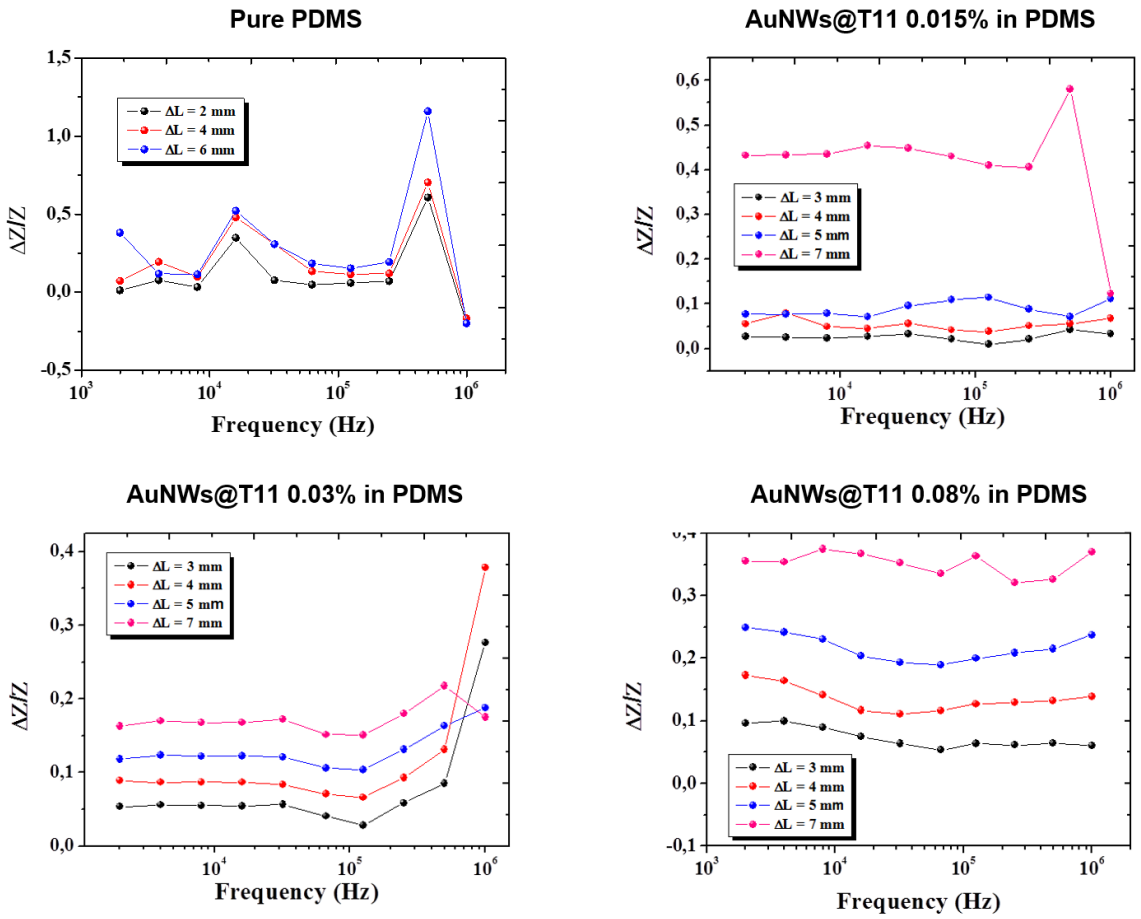

Figure 2.4.7 – Recorded variation of impedance as a function of the current frequency for spin-coated PDMS nanocomposites at different loading of AuNWs.

of the lower concentration of AuNWs. On the contrary, the sample with 0.035% Au showed good linearity of the response in a significant strain range (elongation of about 140%). Sensitivity is of about 0.1% impedance variation for a unit strain (considering this kind of sample and the chosen frequency). Finally, the sample with 0.08% AuNWs, linearity gets slightly worst.

The absolute value of impedance came back to the original value when the strain was removed and the device length was restored for all the kind of sample, even if a better behaviour can be for sure observed for devices with 0.03% of AuNWs (**Figure 2.4.8**).

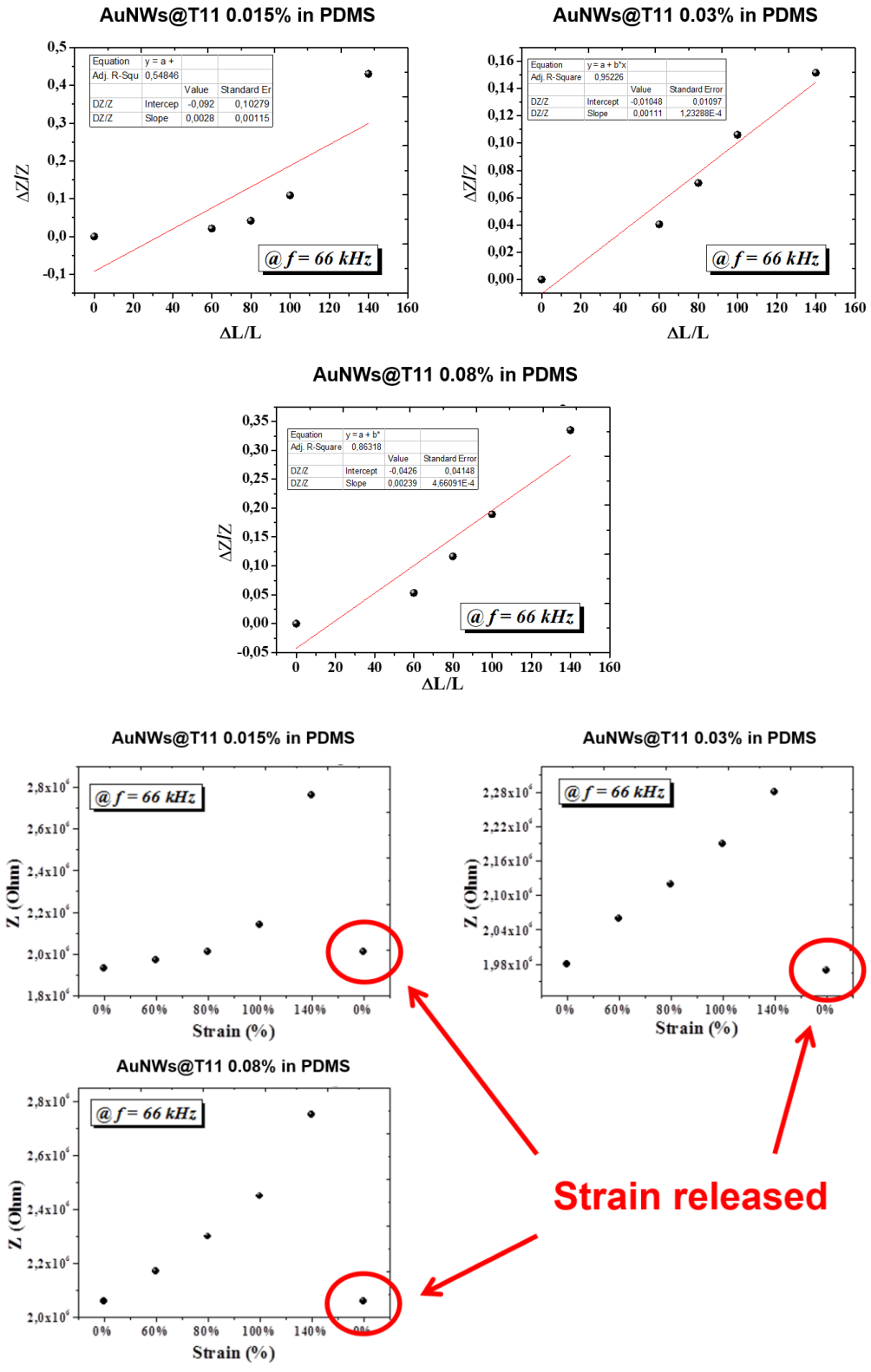

Figure 2.4.8 – Scattering plots of the impedance recorded at 66 kHz as a function of the measured elongation of the nanocomposite strip with different Au loadings. A linear relationship was fitted for each specimen, but acceptable linearity was observed only for the samples containing 0.3% and 0.8% of Au. Below, Analogous plots of the measured absolute impedance, showing that when the strain is released, the impedance drops back to its original value.

With these preliminary results, we reported the implementation of stabilized ultrathin gold nanowires at very low loadings that suggests the possible future implementation of the nanocomposite for the manufacturing of stretchable and transparent motion sensors, since they have proven to give a steady and predictable response in the measured impedance upon stretching and elongation.

Other strain sensors have been produced in the literature using conductive metal nanowires (mostly silver). For example, Shengbo et al. reported in 2018 the implementation of wearable conductive strain sensor using silver nanowires and nanoparticles in PDMS matrices. [289] In their work, the authors reported linear variations of the recorded resistivity as a function of the stretching of the nanocomposite. However, this was performed by depositing a layer of conductive nanomaterial sandwiched between two layers of PDMS and not by dispersing the nanostructures throughout all the polymer. Our work applies similar approaches and follows a similar path, and our preliminary but promising results offer an alternative approach for the formulation of strain sensors with very low loadings of ultrathin gold nanowires that do not act as conductors but rather as capacitors.

Possible future experiments may include the assessment of the variation of the electronic properties of the nanocomposite upon twisting and compressing.

CHAPTER 3

ADDITIVE MANUFACTURING

3.1 Introduction

3.1.1 Additive Manufacturing [290]

The American Society of Testing and Materials (ASTM) defines additive manufacturing (AM), or three-dimensional (3D) printing as "*the process of joining materials to make objects from 3D model data, usually layer upon layer, as opposed to subtractive manufacturing methodologies*". [291] The basic principle of additive manufacturing is building up an object layer by layer; in a first stage the design of the desired object is created by Computer-Aided Design (CAD) and the virtual model is then digitally sliced into horizontal layers for a printable command sequence. Via a command file usually named G-code, the virtual coordinates are sent to the 3D printer, which deposits the material in predesigned locations at the x-y plane and the entire process is repeated along the z-axis (**Figure 3.1.1**). Compared to traditional manufacturing techniques, modifications in the shape of the 3D printed manufactures can be easily done by modifying the digital object, without the need for unique tools for a single modification.[292] Furthermore, 3D printing is a sustainable manufacturing process, as additive fabrication results in much fewer materials waste.[293]

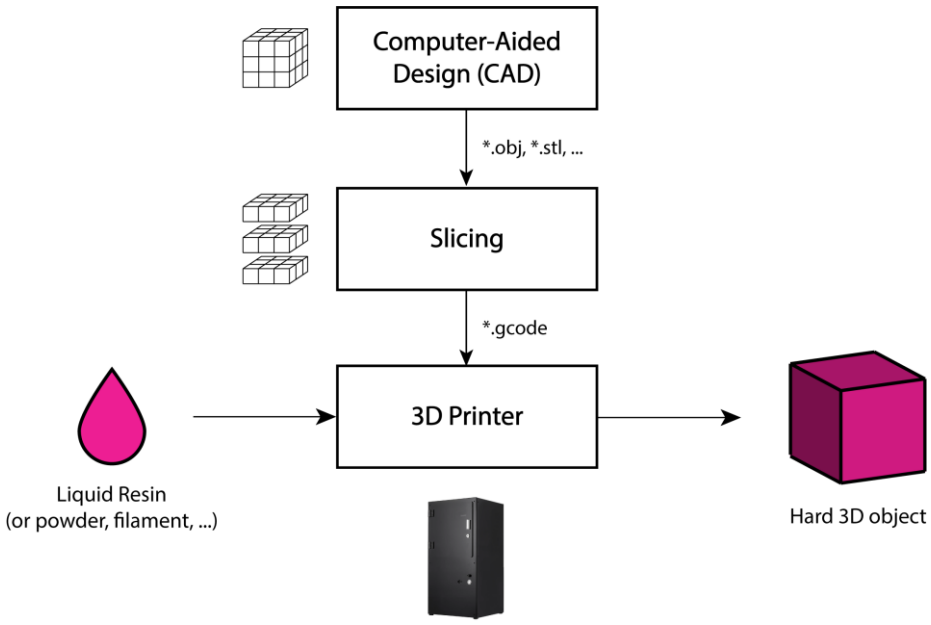

Figure 3.1.1. General workflow for additive manufacturing. Firstly, a 3D object is created by computer-aided design and exported as a three-dimensional object, then it is sliced and the G-code is written as a sequence of 2D layers, with all the instrumental parameters for the printer encoded in the file. This file is finally sent to the 3D printer, which uses the information provided to build a 3D object from raw material (generally a powder, a liquid resin or a polymer filament).

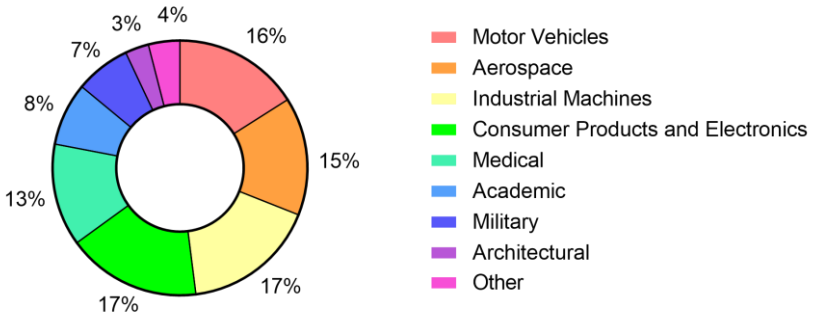

Figure 3.1.2. Main industrial applications of 3D printing in 2016. Data from ref. [294]

The first attempt to produce a three-dimensional object by building it layer-by-layer was performed in 1987 by Chuck Hull, CTO and former president of 3D Systems, who firstly developed a system that selectively solidifies a liquid photocurable resin into a 3D object using a laser. He coined the term stereolithography in the same year, starting the commercialization of 3D printing machines. [295] The technology expanded exponentially in the industries during the following years, leading to what will be recalled as the third industrial revolution [296]; the characteristics of AM that led to such fast growth are related to its cheaper manufacturing industrial processes, the possibility to decentralize the manufacturing and to customize the production. [297] Nowadays, AM technologies are mainly exploited for producing motor vehicles, aerospace parts, industrial machines and electronics, but the applications of 3D printing for biomedical devices and textiles are rapidly expanding (**Figure 3.1.2**). Due to its great versatility, additive manufacturing is suitable for the production of customized pieces, which must be produced readily and in short times. Amongst the other applications, 3D printing technology is taking space in the textile/fashion industry due to its ability to directly produce clothing from 3D printable raw materials in a single manufacturing operation. The application of AM to the textile industry is currently driven by the possibility to easily personalize clothing and to reduce the manufacturing costs, together with the possible implementation of a wide spectrum of new materials that could not find a place in the traditional textile manufacturing.[298]

However, additive manufacturing has shown its limitations when compared to other traditional manufacturing techniques in several aspects. The main challenge is represented by the fact that mechanical properties of printed materials are strongly limited by the narrow range of employable raw materials and by the intrinsic anisotropy of materials which are built

layer-by-layer. Moreover, 3D printed object often suffer from lower resolutions and small deviation from the original 3D model that limits its applicability for printing objects that require very high accuracy: Finally, AM techniques are not able yet to achieve the production speed of other industrial mass-production technologies such as injection moulding. [299]

Additive manufacturing technologies [300]

In their report, the ASTM classified the different 3D printing technologies, as reported in **Table 3.1.1**, based on the implementation and the methodology that allows the production of the 3D object from different materials. The most widespread and performing techniques will be described in this paragraph, with a focus on the advantages and disadvantages of each one of them and their versatility in terms of printed materials and their mechanical properties.

Process Categories	Technology	Materials
Material Jetting	Binder-jetting Ink-jetting S-Print M-Print	Metals Polymers Ceramics
Direct Energy Deposition	Direct Metal Deposition (DMD) Laser Deposition Laser Consolidation Electron Beam Direct Melting	Metals: powder and wire
Material Extrusion	Fused Deposition Modelling (FDM)	Polymers
Powder Bed Fusion	Selective Laser Sintering (SLS) Selective Laser Melting (SLM) Electron Beam Melting (EBM)	Metals Polymers Ceramics
Sheet Lamination	Ultrasonic Consolidation Laminated Object Manufacture (LOM)	Hybrids Metals Ceramics
Vat Photopolymerization	Stereolithography (SLA) Digital Light Processing (DLP)	Photopolymers Ceramics

Table 3.1.1 – Classification of AM technologies according to ASTM. [291]

1) Material Extrusion

The most common technique available, thanks to the low cost and huge availability of the materials and the relatively simple mechanics of the printer. This technique mainly consists of the continuous deposition of a soft material through a mobile nozzle that builds up a 3D object layer-by-layer. It is mainly composed of two sub-categories, depending on the type of extruded material:

Fused Deposition Modelling (FDM)

A filament of thermoplastic polymeric material is pushed by two rollers through a heated nozzle (typically at 100-300°C) that moves along the horizontal plane. This causes the softening (and often melting) of the polymer enabling its extrusion and the deposition of the softened material onto the building platforms, generating a layer of polymer with a well-defined thickness that quicky solidifies upon cooling. At this point, the printing head moves upwards along the z-axis and the process is repeated for each successive layer until the object is complete (**Figure 3.1.3**).[301] The commercially available filament materials are mainly composed of ABS (acrylonitrile-butadiene-styrene, [302,303]), PLA (polylactic acid, [304,305]), PC (polycarbonate, [306,307]), HDPE (high-density polyethylene [308]), PP (polypropylene, [309]), PEEK (polyether ether ketone, [310,311]) and PA (polyamide, [312,313]). FDM is a cheap manufacturing technique that hardly allows achieving acceptable resolution at the sub-millimetre scale, but it can be efficiently exploited by untrained operators for everyday use.

Direct Ink Writing (DIW) and Bioprinting

With this technique, a shear-thinning liquid ink is extruded through a moving nozzle by applying air pressure to the ink cartridge, which enables controlled flow rates. The material is deposited onto a substrate along pre-defined paths and a 3D object is build layer-by-layer (**Figure 3.1.3**). [314] The main requirements for DIW inks are its shear-thinning properties since the material needs to be able to reduce its viscosity when stressed by the extrusion through the small nozzle and to retrieve its viscosity once the stress is removed. However, this includes a great variety of materials, but DIW usually exploits the shear-thinning properties of hydrogels. [315] The extruded material is often crosslinked post-printing to harden the structure, usually by irradiating it with UV light or by soaking it in a secondary crosslinking solution.

Laponite is often used as a shear-thinning agent for PA gels (polyacrylamide, [316]) but the implementation of inks based on polysaccharides such as xanthan and gellan gums [317,318] and cellulose nanocrystals (CNCs, [319]) is rapidly expanding.

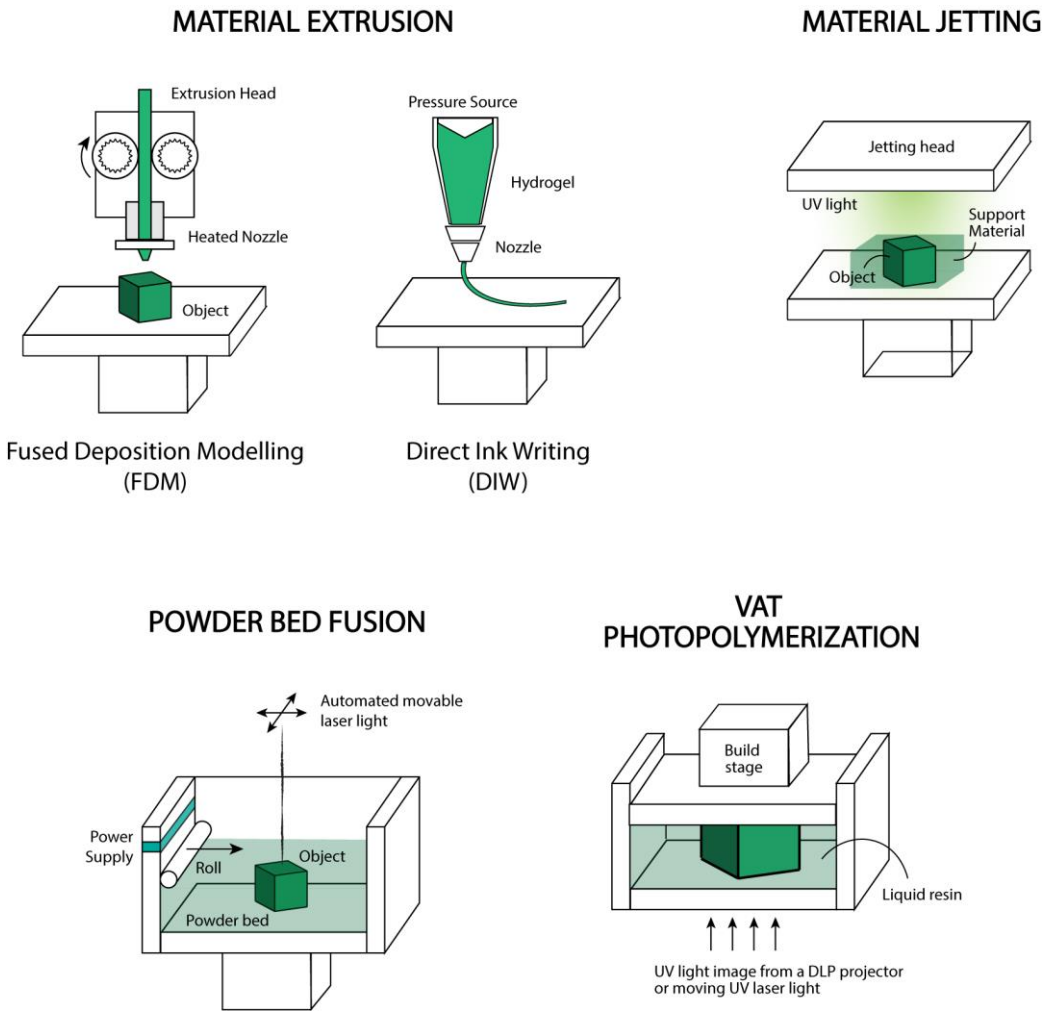

Figure 3.1.3. Schematics of the functioning principles of the main additive manufacturing techniques. In all techniques, the object is built layer-by-layer but the range of printable materials includes metals, polymers and hydrogels.

Thanks to the easy biocompatibilization of the inks, DIW technique has rapidly branched towards *bioprinting*, in which living cells are mixed with the hydrogel before 3D printing and they are grown inside the 3D structure for biomedical applications, such as the artificial construction of biological tissues and living organs. [320]

2) Powder Bed Fusion

A powder layer is deposited onto a substrate and selectively melted or sintered by a laser. This cause the irradiated material to harden and, by repeating the process depositing a further powder layer, the 3D object is built (**Figure 3.1.3**). [321] Depending on the range of laser energies employed, and thus on the physical phenomenon that causes the powder to harden, two sub-categories of powder bed fusion are defined: *Selective Laser Sintering* (SLS) is generally

employed with ceramics and polymers, it deals with lower energies and causes the powder particles to stick together thanks to the fusion of only a thin layer of material on the surface of the particles. [322] The most diffused thermoplastic polymers for SLS are PP (polypropylene, [323,324], PA (polyamides, nylon, [325,326]), PS (polystyrene, [327,328]) and PEEK (polyether ether ketone, [329], but also biodegradable polymers such as PCL (polycaprolactone, [330,331]) and PHAs (polyhydroxyalkanoates, [332]). On the other hand, *Selective Laser Melting* (SLM) is applied to metallic and ceramic powders, and it often allows for the complete melting of the particles. Typical employed materials are steel [333,334], titanium [335,336] , nickel [337,338], aluminium [339] and their alloys, plus alumina-, silica-, yttria- and zirconia-based ceramics and composites [340,341].

3) Vat Photopolymerization [342]

This technique was invented and patented in 1993 by Chuck Hull, who coined the term *Stereolithography* to describe a new form of additive manufacturing that exploited the light-induced polymerization of a liquid photocurable resin contained in a vat. [342] UV-light is used to cure a thin layer of the liquid resin attached to an upper build stage, allowing for the layer-by-layer manufacturing of a 3D object (**Figure 3.1.3**).

A metal build stage is immersed in the vat containing the photocurable ink at a distance from the UV-transparent bottom of the vat that determines the z-resolution of the printed structure. Afterwards, a region of the thin layer of resin between the build stage and the bottom of the vat is irradiated and hardened by UV-light. Then, the build stage is slightly moved upwards (together with the hardened layer) and the process is repeated for the second and each successive layer. Since the build stage is above the vat, 3D printed object is built upside-down. There are several sub-classes of stereolithography that mainly differ by the source of UV light that they employ:

- Laser stereolithography. Commonly known simply as stereolithography (SLA) it exploits a moving UV laser (typically at 360-380 nm) that follows pre-determined paths to harden the liquid resin layer. It is the most versatile techniques and it is much faster than the other when dealing with the printing of hollow structures.
- Digital Light Processing (DLP) and Liquid Crystal Display (LCD) are very similar techniques since with both techniques all the layer that needs to be cured is irradiated at once. In this case, light is generated by a DLP projector or by an LCD screen and passed through a mask that defines the shape of the layer to be cured.

4) Material Jetting [343]

In material jetting machines, a photocurable mixture is heated, nebulized and selectively deposited onto a substrate. The layer is then hardened by UV photopolymerization and the process is repeated for the next layers. This technique allows for the manufacturing of 3D objects with high build speed and dimensional accuracy. The printing speed is only slightly affected by serial production of multiple parts, therefore this technique is very convenient for small scale productions. On the other hand, material jetting is the most expensive AM technique since it requires machines with big size and advanced technology for the production of high-quality components. Besides, the range of employable photocurable inks is quite narrow, since they need to be easily nebulized and rapidly UV-cured. As well as for stereolithography, the printed object suffers from poor mechanical properties. Details of the most common photocurable formulations will be explored in the following paragraphs.

3.1.2 Photocurable resins for stereolithography

Resins for stereolithography are mixtures of several different components that allow for a fast but confined polymerization upon UV-light exposure. The main component is usually the monomer that can undergo radical polymerization. In order for the cured polymer to display the mechanical properties required for the printed object to sustain itself, it is sometimes required to add multifunctional monomers that act as crosslinkers. Also, photoinitiators allow for the efficient conversion of UV photons into reactive radicals, radical inhibitors avoid the spreading of the radical chain reaction outside of the irradiated region and functional smart additives can be added to give additional properties to the 3D printed material.
Novel and most promising materials for SLA 3D printing allow for the production of 3D printed polymers with shape-memory effect [344], stimuli-responsive materials [345], stretchable hydrogels [346] and elastomers [347] for applications ranging from tissue engineering to material science.[348,349]

Monomers

Commercially available inks for SLA are mostly composed of acrylate-based mixtures. The most common approach is the employment of acrylate or methacrylate monomers or polymers, such as poly(ethylene glycol) diacrylate, poly(propylene glycol) diacrylate, bisphenol-A glycidyl methacrylate, methacrylic acid and methacrylate aliphatic diols, together with pentaerythritol tetraacrylate as crosslinker (**Figure 3.1.4**). [350–353] Esters of acrylic and methacrylic acid easily undergo radical chain polymerization in the presence of a radical initiator (**Figure 3.1.5a**). However, acrylates are sensitive to dissolved O_2 since it forms unreactive peroxy-radicals and they are subjected to shrinkage upon photocuring. On the other hand, methacrylates are generally less reactive but they are way less toxic. In addition, the radical addition of thiols to alkenes (generally known as thiol-ene reactions) represent a valuable alternative to the polymerization of acrylates and methacrylates since they exhibit less sensitivity to molecular oxygen, more uniform crosslinking, sharper glass transition temperatures and reduced shrinkage stress. [354,355] In a first step, a thiyl radical adds to an unsaturated π system, followed by a radical chain transfer from the resulting carbon radical to a second thiol molecule, regenerating the thiyl radical (Figure 3.1.4b). By combining compounds that display multiple SH with multiple vinyl residues, the radical reaction leads to thiol-ene polymers. Nevertheless, thiol-ene systems are much more reactive since the thiol can act as a strong H-donor and start the cationic polymerization

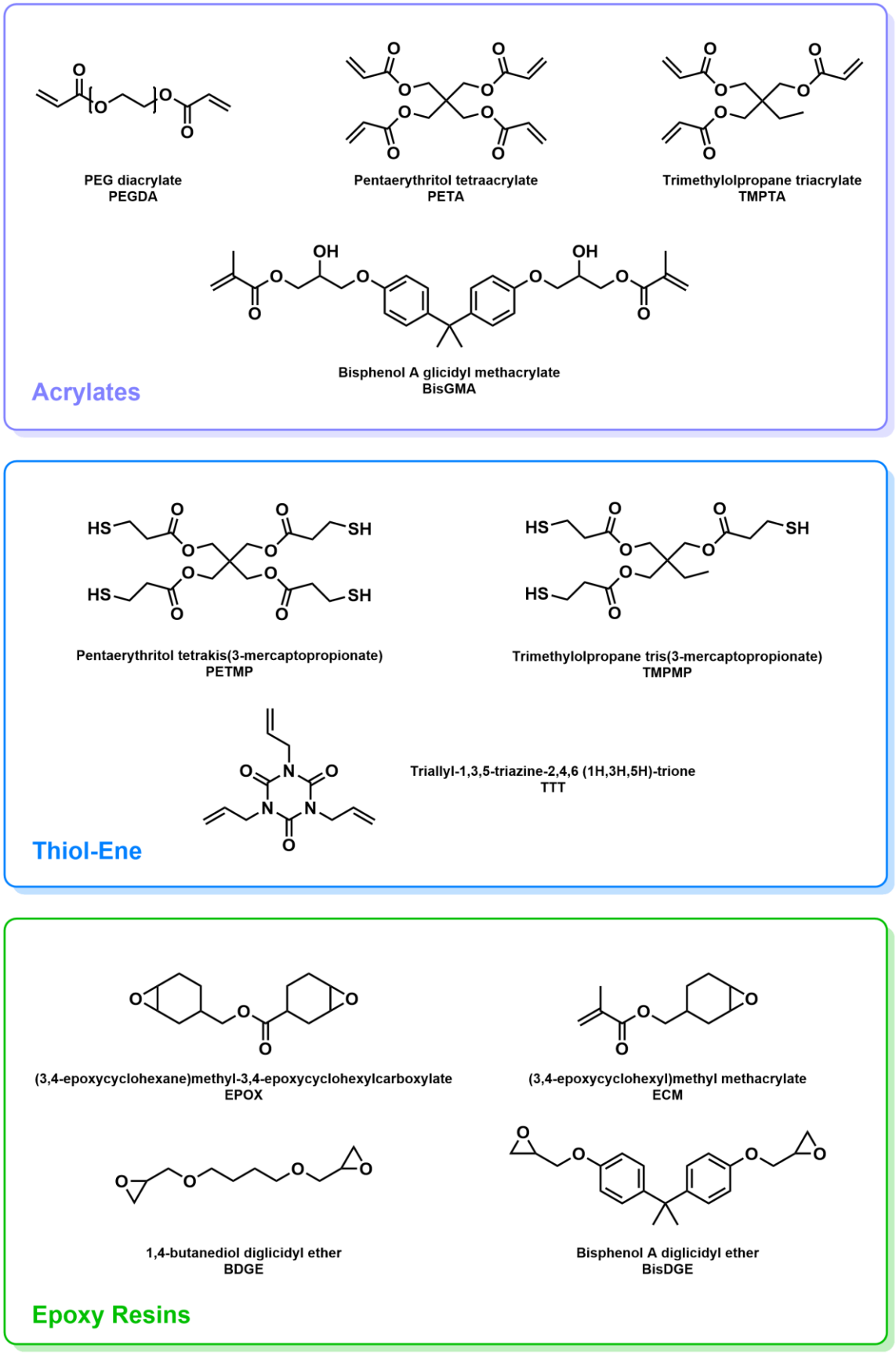

Figure 3.1.4. Most commonly employed monomers in resins for stereolithography.

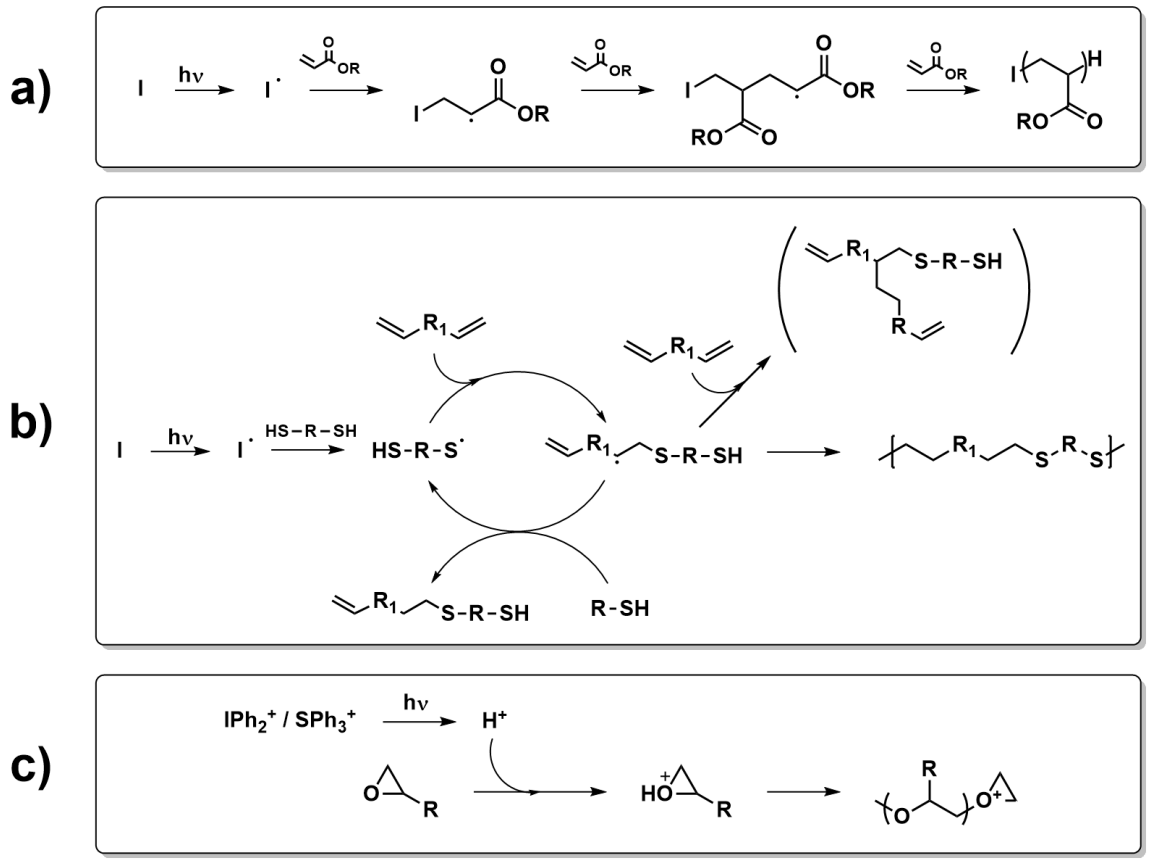

Figure 3.1.5. Most common classes of photopolymerization reactions in stereolithography-based 3D printing techniques. a) Photopolymerization of acrylate esters. Firstly, the initiator absorbs light generating a radical species that react with the monomer, transferring the radical species to it. The radical chain reaction continues until the monomer is no longer available. b) Thiol-ene photopolymerization. As before, the initiator generates the radical species upon irradiation, then it reacts with a thiol group forming the thiyl radical which attacks a vinyl group on the co-monomer. This step-growth mechanism is accompanied by a chain-growth process in which carbon radical species attack vinyl moieties, speeding up the overall polymerization process. c) Curing of epoxy resins. The epoxide is protonated by diaryliodonium and triaryl sulfonium salts that act as photoacids, extracting protons from a monomer or the solvent upon UV irradiation. Once the reactive species is formed, the chain reaction hardens the liquid mixture.

without the need for any photoinitiator. This makes it challenging to formulate a stable ink, but the scientific community is making considerable efforts to find new and efficient stabilizers for thiol-ene resin systems. [356] Generally employed thiols include pentaerythritol tetrakis(3-mercapropropionate) and trimethylolpropane tris(3-mercaptopropionate) together with various alkenes obtained by functionalizing different organic molecules with multiple vinyl residues (**Figure 3.1.5b**). [357,358]

The hardening of the resin is sometimes performed exploiting the ionic chain polymerization of epoxides, such as 3,4-epoxycyclohexylmethyl-3',4'-epoxy

cyclohexane carboxylate, with branched diols like 1,4-butanediol diglycidyl ether (Figure 3.1.5). [359,360] The cationic polymerization of epoxy resins is efficiently initiated by photoacids such as diaryliodonium and triaryl sulfonium salts: upon light absorption, these species decomposes to give reactive intermediates that are able to act as Bronsted acids by extracting a proton from the monomers or the solvent, initiating and then propagating the polymerization (**Figure 3.1.5c**). [361,362]

Photoinitiators

Many photocurable mixtures require the presence of a chemical species that is able to absorb the UV light generating radical species able to start the radical chain polymerization. The task is performed by photoinitiators, mainly divided into two classes, denoted as:

- Type I: these molecules undergo α-cleavage reaction generating radical fragments upon light irradiation. The optimal wavelength for the generation of radical species depends on the chemical structure of the initiator, it is, therefore, crucial to adapt the resin composition as a function of the energy and intensity of the light employed by the 3D printer. [363] Acetophenones such as 2,2-diethoxyacetophenone (DEAPH) and 2-hydroxy-4'-(2-hydroxyethoxy)-2-methylpropiophenone (Irgacure 2959) display $n \rightarrow \pi^*$ transition energies corresponding to wavelengths in the UV range (250-320 nm), while phosphine oxide-based compounds such as (phenylbis(2,4,6-trimethylbenzoyl)phosphine oxide (BAPO) and diphenyl(2,4,6-trimethylbenzoyl) phosphine oxide (MAPO) have π^* states with lower energies, leading to photoinitiating systems that absorb light closer to the visible range (350-400 nm). Water-soluble phosphine oxide derivatives have also been reported. [346]
- Type II. These are two-component initiating systems, where uncleavable sensitizers and a co-initiator form excited triplet states upon irradiation. [364] The typical sensitizers are camphorquinones, benzophenones and thioxanthones which, in the presence of co-initiators (typically tertiary amines) undergo hydrogen abstraction or electron transfer processes. [365,366]

Polymerization inhibitors and photoabsorbers

Another important component of photocurable inks is indeed a polymerization inhibitor, usually a phenol such as methyl hydoquinone (MHQ) and 2,6-diterbutyl-4-methylphenol (BHT). It plays an important role in increasing the resolution of 3D printed parts since it is required to avoid the diffusion of radical species outside the irradiated regions, which could start a spatially unconfined polymerization. [367]

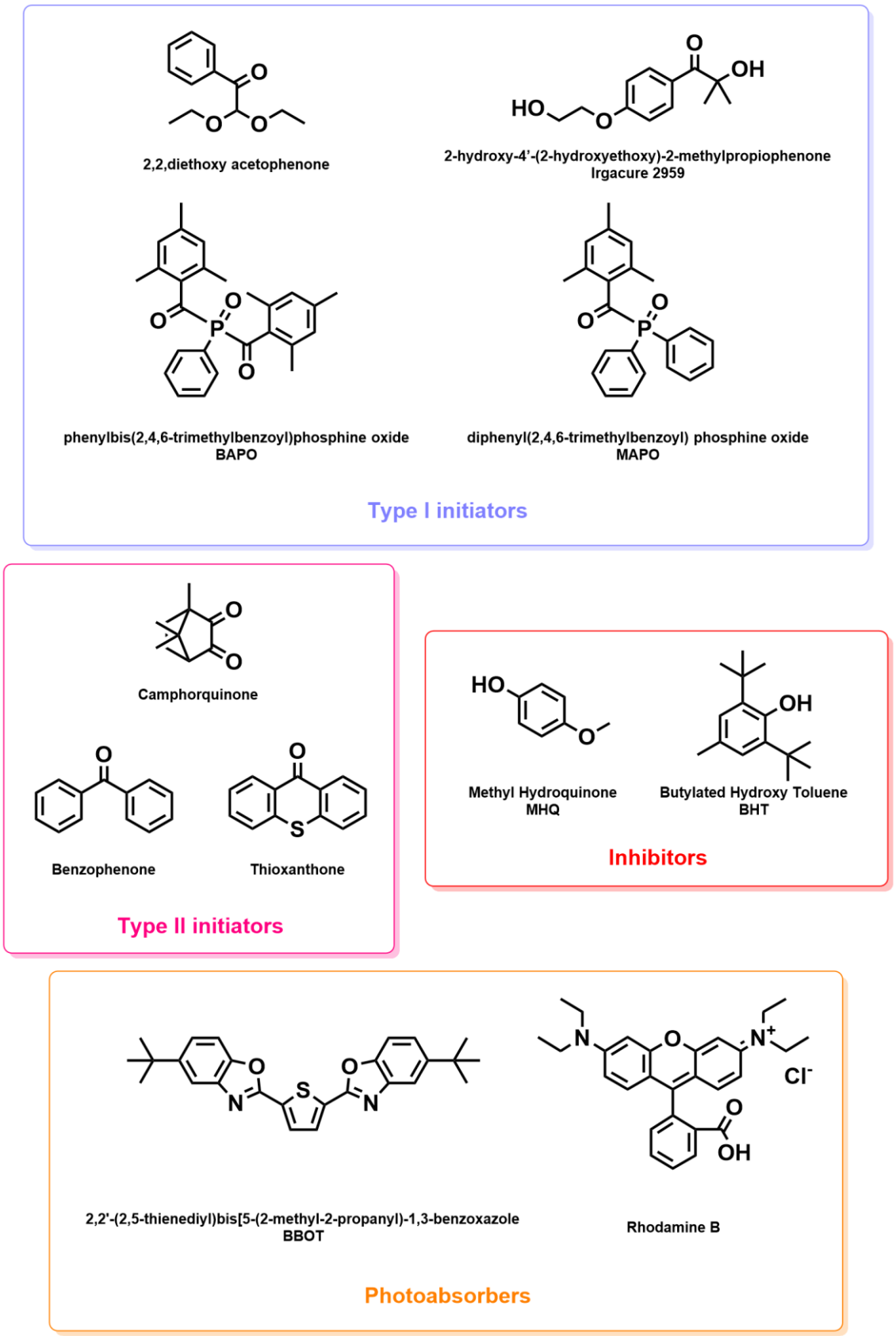

Figure 3.1.6. Most commonly employed additives in resins for stereolithography.

Parallelly, the spatial resolution of 3D printed object can be increased by adding light-absorbing molecules, which reduce the penetration depth of the incident UV again preventing the **s**preading of the polymerization front outside the irradiated regions. Moreover, photoabsorbers allow reducing the thickness of each printed layer, allowing to increase the z-resolution to less than 50 μm. [368] These molecules are UV-VIS dyes such as Rhodamine B and 2,2'-(2,5-thienediyl)bis[5-(2-methyl-2-propanyl)-1,3-benzoxazole (BBOT).

Functional smart additives

Thanks to the flexibility of light-based technologies, it is possible to play with the resin composition in order to insert new functionalities. By adding functional additives to the resin, it is possible to enhance electrical, luminescent, piezoresistive, piezoelectric, behaviours. [369–371] Loading of nanoparticles is usually quite limited since the could have a negative impact on the processability of the polymer by increasing viscosity and altering the light absorption and photocuring properties.

A recent example of functionalized ink is the one reported by Fantino et al. in 2016. [372] The authors of this work achieved the *in situ* generation on Ag nanoparticles during DLP 3D printing with a suitable photocurable resin in which silver salts were dissolved. The incident light allowed both the polymerization of the acrylate matrix and the reduction of silver ions, leading to conductive 3D printed objects.

In another example of functional resin was shown by Mu et al. in 2017, when they described the stereolithographic 3D printing of conductive materials by incorporating multi-walled carbon nanotubes (MWCNTs) in epoxy resins. [370] Such conductive structures could be efficiently implemented for organic electronics applications, such as for capacitive sensors and smart structures with shape memory effects.

3.1.3 Aim of the work

This chapter will be mainly focused on the development of a novel resin for stereolithographic DLP 3D printing based on renewable resources, which was performed in the final part of my PhD studies. A new approach for the incorporation of bio-based platform molecules into photocurable compositions for stereolithography will be discussed, allowing to achieve a total biobased content of 3D printed objects as high as 96%. The synthetic components will be deeply characterized chemically and rheologically, then printed into 3D shapes that will be deeply characterized in terms of their mechanical properties. In addition, phosphorescent Ir(III) complexes will be admixed into the formulation as smart functional additive, to achieve hybrid phosphorescent organic-inorganic 3D printed materials that will be characterized in terms of their emissive behaviours. The good mechanical properties (in particular the exceptional high elongation at break) will suggest possible application in the fashion industry. Moreover, this chapter will also describe the ongoing project that I started during the period I spent at the Johns Hopkins University (Baltimore, MD, USA) as a Visiting Graduate Student under the supervision of Prof. David Gracias, at the Department of Chemical and Biochemical Engineering. During this period, I worked on the development of a thermoresponsive polysaccharide-based self-healing hydrogel for applications in extrusion-based 3D printing. Since the work is still ongoing, only the details of the chemical reactions and the formulation will be provided, while actuation studies on thermoresponsiveness and self-healing properties are still at the earliest stage.

3.2 Phosphorescent bio-based resin for digital light processing (DLP) 3D-printing

Maturi, M.; Pulignani, C.; Locatelli, E.; Vetri Buratti, V.; Tortorella, S.; Sambri, L.; Comes Franchini, M. *Green Chem.* 2020, *22* (18), 6212–6224.

3.2.1 Introduction

AM techniques such as SLS [373] and FDM [374,375] have been widely explored for applications in this field. Surprisingly, very little effort has been yet directed towards the employment of photocured materials (SLA/DLP) for textile applications. This is probably due to the main challenge among the different mechanical properties needed, the elongation at break which has to be high but maintaining good mechanical resistance and lower fragility. Thanks to the possible organic manipulation of suitable building blocks from natural sources we believe this technique might be a future system for the green fashion industry.

In general, most of the developed formulations for SLA/DLP are still derived from non-renewable resources, and often cost-effective.[376] Only a few examples of publications in the recent literature with strong efforts toward the implementation of biomasses in stereolithography can be found, but the biomass loading into these resins remain very low (<15%). [377–379] Therefore, there is a need for the implementation of bio-based compounds into the formulations for 3D printing to the final consumer. This would allow the overall reduction of the carbon footprint of 3D printing technologies as a green and sustainable approach to rapid prototyping. The most promising bio-derived photocurable monomer is indeed itaconic acid, obtained by distillation of citric acid or by direct fermentation of glucose by specifically engineered bacterial strains.[380–382] It can undergo slower photopolymerization compared to acrylates and methacrylates due to its more hindered unsaturation, but its polyesters have been widely explored as a novel class of photocurable bio-based polymers.[383,384] Interestingly, a cyclodextrin derivative of itaconic acid (cyclodextrin itaconate) is used for the modification of cotton fabric, a market expected to rise remarkably.[385] Indeed, the impressive progress in the textile industry, with enormous production of cotton, is designed to increasingly open to the itaconic acid market.

Herein, we present the development of a fully bio-based resin for DLP 3D printing for applications in rapid prototyping and modelling, and thanks to the mechanical properties obtained a potential outlet in the textile/fashion industry. So far, no successful attempt in developing such a total bio-based resin has ever been reported. To improve printing

resolution, we also describe a series of crosslinkers able to make objects in reasonable timescales without diffusion of the polymerization front outside the irradiated regions and with acceptable light penetration. We show here a total bio-based content of the novel ink as high as 96.5%, as far as we know this is the highest percentage ever reached. To achieve the final mechanical performances, i.e. elongation at break, the suitable combination of itaconic acid and the two polyols has been deeply investigated. Therefore, mechanical performances of the 3D printed objects are evaluated in light of potential applications as both rigid and flexible structures [386], the latter being potentially suitable in the textile industry.

The resin is formulated with different dyes and phosphorescent Ir(III) complexes as an additional proof-of-concept. We approached the addition of phosphorescent iridium complexes in order to demonstrate the versatility of the resin, the photostability of said complexes to prolonged irradiation during 3D printing and their effectiveness at very low concentrations. To the best of our knowledge, this has never been demonstrated in the literature. The only implementation of transition metal complexes in stereolithography 3D printing techniques in the literature is the one reported by Lim et al., in which they employed tris-bipyridyl ruthenium as the photoinitiator, but no photoluminescence property was discussed.[387]

3.2.2 Results

Photocurable polyester

Since itaconic acid is a water-soluble solid diacid, its derivatization is required in order to obtain a liquid 3D-printable resin. Based on a previous study by Barrett et al.,[384] itaconic acid was reacted with different alcohols at high temperatures under vacuum to obtain photocurable liquid polyesters that, being the main component of the developed ink, could be formulated for the desired application. For the preparation of the optimum liquid polyester, polycondensation under vacuum without solvent was employed: several different biobased hydroxy derivatives such as alcohols, diols, polyols, and hydroxy acids have been tested, alone or in mixtures, but eventually most of them have been discarded either for their low printability, their high cost or the worse performances of their poly-itaconates.

Finally, the bio-based monomers which allowed the formation of itaconic acid polyesters with acceptable mass yield (35%), easy purification and DLP printability were glycerol, 1,3-propanediol and vanillic acid (**Figure 3.2.1**) in 0.5 : 0.5 : 0.22 mixture compared to itaconic acid, respectively. 1,3-Propanediol is industrially manufactured by DuPont by fermentation of corn syrup and glycerol is the main waste material in the production of biodiesel. Besides, vanillic acid can be obtained by oxidation of vanillin, but it is also naturally occurring.[388–391] The key component that allowed the preparation of a fully printable ink for DLP 3D printing was indeed vanillic acid. Even though being a hydroxy acid it does not compete with the other components during the formation of the polyester, it played a fundamental role in

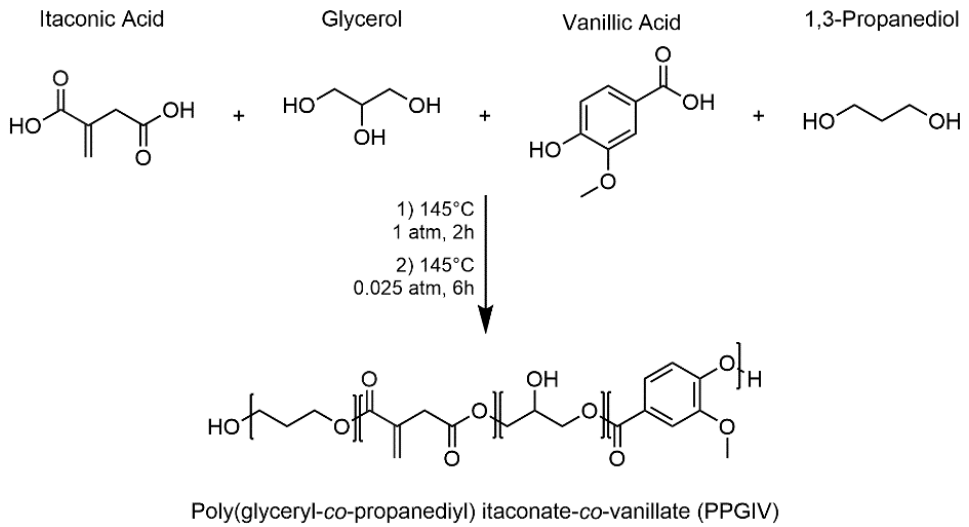

Figure 3.2.1. Selected monomers and experimental conditions for the preparation of the photocurable polyester.

the light-absorption processes taking place during the photopolymerization. Most of the time, in photopolymerization-based 3D printing techniques the addition of photoabsorbers such as 2,5-bis(5-tert-butyl-benzoxazol-2-yl)thiophene (BBOT) or dyes is essential.[392] This is because it is often required to limit the diffusion of high-energy photons into the resin during the photopolymerization process, to avoid diffusion of the polymerization front outside the irradiated section which can cause a drastic reduction in the x–y resolution of the printed object. In our case, the task is performed by a combination of the effect of the vanillic acid monomers contained in the polyester chains and the dyes added to the formulation. Less remarkably, the incorporation of vanillic acid into the resin gives it a pleasant, sweet vanilla flavour, as opposed to commercial resin which displays the unpleasant characteristic smell of acrylate compounds. The synthesized itaconic acid-based photocurable polyester poly(1,3-propanediyl-co-glyceryl) itaconate-co-vanillate (PPGIV) was characterized by NMR spectroscopy (^{1}H-, ^{13}C-, qHSQC and qHMBC), to evaluate its purity and the effective incorporation of all the selected components (**Figure 3.2.2**). NMR analysis reveals the presence of peaks related to each of the employed monomers, but no unreacted reagents are present. The application of ^{13}C NMR to determine whether the glycerol units lead to branched structures by the reaction of their secondary alcohol moiety has been previously described by Somisetti et al.[393] In their work, the authors related the middle carbon in glycerol units to a ^{13}C-NMR peak around 69 ppm for branched glycerol units and a peak around 65 ppm for linear or terminal ones. In our case, we observe peaks in both regions, suggesting the coexistence of terminal, linear and branched glycerol units in the synthesized polyester. This is also confirmed by the qHSQC and qHMBC spectra of PPGIV reported in **Figure 3.2.3**.
The weight and molar compositions of the obtained polymeric resin were evaluated on a fully hydrolysed polyester sample by NMR spectroscopy. Results are reported in **Table 3.2.1**. Strongly alkaline conditions such as NaOH 3 M in deionized water and high working temperatures (around 80 °C) allowed for the complete saponification of the polyester resin, generating much simpler NMR spectra which display the signals for each employed monomer (**Figure 3.2.4**). The average molecular weight of the polyester was determined by size exclusion chromatography (SEC)/gel permeation chromatography (GPC), revealing that for the prepared polymer Mn = 1500 g mol^{-1} and Mw = 1650 g mol^{-1}, corresponding to PDI = 1.1. A low polymerization degree is expected for catalyst-free thermal polycondensations, and it is required for the obtainment of relatively low viscosity liquid solutions that could be efficiently formulated into liquid resins for 3D printing.

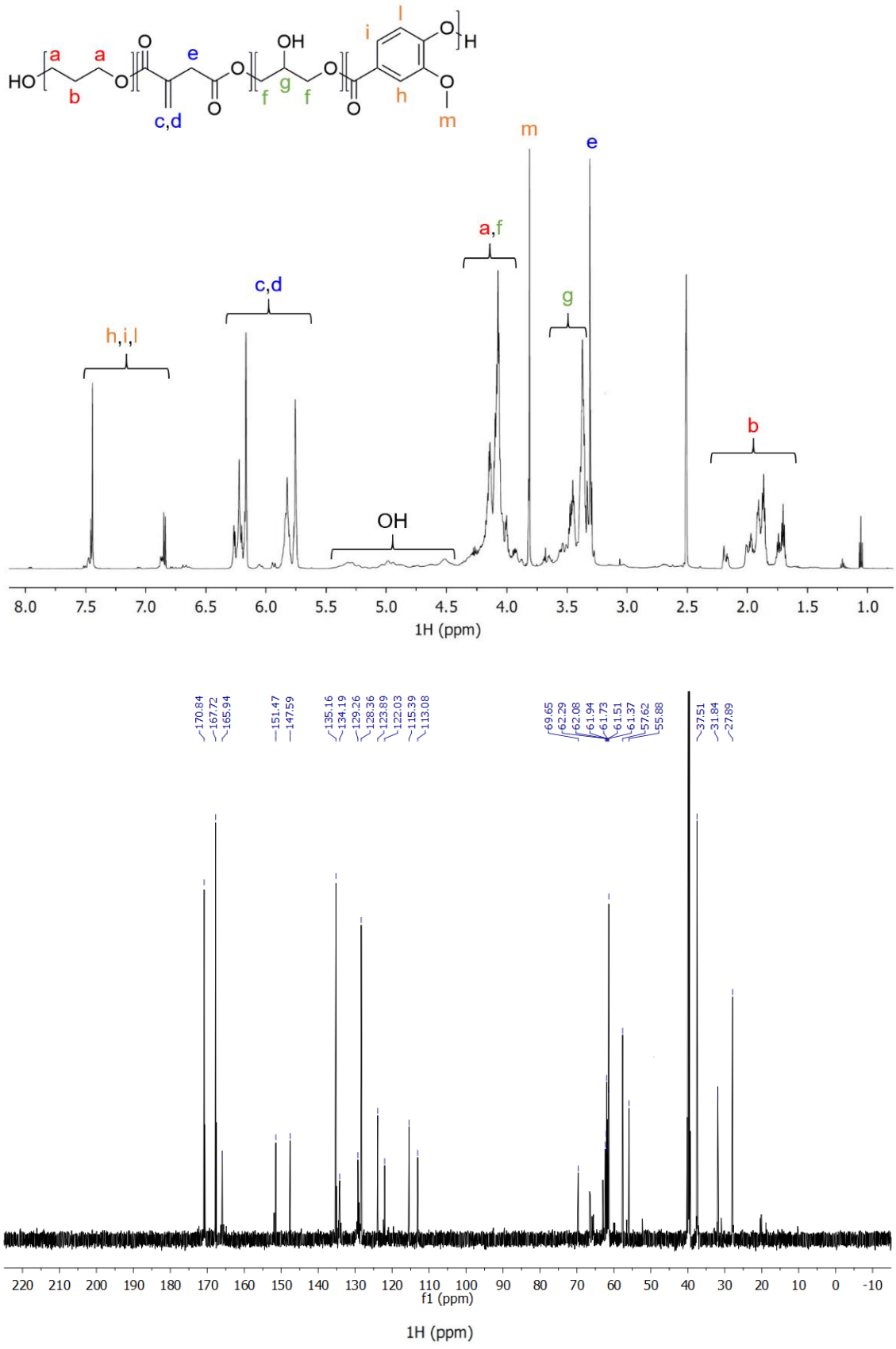

Figure 3.2.2. 1D NMR analysis of PPGIV. Top: ^{1}H-NMR spectrum (600 MHz, DMSO-d_6) of PPGIV, with the assignment of peaks to the related monomers or functional groups. Bottom: ^{13}C-NMR (150 MHz, DMSO-d_6) of PPGIV.

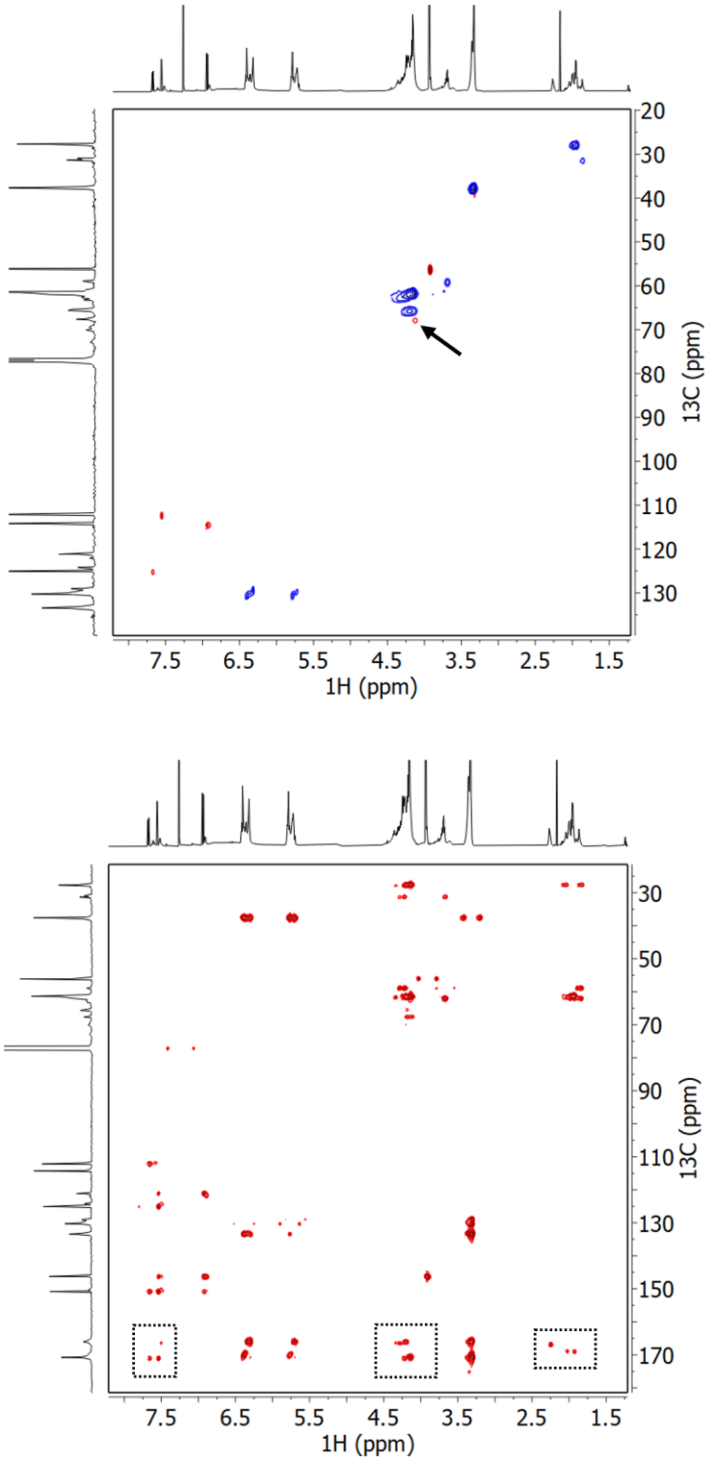

Figure 3.2.3 - ^{1}H-^{13}C gHSQC (top) and gHMBC (bottom) NMR spectra (600 MHz, $CDCl_3$) of PPGIV. Since gHSQC experiment is phase-sensitive, it allows distinguishing between CH + CH_3 (red cross-peaks) and CH_2 groups (blue cross-peaks). The cross peak pointed with the arrow corresponds to CH residues on branched glycerol units, confirming that with the employed polymerization conditions glycerol is able to form branched structures. However, the analogous cross peak corresponding to linear or terminal glycerol units is most probably overlapped with the other polyols signals (in the region between 60-70 ppm for ^{13}C and 3.5-4.5 ppm for ^{1}H). The gHMBC spectrum displays ^{1}H-^{13}C correlations at a longer distance than gHSQC, allowing to observe some inter-monomer correlations (cross-peaks in dotted boxes).

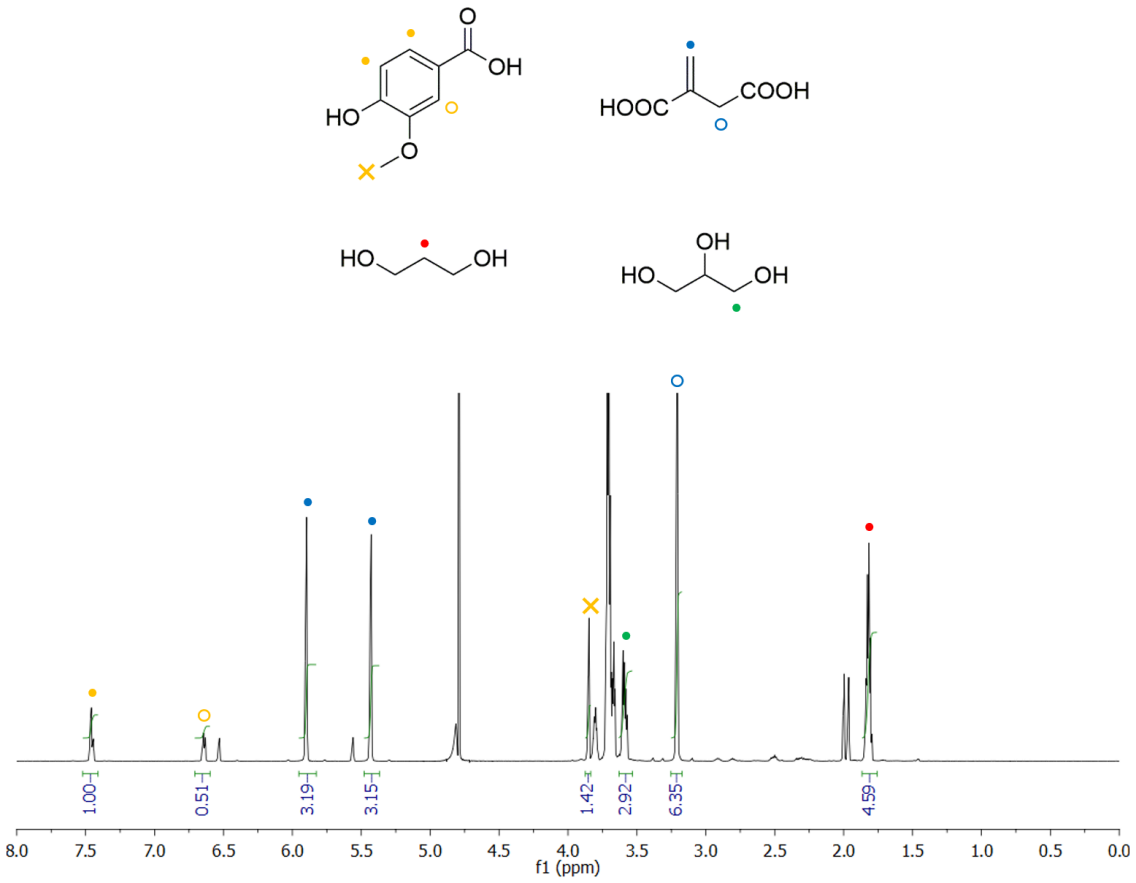

Figure 3.2.4 - ^{1}H-NMR (600 MHz, D_2O/H_2O 1:1) of PPGIV after hydrolysis. Unambiguously assignable peaks have been integrated in order to establish the molar composition of the prepared oligomer.

Component	Molar Ratios	Weight Percentage
Itaconic Acid	6.5	51%
1,3-propanediol	4.7	22%
Glycerol	3.0	17%
Vanillic Acid	1.0	10%

Table 3.2.1 - Monomer composition of the synthesized PPGIV and the corresponding minimum molecular structure representing the proportions between the monomers.

Crosslinkers

Even though PPGIV is rich in itaconic acid, and thus in photocurable double bonds, their concentration is too low for applications in DLP. The photopolymerization of the polyester itself leads to a cured polymer which does not display the mechanical performances required for it to keep its shape during the 3D printing process, causing the structure collapse under its weight. Moreover, even at low molecular weights, the viscosity remains too high, preventing its diffusion onto the resin vessel between the curing of one layer and the next during the 3D printing process, making it extremely hard to employ it as-it-is for the final application. In order to overcome both these problems, the new compounds bis(HEMA)itaconate (BHI) and tris(HEMA) citrate (THC) crosslinkers have been synthesized by adapting a procedure available in the literature for the formation of the bis(isopropyl) ester of itaconic acid (**Figure 3.2.5**). [394] The required chemicals are cheap, and the reactions allow producing large amounts of crosslinkers (yields for BHI of 77% and THC of 81%) with high purity and little efforts for their purification. Notably, the two compounds are both liquids with low viscosity and low volatility; they are totally biobased and display a high density of photocurable groups. In addition, the use of 2-hydroxyethyl methacrylate (HEMA) for the preparation of the crosslinkers is preferred, due to its low toxicity and low volatility compared to other acrylate compounds, [395,396] and the biocompatibility and biodegradability of many polyHEMA copolymers have been well established in the literature. [397–399] Furthermore, HEMA can be obtained via renewable oil-free processes, as it is often produced by esterification of methacrylic acid with ethylene glycol: the former can be produced by catalytic oxidative dehydrogenation of biosynthesised isobutyric acid, and the latter can be obtained by

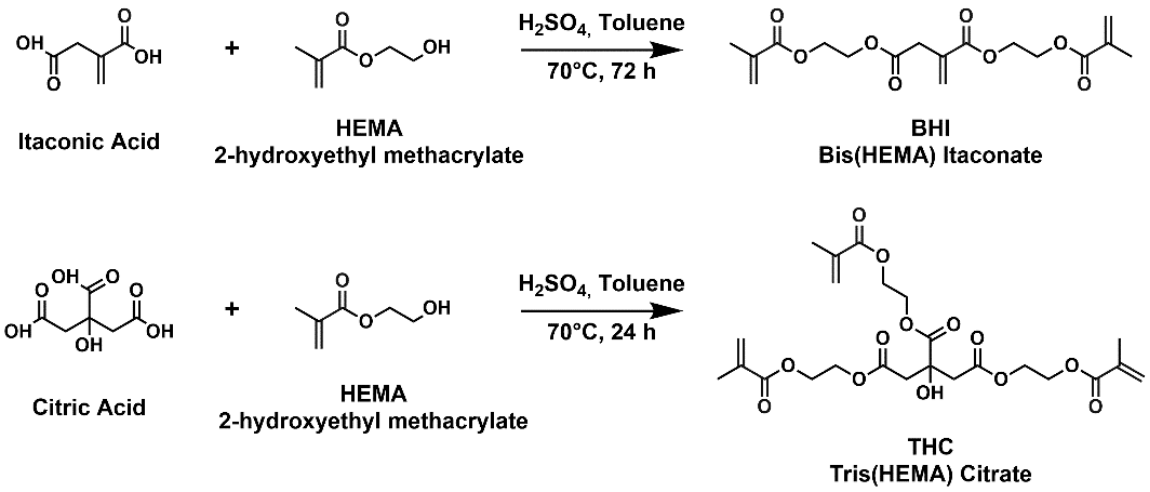

Figure 3.2.5 - Chemical reactions for the synthesis of the crosslinkers.

fermentation of D-xylose in engineered *E. coli*. [400–404] The employment of different acrylate crosslinkers for DLP 3D printing such as isobornyl acrylate, pentaerythritol tetraacrylate and multifunctional acrylate oligomers was previously reported, but these derivatives suffer from several drawbacks such as high cost, low bio-content and the required employment of toxic acrylates during their production. [405]

Ink formulation

Besides the photopolymerizable substrate, the main components required for the 3D printing are (i) photopolymerization initiators, (ii) photopolymerization inhibitor, (iii) crosslinkers and (iv) dyes (**Figure 3.2.6**). As initiators, we observed that the fastest curing is achieved with the combination of two acylphosphine oxides (phenylbis(2,4,6-trimethylbenzoyl)phosphine oxide, BAPO, and diphenyl(2,4,6-trimethylbenzoyl)phosphine oxide, MAPO) together with 2,2-diethoxy acetophenone (DEAPH). The initiators are required to efficiently absorb the UV light generating reactive radicals that can propagate in the ink leading to the polymerization of the double bonds. As a terminator, 4-methoxyphenol (MHQ) has been selected as it is relatively safe, low cost and very effective.[406] The crosslinkers have already been discussed in the previous paragraph. As aforementioned, dyes participate together with vanillic acid residues in the absorption of UV light diffusing into the resin outside of the irradiated regions, allowing for better printing resolution.[407] In order to demonstrate the great versatility of the final formulation, we explored four organic dyes to cover the full visible spectrum of colours: methyl red (red), cresol red (yellow), solvent green 3 (1,4-bis(p-tolylamino) anthraquinone, green) and unisol blue AS (1,4-bis(p-isopropylamino) anthraquinone, blue)

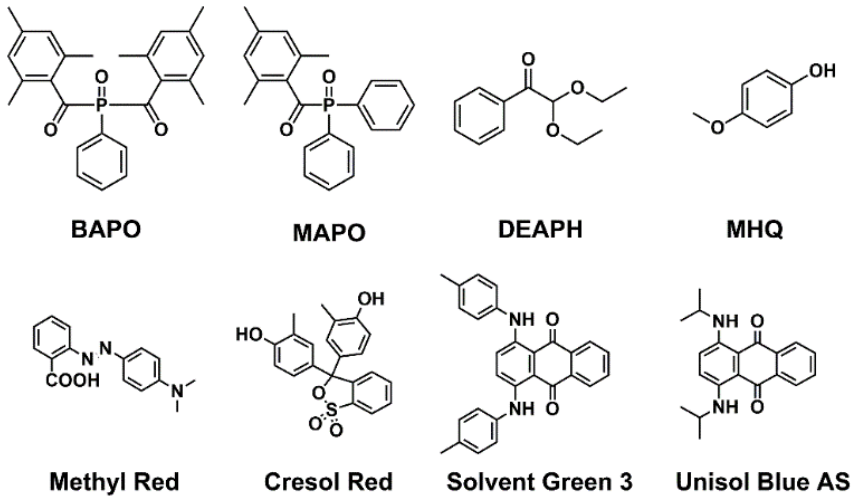

Figure 3.2.6 - Chemical structure of the selected photopolymerization initiators (MAPO, BAPO and DEAPH), terminator (MHQ) and dyes.

(**Figure 3.2.6)**. The red and yellow dyes are commonly employed acid–base indicators: since the prepolymer displays free carboxylic groups from terminal itaconic acid monomers, they display their acid colour when formulated into the ink. The green and blue dyes, instead, are anthraquinone derivatives, which can be employed in ppm concentrations thanks to their extensive molar absorption coefficients. The ink was then formulated by mixing all the required components in pre-defined ratios with organic solvents such as ethanol, methanol, ethyl acetate or chloroform at room temperature. The evaporation of the solvent, firstly by rotary evaporation and then by applying high vacuum, allowed for the obtainment of a homogeneous photocurable ink ready to be subjected to the 3D printing process. The optimal relative amount of the different components is reported in **Figure 3.2.7**. To recap, the final formulation contained 48.5 wt.% of PPGIV, 24.0 wt.% of BHI and 24.0 wt.% of THC, 1.5 wt.% of initiators, 2.0 wt.% of terminator and 0.01 wt.% of dyes. Since the first three components can be considered as bio-based, the herein reported formulation has a nominal biobased content of around 96.5%. In order to avoid photopolymerization of the resin induced by environmental light, the developed resins have been stored at room temperature in amber glass containers. Under these conditions, the resin demonstrated stability and

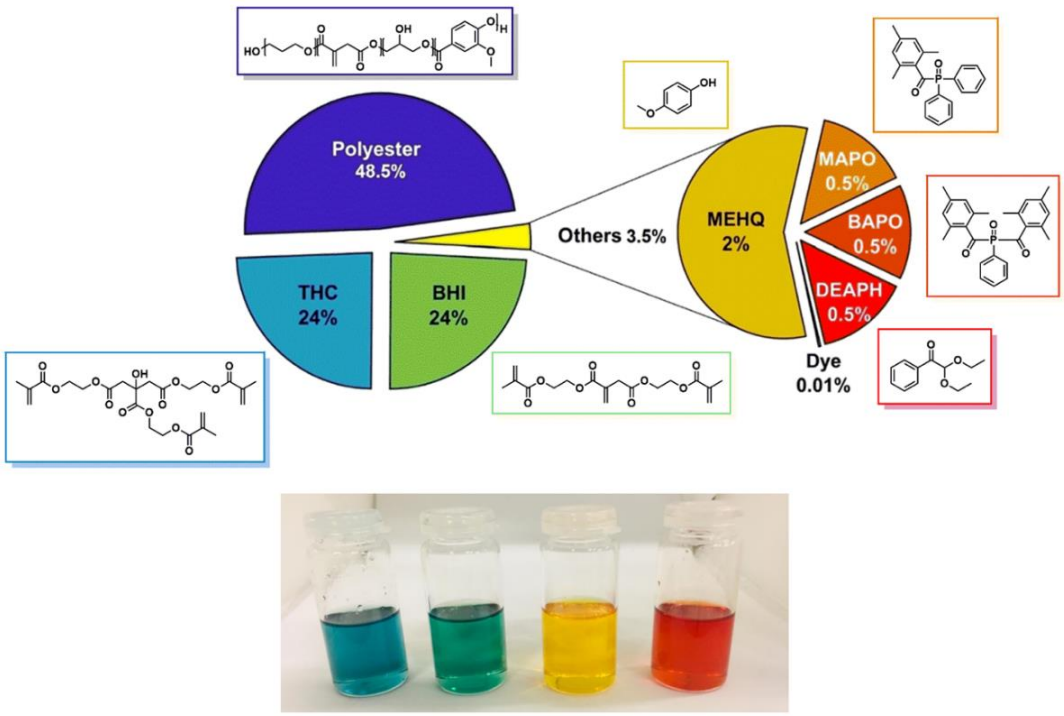

Figure 3.2.7 - Top: weight composition of the developed bio-based ink for DLP 3D printing. Bottom: optical picture of the developed resins with the four different dyes.

printability up to 12 months due to the presence of the inhibitor MHQ that would immediately quench any possible radical species spontaneously formed.

Rheological analysis has been performed on the formulated resin to determine its printability via DLP and stereolithographic technique. If the viscosity of the ink is too high, it will require longer printing times: it will be required to reduce the speed of the moving platform to allow the resin to fully flow underneath it, between the irradiation of one layer and the next. In addition, if the ink displays marked non-Newtonian shear thickening behaviour, it will react to the movement of the building platform inside it with a variation in its overall viscosity, again resulting in a need for a reduction of the platform movement speed. As shown in **Figure 3.2.8**, the developed biobased ink displayed viscosity in the 0.07–0.3 Pa s range, and a Newtonian behaviour is observed. Nevertheless, the measured viscosity in the range of operating temperatures (15–35 °C) would indeed allow for the resin to flow and fully cover the printer's resin vessel in the minimum timeframe of 3 s. The fluid behaviour of the ink was also confirmed by oscillometric viscoelasticity studies as a function of temperature (**Figure 3.2.8**). As the phase remained constant throughout all the temperature range around 90°, the

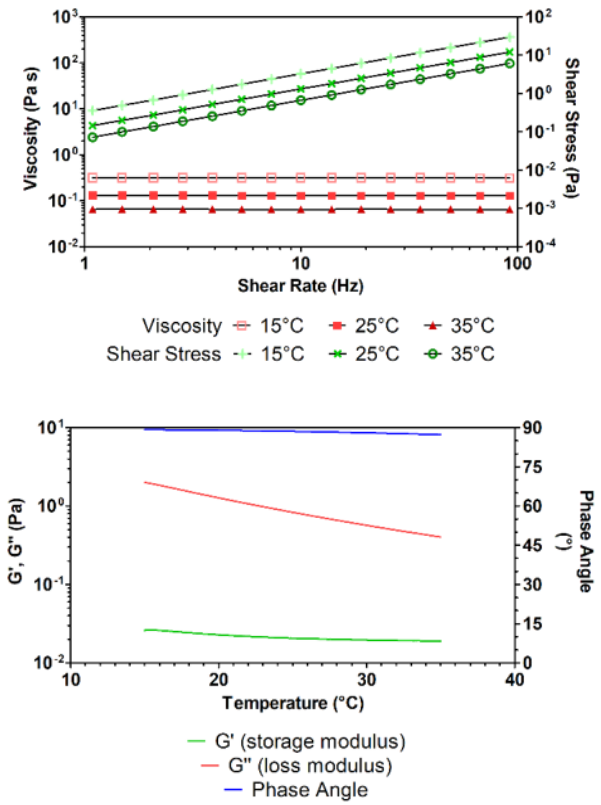

Figure 3.2.8 - Rheological analysis of the photocurable ink. Left: shear stress and viscosity vs. shear rate relationships at different temperatures. Right: temperature dependence of storage and loss moduli for the developed ink and the corresponding phase angle, obtained by oscillatory viscoelastic analysis.

ink mostly resembled the features of a liquid, as it is also observed by the low storage modulus. The developed formulation was able to undergo DLP 3D printing leading to the formation of well-resolved solid objects. Several irradiation times have been tested to minimize the printing time while still maintaining good resolution and structural stability. The identified optimal irradiation time was 3000 ms and, accordingly, several test samples have been printed and underwent mechanical analysis to assess the mechanical properties of the formulated ink. In particular, flexural and tensile strength analysis, Charpy impact test and evaluation of shore-D hardness have been performed on 3D printed specimens. The results of the mechanical tests are summarized in **Table 3.2.2**. For tensile tests, dog-bones have been printed according to ISO-527-1BA specifications, while flexural tests have been performed on 80 × 10 × 4 mm rectangular bars.

3D printed objects

It is worth mentioning that the mechanical properties of layered objects printed by AM are intrinsically anisotropic, and the outcome of these tests is strongly dependent on the direction along which the mechanical stress is applied.[408] This makes it very trivial to evaluate mechanical performances of commercially available resin formulations if the printing geometry is not described or standardized. In our case, the tensile stress vector was tilted 15° with respect to the z printing direction, while the bending stress vectors were tilted 75° with respect to it. First of all, we can notice good mechanical resistance and lower fragility which are the minimum requirements to get a printed object. For instance, the object made with the developed formulation displays four times greater impact strength (internal data on a

Tensile Test				
E_t tensile modulus	σ_{tb} ultimate tensile strength	ε_{tb} elongation at break	**Hardness**	**Impact Strength**
[MPa]	[MPa]	[%]	[Shore-D]	[KJ m^{-2}]
62 ± 5	5.4 ± 0.7	18.0 ± 2.9	72 ± 1	4.77 ± 2.81
Flexural Test				
E_f flexural modulus	σ_{fm} maximum flexural strength	ε_{fm} deformation at maximum strength	σ_{fb} ultimate flexural strength	ε_{fb} deformation at break
[MPa]	[MPa]	[%]	[MPa]	[%]
350 ± 25	12.6 ± 1.8	5.4 ± 0.7	12.6 ± 1.8	5.4 ± 0.7

Table 3.2.2 - Mechanical properties of 3D printed objects built with the developed ink.

commercial resin) with a value of 4.77 kJ m^{-2}. Moreover, the fabricated objects display good flexural properties, enabling bending deformations up to 6%, with flexural strengths around 12.6 MPa. The textile industry needs flexibility and indeed the first thing to be noticed is the low tensile modulus of our bio-based construct, revealing that the polyester-based ink displays increased elasticity. Compared to acrylate-based formulations, the presence of low molecular weight polyesters gives higher elasticity. This is also confirmed by its very high elongation at break up to 18%; in comparison commercial resins give values in the range of 2–5%. The developed ink also displays low ultimate tensile strength: due to the fact that the tensile test has been performed in the direction perpendicular to the printed layers, it is reasonable to suppose that the lower value is due to a lower adhesion between the printed layers which, upon traction, detach from each other by weaker forces. The effective polymerization of the mixture was confirmed by ATR-FTIR spectroscopy performed on the 3D printed objects compared to the uncured resin (**Figure 3.2.9a,b**). The absorption at 1636 cm^{-1}, attributed to the stretching of the C=C group, and the ones at 944 and 815 cm^{-1}, related to C=C-H deformations, are strongly reduced in intensity, suggesting the effective formation of a network of saturated C-C bonds at the expense of itaconic and methacrylate groups. Then, scanning electron microscopy (SEM) was employed to assess the actual printing resolution achievable with the developed resin (**Figure 3.2.9c-e**), allowing not only the visualization of the juncture of the printed layers, but also the size of the actual pixel irradiated by the DLP projector, confirming the 50 × 50 μm *x*–*y* resolution declared by the printer manufacturers and the 50 μm layer thickness set in the slicing phase. It is also possible to notice the great homogeneity of the printed surface at the micron scale, with little or no fractures and well defined edges and vertices. Finally, thermal analyses (DSC and TGA) have been performed on the printed objects (**Figure 3.2.9f,g**). DSC reveals the presence of one T_g for the polyester-based photocured material, which can be attributed to the glass-to-plastic transition of the polyester chains in the polyacrylate network. On the other hand, TGA reveals thermal decomposition of the printed objects starting at around 120 °C, with a first 50% mass loss below 400 °C. Compared to a commercial monomeric analogue, it degrades faster with increasing temperature, but it allows reaching comparable ash residue after calcination in air at 600 °C.

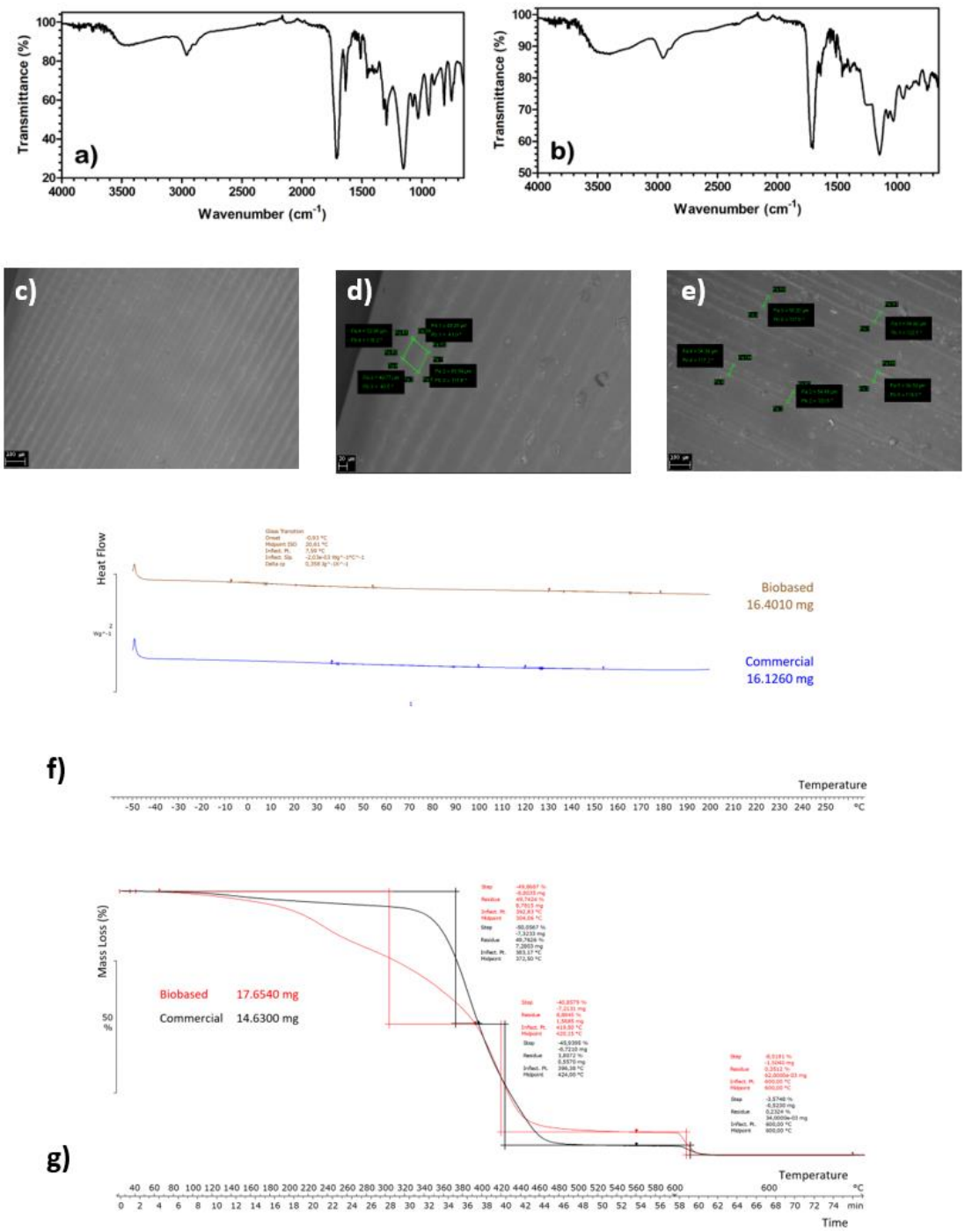

Figure 3.2.9. - ATR-FTIR analysis on the photocurable ink before (a) and after (b) the 3D printing process. Morphology of the 3D printed material explored by SEM. c,d) Top view of the irradiated slice, which allows to distinguish projected squared pixels and to measure their size. e) Lateral view of the printed object, which allows to measure the distance between printed layers. f) Comparison of DSC traces of photopolymerized commercial and biobased inks. The curve related to the material printed with the developed biobased ink display a small endothermic process occurring at around 7.6°C, which can be attributed to a glass transition of PPGIV. g) Comparison of TGA analyses performed on photopolymerized commercial and biobased inks. The developed biobased ink displays lower temperature stability compared to the commercial counterpart but comparable residual mass after complete calcination.

Phosphorescent inks

Undoubtedly, the textile/fashion industry is increasing its demands towards luminescent materials, as they are widely employed, for example, in safety clothing where the luminescence allows increasing the visibility of the wearer in dangerous environments. Moreover, in recent years luminescence of textiles has not been strictly employed as a purely functional attribute, but more and more to add a novel touch on basic design. [409] Currently, phosphorescent textiles are produced by deposition or chemical linking of phosphors to polymer fibres, which are then employed in the manufacturing of clothing. [410,411] Herein, as a proof-of-concept, four luminescent inks have been prepared by addition of phosphorescent iridium(III)

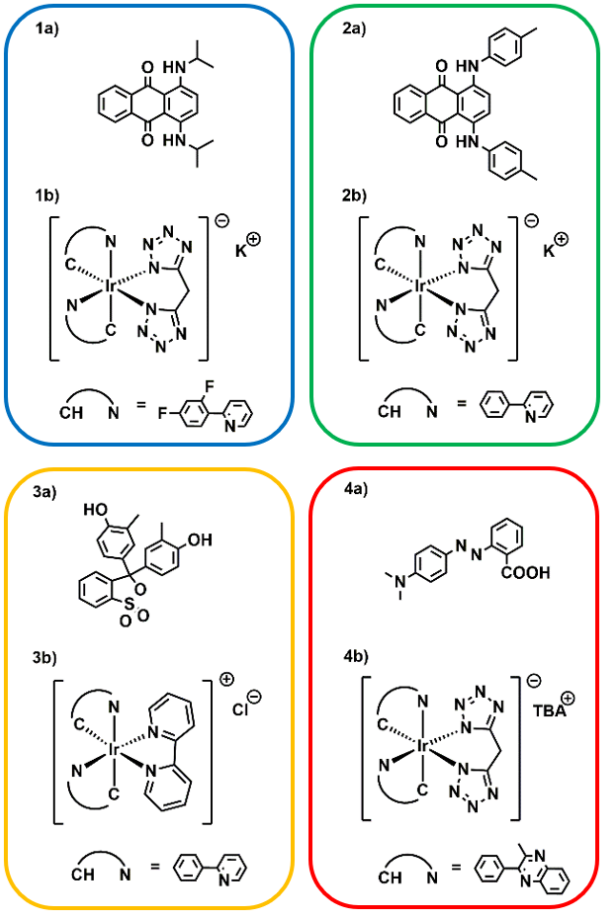

Figure 3.2.10 - Compatible dye-complex pairs selected for the formulation of the four phosphorescent resins. 1a) Unisol Blue AS and 1b) $[Ir(dfppy)_2(b\text{-}trz)]^-K^+$. 2a) Solvent Green 3 and 2b) $[Ir(ppy)_2(b\text{-}trz)]^-K^+$. 3a) Cresol Red and 3b) $[Ir(ppy)_2(bpy)]^+Cl^-$. 4a) Methyl Red and 4b) $[Ir(pqu)_2(b\text{-}trz)]$-TBA+. Emission spectra of 3D printed luminescent dog-bones revealed that the emissive behaviour of the complexes has been maintained after the photopolymerization (Figure 8a). Moreover, it was possible to notice with the naked eye the increase of emission intensity after the printing, induced by the molecular rigidity given by the liquid-to-solid transition of the polymer matrix in which the complexes have been dissolved.

cyclometalated complexes to the developed resin; this allowed the obtainment of inks capable of light emission throughout all the visible spectrum by excitation in the near UV range. The selected complexes are $[Ir(dfppy)_2(b\text{-}trz)]^-K^+$ as a blue emitter, $[Ir(ppy)_2(b\text{-}trz)]^-K^+$ as a green emitter, $[Ir(ppy)_2(bpy)]^+Cl^-$ as a yellow emitter and $[Ir(pqu)_2(b\text{-}trz)]^-TBA^+$ as a red emitter. [412,413] Considering that the dyes added to the formulation can absorb the light produced by the above-listed phosphors, a proper selection of suitable complex-dye pairs (**Figure 3.2.10**) which displayed compatible emission and absorption behaviours was found to be fundamental; i.e. the dye should absorb in a region different from the emission region of the complex in order to avoid auto-absorption. It should be mentioned that cyclometalated Ir(III) complexes have been previously employed to generate reactive radical species upon light irradiation.[414–416] Therefore, we explored the possibility of employing the luminescent additives as photopolymerization initiators, but no hardening of the resin was observed for concentrations up to 0.5 wt.% and irradiation times up to 10 s. Emission spectra of 3D printed luminescent dog-bones revealed that the emissive behaviour of the complexes has been maintained after the photopolymerization (**Figure 3.2.15a**). Moreover, it was possible to notice with the naked eye the increase of emission intensity after the printing, induced by the molecular rigidity given by the liquid-to-solid transition of the polymer matrix in which the complexes have been dissolved. Three-dimensional emission maps are shown in **Figure 3.2.11-14**.

Good emission intensities have been obtained with complex concentrations as low as 0.05 wt.% for blue, green and yellow complexes, while it required 0.15 wt.% of the red complex to give a noticeable emission, owing to the avowed lower phosphorescence quantum yield of the red complex.[413] Very interestingly, reversible flexibility of the printed objects is clear from **Figure 3.2.15d** and this confirms the very high elongation at break obtained and finally, in order to prove the overall performances of the developed ink in terms of printability and resolution, a bigger model was printed. The selected model represents the historical towers "Le Due Torri" from the city of Bologna, Italy (**Figure 3.2.15e**). The selected ink contained the green complex–dye pairs and allowed for the reproduction of high-resolution details in the overall construction.

1) Blue Ink

DYE = Unisol Blue AS

COMPLEX = $[Ir(dfppy)_2(b\text{-}trz)]^- K^+$

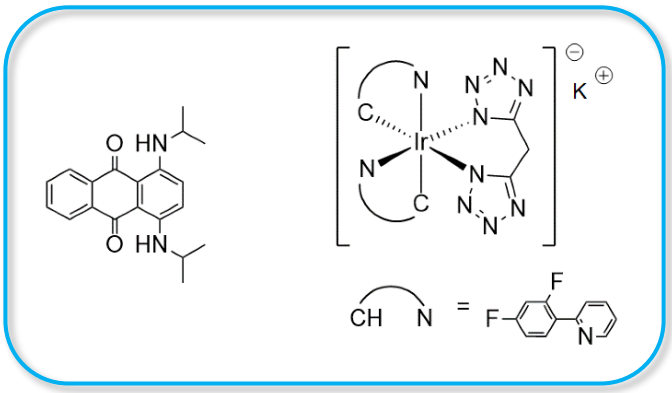

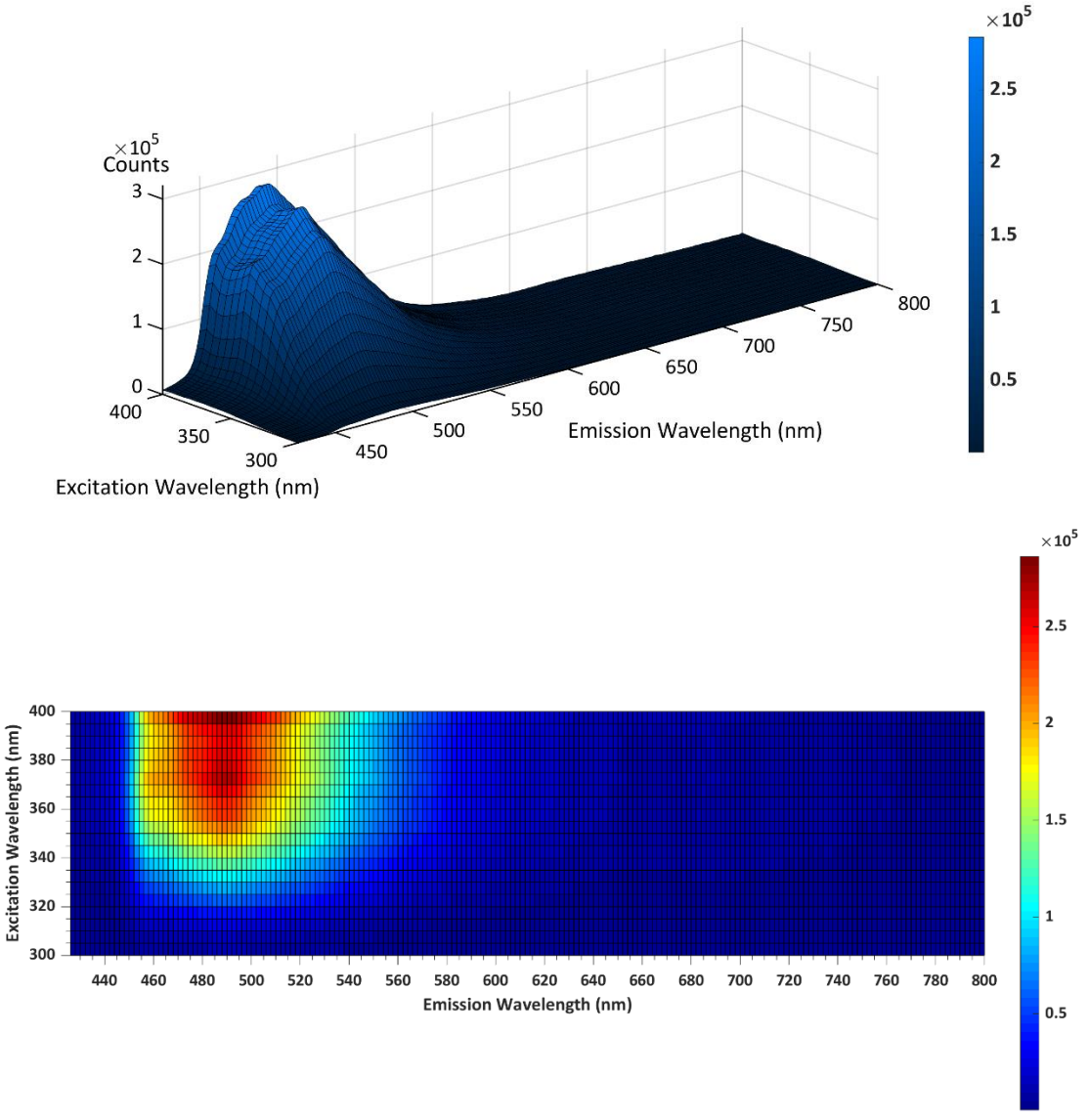

Figure 3.2.11 - Emission maps of the 3D printed blue phosphorescent ink (small dog-bone, top, left). The same emission data are represented with a 3D surface plot (top, right) and with a colour-scale 2D image plot (bottom). Colour scale bars represent counts of the photodetector.

2) Green Ink

DYE = Solvent Green 3

COMPLEX = $[Ir(ppy)_2(b\text{-}trz)]^- K^+$

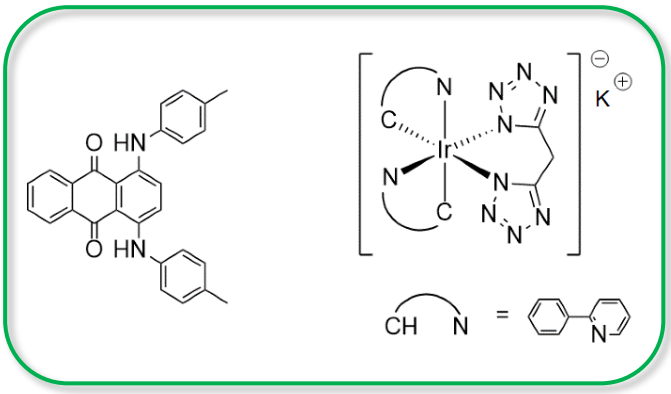

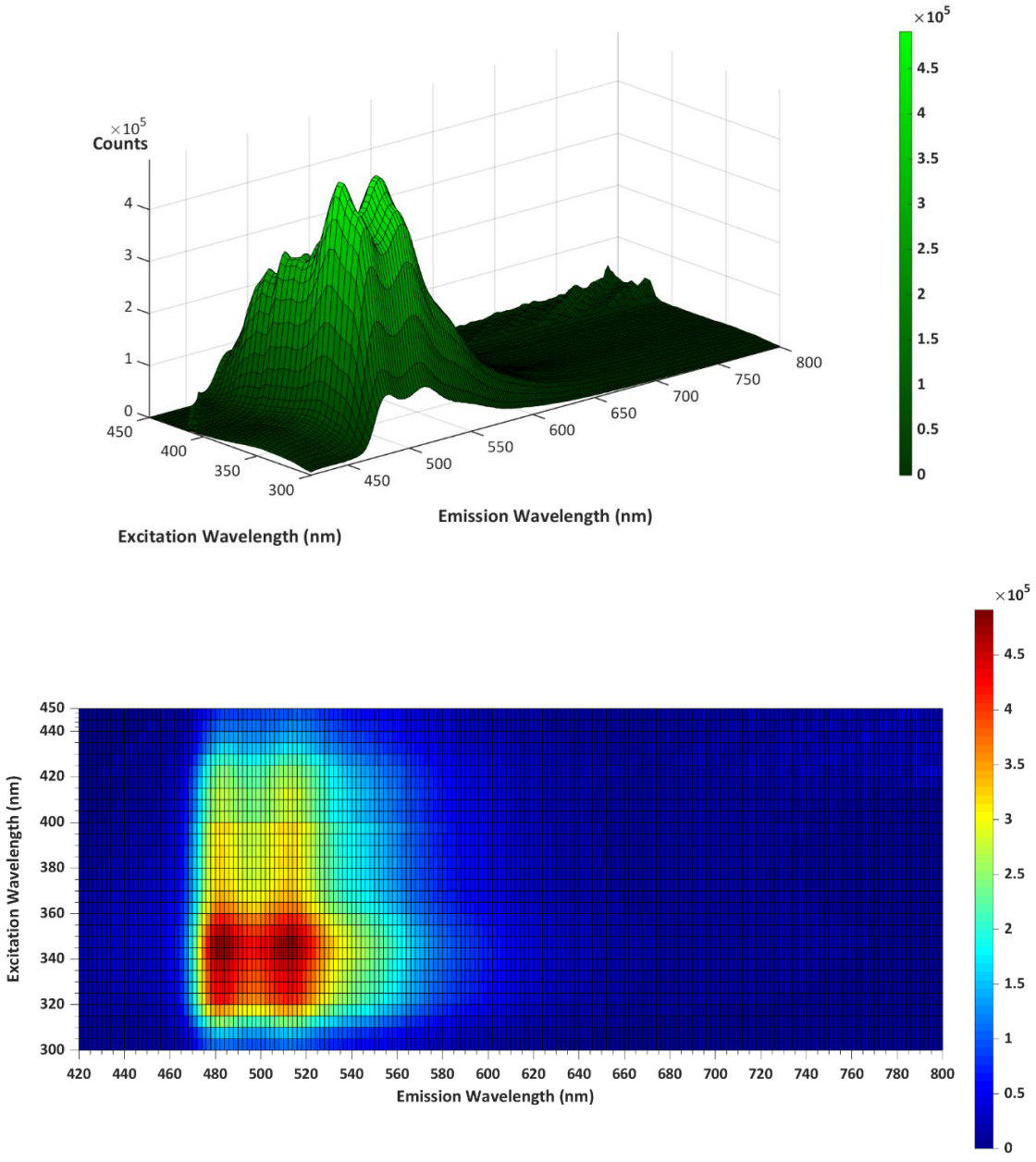

Figure 3.2.12 – Emission maps of the 3D printed green phosphorescent ink (small dog-bone, top, left). The same emission data are represented with a 3D surface plot (top, right) and with a colour-scale 2D image plot (bottom). Colour scale bars represent counts of the photodetector.

3) Yellow Ink

DYE = Cresol Red

COMPLEX = $[Ir(ppy)_2(bpy)]^+ Cl^-$

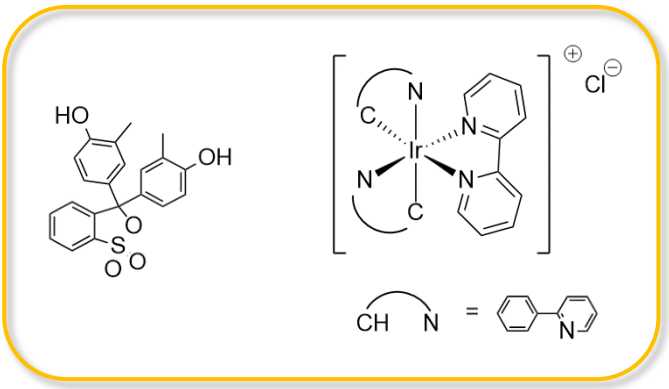

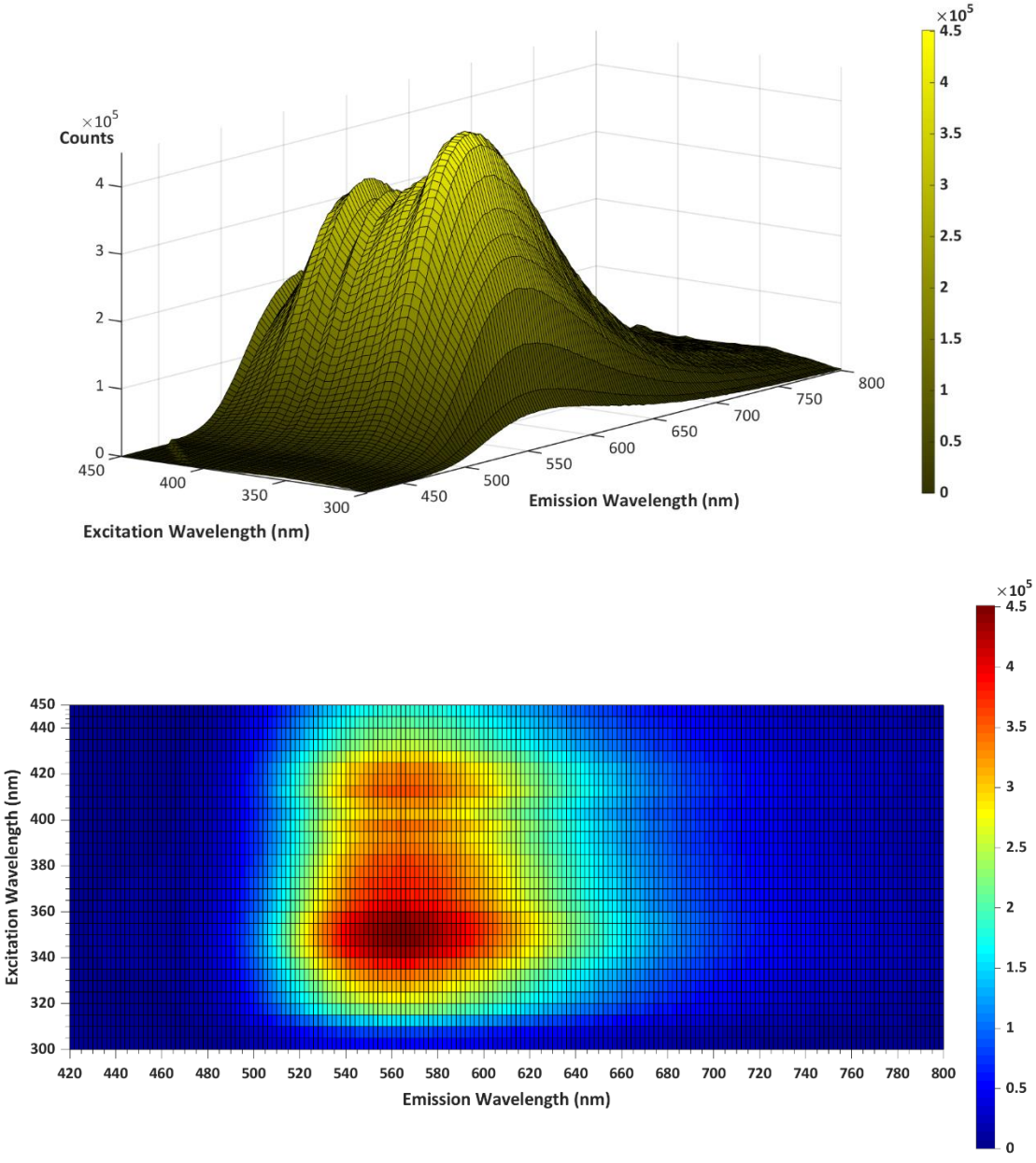

Figure 3.2.13 – Emission maps of the 3D printed yellow phosphorescent ink (small dog-bone, top, left). The same emission data are represented with a 3D surface plot (top, right) and with a colour-scale 2D image plot (bottom). Colour scale bars represent counts of the photodetector.

4) Red Ink

DYE = Methyl Red

COMPLEX = $[Ir(pqu)_2(b\text{-}trz)]^- TBA^+$

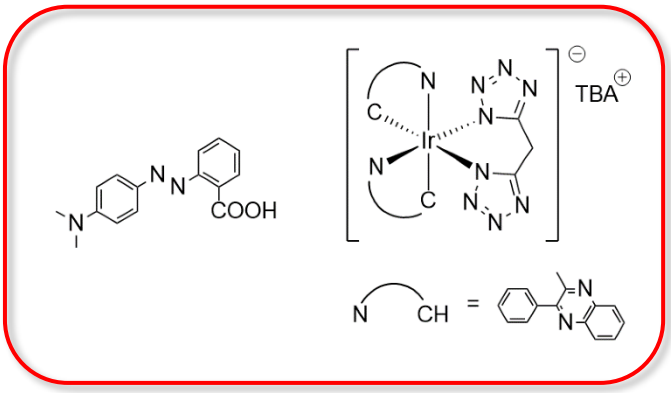

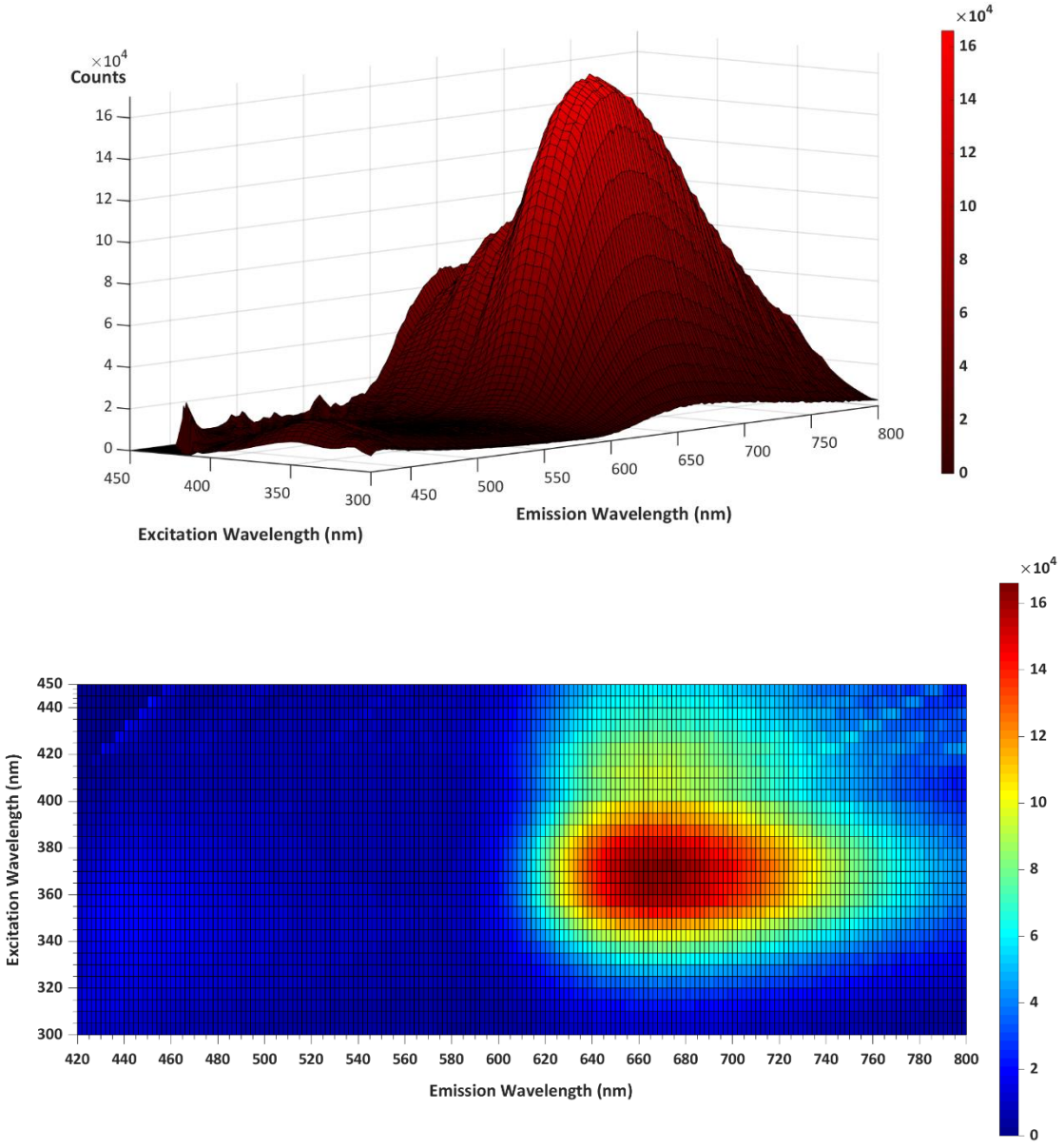

Figure 3.2.14 - Emission maps of the 3D printed red phosphorescent ink (small dog-bone, top, left). The same emission data are represented with a 3D surface plot (top, right) and with a colour-scale 2D image plot (bottom). Colour scale bars represent counts of the photodetector.

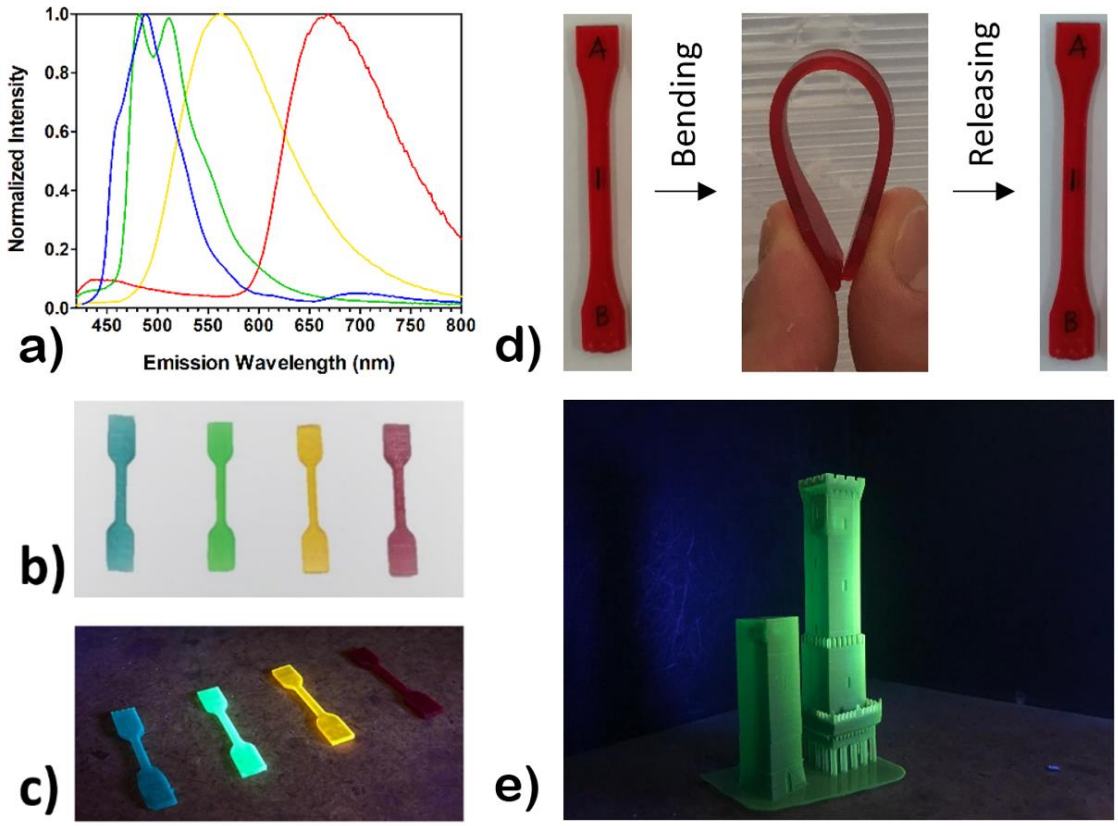

Figure 3.2.15. DLP 3D printing of flexible and phosphorescent resins. a) Normalized emission profiles of the iridium-containing 3D printed dog-bones. Each curve colour corresponds to the emission colour of the corresponding Ir(III) complex. The excitation wavelength is 360 nm for all emission spectra. b) Optical camera pictures of the phosphorescent dog-bones exposed to visible and c) UV (365 nm) light. Dog-bones dimensions are 6x1.8x35 mm. d) Demonstration of the reversible flexibility of the printed objects. Dog-bone dimensions are 77x10x2 mm. e) Picture of a 3D printed green phosphorescent model of "Le Due Torri" of the city of Bologna, under UV irradiation. Structure dimensions are 56x40x96 mm.

In vitro biocompatibility tests

Since a possible future target is the use of our resin in textile applications, an in vitro analysis of the pro-sensitising potential was carried out. For assessing the biocompatibility of our printed samples and with the aim of demonstrating that there is no intrinsic cytotoxicity, we carried out two different tests: a human keratinocyte viability test and an evaluation of pro-sensitising activity (according to OECD 442E) on human monocytes through FACS analysis. Human keratinocytes seeded on polystyrene Petri dishes and exposed for 24 h to the sample eluate did not display any difference in terms of morphology, adhesion and proliferation. Optical microscopy observation and cell counting demonstrated that HaCaT cells can adhere and proliferate in the presence of sample's eluate (**Figure 3.2.16**). For what concerns the pro-

sensitising activity, the purpose of the test was to assess the absence of pro-sensitising skin effects from finished products or raw materials intended for contact with the skin or mucous membranes. In the assay, human monocytes cell line (THP-1) as a prototypic blood-derived immunologically active cell was used. On these cells, the expression of two costimulatory molecules, CD54 (Intercellular Adhesion Molecule) and CD86 (B7.2), was tested, using as a positive control Nickel sulphate, a well-known contact sensitising agent. Nickel sulphate is able to cause in vivo allergic immune reactions (skin sensitization) and it is also widely used to study in vitro immune response modulation. The increasing expression level of CD54 and CD86 on monocytes is a signal of activation of the immune response derived from the exposition to a potentially sensitising contact antigen. The expression of co-stimulatory molecules on the dendritic cells means activation of the immunological response in terms of capability to present the antigen in the typical tissues (skin in this case), where, in vivo, the immune protective response is triggered. The costimulatory molecule expression is compared to the behaviour of nickel characterised by (a) high increase of both the markers; (b) direct correlation between concentration and intensity of the response; (c) relevant effects even at very low doses. The tested dose of 4 $\mu g\ ml^{-1}$ of nickel sulphate ($NiSO_4 \cdot 6H_2O$) corresponds to more or less 1 ppm of Ni, dosage that is around the minimal sensitising threshold in already sensitised individuals with irritated skin. The concentration that is able to cause an allergic reaction in most of the sensitive subjects is anyway around higher value, over the 100 ppm of Nickel in contact with safe and intact skin. The assay has been recognized as valid in compliance with the aforementioned method acceptance criteria, namely a percentage of living cells >80% tested by MTT assay and an MFI value of the $NiSO_4$ control (at the lower tested Ni concentration) >10% compared to the negative control with culture medium. The MFI must display a dose–response increasing pattern with the other two tested doses. As the final result of the sensitisation assay in this in vitro model, the eluted samples do not affect the expression of the investigated markers in immunocompetent cells, and hence it does not show any stimulating potential on the immune cellular response mediated by monocytes/macrophages.

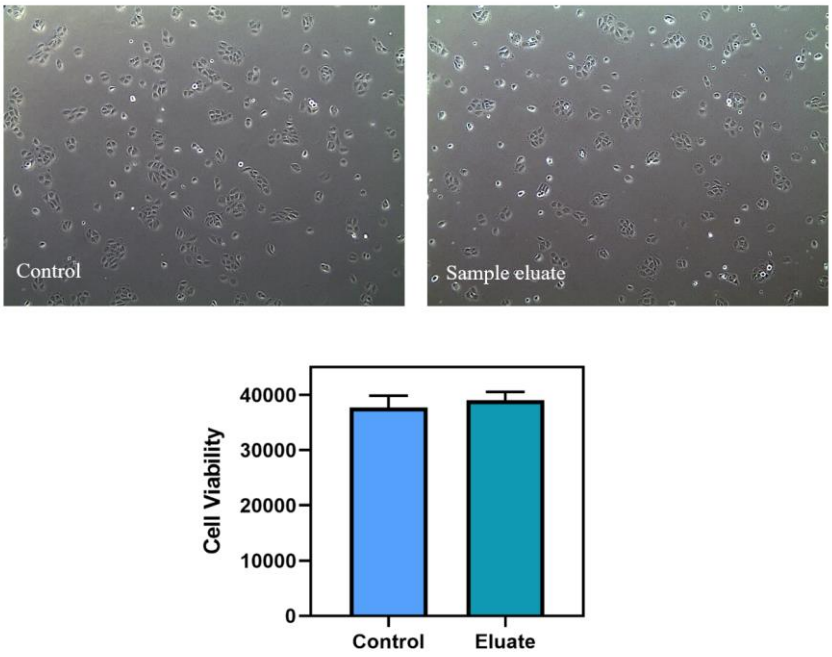

Figure 3.2.16 - HaCaT cell viability test. HaCaT cells seeded on multiwell-6 polystyrene plate with and without exposure to the printed sample eluate: the control (on the left) and the treated (on the right) show no difference in cell morphology (optical microscope image above) and the 24h count displays how even if in presence of the eluate, cell viability is not adversely affected.

3.3 Biopolymer-based reversible self-healing hydrogel for direct ink writing (DIW) 3D printing

Maturi, M.; Comes Franchini, M.; Gracias D. H.[♪] et al. *Manuscript in preparation*

[♪] Department of Chemical and Biochemical Engineering, Johns Hopkins University (JHU), Baltimore (MD, USA)

Work performed in the frame of a Marco Polo fellowship during a 6-month period spent at the Johs Hopkins University (JHU) in Baltimore (MD, USA) as Visitng Graduate Student.

3.3.1 Introduction

Hydrogels are composed of a network of hydrophilic and crosslinked polymeric chains, that form stable 3D polymeric structures with high water contents (usually > 90%). The range of materials that can be employed for the formation is hydrogel is extremely wide, including synthetic polymers such as polyacrylamide or polyvinyl alcohol together with natural biopolymers like cellulose, chitosan and alginic acid and many others. [417,418] Also, the chemistry of the crosslinks that are able to form the interconnected 3D network can vary depending on the functional groups that are present on the polymers. Hydrogen-bonding plays an important role in the formation of hydrogels, but ionic interactions can also be exploited for the formation of stable 3D networks, as in the case of the well-known Ca^{2+}-alginate interaction. [419] However, coupling agents and crosslinkers are often added to induce the formation of covalent bonds using simple organic chemistry. As an example, EDC-coupling is often exploited to covalently crosslink amines with carboxylic acids, but other reactions (such as Diels-Alder cycloadditions) can be exploited to form interconnected polymer networks in water. [420–422]

A self-healing hydrogel (SHH) is one that is able to repair crack and fractures either autonomously or by applying external stimuli. [423,424] The self-healing mechanism in polymeric hydrogels has been deeply investigated in the last decade; this phenomenon is often observed when in a hydrogel a mobile phase enables the reconnection of two interfaces of the same material placed in contact through mass transfer and by reconnection of broken links in the material. [425] This allows for the production of more durable manufactures, that can efficiently resist prolonged mechanical stress without braking. In the most recent literature, it is described how an SHH with acceptable mechanical properties need to be composed of a

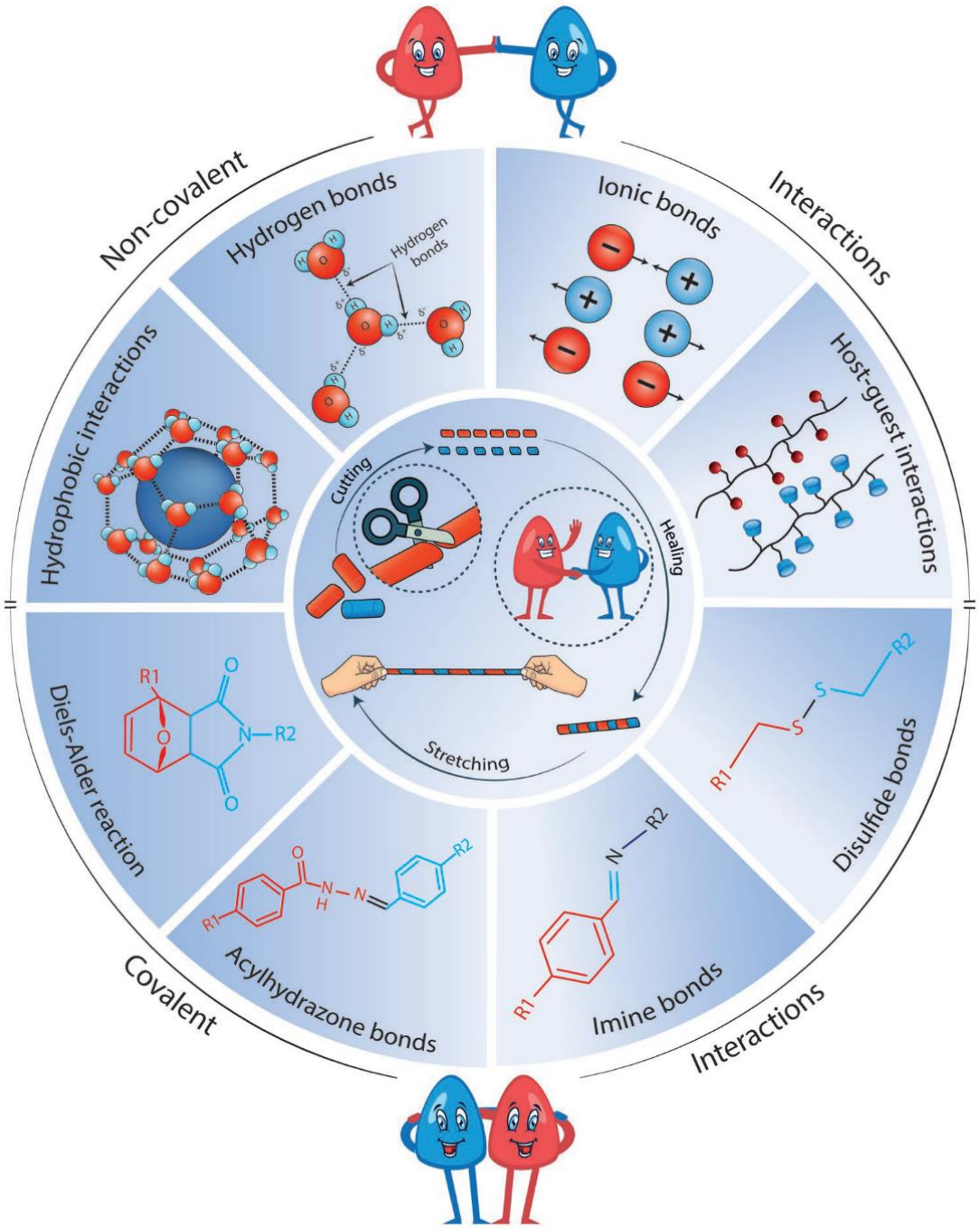

Figure 3.3.1 – Schematic representation of the macroscopic properties of self-healing hydrogels and the main chemical interaction that allow for a hydrogel to self-heal. Reproduced from ref. [426]

strong polymeric network of covalent bonds interconnected with a secondary network made by weak reversible interactions such as H-bonding, hydrophobic interactions, host-guest interactions, ionic bonding and dynamic covalent bonding (**Figure 3.3.1**). [427–430] The weak interactions are the ones that allow for the self-healing properties, allowing to form new weak

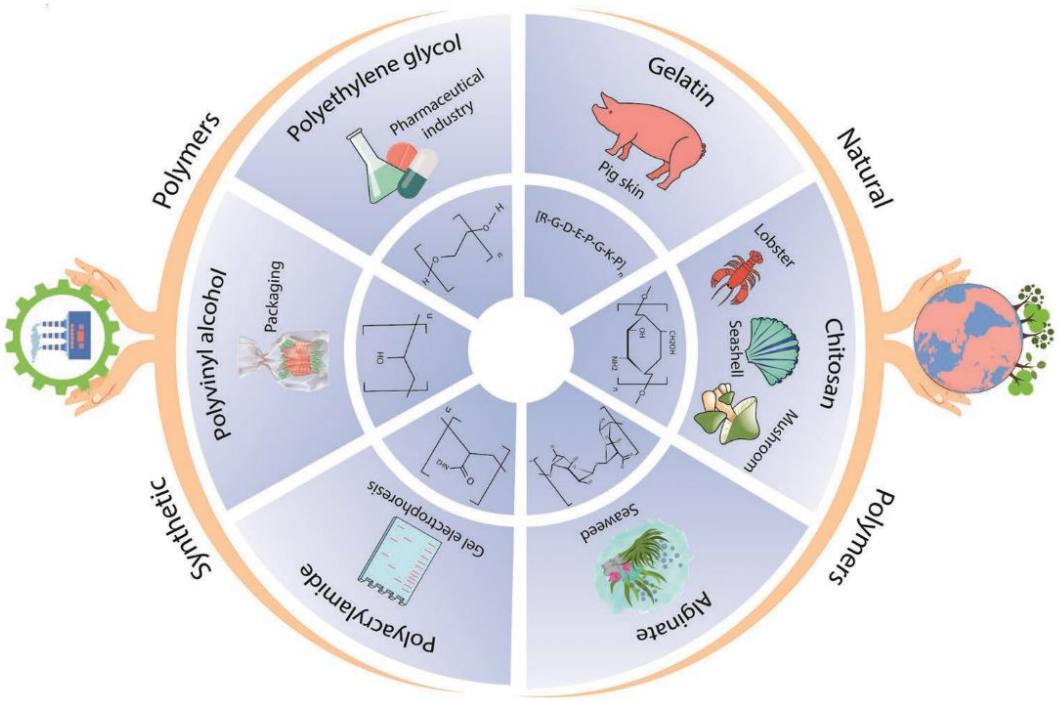

Figure 3.3.2 – Principal polymers for self-healing hydrogels, divided into oil-based (left) and bio-based (right)

interactions at the crack junction, while the covalent network gives to the hydrogel the desired mechanical performances. Moreover, self-healing hydrogel has been prepared by photocuring charged monomers that are able to reconnect hydrogel surfaces by electrostatic interaction between oppositely charged moieties included in the hydrogel. [431] Amongst other polymeric compounds, polysaccharides have recently found applications in this field due to their bioavailability and biocompatibility, together with their versatility and easy chemical functionalization (**Figure 3.3.2)**. [432–434] In particular, chitosan has been widely employed as biocompatible components of self-healing hydrogels, since it carries reactive amino groups able to form dynamic imine bonds when reacting with aldehydes. [435] In the recent literature, chitosan and some of its close derivatives such as carboxymethyl and carboxyethyl chitosan have been mostly employed to produce SHHs by reacting the free amino groups of chitosan in aqueous solutions with dialdehyde crosslinkers such as dialdehyde-functionalized PEGs, forming reversible imine crosslinking between the amino groups of chitosan and the functional PEGs and allowing the system for displaying self-healing properties. [436–439]

Only a few studies present SHHs in which chitosan has been crosslinked using other polysaccharides carrying aldehyde groups, which are generally obtained by periodate oxidation

of the native polysaccharide, leading to injectable hydrogels widely tested for biomedical applications.[440–442] Notwithstanding their interesting mechanical and healing properties, very few reported hydrogels have been employed for 3D printing and still, none of them is further employed as stimuli-responsive actuators. [443,444]

Aim of the research as Visiting Graduate Student at JHU

In this chapter, we will describe a new approach for the preparation of direct ink writing (DIW) 3D printable self-healing hydrogel based on photocurable chitosan derivative and periodate-oxidized polysaccharides. Firstly, a shear-thinning and 3D printable pre-gel will be prepared by mixing chemically modified biopolymers with small-molecule acrylate monomers; after 3D printing into the desired shape, the hydrogel is cured using UV light, to afford a tougher and thermoresponsive cured gel that shows reversible self-healing properties. The photopolymerized polyacrylate network will allow for the gel to display good mechanical properties while the weak and reversible interactions amongst the biopolymers and the acrylate monomers will give rise to the self-healing phenomenon. Acrylate monomers play an important role in contributing to the self-healing process: we selected oppositely charged monomers (potassium 3-sulfopropyl methacrylate (KSPMA) and methacrylate choline chloride (MCC)) to allow for the formation of ionic interactions between different regions of the cured hydrogel network, charge recombination phenomena happening amongst these two monomers at the interface of broken hydrogel pieces could assist the self-healing process making it faster and more effective. Parallelly, NIPAM has been selected as the main small molecule monomer due to the well-known thermoresponsive properties of its hydrogels. [445,446]

3.3.2 Chemical modification of polysaccharides

Synthesis of Chitosan 6-O-itaconate (CSI)

The chemical modification of the polysaccharides has been performed as schematically represented in **Figure 3.3.3**. The first reaction, which involves the partial functionalization of chitosan with itaconic acid, was performed as previously described for the preparation of chitosan succinate using succinic anhydride, but using itaconic anhydride instead, in a water/methanol mixture containing around 6% of acetic acid. After thorough purification, the outcome of the reaction was assessed by ^{1}H and ^{13}C-NMR (**Figure 3.3.4** and **Figure 3.3.5**), which revealed the effectiveness of the chemical modification and allowed for the quantification of the percentage of functionalized monomers in chitosan chains. We believed that the nucleophile able to efficiently attack the anhydride was indeed the primary alcohol group in position 6 rather than the amino group of chitosan: the acidity of the reaction environment ensured protonation of amino groups on chitosan and therefore their nucleophilicity was strongly compromised. Moreover, the primary alcohol in less basic and less hindered sterically. The esterification of chitosan in position 6 was fully confirmed by detailed NMR analysis which included ^{1}H, ^{13}C and ^{1}H-^{1}H COSY NMR analysis (**Figure 3.3.6**). By careful spectral peak assignment and integration, we firstly determined the degree of acetylation (DD) of non-functionalized chitosan is equal to 91.5%. Then, we determined the

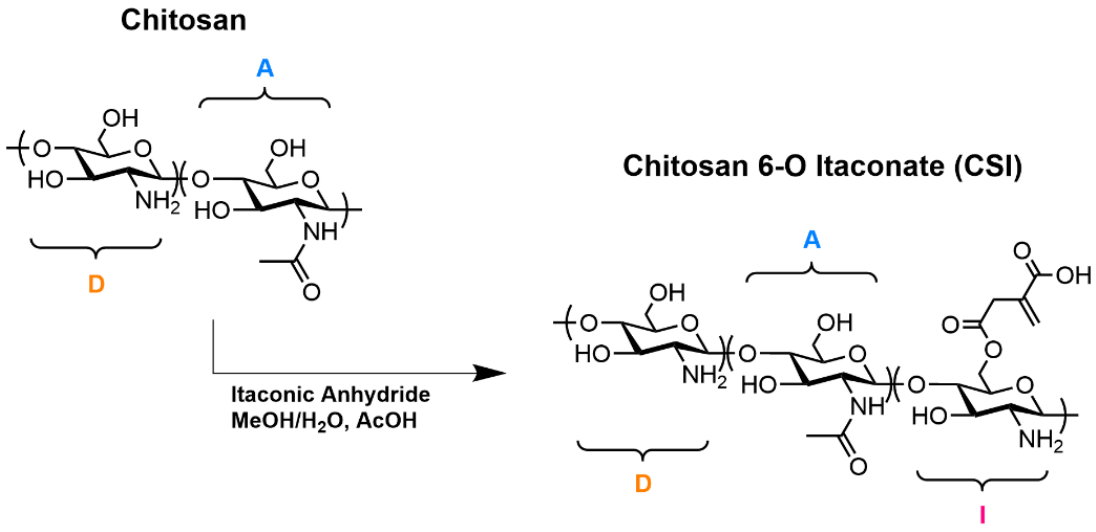

Figure 3.3.3 - Schematic representation of the partial modification of chitosan to chitosan 6-O itaconate. It is produced by reacting the OH group in position 6 of chitosan with itaconic anhydride in the presence of acetic acid. This lead to the formation of a polymer containing three different monomers: N-deacetylated D-glucosamine (D), N-acetylated D-glucosamine (A) and O-itaconate D-glucosamine (I).

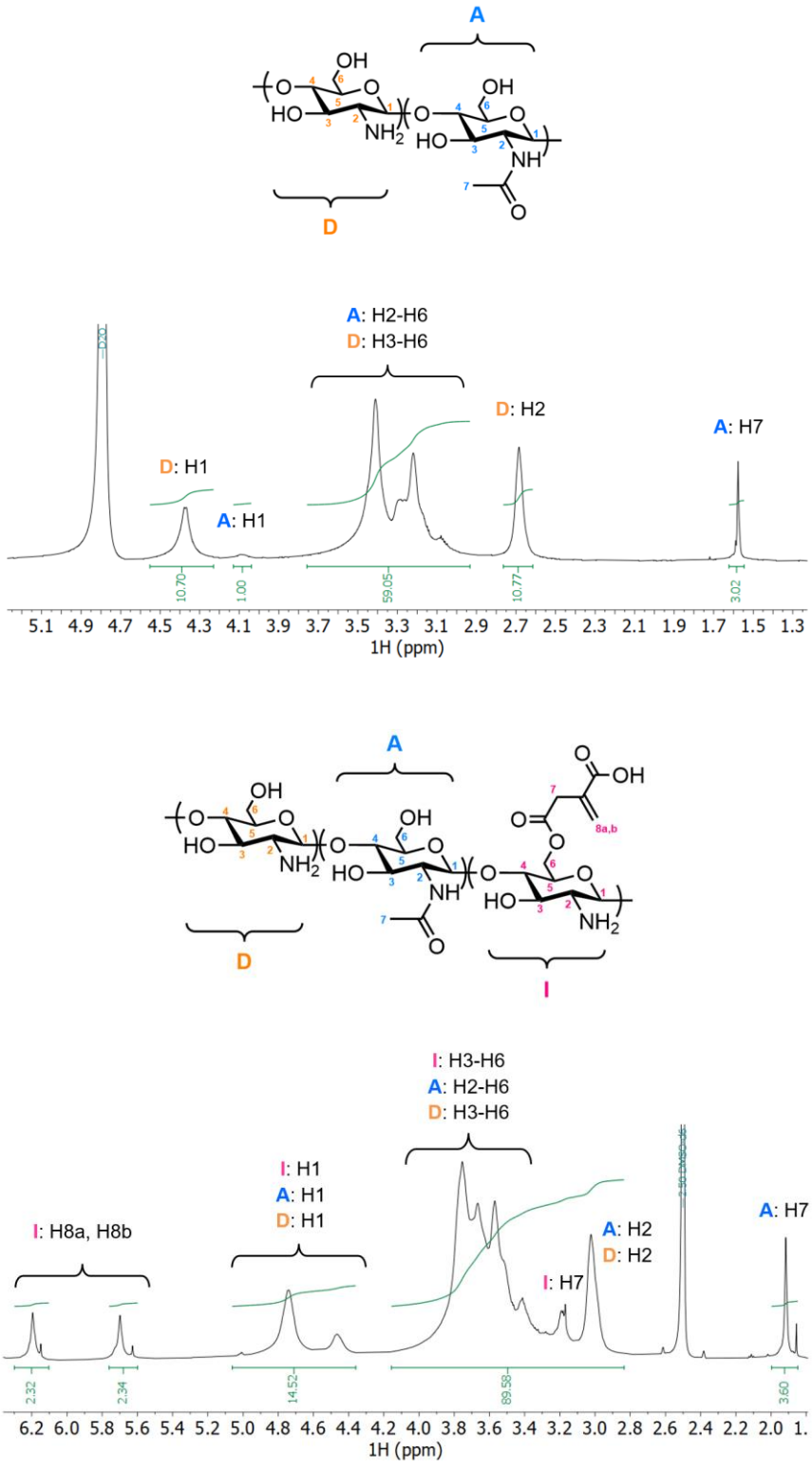

Figure 3.3.4 - 1D NMR analysis. Top: ^{1}H-NMR (600 MHz, TFA-*d* 1% in D_2O) of commercial chitosan powder and the corresponding peak assignments. The deacetylation degree (DD) was measured by integration to be equal to 91.5%. Bottom: ^{1}H-NMR (600 MHz, TFA-*d*/DMSO-d_6/D_2O 1:1:1) of chitosan itaconate (CSI) and peak assignments. Labile protons (-OH and -COOH, -CONHR and -NH_2) cannot be seen due to the presence of high concentration D^+ ions. By integration of the NMR spectrum, it is possible to calculate that 16.5% of chitosan monomers are efficiently functionalized with photocurable itaconic acid units.

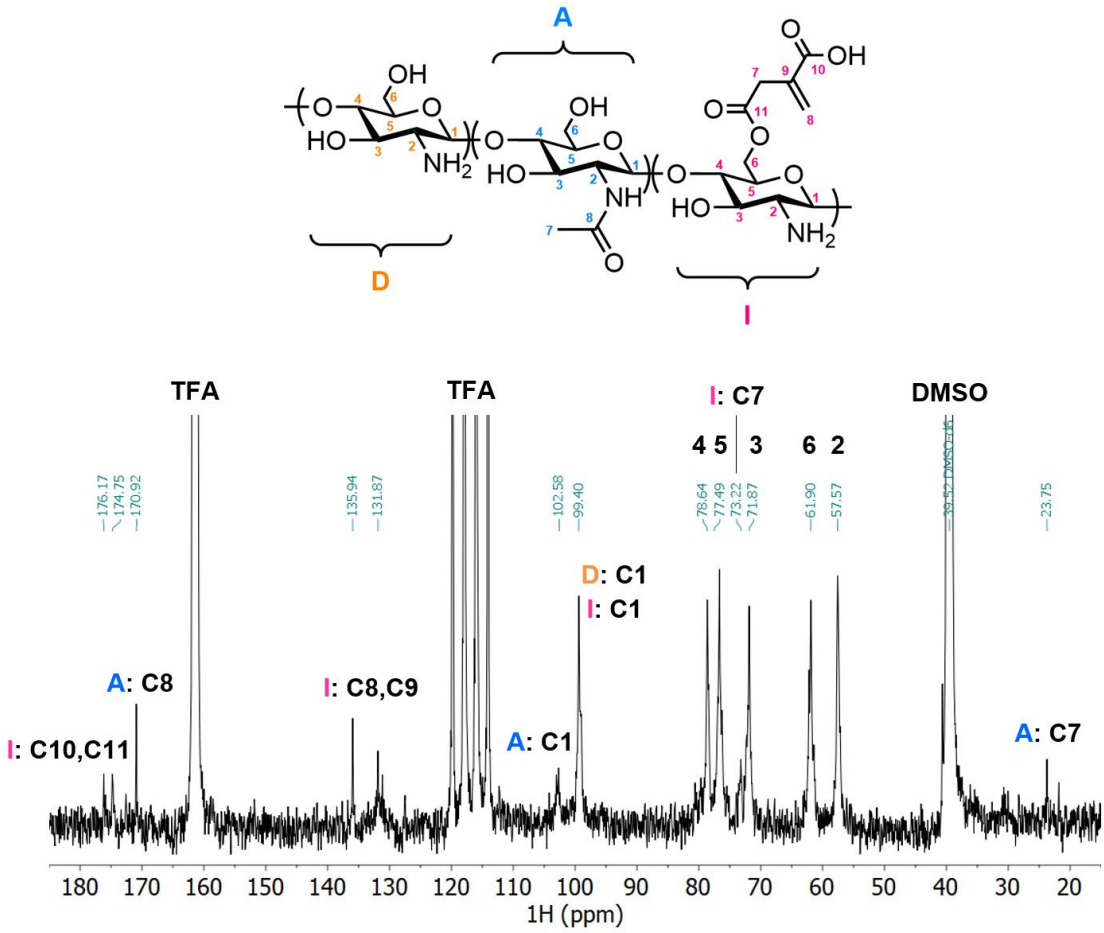

Figure 3.3.5 - ^{13}C-NMR (150 MHz, TFA-*d*/DMSO-d_6/D_2O 1:1:1) of chitosan itaconate (CSI) and full peak assignment.

number of monomers efficiently functionalized with itaconic acid on CSI as 16.5%, while still confirming that 8.5% of monomers were acetylated. ATR-FTIR analysis confirmed the efficient functionalization displaying two new distinct carbonyl bands at 1530 and 1630 cm^{-1} relatable to the ester and acid groups of CSI, respectively.

Methanol was observed to be required in the reaction mixture for the dissolution of itaconic anhydride, which is poorly soluble in acidic water. However, this leads to the preferential alcoholysis of itaconic anhydride from methanol, leading to monomethyl itaconate, as suggested by the quite low degree of functionalization. Despite this, the application for SHHs requires the availability of free amino groups that need to be able to efficiently form imine crosslinks and therefore the low substitution degree is preferred as it leads to a polymer with plenty of NH_2 groups and with pH-depending properties given by the coexistence of acidic and basic functional groups on the polymeric chain.

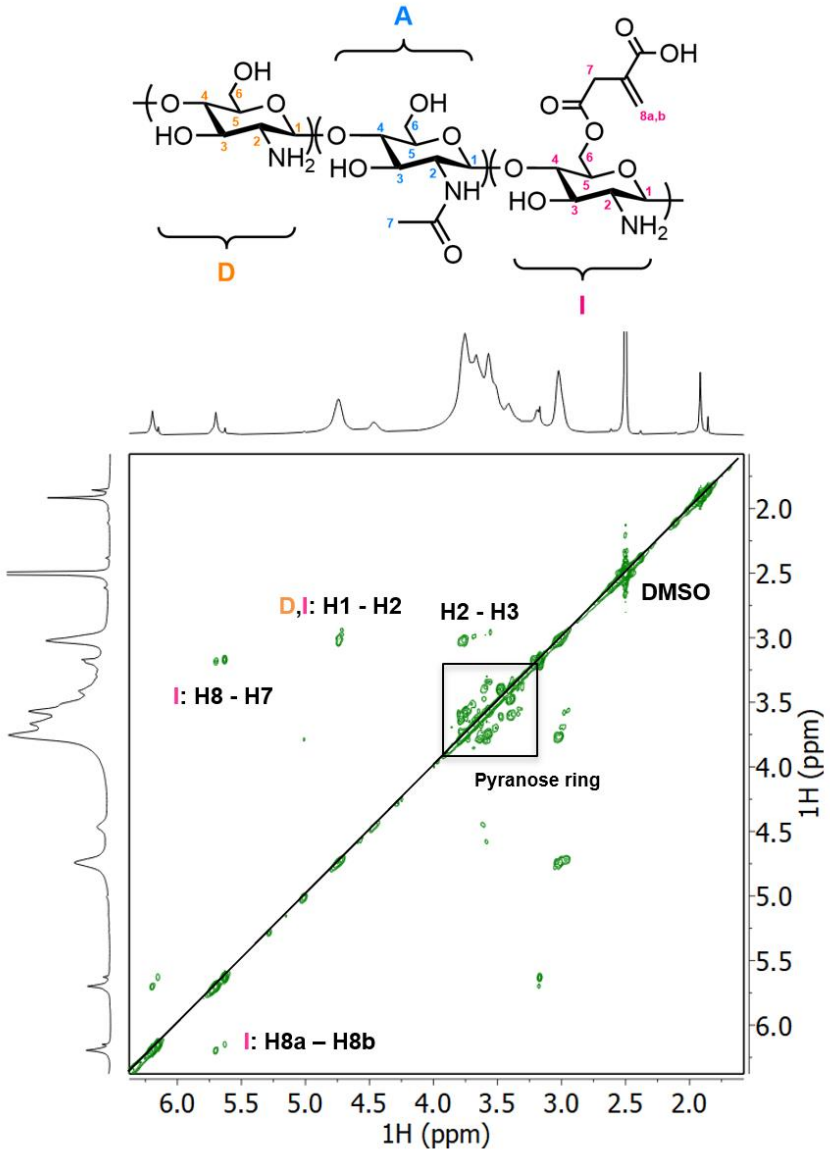

Figure 3.3.6 - ^{1}H-^{1}H COSY NMR (600 MHz, TFA-*d*/DMSO-d_6/D_2O 1:1:1) of chitosan itaconate (CSI).

Synthesis of polyaldehyde crosslinkers

In order to prepare carbohydrate-based dialdehyde crosslinkers responsible for the self-healing properties of the final hydrogel, we selected xanthan gum (XG) and hydroxypropyl cellulose (HPC) and we tested their oxidation with sodium periodate in water (**Figure 3.3.6**). The reaction of $NaIO_4$ with vicinal diols leads to the cleavage of the C-C bond amongst vicinal hydroxyl groups by oxidation of the two carbon atoms to aldehydes, [447] and it has been thoroughly studied on polysaccharides in the last decades to generate reactive groups on the

biopolymeric chain for attaching dyes, drugs, other functional molecules or for producing aldehyde-crosslinked hydrogels.[448–450] Xanthan gum, a polysaccharidic gum defined by a pentameric unit was selected thanks to its shear-thinning behaviour, which could demonstrate its efficacy in forming an SHH that could be efficiently extruded and 3D printed.[317] It displays four vicinal diols in each pentamer, suggesting promising crosslinking ability after oxidation. On the other hand, HPC was believed to be able to form sticky hydrogels, due to the extensive presence of hydroxy groups able of H- bonding. Its oxidation was expected to occur in much lower extent compared to XG due to the presence of much less oxidizable vicinal diols since the -OH groups on the pyranose ring are randomly substituted with hydroxypropyl moieties (**Figure 3.3.7**). However, the oxidation reactions were previously reported on fully substituted saccharides, even if with lower reaction rates.[449] Previous applications of dialdehyde oxidized HPC are limited to basic studies on its applications as cationic thiomer. [451]

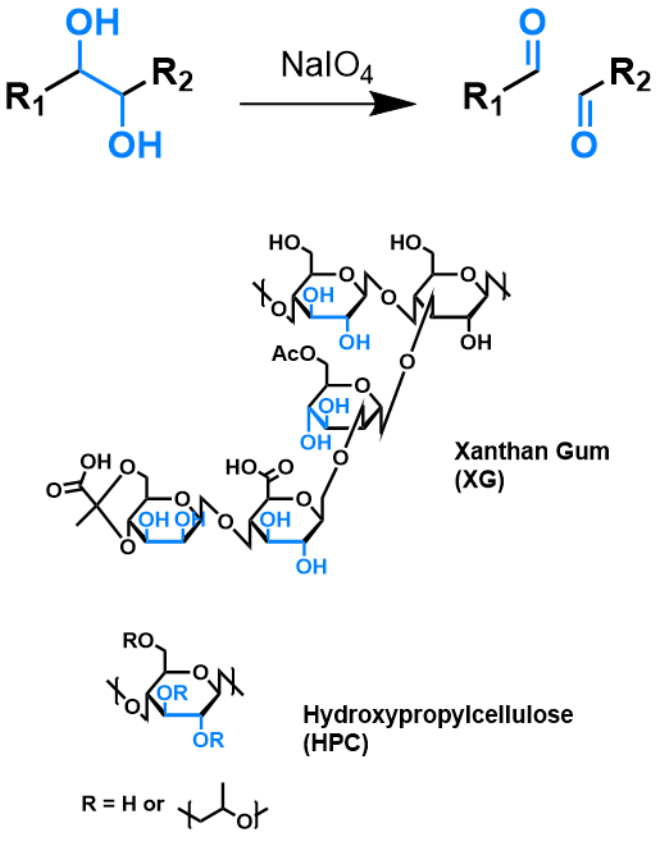

Figure 3.3.7 - Periodate oxidation of polysaccharides. Generic reaction scheme for the periodate oxidation of vicinal diols (top) and chemical structures of xanthan gum (XG) and hydroxypropyl cellulose (HPC). The oxidizable vicinal diol groups are highlighted in blue.

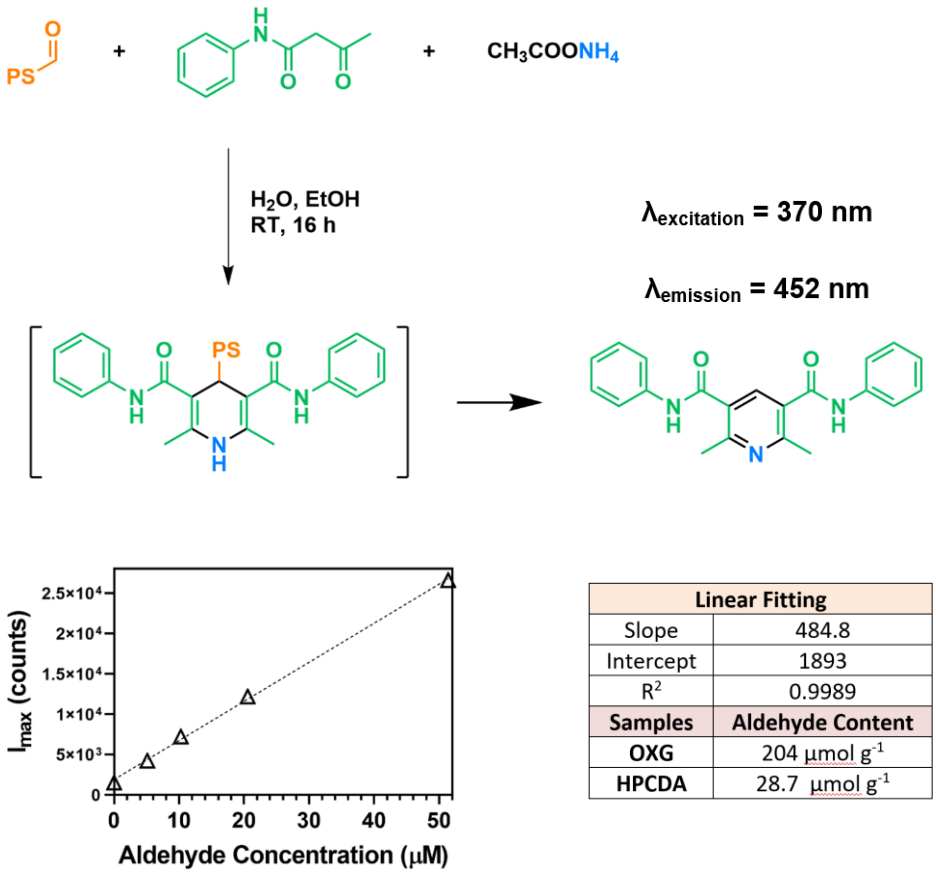

Linear Fitting	
Slope	484.8
Intercept	1893
R^2	0.9989
Samples	**Aldehyde Content**
OXG	204 μmol g^{-1}
HPCDA	28.7 μmol g^{-1}

Figure 3.3.8 – Aldehyde content assay. Top) Schematic representation of the reaction exploited to determine the aldehyde content of oxidized polysaccharides by fluorometric quantification of the formed Hantzsch amide. PS = polysaccharide. Bottom) Calibration curve and linear fitting of fluorescence intensity at the maximum of emission (452 nm) against concentration. Aldehyde content has been obtained by interpolation of the emission intensities at the maximum measured for adequately diluted solutions of OXG and HPCDA treated with the reactive mixture.

In order to quantitatively assess the outcome of the oxidation reactions, a fluorescence assay was optimized on the basis of a previously published analytical method.[452] The assay involved the reaction of the aldehyde-functionalized macromolecule with acetoacetanilide and ammonium acetate as reported in **Figure 3.3.8**. It exploits the quantitative reaction between most aldehydes, acetoacetanilide and ammonium acetate leading to the formation of a fluorescent pyridine 3,5-dicarboxamide derivative that can be efficiently quantified by measuring its emission intensity at its maximum (452 nm) by excitation with 370 nm light. A calibration curve was built using 4-chlorobenzaldehyde as a solid aldehyde standard and linearity between emission intensity and aldehyde was observed in the 5-50 μM range. Samples of OXG and HPCDA have been parallelly treated with the reactive mixture of acetoacetanilide

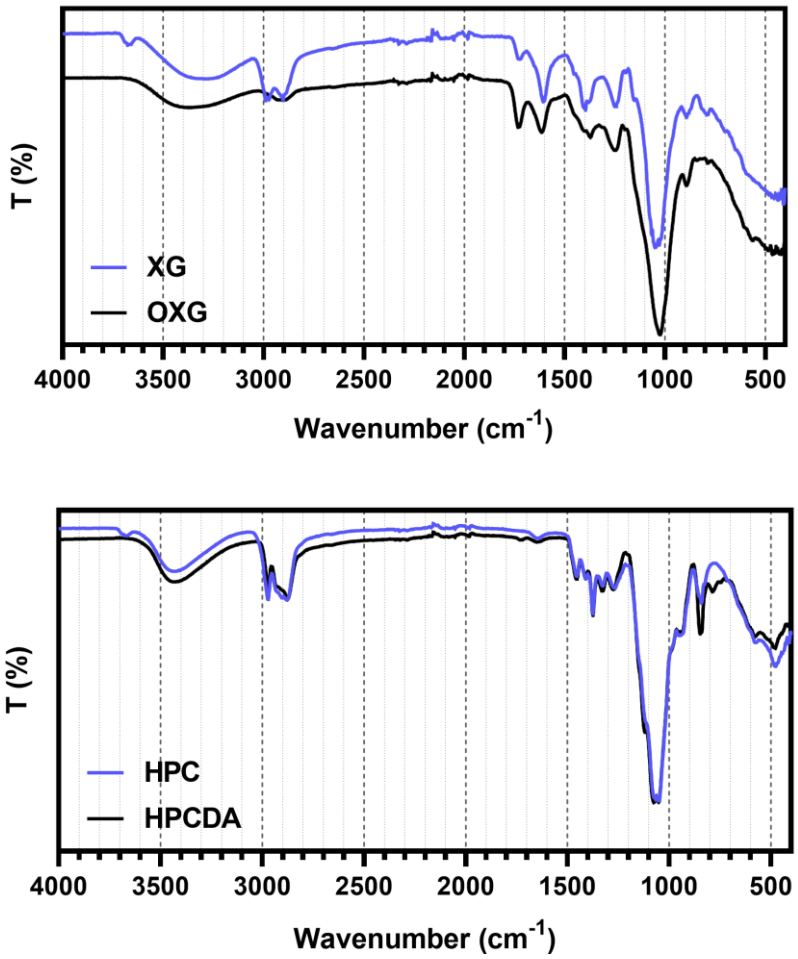

Figure 3.3.9. ATR-FTIR spectra of the periodate-oxidized polysaccharidic materials before (blue) and after (black) the chemical modification. XG = xanthan gum; OXG = oxidized xanthan gum; HPC = hydroxypropyl cellulose; HPCDA = hydroxypropylcellulose dialdehyde

and ammonium acetate and underwent fluorescence analysis. By interpolating the emission intensity at the maximum in the previously built calibration curve, the aldehyde content of the two oxidized products has been determined. The method allowed to estimate the aldehyde content of OXG and HPCDA ad 204 and 28.7 μmol of aldehyde groups per gram of polysaccharide, respectively, compared to unmodified XG and HPC which gave responses very close to the blank sample. ATR-FTIR spectroscopy was employed to confirm that the main polysaccharidic backbone was kept unmodified by the oxidation process for both OXG and HPCDA (**Figure 3.3.9**). Aldehyde groups in polysaccharides have demonstrated to be difficultly detected by IR spectroscopy due to the reversible formation of hemiacetal by the reaction of the aldehyde functionality with the abundant hydroxyl groups in the macromolecules. [453]

3.3.3 Formulation and 3D printing of the self-healing hydrogel

Once the modified polysaccharides were purified and dried, the self-healing pre-gel was prepared by mixing a 5% CSI solution in HCl 1 mM with an aqueous solution containing N-isopropyl acrylamide (NIPAM), potassium 3-sulfopropyl methacrylate (KSPMA), methacrylate choline chloride (MCC) and the oxidized polysaccharides, OXG and HPCDA, together with Irgacure 2959, the photopolymerization initiator. The optimal composition was found by trial and error (and reported in **Figure 3.3.10**) by adjusting the composition to achieve a pre-gel that could be easily extruded through the nozzle employed for the 3D printing process (**Figure 3.3.11**). With the final optimal composition, the mixture gelified overnight leading to a sticky and extrudable self-healing hydrogel.

Unlike chitosan, CSI was soluble at neutral pH, forming a thick hydrogel due to the partial zwitterionic properties of its polymeric backbone. When dissolved at neutral pH, it showed limited but noticeable self-healing properties due to charge recombination at the reconnected interfaces but no printability whatsoever. Its dissolution in HCl at pH 3 ensures protonation of both amino and carboxyl groups of CSI, leading to a softer and solution. Its mixing with other components leads to a slightly acidic pH of the SHH of about 5. The physical-chemical interactions that play a role in the formation of the extrudable SHH are mainly H-bonding and Schiff's base formation by the interaction of the functional groups in the polysaccharides. At this stage, the acrylate and methacrylate monomers play a limited role in the self-healing properties of the hydrogel.

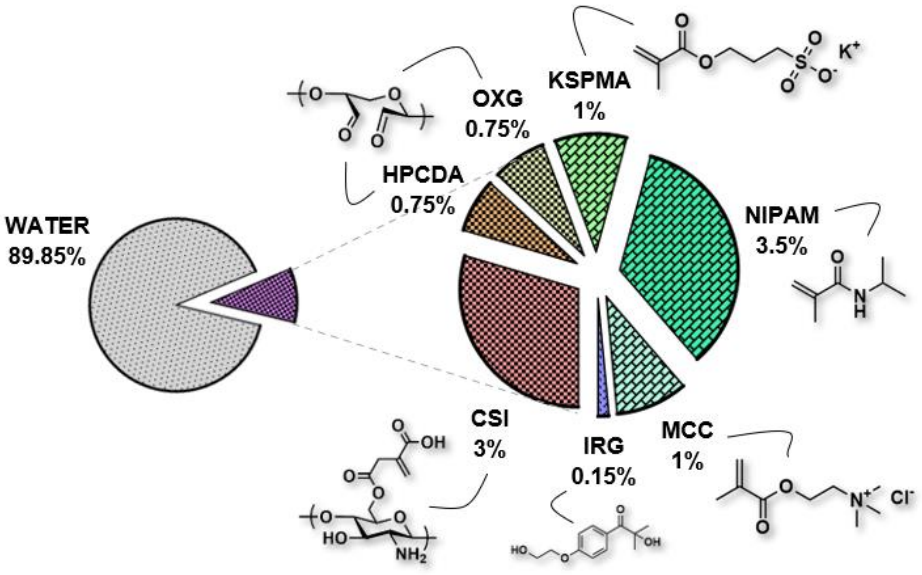

Figure 3.3.10 - Left: composition of the pre-gel formulated for DIW 3D printing.

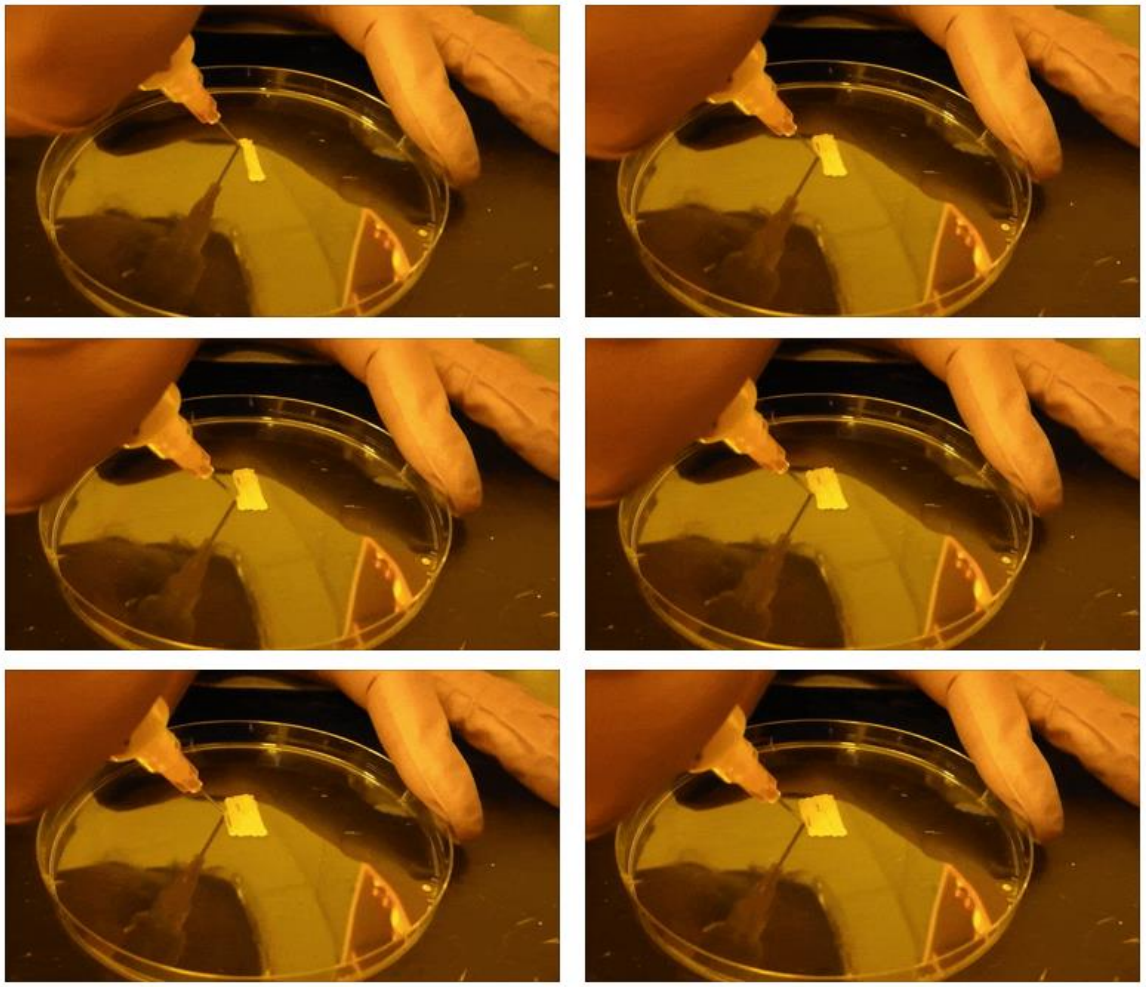

Figure 3.3.11 - Optical camera pictures of the hand extrusion of the self-healing hydrogel from a 20 G nozzle proving good extrudability with low extrusion pressures.

The ink was then loaded into a syringe and piped into UV shielded cartridges. It was centrifuged at 1500 rpm for 2 minutes to remove air bubbles. The inks were then aged for a week to allow for the dynamic bonds to form and for the ink to attain the desired shear thinning and mechanical properties. For direct ink writing, we used the Cellink Inkredible + bioprinter. We loaded the cartridges on the printer and extruded the ink through a 20 G (0.6 mm inner diameter) to ensure a smooth clog-free print. We produced STL (Standard Tessellation Language) files for our structures using Solidworks (Dassault Systèmes) and sliced the files using Slic3r software to generate g-code files (Layer height-0.6mm; Infill pattern-rectilinear; Infill percentage- 60%; Printing speed- 5mm/s). All our structures were printed on glass slides with chemical resistant PTFE strips (McMaster Carr) to allow easy removal. The extrusion pressure for a continuous filament if our ink was around 150 KPa. Optical camera pictures of the printing process are reported in **Figure 3.3.12**.

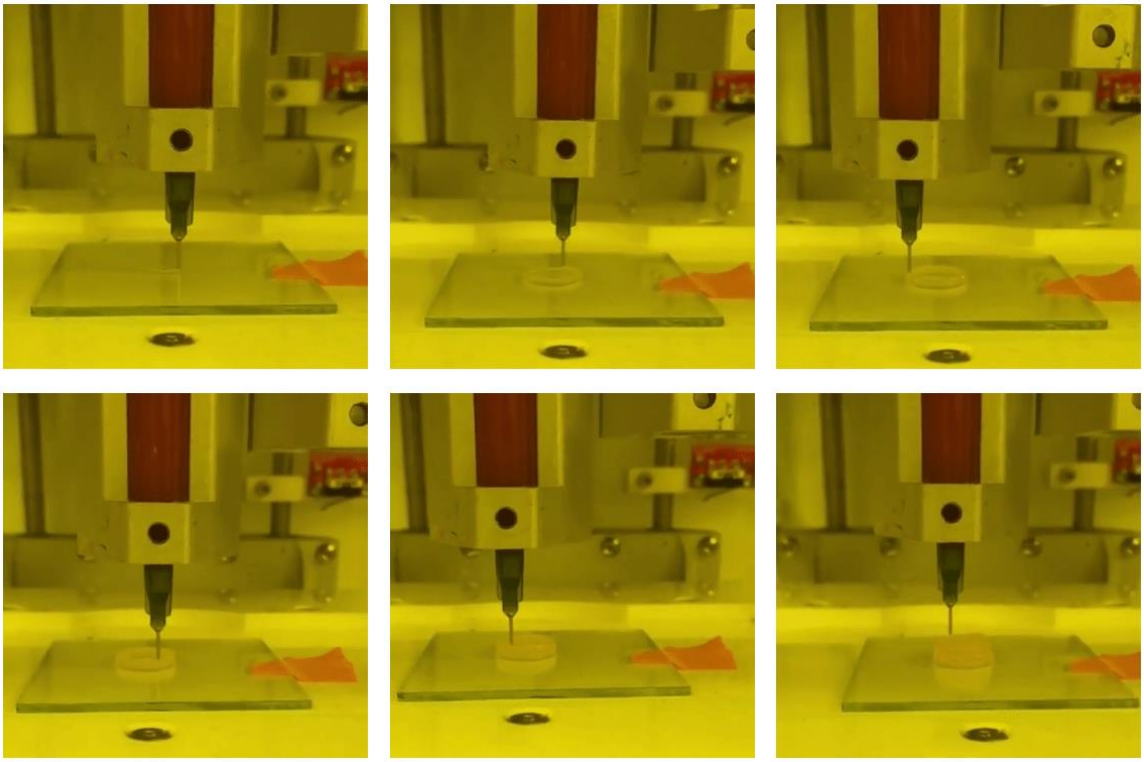

Figure 3.3.12 – Optical camera pictures of the 3D printer extruder head during the 3D printing of the self-healing hydrogel into a cylinder.

The pre-gel was studied through ATR-FTIR spectroscopy. The first was used to confirm the formation of imines, as it displayed multiple peaks in the region between 1640 and 1690 cm^{-1}, the region where C=N bond stretching gives rise to a peak (**Figure 3.3.13**).

Visible light curing of extruded gels

After printing, the hydrogel structures were cured using two OmniCure UV sources (LX 500, Lumen Dynamics) at 80% power. The two UV light-emitting diodes (LED) heads fitted with 12mm lens, emitted UV light at a wavelength of 365nm and a resultant intensity of 0.32 W/cm^2. The structures were kept on a stage rotating at 9.8 RPM to allow uniform curing for the time of 120 seconds with both the probes pointed towards the sides of the structure, 3 cm away from it. A cooling fan was also used to prevent the overheating of the UV curing probes. After this, the structure was slowly removed from the PTFE slides using a slight amount of water and used for actuation studies.

The ATR-FTIR spectrum of a freeze-dried sample of the cured hydrogel revealed no noticeable differences with the spectrum of the pre-gel (**Figure 3.3.13**). This is expected due to the low intensity of the C=C stretching resonance peak, which is the functionality that is

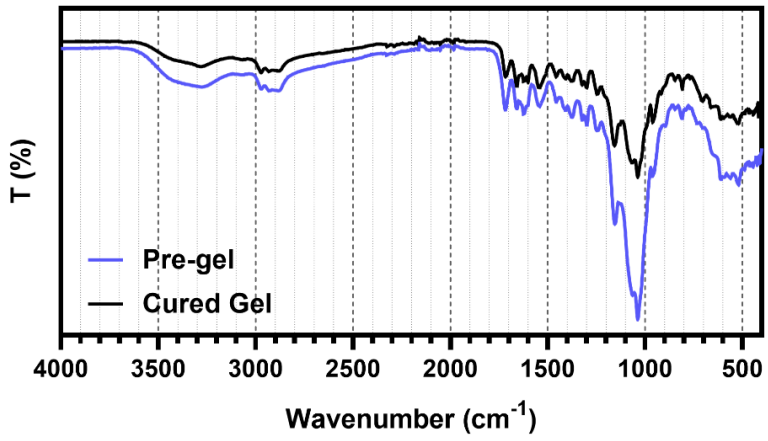

Figure 3.3.13 - ATR-FTIR spectra of the self-healing hydrogel before (blue) and after (black) the UV curing process.

consumed during the polymerization. However, the analysis confirmed that the structure of the hydrogel was mostly unchanged.

To summarily evaluate the microporosity of the gel and the influence that photocuring had on this parameter, SEM analysis was performed on samples of the cured gel and of the pre-gel and images have been compared **(Figure 3.3.14** and **Figure 3.3.15**). Electron microscopy revealed that the pre-gel was characterized by high porosity, with average pore size around 40 µm. After photocuring, the hydrogel porosity almost completely disappears due to the formation of a packed polyacrylate network that closes the pores.

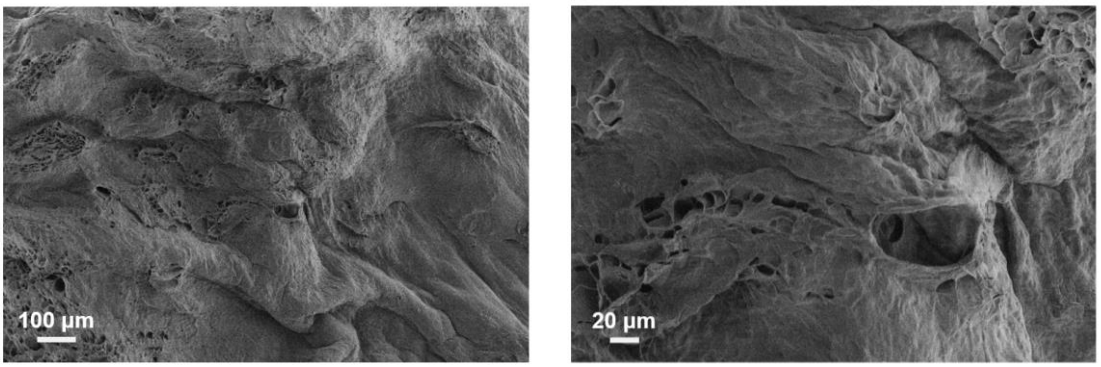

Figure 3.3.14 - SEM image of a freeze-dried sample of the cured gel.

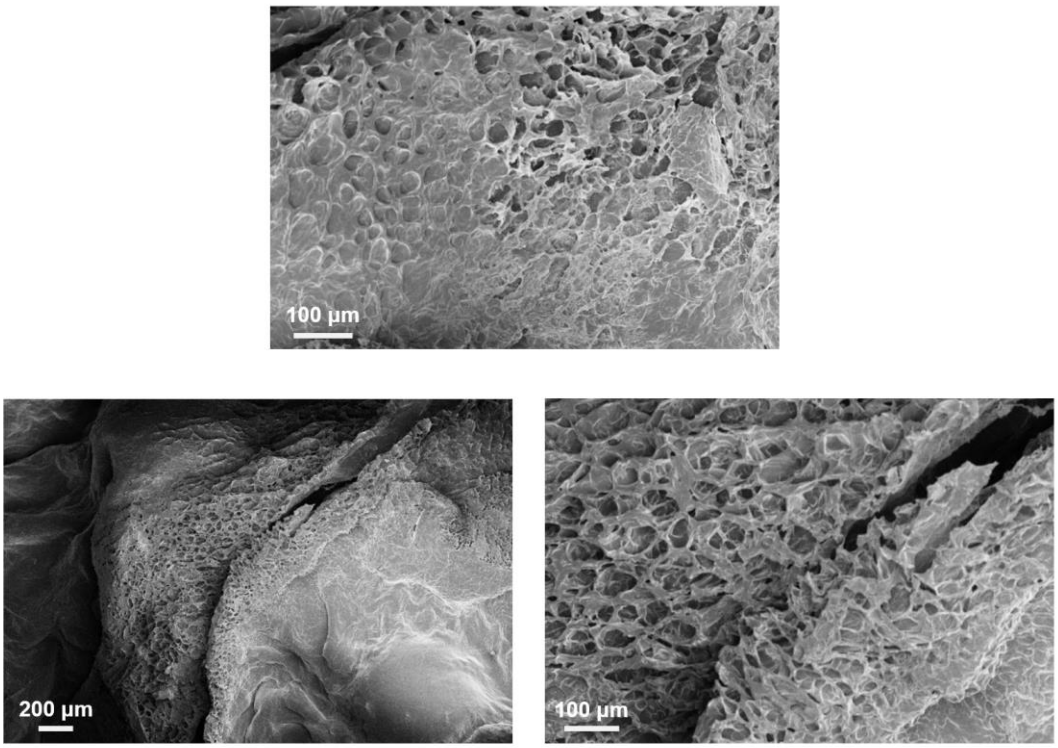

Figure 3.3.15 - SEM images of a freeze-dried sample of the pre-gel.

3.3.4 Future perspectives

The project is still ongoing in collaboration and to the present day, we assessed self-healing and thermoresponsiveness properties of the prepared hydrogels independently. However, we are planning to perform an experiment that combines the two properties of the printed and cured hydrogel that will allow showing, in a single cyclic experiment, the possibility of exploiting the described hydrogel for tissue engineering and soft robotics applications (**Figure 3.3.16**). What we observed is that the hydrogel was able to self-heal when 3D printed and cured, but after being placed in water the hydrogel was able of swelling and the self-healed interfaces were detaching. However, we exploited the temperature-dependent swelling properties of poly(NIPAM) hydrogels to de-swell the unhealed structures by heating them above 40°C in water; the de-swelled structures are now able to self-heal again due to the compression of the polymeric network and the cycle is repeated. To prove this, the following experiment was planned:

- **SELF HEALING**

  In the first phase, two separate rectangular structures are 3D printed, UV cured and placed in contact to assess the self-healing properties. The healed system is then placed in water at room temperature: this causes the poly(NIPAM) network to absorb water leading to the swelling of the polymeric network.

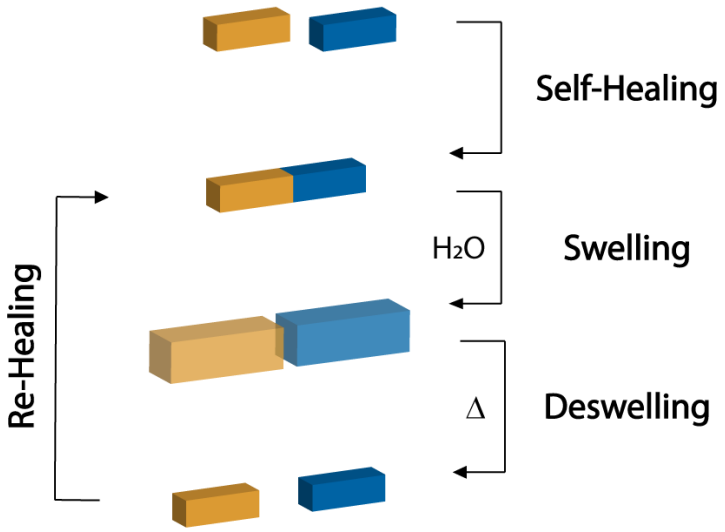

Figure 3.3.16 – Schematic macroscopic representation of the proposed mechanism for the reversible self-healing process.

- **SWELLING**

  The expansion of the covalent network in the hydrogel pulls apart the functional groups that are responsible for the self-healing properties, therefore the healed interfaces separate, and the self-healing properties are lost (**Figure 3.3.17**).

- **DESWELLING**

  Then, by placing the hydrogels in water at 40°C, the poly(NIPAM) network shrinks back to its original density, restoring the self-healing properties of the material.

- **RE-HEALING**

  The two rectangular pieces are now able to self-heal again and to repeat the cycle.

As a final characterization, the rheological behaviour of the pre-gel will be assessed, and the printed and cured structures will undergo traction tests to assess its mechanical properties. Future experiments for tissue engineering applications are also forecasted.

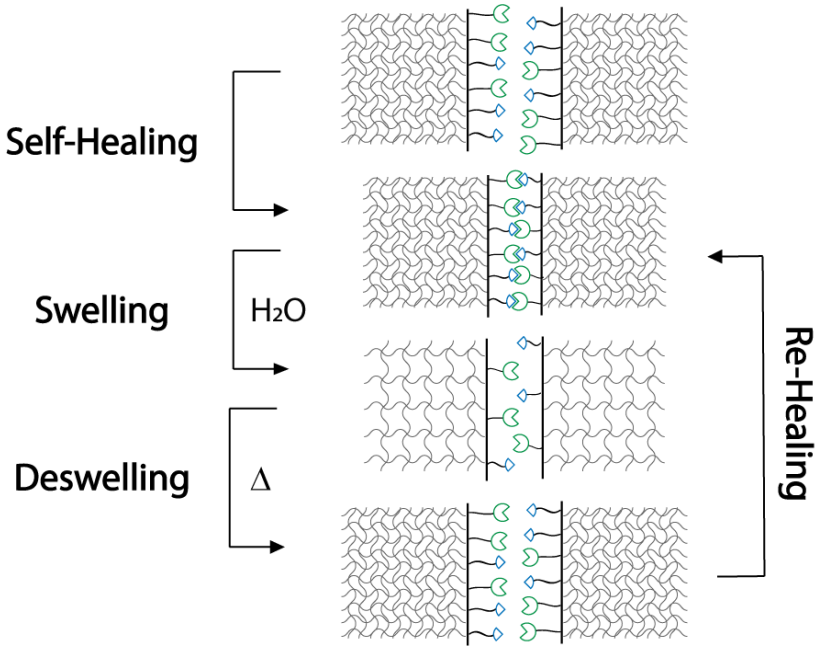

Figure 3.3.17 - Schematic microscopic representation of the proposed mechanism for the reversible self-healing process.

CONCLUSIONS

To summarize, this dissertation provided valuable examples of the implementation of organic-inorganic hybrid approached to materials science and technology such as theranostics, organic electronics and additive manufacturing. The multidisciplinary combination of different fields of chemistry and science, in general, allow for the study of the possible applications of such advanced hybrid structure, and it is essential for approaching the state-of-the-art in applied chemistry and physics. The properties of gold nanostructures in nanomedicine have been described in detail since they represent one of the most promising applications of nanotechnology that are hopefully going to approach soon the clinical phases. Then, we demonstrated how piezoelectric and conductive inorganic nanostructures can be manipulated by coating them with natural or synthetic organic ligands in order to manufacture polymeric nanocomposite with sensing properties towards mechanical or electrical stimuli. Finally, an inorganic material such as phosphorescent transition metal complexes can be implemented in biobased photocurable resins to produce functional 3D printed object loadings of heavy metals limited to less than 0.01%, with potential application for 3D printed textile due to the promising mechanical performances.

ACKNOWLEDGEMENTS

First of all I would like to thank my supervisor, Prof. Mauro Comes Franchini for having given me the chance to follow my ideas and to pursue my interests. I would also like to thank the rest of the research group (Prof. Letizia Sambri, Dr. Erica Locatelli and Dr. Silvia Tortorella, PhDs and students) for the precious daily contribution to my personal scientific experience, which was indeed fundamental for the work discussed in this dissertation.
Besides, a particular thank goes to all collaborators and co-workers outside the University of Bologna, with which I had the chance to improve my multidisciplinarity and to learn how to see my research thing under different perspectives.
In particular, I would like to thank:
- Dr. Massimo Alfano and Dr. Flavio Curnis, Ospedale San Raffaele (Milan, Italy)
- Prof. Irit Sagi, Weizmann Institute of Science (Rehovot, Israel)
- Prof. Robert C. Martin, University of Louisville (Louisville, USA)
- Prof. Luca Menichetti e Paolo Armanetti, Consiglio Nazionale delle Ricerche (Pisa, Italy)
- Prof. Paolo Milani, Dr. Tommaso Santaniello, Sara Moon Villa, Università degli Studi di Milano (Milan, Italy)
- Prof. Annalisa Bonfiglio, Università di Cagliari (Cagliari, Italy)
- Prof. David H. Gracias, Johns Hopkins University (Baltimore, USA)

REFERENCES

1. Funkhouser, J. Reinventing pharma: the theranostic revolution. *Curr Drug Discov* **2002**, *2*, 17–19.
2. Bardhan, R.; Lal, S.; Joshi, A.; Halas, N.J. Theranostic nanoshells: From probe design to imaging and treatment of cancer. *Acc. Chem. Res.* **2011**, *44*, 936–946, doi:10.1021/ar200023x.
3. Cole, A.J.; Yang, V.C.; David, A.E. Cancer theranostics: The rise of targeted magnetic nanoparticles. *Trends Biotechnol.* **2011**, *29*, 323–332, doi:10.1016/j.tibtech.2011.03.001.
4. Huang, H.; Lovell, J.F. Advanced Functional Nanomaterials for Theranostics. *Adv. Funct. Mater.* **2017**, *27*, 1603524, doi:10.1002/adfm.201603524.
5. Kelkar, S.S.; Reineke, T.M. Theranostics: Combining imaging and therapy. *Bioconjug. Chem.* **2011**, *22*, 1879–1903, doi:10.1021/bc200151q.
6. Lim, E.-K.; Kim, T.; Paik, S.; Haam, S.; Huh, Y.-M.; Lee, K. Nanomaterials for Theranostics: Recent Advances and Future Challenges. *Chem. Rev.* **2015**, *115*, 327–394, doi:10.1021/cr300213b.
7. Ferrari, M. Cancer nanotechnology: opportunities and challenges. *Nat. Rev. Cancer* **2005**, *5*, 161–171, doi:10.1038/nrc1566.
8. Kaplan, E.; Prashanth, A.K.; Brennan, C.; Sirovich, L. Optical Imaging: A Review. *Opt. Photonics News* **2000**, *11*, 26, doi:10.1364/OPN.11.7.000026.
9. Na, H. Bin; Song, I.C.; Hyeon, T. Inorganic Nanoparticles for MRI Contrast Agents. *Adv. Mater.* **2009**, *21*, 2133–2148, doi:10.1002/adma.200802366.
10. Jun, Y.W.; Lee, J.H.; Cheon, J. Chemical design of nanoparticle probes for high-performance magnetic resonance imaging. *Angew. Chemie - Int. Ed.* **2008**, *47*, 5122–5135, doi:10.1002/anie.200701674.
11. Gargiulo, S.; Albanese, S.; Mancini, M. State-of-the-Art Preclinical Photoacoustic Imaging in Oncology: Recent Advances in Cancer Theranostics. *Contrast Media Mol. Imaging* **2019**, *2019*, 1–24, doi:10.1155/2019/5080267.
12. Maturi, M.; Locatelli, E.; Monaco, I.; Comes Franchini, M. Current concepts in nanostructured contrast media development for: In vivo photoacoustic imaging. *Biomater. Sci.* **2019**, *7*, 1746–1775, doi:10.1039/c8bm01444b.
13. Deng, H.; Zhong, Y.; Du, M.; Liu, Q.; Fan, Z.; Dai, F.; Zhang, X. Theranostic Self-Assembly Structure of Gold Nanoparticles for NIR Photothermal Therapy and X-Ray Computed Tomography Imaging. *Theranostics* **2014**, *4*, 904–918, doi:10.7150/thno.9448.
14. Curry, T.; Kopelman, R.; Shilo, M.; Popovtzer, R. Multifunctional theranostic gold nanoparticles for targeted CT imaging and photothermal therapy. *Contrast Media Mol. Imaging* **2014**, *9*, 53–61, doi:10.1002/cmmi.1563.

15. Monaco, I.; Armanetti, P.; Locatelli, E.; Flori, A.; Maturi, M.; Del Turco, S.; Menichetti, L.; Comes Franchini, M. Smart assembly of Mn-ferrites/silica core-shell with fluorescein and gold nanorods: Robust and stable nanomicelles for in vivo triple modality imaging. *J. Mater. Chem. B* **2018**, *6*, 2993–2999, doi:10.1039/c8tb00453f.

16. Marsh, S.; Liu, G. Pharmacokinetics and pharmacogenomics in breast cancer chemotherapy. *Adv. Drug Deliv. Rev.* **2009**, *61*, 381–387, doi:10.1016/j.addr.2008.10.003.

17. Kinoshita, M.; Watanabe, N. Small molecule inhibitor of mitotic spindle bipolarity identified in a phenotype-based screen. *Tanpakushitsu Kakusan Koso.* **2007**, *52*, 1796–1799.

18. Garnett, M.C. Targeted drug conjugates: Principles and progress. *Adv. Drug Deliv. Rev.* **2001**, *53*, 171–216, doi:10.1016/S0169-409X(01)00227-7.

19. Shewach, D.S.; Kuchta, R.D. Introduction to Cancer Chemotherapeutics. *Chem. Rev.* **2009**, *109*, 2859–2861, doi:10.1021/cr900208x.

20. Ayyar, B.V.; Arora, S.; O'Kennedy, R. Coming-of-Age of Antibodies in Cancer Therapeutics. *Trends Pharmacol. Sci.* **2016**, *37*, 1009–1028, doi:10.1016/j.tips.2016.09.005.

21. Zhou, Z.; Liu, X.; Zhu, D.; Wang, Y.; Zhang, Z.; Zhou, X.; Qiu, N.; Chen, X.; Shen, Y. Nonviral cancer gene therapy: Delivery cascade and vector nanoproperty integration. *Adv. Drug Deliv. Rev.* **2017**, *115*, 115–154, doi:10.1016/j.addr.2017.07.021.

22. Lellouche, E.; Locatelli, E.; Israel, L.L.; Naddaka, M.; Kurlander, E.; Michaeli, S.; Lellouche, J.-P.; Franchini, M.C. Maghemite-containing PLGA–PEG-based polymeric nanoparticles for siRNA delivery: toxicity and silencing evaluation. *RSC Adv.* **2017**, *7*, 26912–26920, doi:10.1039/C7RA00517B.

23. Mellal, I.; Oukaira, A.; Kengene, E.; Lakhssassi, A. Thermal Therapy Modalities for Cancer Treatment: A Review and Future Perspectives. *Int. J. Appl. Sci. - Res. Rev.* **2017**, *04*, doi:10.21767/2394-9988.100064.

24. Noh, S. hyun; Moon, S.H.; Shin, T.H.; Lim, Y.; Cheon, J. Recent advances of magneto-thermal capabilities of nanoparticles: From design principles to biomedical applications. *Nano Today* **2017**, *13*, 61–76, doi:10.1016/j.nantod.2017.02.006.

25. Nikazar, S.; Barani, M.; Rahdar, A.; Zoghi, M.; Kyzas, G.Z. Photo- and Magnetothermally Responsive Nanomaterials for Therapy, Controlled Drug Delivery and Imaging Applications. *ChemistrySelect* **2020**, *5*, 12590–12609, doi:10.1002/slct.202002978.

26. Zhi, D.; Yang, T.; O'Hagan, J.; Zhang, S.; Donnelly, R.F. Photothermal therapy. *J. Control. Release* **2020**, *325*, 52–71, doi:10.1016/j.jconrel.2020.06.032.

27. Rosenholm, J.M.; Meinander, A.; Peuhu, E.; Niemi, R.; Eriksson, J.E.; Sahlgren, C.; Lindén, M. Targeting of porous hybrid silica nanoparticles to cancer cells. *ACS Nano* **2009**, *3*, 197–206, doi:10.1021/nn800781r.

28. Senarath-Yapa, M.D.; Phimphivong, S.; Coym, J.W.; Wirth, M.J.; Aspinwall, C.A.; Saavedra, S.S. Preparation and characterization of poly(lipid)-coated, fluorophore-doped silica nanoparticles for biolabeling and cellular imaging. *Langmuir* **2007**, *23*, 12624–12633, doi:10.1021/la701917w.

29. Wu, G.; Mikhailovsky, A.; Khant, H.A.; Fu, C.; Chiu, W.; Zasadzinski, J.A. Remotely triggered liposome release by near-infrared light absorption via hollow gold nanoshells. *J. Am. Chem. Soc.* **2008**, *130*, 8175–8177, doi:10.1021/ja802656d.

30. Chandra, M.; Dowgiallo, A.M.; Knappenberger, K.L. Controlled plasmon resonance properties of hollow gold nanosphere aggregates. *J. Am. Chem. Soc.* **2010**, *132*, 15782–15789, doi:10.1021/ja106910x.

31. Lu, W.; Huang, Q.; Ku, G.; Wen, X.; Zhou, M.; Guzatov, D.; Brecht, P.; Su, R.; Oraevsky, A.; Wang, L. V.; et al. Photoacoustic imaging of living mouse brain vasculature using hollow gold nanospheres. *Biomaterials* **2010**, *31*, 2617–2626, doi:10.1016/j.biomaterials.2009.12.007.

32. Locatelli, E.; Comes Franchini, M. Biodegradable PLGA-b-PEG polymeric nanoparticles: synthesis, properties, and nanomedical applications as drug delivery system. *J. Nanoparticle Res.* **2012**, *14*, 1316, doi:10.1007/s11051-012-1316-4.

33. Locatelli, E.; Li, Y.; Monaco, I.; Guo, W.; Maturi, M.; Menichetti, L.; Armanetti, P.; Martin, R.; Comes Franchini, M. A novel theranostic gold nanorods- and Adriamycin-loaded micelle for EpCAM targeting, laser ablation, and photoacoustic imaging of cancer stem cells in hepatocellular carcinoma. *Int. J. Nanomedicine* **2019**, *Volume 14*, 1877–1892, doi:10.2147/IJN.S197265.

34. Bazak, R.; Houri, M.; El Achy, S.; Kamel, S.; Refaat, T. Cancer active targeting by nanoparticles: a comprehensive review of literature. *J. Cancer Res. Clin. Oncol.* **2015**, *141*, 769–784, doi:10.1007/s00432-

014-1767-3.

35. Maeda, H.; Wu, J.; Sawa, T.; Matsumura, Y.; Hori, K. Tumor vascular permeability and the EPR effect in macromolecular therapeutics: A review. *J. Control. Release* **2000**, *65*, 271–284, doi:10.1016/S0168-3659(99)00248-5.

36. Torchilin, V. Tumor delivery of macromolecular drugs based on the EPR effect. *Adv. Drug Deliv. Rev.* **2011**, *63*, 131–135, doi:10.1016/j.addr.2010.03.011.

37. Lim, E.K.; Kim, H.O.; Jang, E.; Park, J.; Lee, K.; Suh, J.S.; Huh, Y.M.; Haam, S. Hyaluronan-modified magnetic nanoclusters for detection of CD44-overexpressing breast cancer by MR imaging. *Biomaterials* **2011**, *32*, 7941–7950, doi:10.1016/j.biomaterials.2011.06.077.

38. Hyung, W.; Ko, H.; Park, J.; Lim, E.; Park, S.B.; Park, Y.-J.; Yoon, H.G.; Suh, J.S.; Haam, S.; Huh, Y.-M. Novel hyaluronic acid (HA) coated drug carriers (HCDCs) for human breast cancer treatment. *Biotechnol. Bioeng.* **2008**, *99*, 442–454, doi:10.1002/bit.21578.

39. Bell, A.G. On the production and reproduction of sound by light. *J. Soc. Telegr. Eng.* **1880**, *9*, 404–426, doi:10.1049/jste-1.1880.0046.

40. Bell, A.G. About the Production of Sound by Radiant Energy. *Proc. Am. Assoc. Adv. Sci.* **1881**, *XX*.

41. Tyndall, J. Action of an Intermittent Beam of Radiant Heat upon Gaseous Matter. *Proc. R. Soc. London* **1881**, *31*, 307–317.

42. Rontgen, W.C. Ueber Töne, welche durch intermittirende Bestrahlung eines Gases entstehen. *Ann. Phys.* **1881**, *248*, 155–159.

43. Marìn, E. Thermal wave physics: principles and applications to the characterization of liquids. *Rev. Ciencias Exatas e Nat.* **2004**, *6*, 146–169.

44. Rosencwaig, A. Theory of the photoacoustic effect with solids. *J. Acoust. Soc. Am.* **1975**, *58*, S52, doi:10.1121/1.2002181.

45. Xu, M.; Wang, L. V. Photoacoustic imaging in biomedicine. *Rev. Sci. Instrum.* **2006**, *77*, doi:10.1063/1.2195024.

46. Erpelding, T.N.; Garcia-Uribe, A.; Krumholz, A.; Ke, H.; Maslov, K.; Appleton, C.; Margenthaler, J.; Wang, L. V. A dual-modality photoacoustic and ultrasound imaging system for noninvasive sentinel lymph node detection: preliminary clinical results. *Photons Plus Ultrasound Imaging Sens.* **2014**, *8943*, 894359:1–6, doi:10.1117/12.2040475.

47. Beard, P. Biomedical photoacoustic imaging. *Interface Focus* **2011**, *1*, 1–29, doi:10.1098/rsfs.2011.0028.

48. Yang, J.-M.; Favazza, C.; Chen, R.; Yao, J.; Cai, X.; Maslov, K.; Zhou, Q.; Shung, K.K.; Wang, L. V. Toward dual-wavelength functional photoacoustic endoscopy: laser and peripheral optical systems development. *SPIE BiOS* **2012**, 822316, doi:10.1117/12.909163.

49. Wang, L. V.; Hu, S. Photoacoustic Tomography: In Vivo Imaging from Organelles to Organs. *Science (80-.).* **2012**, *335*, 1458–1462, doi:10.1126/science.1216210.

50. de Juan, A.; Tauler, R. Multivariate Curve Resolution (MCR) from 2000: Progress in concepts and applications. *Crit. Rev. Anal. Chem.* 2006, *36*, 163–176.

51. Ruckebusch, C.; Blanchet, L. Multivariate curve resolution: A review of advanced and tailored applications and challenges. *Anal. Chim. Acta* **2013**, *765*, 28–36, doi:10.1016/j.aca.2012.12.028.

52. de Juan, A.; Tauler, R. Chemometrics applied to unravel multicomponent processes and mixtures: Revisiting latest trends in multivariate resolution. *Anal. Chim. Acta* **2003**, *500*, 195–210, doi:10.1016/S0003-2670(03)00724-4.

53. Gowen, A.A.; O'Donnell, C.P.; Cullen, P.J.; Downey, G.; Frias, J.M. Hyperspectral imaging - an emerging process analytical tool for food quality and safety control. *Trends Food Sci. Technol.* **2007**, *18*, 590–598, doi:10.1016/j.tifs.2007.06.001.

54. Comon, P.; Luciani, X.; de Almeida, A.L.F. Tensor decompositions, alternating least squares and other tales. *J. Chemom.* **2009**, *23*, 393–405, doi:10.1002/cem.1236.

55. Maeder, M. Evolving Factor Analysis for the Resolution of Overlapping Chromatographic Peaks. *Anal. Chem.* **1987**, *59*, 527–530, doi:10.1021/ac00130a035.

56. Luke, G.P.; Myers, J.N.; Emelianov, S.Y.; Sokolov, K. V. Sentinel lymph node biopsy revisited: Ultrasound-guided photoacoustic detection of micrometastases using molecularly targeted plasmonic nanosensors. *Cancer Res.* **2014**, *74*, 5397–5408, doi:10.1158/0008-5472.CAN-14-0796.

57. Weber, J.; Beard, P.C.; Bohndiek, S.E. Contrast agents for molecular photoacoustic imaging. *Nat. Methods* **2016**, *13*, 639–650, doi:10.1038/nmeth.3929.

58. Lao, Y.; Xing, D.; Yang, S.; Xiang, L. Noninvasive photoacoustic imaging of the developing vasculature during early tumor growth. *Phys. Med. Biol.* **2008**, *53*, 4203–4212, doi:10.1088/0031-9155/53/15/013.

59. Allen, T.J.; Hall, A.; Dhillon, A.P.; Owen, J.S.; Beard, P.C. Spectroscopic photoacoustic imaging of lipid-rich plaques in the human aorta in the 740 to 1400 nm wavelength range. *J. Biomed. Opt.* **2012**, *17*, 061209, doi:10.1117/1.JBO.17.6.061209.

60. Helfrich, I.; Stoffels, I.; Morscher, S.; Helfrich, I.; Hillen, U.; Lehy, J.; Bachmann, H.S.; Roesch, A.; Griewank, K.; Schadendorf, D. Metastatic status of sentinel lymph nodes in melanoma determined noninvasively with multispectral optoacoustic imaging. *Sci. Transl. Med.* **2015**, *7*.

61. Gans, R. Über die Form ultramikroskopischer Goldteilchen. *Ann. Phys.* **1912**, *342*, 881–900.

62. Murphy, C.J.; Sau, T.K.; Gole, A.M.; Orendoff, C.J.; Gao, J.; Gou, L.; Hunyadi, S.E.; Li, T. Anisotropic metal nanoparticles: synthesis, assembly and optical applications. *J. Phys. Chem. B* **2005**, *109*, 13857–13870.

63. Link, S.; Mohamed, M.B.; El-sayed, M.A.; Liu, X.; Atwater, M.; Wang, J.; Huo, Q.; Liz-marza, L.M.; Near, R.D.; Hayden, S.C.; et al. Simulation of the Optical Absorption Spectra of Gold Nanorods as a Function of Their Aspect Ratio and the Effect of the Medium Dielectric Constant. *J. Phys. Chem. B* **1999**, *103*, 3073–3077, doi:10.1021/jp990183f.

64. Faraday, M. The Bakerian Lecture: Experimental Relations of Gold (and Other Metals) to Light. *Phylosofical Trans. R. Soc. London* **1857**, *147*, 145–181.

65. Van Der Zande, B.M.I.; Böhmer, M.R.; Fokkink, L.G.J.; Schönenberger, C. Colloidal dispersions of gold rods: Synthesis and optical properties. *Langmuir* **2000**, *16*, 451–458, doi:10.1021/la9900425.

66. Nikoobakht, B.; El-Sayed, M.A. Preparation and Growth Mechanism of Gold Nanorods (NRs) Using Seed-Mediated Growth Method. *Chem. Mater.* **2003**, *15*, 1957–1962, doi:10.1021/cm020732l.

67. Huang, J.-S.; Callegari, V.; Geisler, P.; Brüning, C.; Kern, J.; Prangsma, J.C.; Wu, X.; Feichtner, T.; Ziegler, J.; Weinmann, P.; et al. Atomically flat single-crystalline gold nanostructures for plasmonic nanocircuitry. *Nat. Commun.* **2010**, *1*, 150, doi:10.1038/ncomms1143.

68. Koh, A.L.; McComb, D.W.; Maier, S.A.; Low, H.Y.; Yang, J.K.W. Sub-10 nm patterning of gold nanostructures on silicon-nitride membranes for plasmon mapping with electron energy-loss spectroscopy. *J. Vac. Sci. Technol. B* **2010**, *28*, C6O45, doi:10.1116/1.3501351.

69. Piccionello, A.P.; Menichetti, L.; Armanetti, P.; Flori, A.; Monaco, I.; Maturi, M.; Pace, A.; Locatelli, E. Photoluminescent decoration of iron oxide magnetic nanoparticles for dual-imaging applications. *J. Nanoparticle Res.* **2018**, *20*, doi:10.1007/s11051-018-4365-5.

70. Tortorella, S.; Maturi, M.; Dapporto, F.; Spanu, C.; Sambri, L.; Comes Franchini, M.; Chiariello, M.; Locatelli, E. Surface modification of nanocellulose through carbamate link for a selective release of chemotherapeutics. *Cellulose* **2020**, *5*, doi:10.1007/s10570-020-03390-5.

71. Tortorella, S.; Vetri Buratti, V.; Maturi, M.; Sambri, L.; Comes Franchini, M.; Locatelli, E. Surface-Modified Nanocellulose for Application in Biomedical Engineering and Nanomedicine: A Review. *Int. J. Nanomedicine* **2020**, *Volume 15*, 9909–9937, doi:10.2147/IJN.S266103.

72. Mallidi, S.; Watanabe, K.; Timerman, D.; Schoenfeld, D.; Hasan, T. Prediction of Tumor Recurrence and Therapy Monitoring Using Ultrasound-Guided Photoacoustic Imaging. *Theranostics* **2015**, *5*, 289–301, doi:10.7150/thno.10155.

73. Nam, S.Y.; Ricles, L.M.; Suggs, L.J.; Emelianov, S.Y. In vivo Ultrasound and Photoacoustic Monitoring of Mesenchymal Stem Cells Labeled with Gold Nanotracers. *PLoS One* **2012**, *7*, e37267, doi:10.1371/journal.pone.0037267.

74. Bladder Cancer Treatment (PDQ®)–Health Professional Version Available online: https://www.cancer.gov/types/bladder/hp/bladder-treatment-pdq#section/all (accessed on Oct 29, 2020).

75. Magers, M.J.; Lopez-Beltran, A.; Montironi, R.; Williamson, S.R.; Kaimakliotis, H.Z.; Cheng, L. Staging of bladder cancer. *Histopathology* **2019**, *74*, 112–134, doi:10.1111/his.13734.

76. Yeung, C.; Dinh, T.; Lee, J. The Health Economics of Bladder Cancer: An Updated Review of the Published Literature. *Pharmacoeconomics* **2014**, *32*, 1093–1104, doi:10.1007/s40273-014-0194-2.

77. Nebuloni, M.; Albarello, L.; Andolfo, A.; Magagnotti, C.; Genovese, L.; Locatelli, I.; Tonon, G.; Longhi,

E.; Zerbi, P.; Allevi, R.; et al. Insight On Colorectal Carcinoma Infiltration by Studying Perilesional Extracellular Matrix. *Sci. Rep.* **2016**, *6*, 22522, doi:10.1038/srep22522.

78. Alfano, M.; Nebuloni, M.; Allevi, R.; Zerbi, P.; Longhi, E.; Lucianò, R.; Locatelli, I.; Pecoraro, A.; Indrieri, M.; Speziali, C.; et al. Linearized texture of three-dimensional extracellular matrix is mandatory for bladder cancer cell invasion. *Sci. Rep.* **2016**, *6*, 36128, doi:10.1038/srep36128.

79. Grossman, M.; Ben-Chetrit, N.; Zhuravlev, A.; Afik, R.; Bassat, E.; Solomonov, I.; Yarden, Y.; Sagi, I. Tumor Cell Invasion Can Be Blocked by Modulators of Collagen Fibril Alignment That Control Assembly of the Extracellular Matrix. *Cancer Res.* **2016**, *76*, 4249–4258, doi:10.1158/0008-5472.CAN-15-2813.

80. Penet, M.-F.; Kakkad, S.; Pathak, A.P.; Krishnamachary, B.; Mironchik, Y.; Raman, V.; Solaiyappan, M.; Bhujwalla, Z.M. Structure and Function of a Prostate Cancer Dissemination–Permissive Extracellular Matrix. *Clin. Cancer Res.* **2017**, *23*, 2245–2254, doi:10.1158/1078-0432.CCR-16-1516.

81. Curnis, F.; Sacchi, A.; Longhi, R.; Colombo, B.; Gasparri, A.; Corti, A. IsoDGR-Tagged Albumin: A New αvβ3 Selective Carrier for Nanodrug Delivery to Tumors. *Small* **2013**, *9*, 673–678, doi:10.1002/smll.201202310.

82. Curnis, F.; Fiocchi, M.; Sacchi, A.; Gori, A.; Gasparri, A.; Corti, A. NGR-tagged nano-gold: A new CD13-selective carrier for cytokine delivery to tumors. *Nano Res.* **2016**, *9*, 1393–1408, doi:10.1007/s12274-016-1035-8.

83. Martin, R.C.G.; Locatelli, E.; Li, Y.; Zhang, W.; Li, S.; Monaco, I.; Franchini, M.C. Gold nanorods and curcumin-loaded nanomicelles for efficient in vivo photothermal therapy of Barrett's esophagus. *Nanomedicine* **2015**, *10*, 1723–1733, doi:10.2217/nnm.15.25.

84. Choi, W.J.; Kim, H.H.; Cha, J.H.; Shin, H.J.; Kim, H.; Chae, E.Y.; Hong, M.J. Predicting Prognostic Factors of Breast Cancer Using Shear Wave Elastography. *Ultrasound Med. Biol.* **2014**, *40*, 269–274, doi:10.1016/j.ultrasmedbio.2013.09.028.

85. Li, C.; Guan, G.; Zhang, F.; Song, S.; Wang, R.K.; Huang, Z.; Nabi, G. Quantitative elasticity measurement of urinary bladder wall using laser-induced surface acoustic waves. *Biomed. Opt. Express* **2014**, *5*, 4313, doi:10.1364/BOE.5.004313.

86. Ferro, M.; Vartolomei, M.D.; Cantiello, F.; Lucarelli, G.; Di Stasi, S.M.; Hurle, R.; Guazzoni, G.; Busetto, G.M.; De Berardinis, E.; Damiano, R.; et al. High-Grade T1 on Re-Transurethral Resection after Initial High-Grade T1 Confers Worse Oncological Outcomes: Results of a Multi-Institutional Study. *Urol. Int.* **2018**, *101*, 7–15, doi:10.1159/000490765.

87. Ogata, H.; Decaneto, E.; Grossman, M.; Havenith, M.; Sagi, I.; Lubitz, W.; Knipp, M. Crystallization and preliminary X-ray crystallographic analysis of the catalytic domain of membrane type 1 matrix metalloproteinase. *Acta Crystallogr. Sect. F Struct. Biol. Commun.* **2014**, *70*, 232–235, doi:10.1107/S2053230X13034857.

88. Scheepbouwer, C.; Meyer, S.; Burggraaf, M.J.; Jose, J.; Molthoff, C.F.M. A Multimodal Imaging Approach for Longitudinal Evaluation of Bladder Tumor Development in an Orthotopic Murine Model. *PLoS One* **2016**, *11*, e0161284, doi:10.1371/journal.pone.0161284.

89. Lurie, K.L.; Zlatev, D. V.; Angst, R.; Gao, J.; Li, S.; Mach, K.E.; Ellerbee, A.K.; Liao, J.C. Virtual 3D Bladder Reconstruction from White Light Cystoscopy. *J. Urol.* **2015**, *193*, e561, doi:10.1016/j.juro.2015.02.1653.

90. Chin-Hsing, C.; Ann-Shu, L.; Jiann-Der, L.; Yang, W.H. 3D image reconstruction of bladder by nonlinear interpolation. *Math. Comput. Model.* **1995**, *22*, 61–72, doi:10.1016/0895-7177(95)00155-U.

91. Niu, H.; He, W.; Wu, M.; Li, R.; Jia, S.; Pu, F.; Li, S.-Y.; Li, D.; Fan, Y. Reconstruction of 3D Bladder Model and Computation of Intra-Vesical Volume During Storing Based on Magnetic Resonance Imaging. In Proceedings of the 2nd International Conference on Bioinformatics and Biomedical Engineering; IEEE, 2008; Vol. d, pp. 1840–1842.

92. Charan, S.; Sanjiv, K.; Singh, N.; Chien, F.-C.; Chen, Y.-F.; Nergui, N.N.; Huang, S.-H.; Kuo, C.W.; Lee, T.-C.; Chen, P. Development of Chitosan Oligosaccharide-Modified Gold Nanorods for in Vivo Targeted Delivery and Noninvasive Imaging by NIR Irradiation. *Bioconjug. Chem.* **2012**, *23*, 2173–2182, doi:10.1021/bc3001276.

93. Maquoi, E.; Assent, D.; Detilleux, J.; Pequeux, C.; Foidart, J.-M.; Noël, A. MT1-MMP protects breast carcinoma cells against type I collagen-induced apoptosis. *Oncogene* **2012**, *31*, 480–493, doi:10.1038/onc.2011.249.

94. Lizzi, F.L.; Greenebaum, M.; Feleppa, E.J.; Elbaum, M.; Coleman, D.J. Theoretical framework for spectrum analysis in ultrasonic tissue characterization. *J. Acoust. Soc. Am.* **1983**, *73*, 1366–1373, doi:10.1121/1.389241.

95. Curnis, F.; Gasparri, A.M.; Longhi, R.; Colombo, B.; D'Alessio, S.; Pastorino, F.; Ponzoni, M.; Corti, A. Chromogranin A binds to αvβ6-integrin and promotes wound healing in mice. *Cell. Mol. Life Sci.* **2012**, *69*, 2791–2803, doi:10.1007/s00018-012-0955-z.

96. Paradise, R.K.; Lauffenburger, D.A.; Van Vliet, K.J. Acidic Extracellular pH Promotes Activation of Integrin αvβ3. *PLoS One* **2011**, *6*, e15746, doi:10.1371/journal.pone.0015746.

97. Evans, D.F.; Allen, M.; Ninham, B.W.; Fouda, A. Critical micelle concentrations for alkyltrimethylammonium bromides in water from 25 to 160°C. *J. Solution Chem.* **1984**, *13*, 87–101, doi:10.1007/BF00646042.

98. Gallina, M.E.; Zhou, Y.; Johnson, C.J.; Harris-Birtill, D.; Singh, M.; Zhao, H.; Ma, D.; Cass, T.; Elson, D.S. Aptamer-conjugated, fluorescent gold nanorods as potential cancer theradiagnostic agents. *Mater. Sci. Eng. C* **2016**, *59*, 324–332, doi:10.1016/j.msec.2015.09.101.

99. Lavertu, M.; Xia, Z.; Serreqi, A.N.; Berrada, M.; Rodrigues, A.; Wang, D.; Buschmann, M.D.; Gupta, A. A validated 1H NMR method for the determination of the degree of deacetylation of chitosan. *J. Pharm. Biomed. Anal.* **2003**, *32*, 1149–1158, doi:10.1016/S0731-7085(03)00155-9.

100. Uchinomiya, S.; Nonaka, H.; Fujishima, S.; Tsukiji, S.; Ojida, A.; Hamachi, I. Site-specific covalent labeling of His-tag fused proteins with a reactive Ni(ii)–NTA probe. *Chem. Commun.* **2009**, 5880, doi:10.1039/b912025d.

101. Bartoschik, T.; Galinec, S.; Kleusch, C.; Walkiewicz, K.; Breitsprecher, D.; Weigert, S.; Muller, Y.A.; You, C.; Piehler, J.; Vercruysse, T.; et al. Near-native, site-specific and purification-free protein labeling for quantitative protein interaction analysis by MicroScale Thermophoresis. *Sci. Rep.* **2018**, *8*, 4977, doi:10.1038/s41598-018-23154-3.

102. Jensen, J.B.; Parmar, M. Strengths and Limitations of the Neurosphere Culture System. *Mol. Neurobiol.* **2006**, *34*, 153–162, doi:10.1385/MN:34:3:153.

103. Schatton, T.; Frank, M.H. The In Vitro Spheroid Melanoma Cell Culture Assay: Cues on Tumor Initiation? *J. Invest. Dermatol.* **2010**, *130*, 1769–1771, doi:10.1038/jid.2010.135.

104. Vescovi, A.L.; Reynolds, B.A.; Fraser, D.D.; Weiss, S. bFGF regulates the proliferative fate of unipotent (neuronal) and bipotent (neuronal/astroglial) EGF-generated CNS progenitor cells. *Neuron* **1993**, *11*, 951–966, doi:10.1016/0896-6273(93)90124-A.

105. Llovet, J.M.; Montal, R.; Sia, D.; Finn, R.S. Molecular therapies and precision medicine for hepatocellular carcinoma. *Nat. Rev. Clin. Oncol.* **2018**, *15*, 599–616, doi:10.1038/s41571-018-0073-4.

106. Lohitesh, K.; Chowdhury, R.; Mukherjee, S. Resistance a major hindrance to chemotherapy in hepatocellular carcinoma: an insight. *Cancer Cell Int.* **2018**, *18*, 44, doi:10.1186/s12935-018-0538-7.

107. Lai, C.-L.; Lok, A.S.-F.; Wu, P.-C.; Chan, G.C.-B.; Lin, H.-J. Doxorubicin versus no antitumor therapy in inoperable hepatocellular carcinoma. A prospective randomized trial. *Cancer* **1988**, *62*, 479–483, doi:10.1002/1097-0142(19880801)62:3<479::AID-CNCR2820620306>3.0.CO;2-L.

108. Li, Y.; Farmer, R.W.; Yang, Y.; Martin, R.C.G. Epithelial cell adhesion molecule in human hepatocellular carcinoma cell lines: a target of chemoresistence. *BMC Cancer* **2016**, *16*, 228, doi:10.1186/s12885-016-2252-y.

109. Locatelli, E.; Monaco, I.; Comes Franchini, M. Surface modifications of gold nanorods for applications in nanomedicine. *RSC Adv.* **2015**, *5*, 21681–21699, doi:10.1039/C4RA16473C.

110. Manohar, S.; Ungureanu, C.; Van Leeuwen, T.G. Gold nanorods as molecular contrast agents in photoacoustic imaging: the promises and the caveats. *Contrast Media Mol. Imaging* **2011**, *6*, 389–400, doi:10.1002/cmmi.454.

111. Li, W.; Chen, X. Gold nanoparticles for photoacoustic imaging. *Nanomedicine* **2015**, *10*, 299–320, doi:10.2217/nnm.14.169.

112. Huang, X.; El-Sayed, I.H.; Qian, W.; El-Sayed, M.A. Cancer cell imaging and photothermal therapy in the near-infrared region by using gold nanorods. *J. Am. Chem. Soc.* **2006**, *128*, 2115–2120, doi:10.1021/ja057254a.

113. Alkilany, A.M.; Thompson, L.B.; Boulos, S.P.; Sisco, P.N.; Murphy, C.J. Gold nanorods: Their potential for photothermal therapeutics and drug delivery, tempered by the complexity of their biological

interactions. *Adv. Drug Deliv. Rev.* **2012**, *64*, 190–199, doi:10.1016/j.addr.2011.03.005.

114. Yang, H.; Zhao, J.; Wu, C.; Ye, C.; Zou, D.; Wang, S. Facile synthesis of colloidal stable MoS2 nanoparticles for combined tumor therapy. *Chem. Eng. J.* **2018**, *351*, 548–558, doi:10.1016/j.cej.2018.06.100.

115. Zhao, J.; Xie, P.; Ye, C.; Wu, C.; Han, W.; Huang, M.; Wang, S.; Chen, H. Outside-in synthesis of mesoporous silica/molybdenum disulfide nanoparticles for antitumor application. *Chem. Eng. J.* **2018**, *351*, 157–168, doi:10.1016/j.cej.2018.06.101.

116. Yamashita, T.; Budhu, A.; Forgues, M.; Wang, X.W. Activation of Hepatic Stem Cell Marker EpCAM by Wnt–β-Catenin Signaling in Hepatocellular Carcinoma. *Cancer Res.* **2007**, *67*, 10831–10839, doi:10.1158/0008-5472.CAN-07-0908.

117. Gentili, D.; Ori, G.; Comes Franchini, M. Double phase transfer of gold nanorods for surface functionalization and entrapment into PEG-based nanocarriers. *Chem. Commun.* **2009**, 5874–5876, doi:10.1039/b911582j.

118. Li, Y.; Shi, X.; Zhang, J.; Zhang, X.; Martin, R.C.G. Hepatic protection and anticancer activity of curcuma: a potential chemopreventive strategy against hepatocellular carcinoma. *Int. J. Oncol.* **2014**, *44*, 505–13, doi:10.3892/ijo.2013.2184.

119. Huang, X.; El-Sayed, M.A. Plasmonic photo-thermal therapy (PPTT). *Alexandria J. Med.* **2011**, *47*, 1–9, doi:10.1016/j.ajme.2011.01.001.

120. Bucharskaya, A.B.; Maslyakova, G.N.; Chekhonatskaya, M.L.; Terentyuk, G.S.; Navolokin, N.A.; Khlebtsov, B.N.; Khlebtsov, N.G.; Bashkatov, A.N.; Genina, E.A.; Tuchin, V. V. Plasmonic photothermal therapy: Approaches to advanced strategy. *Lasers Surg. Med.* **2018**, *50*, 1025–1033, doi:10.1002/lsm.23001.

121. Norouzi, H.; Khoshgard, K.; Akbarzadeh, F. In vitro outlook of gold nanoparticles in photo-thermal therapy: a literature review. *Lasers Med. Sci.* **2018**, *33*, 917–926, doi:10.1007/s10103-018-2467-z.

122. Aravalli, R.N.; Steer, C.J.; Cressman, E.N.K. Molecular mechanisms of hepatocellular carcinoma. *Hepatology* **2008**, *48*, 2047–2063, doi:10.1002/hep.22580.

123. Yahyazadeh Mashhadi, S.M.; Kazemimanesh, M.; Arashkia, A.; Azadmanesh, K.; Meshkat, Z.; Golichenari, B.; Sahebkar, A. Shedding light on the EpCAM: An overview. *J. Cell. Physiol.* **2019**, *234*, 12569–12580, doi:10.1002/jcp.28132.

124. Goldberg, S.N. Radiofrequency Tumor Ablation: Principles and Techniques. In *Multi-Treatment Modalities of Liver Tumours*; Habib, N.A., Ed.; Springer US: Boston, MA, 2002; pp. 87–118 ISBN 978-1-4615-0547-1.

125. Li, Y.; Brown, R.E.; Martin, R.C.G. Incomplete thermal ablation of hepatocellular carcinoma: effects on tumor proliferation. *J. Surg. Res.* **2013**, *181*, 250–255, doi:10.1016/j.jss.2012.07.014.

126. Stoffels, I.; Morscher, S.; Helfrich, I.; Hillen, U.; Leyh, J.; Lehy, J.; Burton, N.C.; Sardella, T.C.P.; Claussen, J.; Poeppel, T.D.; et al. Metastatic status of sentinel lymph nodes in melanoma determined noninvasively with multispectral optoacoustic imaging. *Sci. Transl. Med.* **2015**, *7*, doi:10.1126/scitranslmed.aad1278.

127. Upputuri, P.K.; Pramanik, M. Recent advances in photoacoustic contrast agents for in vivo imaging. *WIREs Nanomedicine and Nanobiotechnology* **2020**, *12*, 1–23, doi:10.1002/wnan.1618.

128. Fu, Q.; Zhu, R.; Song, J.; Yang, H.; Chen, X. Photoacoustic Imaging: Contrast Agents and Their Biomedical Applications. *Adv. Mater.* **2018**, *31*, 1805875, doi:10.1002/adma.201805875.

129. Knights, O.B.; Ye, S.; Ingram, N.; Freear, S.; McLaughlan, J.R. Optimising gold nanorods for photoacoustic imaging in vitro. *Nanoscale Adv.* **2019**, *1*, 1472–1481, doi:10.1039/C8NA00389K.

130. Yan, N.; Wang, X.; Lin, L.; Song, T.; Sun, P.; Tian, H.; Liang, H.; Chen, X. Gold Nanorods Electrostatically Binding Nucleic Acid Probe for In Vivo MicroRNA Amplified Detection and Photoacoustic Imaging-Guided Photothermal Therapy. *Adv. Funct. Mater.* **2018**, *28*, 1800490, doi:10.1002/adfm.201800490.

131. Cai, K.; Zhang, W.; Foda, M.F.; Li, X.; Zhang, J.; Zhong, Y.; Liang, H.; Li, H.; Han, H.; Zhai, T. Miniature Hollow Gold Nanorods with Enhanced Effect for In Vivo Photoacoustic Imaging in the NIR-II Window. *Small* **2020**, *16*, 2002748, doi:10.1002/smll.202002748.

132. Yin, D.; Li, X.; Ma, Y.; Liu, Z. Targeted cancer imaging and photothermal therapy via monosaccharide-imprinted gold nanorods. *Chem. Commun.* **2017**, *53*, 6716–6719, doi:10.1039/C7CC02247F.

133. Keshava, N.; Mustard, J.F. Spectral unmixing. *IEEE Signal Process. Mag.* **2002**, *19*, 44–57, doi:10.1109/79.974727.

134. Williams, P.; Geladi, P.; Fox, G.; Manley, M. Maize kernel hardness classification by near infrared (NIR) hyperspectral imaging and multivariate data analysis. *Anal. Chim. Acta* **2009**, *653*, 121–130, doi:10.1016/j.aca.2009.09.005.

135. Jun, W.; Kim, M.S.; Lee, K.; Millner, P.; Chao, K. Assessment of bacterial biofilm on stainless steel by hyperspectral fluorescence imaging. *Sens. Instrum. Food Qual. Saf.* **2009**, *3*, 41–48, doi:10.1007/s11694-009-9069-1.

136. Yin, J.; Xia, Y.; Lu, M. Concentration profiles of collagen and proteoglycan in articular cartilage by Fourier transform infrared imaging and principal component regression. *Spectrochim. Acta - Part A Mol. Biomol. Spectrosc.* **2012**, *88*, 90–96, doi:10.1016/j.saa.2011.12.002.

137. Khan, Z.; Shafait, F.; Mian, A. Joint Group Sparse PCA for Compressed Hyperspectral Imaging. *IEEE Trans. Image Process.* **2015**, *24*, 4934–4942, doi:10.1109/TIP.2015.2472280.

138. Bertani, F.R.; Mozetic, P.; Fioramonti, M.; Iuliani, M.; Ribelli, G.; Pantano, F.; Santini, D.; Tonini, G.; Trombetta, M.; Businaro, L.; et al. Classification of M1/M2-polarized human macrophages by label-free hyperspectral reflectance confocal microscopy and multivariate analysis. *Sci. Rep.* **2017**, *7*, 1–9, doi:10.1038/s41598-017-08121-8.

139. Yasuda, M.; Takeshita, N.; Shigeto, S. Inhomogeneous Molecular Distributions and Cytochrome Types and Redox States in Fungal Cells Revealed by Raman Hyperspectral Imaging Using Multivariate Curve Resolution-Alternating Least Squares. *Anal. Chem.* **2019**, *91*, 12501–12508, doi:10.1021/acs.analchem.9b03261.

140. Felten, J.; Hall, H.; Jaumot, J.; Tauler, R.; de Juan, A.; Gorzsás, A. Vibrational spectroscopic image analysis of biological material using multivariate curve resolution–alternating least squares (MCR-ALS). *Nat. Protoc.* **2015**, *10*, 217.

141. Rajkó, R. Some surprising properties of multivariate curve resolution-alternating least squares (MCR-ALS) algorithms. *J. Chemom.* **2009**, *23*, 172–178, doi:10.1002/cem.1228.

142. Wang, P.; Wang, P.; Wang, H.-W.; Cheng, J.-X. Mapping lipid and collagen by multispectral photoacoustic imaging of chemical bond vibration. *J. Biomed. Opt.* **2012**, *17*, 0960101, doi:10.1117/1.jbo.17.9.096010.

143. Wang, P.; Rajian, J.R.; Cheng, J.X. Spectroscopic imaging of deep tissue through photoacoustic detection of molecular vibration. *J. Phys. Chem. Lett.* **2013**, *4*, 2177–2185, doi:10.1021/jz400559a.

144. Li, R.; Phillips, E.; Wang, P.; Goergen, C.J.; Cheng, J. Label-free in vivo imaging of peripheral nerve by multispectral photoacoustic tomography. *J. Biophotonics* **2016**, *9*, 124–128, doi:10.1002/jbio.201500004.

145. Tzoumas, S.; Deliolanis, N.; Morscher, S.; Ntziachristos, V. Unmixing Molecular Agents From Absorbing Tissue in Multispectral Optoacoustic Tomography. *IEEE Trans. Med. Imaging* **2014**, *33*, 48–60, doi:10.1109/TMI.2013.2279994.

146. Olefir, I.; Tzoumas, S.; Restivo, C.; Mohajerani, P.; Xing, L.; Ntziachristos, V. Deep Learning Based Spectral Unmixing for Optoacoustic Imaging of Tissue Oxygen Saturation. *IEEE Trans. Med. Imaging* **2020**, *0062*, 1–1, doi:10.1109/TMI.2020.3001750.

147. Durairaj, D.A.; Agrawal, S.; Johnstonbaugh, K.; Chen, H.; Karri, S.P.K.; Kothapalli, S.-R. Unsupervised deep learning approach for photoacoustic spectral unmixing. In Proceedings of the Photons Plus Ultrasound: Imaging and Sensing 2020; Oraevsky, A.A., Wang, L. V., Eds.; SPIE, 2020; Vol. 11240, p. 125.

148. Monaco, I.; Maturi, M.; Matteucci, E.; Locatelli, E.; Baschieri, A.; Zani, P.; Armanetti, P.; Menichetti, L.; Sambri, L.; Comes Franchini, M. Phosphorescent iridium-containing nanomicelles: synthesis, characterization and preliminary applications in nanomedical imaging. *RSC Adv.* **2018**, *8*, 34162–34167, doi:10.1039/C8RA05368E.

149. Jaumot, J.; Gargallo, R.; de Juan, A.; Tauler, R. A graphical user-friendly interface for MCR-ALS: A new tool for multivariate curve resolution in MATLAB. *Chemom. Intell. Lab. Syst.* **2005**, *76*, 101–110, doi:10.1016/j.chemolab.2004.12.007.

150. Jaumot, J.; de Juan, A.; Tauler, R. MCR-ALS GUI 2.0: New features and applications. *Chemom. Intell. Lab. Syst.* **2015**, *140*, 1–12, doi:10.1016/j.chemolab.2014.10.003.

151. Yao, J.; Wang, L. V. Sensitivity of photoacoustic microscopy. *Photoacoustics* **2014**, *2*, 87–101, doi:10.1016/j.pacs.2014.04.002.

152. Guney, G.; Uluc, N.; Demirkiran, A.; Aytac-Kipergil, E.; Unlu, M.B.; Birgul, O. Comparison of noise reduction methods in photoacoustic microscopy. *Comput. Biol. Med.* **2019**, *109*, 333–341, doi:10.1016/j.compbiomed.2019.04.035.

153. Omidikia, N.; Beyramysoltan, S.; Mohammad Jafari, J.; Tavakkoli, E.; Akbari Lakeh, M.; Alinaghi, M.; Ghaffari, M.; Khodadadi Karimvand, S.; Rajkó, R.; Abdollahi, H. Closure constraint in multivariate curve resolution. *J. Chemom.* **2018**, *32*, e2975, doi:10.1002/cem.2975.

154. Shaw, J.M.; Seidler, P.F. Organic electronics: Introduction. *IBM J. Res. Dev.* **2001**, *45*, 3–9, doi:10.1147/rd.451.0003.

155. Kelley, T.W.; Baude, P.F.; Gerlach, C.; Ender, D.E.; Muyres, D.; Haase, M.A.; Vogel, D.E.; Theiss, S.D. Recent progress in organic electronics: Materials, devices, and processes. *Chem. Mater.* **2004**, *16*, 4413–4422, doi:10.1021/cm049614j.

156. Douglas F. Gray OLED set to become talk of display show.

157. Kodak Kodak Digital Camera First To use Active-Matrix OLED Displays; Kodak EasyShare LS633 Camera Ushers in New Era of Easy-to-View Displays.

158. Yen-Yi Lin; Gundlach, D.I.; Nelson, S.F.; Jackson, T.N. Pentacene-based organic thin-film transistors. *IEEE Trans. Electron Devices* **1997**, *44*, 1325–1331, doi:10.1109/16.605476.

159. Gundlach, D.J.; Nichols, J.A.; Zhou, L.; Jackson, T.N. Thin-film transistors based on well-ordered thermally evaporated naphthacene films. *Appl. Phys. Lett.* **2002**, *80*, 2925–2927, doi:10.1063/1.1471378.

160. De Boer, R.W.I.; Klapwijk, T.M.; Morpurgo, A.F. Field-effect transistors on tetracene single crystals. *Appl. Phys. Lett.* **2003**, *83*, 4345–4347, doi:10.1063/1.1629144.

161. Podzorov, V.; Pudalov, V.M.; Gershenson, M.E. Field-effect transistors on rubrene single crystals with parylene gate insulator. *Appl. Phys. Lett.* **2003**, *82*, 1739–1741, doi:10.1063/1.1560869.

162. Murphy, A.R.; Fréchet, J.M.J.; Chang, P.; Lee, J.; Subramanian, V. Organic Thin Film Transistors from a Soluble Oligothiophene Derivative Containing Thermally Removable Solubilizing Groups. *J. Am. Chem. Soc.* **2004**, *126*, 1596–1597, doi:10.1021/ja039529x.

163. Zhang, H.; Wang, Y.; Shao, K.; Liu, Y.; Chen, S.; Qiu, W.; Sun, X.; Qi, T.; Ma, Y.; Yu, G.; et al. Novel butterfly pyrene-based organic semiconductors for field effect transistors. *Chem. Commun.* **2006**, 755–757, doi:10.1039/b515433b.

164. Gelinck, G.H.; Huitema, H.E.A.; Veenendaal, E. Van; Cantatore, E.; Schrijnemakers, L.; Van Der Putten, J.B.P.H.; Geuns, T.C.T.; Beenhakkers, M.; Giesbers, J.B.; Huisman, B.H.; et al. Flexible active-matrix displays and shift registers based on solution-processed organic transistors. *Nat. Mater.* **2004**, *3*, 106–110, doi:10.1038/nmat1061.

165. Gundlach, D.J.; Li Li Jia; Jackson, T.N. Pentacene TFT with improved linear region characteristics using chemically modified source and drain electrodes. *IEEE Electron Device Lett.* **2001**, *22*, 571–573, doi:10.1109/55.974580.

166. Sirringhaus, H.; Kawase, T.; Friend, R.H.; Shimoda, T.; Inbasekaran, M.; Wu, W.; Woo, E.P. High-Resolution Inkjet Printing of All-Polymer Transistor Circuits. *Science (80-.).* **2000**, *290*, 2123–2126, doi:10.1126/science.290.5499.2123.

167. Lu, J.; Pinto, N.J.; MacDiarmid, A.G. Apparent dependence of conductivity of a conducting polymer on an electric field in a field effect transistor configuration. *J. Appl. Phys.* **2002**, *92*, 6033–6038, doi:10.1063/1.1511291.

168. Huang, D.; Liao, F.; Molesa, S.; Redinger, D.; Subramanian, V. Plastic-Compatible Low Resistance Printable Gold Nanoparticle Conductors for Flexible Electronics. *J. Electrochem. Soc.* **2003**, *150*, G412, doi:10.1149/1.1582466.

169. Liu, H.; Jian, R.; Chen, H.; Tian, X.; Sun, C.; Zhu, J.; Yang, Z.; Sun, J.; Wang, C. Application of Biodegradable and Biocompatible Nanocomposites in Electronics: Current Status and Future Directions. *Nanomaterials* **2019**, *9*, 950, doi:10.3390/nano9070950.

170. Sun, J.; Zhuang, J.; Shi, J.; Kormakov, S.; Liu, Y.; Yang, Z.; Wu, D. Highly elastic and ultrathin nanopaper-based nanocomposites with superior electric and thermal characteristics. *J. Mater. Sci.* **2019**, *54*, 8436–8449, doi:10.1007/s10853-019-03472-1.

171. Sun, J.; Zhao, Y.; Yang, Z.; Shen, J.; Cabrera, E.; Lertola, M.J.; Yang, W.; Zhang, D.; Benatar, A.; Castro, J.M.; et al. Highly stretchable and ultrathin nanopaper composites for epidermal strain sensors. *Nanotechnology* **2018**, *29*, doi:10.1088/1361-6528/aacc59.

172. Zhao, Y.; Cabrera, E.D.; Zhang, D.; Sun, J.; Kuang, T.; Yang, W.; Lertola, M.J.; Benatar, A.; Castro, J.M.; Lee, L.J. Ultrasonic processing of MWCNT nanopaper reinforced polymeric nanocomposites. *Polymer (Guildf).* **2018**, *156*, 85–94, doi:10.1016/j.polymer.2018.09.053.

173. Young, R.J.; Kinloch, I.A.; Gong, L.; Novoselov, K.S. The mechanics of graphene nanocomposites: A review. *Compos. Sci. Technol.* **2012**, *72*, 1459–1476, doi:10.1016/j.compscitech.2012.05.005.

174. Tan, B.; Thomas, N.L. A review of the water barrier properties of polymer/clay and polymer/graphene nanocomposites. *J. Memb. Sci.* **2016**, *514*, 595–612, doi:10.1016/j.memsci.2016.05.026.

175. Ramadas, M.; Bharath, G.; Ponpandian, N.; Ballamurugan, A.M. Investigation on biophysical properties of Hydroxyapatite/Graphene oxide (HAp/GO) based binary nanocomposite for biomedical applications. *Mater. Chem. Phys.* **2017**, *199*, 179–184, doi:10.1016/j.matchemphys.2017.07.001.

176. Wang, Q.; Ling, S.; Liang, X.; Wang, H.; Lu, H.; Zhang, Y. Self-Healable Multifunctional Electronic Tattoos Based on Silk and Graphene. *Adv. Funct. Mater.* **2019**, *29*, 1808695, doi:10.1002/adfm.201808695.

177. Gong, S.; Schwalb, W.; Wang, Y.; Chen, Y.; Tang, Y.; Si, J.; Shirinzadeh, B.; Cheng, W. A wearable and highly sensitive pressure sensor with ultrathin gold nanowires. *Nat. Commun.* **2014**, *5*, 3132, doi:10.1038/ncomms4132.

178. Ponnamma, D.; Chamakh, M.M.; Deshmukh, K.; Basheer Ahamed, M.; Erturk, A.; Sharma, P.; Al-Maadeed, M.A.-A. Ceramic-Based Polymer Nanocomposites as Piezoelectric Materials. In *Smart Polymer Nanocomposites*; 2017; pp. 77–93.

179. Ponnamma, D.; Ogunleye, G.J.; Sharma, P.; AlMaadeed, M.A. Piezo- and Thermoelectric Materials From Biopolymer Composites. In *Biopolymer Composites in Electronics*; Elsevier, 2017; pp. 333–352 ISBN 9780081009741.

180. Mishra, S.; Unnikrishnan, L.; Nayak, S.K.; Mohanty, S. Advances in Piezoelectric Polymer Composites for Energy Harvesting Applications: A Systematic Review. *Macromol. Mater. Eng.* **2019**, *304*, 1–25, doi:10.1002/mame.201800463.

181. Cui, H.; Hensleigh, R.; Yao, D.; Maurya, D.; Kumar, P.; Kang, M.G.; Priya, S.; Zheng, X. (Rayne) Three-dimensional printing of piezoelectric materials with designed anisotropy and directional response. *Nat. Mater.* **2019**, *18*, 234–241, doi:10.1038/s41563-018-0268-1.

182. Goldschmidt, V.M. Die gesetze der krystallochemie. *Naturwissenschaften* **1926**.

183. Bhalla, A.S.; Guo, R.; Roy, R. The perovskite structure—a review of its role in ceramic science and technology. *Mater. Res. Innov.* **2000**, *4*, 3–26, doi:10.1007/s100190000062.

184. Jiang, J.C.; Lin, Y.; Chen, C.L.; Chu, C.W.; Meletis, E.I. Microstructures and surface step-induced antiphase boundaries in epitaxial ferroelectric Ba 0.6Sr 0.4TiO 3 thin film on MgO. *J. Appl. Phys.* **2002**, *91*, 3188–3192, doi:10.1063/1.1446221.

185. Geller, S. Crystal Structure of Gadolinium Orthoferrite, GdFeO3. *J. Chem. Phys.* **1956**, *24*, 1236–1239, doi:10.1063/1.1742746.

186. Kay, H.F.; Bailey, P.C. Structure and properties of CaTiO3. *Acta Crystallogr.* **1957**, *10*, 219–226, doi:10.1107/S0365110X57000675.

187. Takeda, Y.; Kanamura, F.; Shimada, M.; Koizumi, M. The crystal structure of BaNiO3. *Acta Crystallogr. Sect. B Struct. Crystallogr. Cryst. Chem.* **1976**, *32*, 2464–2466, doi:10.1107/S056774087600798X.

188. Lee, J.G.; Hwang, J.; Hwang, H.J.; Jeon, O.S.; Jang, J.; Kwon, O.; Lee, Y.; Han, B.; Shul, Y.G. A New Family of Perovskite Catalysts for Oxygen-Evolution Reaction in Alkaline Media: BaNiO3 and BaNi0.83O2.5. *J. Am. Chem. Soc.* **2016**, *138*, 3541–3547, doi:10.1021/jacs.6b00036.

189. Ishigaki, T.; Yamauchi, S.; Kishio, K.; Mizusaki, J.; Fueki, K. Diffusion of oxide ion vacancies in perovskite-type oxides. *J. Solid State Chem.* **1988**, *73*, 179–187, doi:10.1016/0022-4596(88)90067-9.

190. Cherry, M.; Islam, M.S.; Catlow, C.R.A. Oxygen Ion Migration in Perovskite-Type Oxides. *J. Solid State Chem.* **1995**, *118*, 125–132, doi:10.1006/jssc.1995.1320.

191. Jiang, J.C.; Pan, X.Q.; Chen, C.L. Microstructure of epitaxial SrRuO3 thin films on (001) SrTiO3. *Appl. Phys. Lett.* **1998**, *72*, 909–911, doi:10.1063/1.120870.

192. He, J.; Jiang, J.C.; Liu, J.; Collins, G.; Chen, C.L.; Lin, B.; Giurgiutiu, V.; Guo, R.Y.; Bhalla, A.; Meletis, E.I. Ferroelectric BaTiO3 Thin Films on Ti Substrate Fabricated Using Pulsed-Laser Deposition. *J. Nanosci. Nanotechnol.* **2010**, *10*, 6245–6250, doi:10.1166/jnn.2010.2567.

193. Hona, R.K.; Huq, A.; Mulmi, S.; Ramezanipour, F. Transformation of Structure, Electrical Conductivity, and Magnetism in AA'Fe 2 O 6−δ , A = Sr, Ca and A' = Sr. *Inorg. Chem.* **2017**, *56*, 9716–9724, doi:10.1021/acs.inorgchem.7b01228.

194. Lufaso, M.W.; Woodward, P.M. Jahn–Teller distortions, cation ordering and octahedral tilting in perovskites. *Acta Crystallogr. Sect. B Struct. Sci.* **2004**, *60*, 10–20, doi:10.1107/S0108768103026661.

195. Van Roosmalen, J.A.M.; Cordfunke, E.H.P.; Helmholdt, R.B.; Zandbergen, H.W. The Defect Chemistry of LaMnO3±δ. *J. Solid State Chem.* **1994**, *110*, 100–105, doi:10.1006/jssc.1994.1141.

196. Ronald E. Cohen Origin of ferroelectricity in perovskite oxides. *Nature* **1992**, *358*, 136–138.

197. Matthias, B.; von Hippel, A. Domain Structure and Dielectric Response of Barium Titanate Single Crystals. *Phys. Rev.* **1948**, *73*, 1378–1384, doi:10.1103/PhysRev.73.1378.

198. Izyumskaya, N.; Alivov, Y.; Morkoç, H. Oxides, Oxides, and More Oxides: High-ϰ Oxides, Ferroelectrics, Ferromagnetics, and Multiferroics. *Crit. Rev. Solid State Mater. Sci.* **2009**, *34*, 89–179, doi:10.1080/10408430903368401.

199. Jiang, B.; Iocozzia, J.; Zhao, L.; Zhang, H.; Harn, Y.W.; Chen, Y.; Lin, Z. Barium titanate at the nanoscale: Controlled synthesis and dielectric and ferroelectric properties. *Chem. Soc. Rev.* **2019**, *48*, 1194–1228, doi:10.1039/c8cs00583d.

200. Acosta, M.; Novak, N.; Rojas, V.; Patel, S.; Vaish, R.; Koruza, J.; Rossetti, G.A.; Rödel, J. BaTiO3-based piezoelectrics: Fundamentals, current status, and perspectives. *Appl. Phys. Rev.* **2017**, *4*, doi:10.1063/1.4990046.

201. Zheng, T.; Wu, J.; Xiao, D.; Zhu, J. Recent development in lead-free perovskite piezoelectric bulk materials. *Prog. Mater. Sci.* **2018**, *98*, 552–624, doi:10.1016/j.pmatsci.2018.06.002.

202. Scharnowski, K.; Krone, M.; Sadlo, F.; Beck, P.; Roth, J.; Trebin, H.-R.; Ertl, T. Visualizing Polarization Domains in Barium Titanate. *IEEE Comput. Graph. Appl.* **2013**, *33*, 9–17.

203. Pradhan, S.; Roy, G.S. Study the Crystal Structure and Phase Transition of BaTiO3 – A Pervoskite. *Researcher* **2013**, *55*, 63–67.

204. Tao, H.; Wu, J. New poling method for piezoelectric ceramics. *J. Mater. Chem. C* **2017**, *5*, 1601–1606, doi:10.1039/c6tc05328a.

205. Lee, M.K.; Nath, T.K.; Eom, C.B.; Smoak, M.C.; Tsui, F. Strain modification of epitaxial perovskite oxide thin films using structural transitions of ferroelectric BaTiO3 substrate. *Appl. Phys. Lett.* **2000**, *77*, 3547–3549, doi:10.1063/1.1328762.

206. Pradhan, S.; Roy, G.S. Study the Crystal Structure and Phase Transition of BaTiO3 – A Pervoskite. *Researcher* **2013**, *55*, 63–67.

207. Ahmad, G.; Dickerson, M.B.; Cai, Y.; Jones, S.E.; Ernst, E.M.; Vernon, J.P.; Haluska, M.S.; Fang, Y.; Wang, J.; Subramanyam, G.; et al. Rapid bioenabled formation of ferroelectric BaTiO3 at room temperature from an aqueous salt solution at near neutral pH. *J. Am. Chem. Soc.* **2008**, *130*, 4–5, doi:10.1021/ja0744302.

208. Damjanovic, D. Ferroelectric, dielectric and piezoelectric properties of ferroelectric thin films and ceramics. *Reports Prog. Phys.* **1998**, *61*, 1267–1324, doi:10.1088/0034-4885/61/9/002.

209. Hong, J.; Fang, D. Size-dependent ferroelectric behaviors of BaTiO3 nanowires. *Appl. Phys. Lett.* **2008**, *92*, 2006–2009, doi:10.1063/1.2830662.

210. Zhao, Z.; Buscaglia, V.; Viviani, M.; Buscaglia, M.T.; Mitoseriu, L.; Testino, A.; Nygren, M.; Johnsson, M.; Nanni, P. Grain-size effects on the ferroelectric behavior of dense nanocrystalline BaTiO3 ceramics. *Phys. Rev. B* **2004**, *70*, 024107, doi:10.1103/PhysRevB.70.024107.

211. Phan, T.T.M.; Chu, N.C.; Luu, V.B.; Nguyen Xuan, H.; Pham, D.T.; Martin, I.; Carrière, P. Enhancement of polarization property of silane-modified BaTiO3 nanoparticles and its effect in increasing dielectric property of epoxy/BaTiO3 nanocomposites. *J. Sci. Adv. Mater. Devices* **2016**, *1*, 90–97, doi:10.1016/j.jsamd.2016.04.005.

212. Kim, P.; Jones, S.C.; Hotchkiss, P.J.; Haddock, J.N.; Kippelen, B.; Marder, S.R.; Perry, J.W. Phosphonic acid-modified barium titanate polymer nanocomposites with high permittivity and dielectric strength. *Adv. Mater.* **2007**, *19*, 1001–1005, doi:10.1002/adma.200602422.

213. Gonsalves, K.E.; Kembaiyan, K.T. Synthesis of advanced ceramics and intermetallics from organometallic/polymeric precursors. *Solid State Ionics* **1989**, *32–33*, 661–668, doi:https://doi.org/10.1016/0167-2738(89)90342-1.

214. Testino, A.; Buscaglia, M.T.; Buscaglia, V.; Viviani, M.; Bottino, C.; Nanni, P. Kinetics and Mechanism of Aqueous Chemical Synthesis of BaTiO3 Particles. *Chem. Mater.* **2004**, *16*, 1536–1543, doi:10.1021/cm031130k.

215. Zhu, X.; Zhu, J.; Zhou, S.; Liu, Z.; Ming, N.; Hesse, D. BaTiO3 nanocrystals: Hydrothermal synthesis and structural characterization. *J. Cryst. Growth* **2005**, *283*, 553–562, doi:10.1016/j.jcrysgro.2005.05.080.

216. Chan, C.S.; De Stasio, G.; Welch, S.A.; Girasole, M.; Frazer, B.H.; Nesterova, M. V.; Fakra, S.; Banfield, J.F. Microbial Polysaccharides Template Assembly of Nanocrystal Fibers. *Science (80-.).* **2004**, *303*, 1656–1658, doi:10.1126/science.1092098.

217. Chen, Y.Y.; Yu, B.Y.; Wang, J.H.; Cochran, R.E.; Shyue, J.J. Template-based fabrication of SrTiO3 and BaTiO3 nanotubes. *Inorg. Chem.* **2009**, *48*, 681–686, doi:10.1021/ic8018887.

218. Yang, Y.; Wang, X.; Sun, C.; Li, L. Phase transition in BaTiO3 nanotube arrays. *J. Appl. Phys.* **2011**, *109*, 1–5, doi:10.1063/1.3530614.

219. Roy, B.; Ahrenkiel, S.P.; Fuierer, P.A. Controlling the size and morphology of TiO2 powder by molten and solid salt synthesis. *J. Am. Ceram. Soc.* **2008**, *91*, 2455–2463.

220. Setasuwon, P.; Kijamnajsuk, S. Synthesis of Na0.5Bi0.5TiO3 Submicron Particles in Molten Salt. *Adv. Mater. Res.* **2008**, *55–57*, 161–164, doi:10.4028/www.scientific.net/AMR.55-57.161.

221. Huango, K.C.; Huango, T.C.; Hsieh, W.F. Morphology-controlled synthesis of barium titanate nanostructures. *Inorg. Chem.* **2009**, *48*, 9180–9184, doi:10.1021/ic900854x.

222. Arachchige, I.U.; Brock, S.L. Sol-gel methods for the assembly of metal chalcogenide quantum dots. *Acc. Chem. Res.* **2007**, *40*, 801–809, doi:10.1021/ar600028s.

223. Niederberger, M. Nonaqueous sol-gel routes to metal oxide nanoparticles. *Acc. Chem. Res.* **2007**, *40*, 793–800, doi:10.1021/ar600035e.

224. Padmanabhan, S.C.; Pillai, S.C.; Colreavy, J.; Balakrishnan, S.; McCormack, D.E.; Perova, T.S.; Gun'ko, Y.; Hinder, S.J.; Kellys, J.M. A simple sol - Gel processing for the development of high-temperature stable photoactive anatase titania. *Chem. Mater.* **2007**, *19*, 4474–4481, doi:10.1021/cm070980n.

225. Yoon, S.; Baik, S.; Kim, M.G.; Shin, N. Formation Mechanisms of Tetragonal Barium Titanate Nanoparticles in Alkoxide-Hydroxide Sol-Precipitation Synthesis. *J. Am. Ceram. Soc.* **2006**, *89*, 1816–1821, doi:10.1111/j.1551-2916.2006.01056.x.

226. Prateek; Thakur, V.K.; Gupta, R.K. Recent Progress on Ferroelectric Polymer-Based Nanocomposites for High Energy Density Capacitors: Synthesis, Dielectric Properties, and Future Aspects. *Chem. Rev.* **2016**, *116*, 4260–4317, doi:10.1021/acs.chemrev.5b00495.

227. Adam, J.; Lehnert, T.; Klein, G.; McMeeking, R.M. Ferroelectric properties of composites containing BaTiO 3 nanoparticles of various sizes. *Nanotechnology* **2014**, *25*, 065704, doi:10.1088/0957-4484/25/6/065704.

228. Ramadan, K.S.; Sameoto, D.; Evoy, S. A review of piezoelectric polymers as functional materials for electromechanical transducers. *Smart Mater. Struct.* **2014**, *23*, 033001, doi:10.1088/0964-1726/23/3/033001.

229. Ren, X.; Fan, H.; Zhao, Y.; Liu, Z. Flexible Lead-Free BiFeO3/PDMS-Based Nanogenerator as Piezoelectric Energy Harvester. *ACS Appl. Mater. Interfaces* **2016**, *8*, 26190–26197, doi:10.1021/acsami.6b04497.

230. Zhao, Y.; Liao, Q.; Zhang, G.; Zhang, Z.; Liang, Q.; Liao, X.; Zhang, Y. High output piezoelectric nanocomposite generators composed of oriented BaTiO3 NPs@PVDF. *Nano Energy* **2015**, *11*, 719–727, doi:10.1016/j.nanoen.2014.11.061.

231. Lee, M.; Chen, C.Y.; Wang, S.; Cha, S.N.; Park, Y.J.; Kim, J.M.; Chou, L.J.; Wang, Z.L. A hybrid piezoelectric structure for wearable nanogenerators. *Adv. Mater.* **2012**, *24*, 1759–1764, doi:10.1002/adma.201200150.

232. Kim, K.; Zhu, W.; Qu, X.; Aaronson, C.; McCall, W.R.; Chen, S.; Sirbuly, D.J. 3D Optical Printing of Piezoelectric Nanoparticle–Polymer Composite Materials. *ACS Nano* **2014**, *8*, 9799–9806, doi:10.1021/nn503268f.

233. Ricotti, L.; Ranzani, T.; Calarota, V.; Menciassi, A. Thin and flexible pressure/deformation sensors based on piezoelectric nanocomposites. *Proc. IEEE Sensors* **2014**, *2014-Decem*, 2070–2073, doi:10.1109/ICSENS.2014.6985443.

234. Zhao, J.; Han, S.; Yang, Y.; Fu, R.; Ming, Y.; Lu, C.; Liu, H.; Gu, H.; Chen, W. Passive and Space-

Discriminative Ionic Sensors Based on Durable Nanocomposite Electrodes toward Sign Language Recognition. *ACS Nano* **2017**, *11*, 8590–8599, doi:10.1021/acsnano.7b02767.

235. Fan, F.R.; Tang, W.; Wang, Z.L. Flexible Nanogenerators for Energy Harvesting and Self-Powered Electronics. *Adv. Mater.* **2016**, *28*, 4283–4305, doi:10.1002/adma.201504299.

236. Li, H.; Tian, C.; Deng, Z.D. Energy harvesting from low frequency applications using piezoelectric materials. *Appl. Phys. Rev.* **2014**, *1*, 041301, doi:10.1063/1.4900845.

237. Tjong, S.C. Structural and mechanical properties of polymer nanocomposites. *Mater. Sci. Eng. R Reports* **2006**, *53*, 73–197, doi:10.1016/j.mser.2006.06.001.

238. Triandafilidi, V.; Hatzikiriakos, S.G.; Rottler, J. Molecular simulations of the piezoionic effect. *Soft Matter* **2018**, *14*, 6222–6229, doi:10.1039/C8SM00939B.

239. us Sarwar, M.S.; Dobashi, Y.; Scabeni Glitz, E.F.; Farajollahi, M.; Mirabbasi, S.; Naficy, S.; Spinks, G.M.; Madden, J.D.W. Transparent and conformal "piezoionic" touch sensor. In Proceedings of the Electroactive Polymer Actuators and Devices (EAPAD) 2015; Bar-Cohen, Y., Ed.; 2015; Vol. 9430, p. 943026.

240. Dobashi, Y.; Allegretto, G.; Sarwar, M.S.; Cretu, E.; Madden, J.D.W. Mechanoionic Transduction of Solid Polymer Electrolytes and Potential Applications. *MRS Adv.* **2016**, *1*, 63–68, doi:10.1557/adv.2016.74.

241. Liu, Y.; Hu, Y.; Zhao, J.; Wu, G.; Tao, X.; Chen, W. Self-Powered Piezoionic Strain Sensor toward the Monitoring of Human Activities. *Small* **2016**, *12*, 5074–5080, doi:10.1002/smll.201600553.

242. Park, S.; Kim, Y.; Jung, H.; Park, J.-Y.; Lee, N.; Seo, Y. Energy harvesting efficiency of piezoelectric polymer film with graphene and metal electrodes. *Sci. Rep.* **2017**, *7*, 17290, doi:10.1038/s41598-017-17791-3.

243. Siddiqui, S.; Lee, H.B.; Kim, D.-I.; Duy, L.T.; Hanif, A.; Lee, N.-E. An Omnidirectionally Stretchable Piezoelectric Nanogenerator Based on Hybrid Nanofibers and Carbon Electrodes for Multimodal Straining and Human Kinematics Energy Harvesting. *Adv. Energy Mater.* **2018**, *8*, 1701520, doi:10.1002/aenm.201701520.

244. Wu, W.; Bai, S.; Yuan, M.; Qin, Y.; Wang, Z.L.; Jing, T. Lead zirconate titanate nanowire textile nanogenerator for wearable energy-harvesting and self-powered devices. *ACS Nano* **2012**, *6*, 6231–6235, doi:10.1021/nn3016585.

245. Jing, Q.; Kar-Narayan, S. Nanostructured polymer-based piezoelectric and triboelectric materials and devices for energy harvesting applications. *J. Phys. D. Appl. Phys.* **2018**, *51*, doi:10.1088/1361-6463/aac827.

246. Lee, C.S.; Joo, J.; Han, S.; Lee, J.H.; Koh, S.K. Poly (vinylidene fluoride) transducers with highly conducting poly (3,4-ethylenedioxythiophene) electrodes. *Synth. Met.* **2005**, *152*, 49–52, doi:10.1016/j.synthmet.2005.07.116.

247. Rajala, S.; Tuukkanen, S.; Halttunen, J. Characteristics of piezoelectric polymer film sensors with solution-processable graphene-based electrode materials. *IEEE Sens. J.* **2015**, *15*, 3102–3109, doi:10.1109/JSEN.2014.2344132.

248. Wang, D.; Zhang, Y.; Lu, X.; Ma, Z.; Xie, C.; Zheng, Z. Chemical formation of soft metal electrodes for flexible and wearable electronics. *Chem. Soc. Rev.* **2018**, *47*, 4611–4641, doi:10.1039/c7cs00192d.

249. Le Bideau, J.; Viau, L.; Vioux, A. Ionogels, ionic liquid based hybrid materials. *Chem. Soc. Rev.* **2011**, *40*, 907–925, doi:10.1039/c0cs00059k.

250. Kholkin, A.L.; Pertsev, N.A.; Goltsev, A. V Piezoelectricity and Crystal Symmetry. In *Piezoelectric and Acoustic Materials for Transducer Applications*; Safari, A., Akdoğan, E.K., Eds.; Springer US: Boston, MA, 2008; pp. 17–38 ISBN 978-0-387-76540-2.

251. Wegner, K.; Piseri, P.; Tafreshi, H.V.; Milani, P. Cluster beam deposition: a tool for nanoscale science and technology. *J. Phys. D. Appl. Phys.* **2006**, *39*, R439–R459, doi:10.1088/0022-3727/39/22/R02.

252. Borghi, F.; Melis, C.; Ghisleri, C.; Podestà, A.; Ravagnan, L.; Colombo, L.; Milani, P. Stretchable nanocomposite electrodes with tunable mechanical properties by supersonic cluster beam implantation in elastomers. *Appl. Phys. Lett.* **2015**, *106*, 121902, doi:10.1063/1.4916350.

253. Yan, Y.; Santaniello, T.; Bettini, L.G.; Minnai, C.; Bellacicca, A.; Porotti, R.; Denti, I.; Faraone, G.; Merlini, M.; Lenardi, C.; et al. Electroactive Ionic Soft Actuators with Monolithically Integrated Gold Nanocomposite Electrodes. *Adv. Mater.* **2017**, *29*, 1606109, doi:10.1002/adma.201606109.

254. Corbelli, G.; Ghisleri, C.; Marelli, M.; Milani, P.; Ravagnan, L. Highly Deformable Nanostructured Elastomeric Electrodes With Improving Conductivity Upon Cyclical Stretching. *Adv. Mater.* **2011**, *23*, 4504–4508, doi:10.1002/adma.201102463.

255. Kim, K.; Zhu, W.; Qu, X.; Aaronson, C.; McCall, W.R.; Chen, S.; Sirbuly, D.J. 3D optical printing of piezoelectric nanoparticle-polymer composite materials. *ACS Nano* **2014**, *8*, 9799–9806, doi:10.1021/nn503268f.

256. Yeon, S.-H.; Kim, K.-S.; Choi, S.; Lee, H.; Kim, H.S.; Kim, H. Physical and electrochemical properties of 1-(2-hydroxyethyl)-3-methyl imidazolium and N-(2-hydroxyethyl)-N-methyl morpholinium ionic liquids. *Electrochim. Acta* **2005**, *50*, 5399–5407, doi:10.1016/j.electacta.2005.03.020.

257. Li, J.; Zhu, Z.; Fang, L.; Guo, S.; Erturun, U.; Zhu, Z.; West, J.E.; Ghosh, S.; Kang, S.H. Analytical, numerical, and experimental studies of viscoelastic effects on the performance of soft piezoelectric nanocomposites. *Nanoscale* **2017**, *9*, 14215–14228, doi:10.1039/C7NR05163H.

258. Uchino, K.; Sadanaga, E.; Hirose, T. Dependence of the Crystal Structure on Particle Size in Barium Titanate. *J. Am. Ceram. Soc.* **1989**, *72*, 1555–1558, doi:10.1111/j.1151-2916.1989.tb07706.x.

259. Al-Shakarchi, E.K.; Mahmood, N.B. Three Techniques Used to Produce BaTiO₃ Fine Powder. *J. Mod. Phys.* **2011**, *02*, 1420–1428, doi:10.4236/jmp.2011.211175.

260. Li, W.; Xu, Z.; Chu, R.; Fu, P.; Hao, J. Structure and electrical properties of BaTiO3 prepared by sol–gel process. *J. Alloys Compd.* **2009**, *482*, 137–140, doi:10.1016/j.jallcom.2009.02.137.

261. Demirelli, K.; Coşkun, M.; Kaya, E. A detailed study of thermal degradation of poly(2-hydroxyethyl methacrylate). *Polym. Degrad. Stab.* **2001**, *72*, 75–80, doi:10.1016/S0141-3910(00)00204-4.

262. Fukagawa, M.; Koshiba, Y.; Fukushima, T.; Morimoto, M.; Ishida, K. Anomalous piezoelectric properties of poly(vinylidene fluoride–trifluoroethylene)/ionic liquid gels. *Jpn. J. Appl. Phys.* **2018**, *57*, 04FL06, doi:10.7567/JJAP.57.04FL06.

263. Mannsfeld, S.C.B.; Tee, B.C.K.; Stoltenberg, R.M.; Chen, C.V.H.-H.; Barman, S.; Muir, B.V.O.; Sokolov, A.N.; Reese, C.; Bao, Z. Highly sensitive flexible pressure sensors with microstructured rubber dielectric layers. *Nat. Mater.* **2010**, *9*, 859–864, doi:10.1038/nmat2834.

264. Ma, Y.; Choi, J.; Hourlier-Fargette, A.; Xue, Y.; Chung, H.U.; Lee, J.Y.; Wang, X.; Xie, Z.; Kang, D.; Wang, H.; et al. Relation between blood pressure and pulse wave velocity for human arteries. *Proc. Natl. Acad. Sci.* **2018**, *115*, 11144–11149, doi:10.1073/pnas.1814392115.

265. Liu, X.; Wu, D.; Wang, H.; Wang, Q. Self-recovering tough gel electrolyte with adjustable supercapacitor performance. *Adv. Mater.* **2014**, *26*, 4370–4375, doi:10.1002/adma.201400240.

266. Park, J.; Lee, Y.; Hong, J.; Lee, Y.; Ha, M.; Jung, Y.; Lim, H.; Kim, S.Y.; Ko, H. Tactile-Direction-Sensitive and Stretchable Electronic Skins Based on Human-Skin-Inspired Interlocked Microstructures. *ACS Nano* **2014**, *8*, 12020–12029, doi:10.1021/nn505953t.

267. Aggarwal, A.; Kirchner, F. Object Recognition and Localization: The Role of Tactile Sensors. *Sensors* **2014**, *14*, 3227–3266, doi:10.3390/s140203227.

268. Iida, F.; Laschi, C. Soft Robotics: Challenges and Perspectives. *Procedia Comput. Sci.* **2011**, *7*, 99–102, doi:10.1016/j.procs.2011.12.030.

269. Wang, H.; Totaro, M.; Beccai, L. Toward Perceptive Soft Robots: Progress and Challenges. *Adv. Sci.* **2018**, *5*, 1800541, doi:10.1002/advs.201800541.

270. Santaniello, T.; Migliorini, L.; Yan, Y.; Lenardi, C.; Milani, P. Supersonic cluster beam fabrication of metal–ionogel nanocomposites for soft robotics. *J. Nanoparticle Res.* **2018**, *20*, 250, doi:10.1007/s11051-018-4352-x.

271. Mahdi, R.I.; Abd Majid, W.H. Piezoelectric and pyroelectric properties of BNT-base ternary lead-free ceramic-polymer nanocomposites under different poling conditions. *RSC Adv.* **2016**, *6*, 81296–81309, doi:10.1039/c6ra12033d.

272. Stewart, M.; Cain, M.G. Direct Piezoelectric Measurement: The Berlincourt Method. In; Springer, Dordrecht, 2014; pp. 37–64.

273. C.M.Kuo, A. Poly(dimethylsiloxane). *Polym. Data Handb.* **1999**, 411–435, doi:10.1021/ja907879q.

274. Cornogolub, A.; Cottinet, P.-J.; Petit, L. Hybrid energy harvesting systems, using piezoelectric elements and dielectric polymers. *Smart Mater. Struct.* **2016**, *25*, 095048, doi:10.1088/0964-1726/25/9/095048.

275. Liu, C.-X.; Choi, J.-W. Improved Dispersion of Carbon Nanotubes in Polymers at High Concentrations. *Nanomaterials* **2012**, *2*, 329–347, doi:10.3390/nano2040329.

276. Ravagnan, L.; Colombo, L.; Milani, P. supersonic cluster beam implantation in elastomers Stretchable nanocomposite electrodes with tunable mechanical properties by supersonic cluster beam implantation in elastomers. **2016**, *121902*, doi:10.1063/1.4916350.

277. Ghisleri, C.; Borghi, F.; Ravagnan, L.; Podestà, A.; Melis, C.; Colombo, L.; Milani, P. Patterning of gold-polydimethylsiloxane (Au-PDMS) nanocomposites by supersonic cluster beam implantation. *J. Phys. D. Appl. Phys.* **2014**, *47*, doi:10.1088/0022-3727/47/1/015301.

278. Kachroudi, A.; Basrour, S.; Rufer, L.; -, al Micro-structured PDMS piezoelectric enhancement through charging conditions Related content Dielectric properties modelling of cellular structures with PDMS for micro-sensor applications. **2016**, doi:10.1088/0964-1726/25/10/105027.

279. Hillenbrand, J.; Sessler, G.M. Quasistatic and Dynamic Piezoelectric Coefficients of Polymer Foams and Polymer Film Systems. *IEEE Trans. Dielectr. Electr. Insul.* **2004**, *11*, 72–79, doi:10.1109/TDEI.2004.1266319.

280. Hillenbrand, J.; Xia, Z.; Zhang, X.; Sessler, G.M. Piezoelectricity of cellular and porous polymer electrets. *Proceedings. 11th Int. Symp. Electrets* **2002**, 46–49, doi:10.1109/ISE.2002.1042940.

281. Fang, P.; Holländer, L.; Wirges, W.; Gerhard, R. Piezoelectric d33coefficients in foamed and layered polymer piezoelectrets from dynamic mechano-electrical experiments, electro-mechanical resonance spectroscopy and acoustic-transducer measurements. *Meas. Sci. Technol.* **2012**, *23*, doi:10.1088/0957-0233/23/3/035604.

282. Chae, I.; Jeong, C.K.; Ounaies, Z.; Kim, S.H. Review on Electromechanical Coupling Properties of Biomaterials. **2018**, doi:10.1021/acsabm.8b00309.

283. Galembeck, F.; Burgo, T.A.L.; Balestrin, L.B.S.; Gouveia, R.F.; Silva, C.A.; Galembeck, A. Friction, tribochemistry and triboelectricity: Recent progress and perspectives. *RSC Adv.* 2014, *4*, 64280–64298.

284. Newnham, R.E.; Sundar, V.; Yimnirun, R.; Su, J.; Zhang, Q.M. Electrostriction: Nonlinear electromechanical coupling in solid dielectrics. *J. Phys. Chem. B* **1997**, *101*, 10141–10150, doi:10.1021/jp971522c.

285. Algueró, M.; Cheng, B.L.; Guiu, F.; Reece, M.J.; Poole, M.; Alford, N. Degradation of the d33 piezoelectric coefficient for PZT ceramics under static and cyclic compressive loading. *J. Eur. Ceram. Soc.* **2001**, *21*, 1437–1440, doi:10.1016/S0955-2219(01)00036-X.

286. Ehterami, A.; Kazemi, M.; Nazari, B.; Saraeian, P.; Azami, M. Fabrication and characterization of highly porous barium titanate based scaffold coated by Gel/HA nanocomposite with high piezoelectric coefficient for bone tissue engineering applications. *J. Mech. Behav. Biomed. Mater.* **2018**, *79*, 195–202, doi:10.1016/j.jmbbm.2017.12.034.

287. Sundar, U.; Lao, Z.; Cook-Chennault, K. Investigation of piezoelectricity and resistivity of surface modified barium titanate nanocomposites. *Polymers (Basel).* **2019**, *11*, doi:10.3390/polym11122123.

288. Feng, H.; Yang, Y.; You, Y.; Li, G.; Guo, J.; Yu, T.; Shen, Z.; Wu, T.; Xing, B. Simple and rapid synthesis of ultrathin gold nanowires, their self-assembly and application in surface-enhanced Raman scattering. *Chem. Commun.* **2009**, 1984, doi:10.1039/b822507a.

289. Shengbo, S.; Lihua, L.; Aoqun, J.; Qianqian, D.; Jianlong, J.; Qiang, Z.; Wendong, Z. Highly sensitive wearable strain sensor based on silver nanowires and nanoparticles. *Nanotechnology* **2018**, *29*, doi:10.1088/1361-6528/aabbba.

290. Gibson, I.; Rosen, D.; Stucker, B. *Additive Manufacturing Technologies*; Second.; Springer, 2015; ISBN 978-1-4939-2113-3.

291. ASTM F2792-12a Standard Terminology for Additive Manufacturing Technologies. *ASTM Int.* 2012, 1–3.

292. Gibson, I.; Rosen, D.W.; Stucker, B. *Additive Manufacturing Technologies*; Springer US, 2010; ISBN 978-1-4419-1119-3.

293. Chua, C.K.; Leong, K.F.; Lim, C.S. *Rapid Prototyping*; World Scientific, 2003; ISBN 978-981-238-117-0.

294. Kianian, B. 3D Printing and Additive Manufacturing State of the Industry, Annual Worldwide Progress Report: Chapters titles: The Middle East, and other countries. In *Wohlers Report - 3D Printing and Additive Manufacturing State of the Industry*; Wohlers Associates, Inc., 2017 ISBN 978-0-9913332-3-3.

295. Wohlers, T.; Gornet, T. History of Additive Manufacturing. In *Wohlers Report - 3D Printing and Additive*

Manufacturing State of the Industry; 2014; pp. 1–34 ISBN 978-0-9913332-0-2.

296. Council, A.; Petch, M. 3D Printing: Rise of the Third Industrial Revolution. *Gyges 3D* **2014**, *116*.

297. Reviews, H.B. 3D Printing Will Change the World Available online: https://hbr.org/2013/03/3-d-printing-will-change-the-world.

298. Zapfl, D. How 3D printing in the textile industry is leading into a new era Available online: https://www.lead-innovation.com/english-blog/3d-printing-in-the-textile-industry (accessed on Jul 15, 2019).

299. Jaroslaw, K. Mechanical properties of commercial rapid prototyping materials. *Rapid Prototyp. J.* **2014**, *20*, 499–510, doi:10.1108/RPJ-06-2012-0052.

300. Calignano, F.; Manfredi, D.; Ambrosio, E.P.; Biamino, S.; Lombardi, M.; Atzeni, E.; Salmi, A.; Minetola, P.; Iuliano, L.; Fino, P. Overview on Additive Manufacturing Technologies. *Proc. IEEE* **2017**, *105*, 593–612, doi:10.1109/JPROC.2016.2625098.

301. Alkaios Bournias Varotsis Introduction to FDM 3D printing Available online: https://www.3dhubs.com/knowledge-base/introduction-fdm-3d-printing/ (accessed on Nov 18, 2020).

302. Ahn, S.; Montero, M.; Odell, D.; Roundy, S.; Wright, P.K. Anisotropic material properties of fused deposition modeling ABS. *Rapid Prototyp. J.* **2002**, *8*, 248–257, doi:10.1108/13552540210441166.

303. McCullough, E.J.; Yadavalli, V.K. Surface modification of fused deposition modeling ABS to enable rapid prototyping of biomedical microdevices. *J. Mater. Process. Technol.* **2013**, *213*, 947–954, doi:10.1016/j.jmatprotec.2012.12.015.

304. Drummer, D.; Cifuentes-Cuéllar, S.; Rietzel, D. Suitability of PLA/TCP for fused deposition modeling. *Rapid Prototyp. J.* **2012**, *18*, 500–507, doi:10.1108/13552541211272045.

305. Zhang, B.; Seong, B.; Nguyen, V.; Byun, D. 3D printing of high-resolution PLA-based structures by hybrid electrohydrodynamic and fused deposition modeling techniques. *J. Micromechanics Microengineering* **2016**, *26*, 025015, doi:10.1088/0960-1317/26/2/025015.

306. Domingo-Espin, M.; Puigoriol-Forcada, J.M.; Garcia-Granada, A.-A.; Llumà, J.; Borros, S.; Reyes, G. Mechanical property characterization and simulation of fused deposition modeling Polycarbonate parts. *Mater. Des.* **2015**, *83*, 670–677, doi:10.1016/j.matdes.2015.06.074.

307. Smith, W.C.; Dean, R.W. Structural characteristics of fused deposition modeling polycarbonate material. *Polym. Test.* **2013**, *32*, 1306–1312, doi:10.1016/j.polymertesting.2013.07.014.

308. Schirmeister, C.G.; Hees, T.; Licht, E.H.; Mülhaupt, R. 3D printing of high density polyethylene by fused filament fabrication. *Addit. Manuf.* **2019**, *28*, 152–159, doi:10.1016/j.addma.2019.05.003.

309. Carneiro, O.S.; Silva, A.F.; Gomes, R. Fused deposition modeling with polypropylene. *Mater. Des.* **2015**, *83*, 768–776, doi:10.1016/j.matdes.2015.06.053.

310. Wang, P.; Zou, B.; Xiao, H.; Ding, S.; Huang, C. Effects of printing parameters of fused deposition modeling on mechanical properties, surface quality, and microstructure of PEEK. *J. Mater. Process. Technol.* **2019**, *271*, 62–74, doi:10.1016/j.jmatprotec.2019.03.016.

311. Hu, B.; Duan, X.; Xing, Z.; Xu, Z.; Du, C.; Zhou, H.; Chen, R.; Shan, B. Improved design of fused deposition modeling equipment for 3D printing of high-performance PEEK parts. *Mech. Mater.* **2019**, *137*, 103139, doi:10.1016/j.mechmat.2019.103139.

312. Basavaraj, C.K.; Vishwas, M. Studies on Effect of Fused Deposition Modelling Process Parameters on Ultimate Tensile Strength and Dimensional Accuracy of Nylon. *IOP Conf. Ser. Mater. Sci. Eng.* **2016**, *149*, 012035, doi:10.1088/1757-899X/149/1/012035.

313. Singh, R.; Singh, S. Development of Nylon Based FDM Filament for Rapid Tooling Application. *J. Inst. Eng. Ser. C* **2014**, *95*, 103–108, doi:10.1007/s40032-014-0108-2.

314. Washington State University Fundamentals of Direct-Ink-Writing Available online: https://labs.wsu.edu/mpml/projects/ (accessed on Nov 21, 2020).

315. Chimene, D.; Lennox, K.K.; Kaunas, R.R.; Gaharwar, A.K. Advanced Bioinks for 3D Printing: A Materials Science Perspective. *Ann. Biomed. Eng.* **2016**, *44*, 2090–2102, doi:10.1007/s10439-016-1638-y.

316. Liu, J.; Erol, O.; Pantula, A.; Liu, W.; Jiang, Z.; Kobayashi, K.; Chatterjee, D.; Hibino, N.; Romer, L.H.; Kang, S.H.; et al. Dual-Gel 4D Printing of Bioinspired Tubes. *ACS Appl. Mater. Interfaces* **2019**, *11*, 8492–8498, doi:10.1021/acsami.8b17218.

317. Liu, Z.; Yao, P. Injectable shear-thinning xanthan gum hydrogel reinforced by mussel-inspired secondary crosslinking. *RSC Adv.* **2015**, *5*, 103292–103301, doi:10.1039/C5RA17246B.

318. Jiang, Z.; Erol, O.; Chatterjee, D.; Xu, W.; Hibino, N.; Romer, L.H.; Kang, S.H.; Gracias, D.H. Direct Ink Writing of Poly(tetrafluoroethylene) (PTFE) with Tunable Mechanical Properties. *ACS Appl. Mater. Interfaces* **2019**, *11*, 28289–28295, doi:10.1021/acsami.9b07279.

319. Siqueira, G.; Kokkinis, D.; Libanori, R.; Hausmann, M.K.; Gladman, A.S.; Neels, A.; Tingaut, P.; Zimmermann, T.; Lewis, J.A.; Studart, A.R. Cellulose Nanocrystal Inks for 3D Printing of Textured Cellular Architectures. *Adv. Funct. Mater.* **2017**, *27*, 1604619, doi:10.1002/adfm.201604619.

320. Murphy, S. V.; Atala, A. 3D bioprinting of tissues and organs. *Nat. Biotechnol.* **2014**, *32*, 773–785, doi:10.1038/nbt.2958.

321. Kruth, J.-P.; Vandenbroucke, B.; Vaerenbergh, J.; Mercelis, P. Benchmarking of different SLS/SLM processes as Rapid Manufacturing techniques. *IEEE Electron Device Lett.* **2005**, *10*.

322. Tiwari, S.K.; Pande, S.; Agrawal, S.; Bobade, S.M. Selection of selective laser sintering materials for different applications. *Rapid Prototyp. J.* **2015**, *21*, 630–648, doi:10.1108/RPJ-03-2013-0027.

323. Amado, A.; Schmid, M.; Wegener, K. Simulation of warpage induced by non-isothermal crystallization of co-polypropylene during the SLS proceb. *AIP Conf. Proc.* **2015**, *1664*, doi:10.1063/1.4918509.

324. Zhu, W.; Yan, C.; Shi, Y.; Wen, S.; Liu, J.; Shi, Y. Investigation into mechanical and microstructural properties of polypropylene manufactured by selective laser sintering in comparison with injection molding counterparts. *Mater. Des.* **2015**, *82*, 37–45, doi:10.1016/j.matdes.2015.05.043.

325. Zhang, X.; Fan, W.; Liu, T. Fused deposition modeling 3D printing of polyamide-based composites and its applications. *Compos. Commun.* **2020**, *21*, 100413, doi:10.1016/j.coco.2020.100413.

326. Peng, X.; Zhang, M.; Guo, Z.; Sang, L.; Hou, W. Investigation of processing parameters on tensile performance for FDM-printed carbon fiber reinforced polyamide 6 composites. *Compos. Commun.* **2020**, *22*, 100478, doi:10.1016/j.coco.2020.100478.

327. Shi, Y.; Wang, Y.; Chen, J.; Huang, S. Experimental investigation into the selective laser sintering of high-impact polystyrene. *J. Appl. Polym. Sci.* **2008**, *108*, 535–540, doi:10.1002/app.27686.

328. Zeng, Z.; Deng, X.; Cui, J.; Jiang, H.; Yan, S.; Peng, B. Improvement on Selective Laser Sintering and Post-Processing of Polystyrene. *Polymers (Basel).* **2019**, *11*, 956, doi:10.3390/polym11060956.

329. Schmidt, M.; Pohle, D.; Rechtenwald, T. Selective Laser Sintering of PEEK. *CIRP Ann.* **2007**, *56*, 205–208, doi:10.1016/j.cirp.2007.05.097.

330. Wiria, F.E.; Leong, K.F.; Chua, C.K.; Liu, Y. Poly-ε-caprolactone/hydroxyapatite for tissue engineering scaffold fabrication via selective laser sintering. *Acta Biomater.* **2007**, *3*, 1–12, doi:10.1016/j.actbio.2006.07.008.

331. Williams, J.M.; Adewunmi, A.; Schek, R.M.; Flanagan, C.L.; Krebsbach, P.H.; Feinberg, S.E.; Hollister, S.J.; Das, S. Bone tissue engineering using polycaprolactone scaffolds fabricated via selective laser sintering. *Biomaterials* **2005**, *26*, 4817–4827, doi:10.1016/j.biomaterials.2004.11.057.

332. Diermann, S.H.; Lu, M.; Edwards, G.; Dargusch, M.; Huang, H. In vitro degradation of a unique porous PHBV scaffold manufactured using selective laser sintering. *J. Biomed. Mater. Res. Part A* **2019**, *107*, 154–162, doi:10.1002/jbm.a.36543.

333. Song, B.; Dong, S.; Liao, H.; Coddet, C. Manufacture of Fe–Al cube part with a sandwich structure by selective laser melting directly from mechanically mixed Fe and Al powders. *Int. J. Adv. Manuf. Technol.* **2013**, *69*, 1323–1330, doi:10.1007/s00170-013-5121-8.

334. Abd-Elghany, K.; Bourell, D.L. Property evaluation of 304L stainless steel fabricated by selective laser melting. *Rapid Prototyp. J.* **2012**, *18*, 420–428, doi:10.1108/13552541211250418.

335. Gu, D.; Hagedorn, Y.-C.; Meiners, W.; Meng, G.; Batista, R.J.S.; Wissenbach, K.; Poprawe, R. Densification behavior, microstructure evolution, and wear performance of selective laser melting processed commercially pure titanium. *Acta Mater.* **2012**, *60*, 3849–3860, doi:10.1016/j.actamat.2012.04.006.

336. Liu, Y.J.; Li, S.J.; Wang, H.L.; Hou, W.T.; Hao, Y.L.; Yang, R.; Sercombe, T.B.; Zhang, L.C. Microstructure, defects and mechanical behavior of beta-type titanium porous structures manufactured by electron beam melting and selective laser melting. *Acta Mater.* **2016**, *113*, 56–67, doi:10.1016/j.actamat.2016.04.029.

337. Vilaro, T.; Colin, C.; Bartout, J.D.; Nazé, L.; Sennour, M. Microstructural and mechanical approaches of

the selective laser melting process applied to a nickel-base superalloy. *Mater. Sci. Eng. A* **2012**, *534*, 446–451, doi:10.1016/j.msea.2011.11.092.

338. Rickenbacher, L.; Etter, T.; Hövel, S.; Wegener, K. High temperature material properties of IN738LC processed by selective laser melting (SLM) technology. *Rapid Prototyp. J.* **2013**, *19*, 282–290, doi:10.1108/13552541311323281.

339. Prashanth, K.G.; Scudino, S.; Klauss, H.J.; Surreddi, K.B.; Löber, L.; Wang, Z.; Chaubey, A.K.; Kühn, U.; Eckert, J. Microstructure and mechanical properties of Al–12Si produced by selective laser melting: Effect of heat treatment. *Mater. Sci. Eng. A* **2014**, *590*, 153–160, doi:10.1016/j.msea.2013.10.023.

340. Gu, D.; Wang, H.; Chang, F.; Dai, D.; Yuan, P.; Hagedorn, Y.C.; Meiners, W. Selective laser melting additive manufacturing of TiC/AlSi10Mg bulk-form nanocomposites with tailored microstructures and properties. *Phys. Procedia* **2014**, *56*, 108–116, doi:10.1016/j.phpro.2014.08.153.

341. Bertrand, P.; Bayle, F.; Combe, C.; Goeuriot, P.; Smurov, I. Ceramic components manufacturing by selective laser sintering. *Appl. Surf. Sci.* **2007**, *254*, 989–992, doi:10.1016/j.apsusc.2007.08.085.

342. Bates, J. VAT Photopolymerisation Available online: https://www.lboro.ac.uk/research/amrg/about/the7categoriesofadditivemanufacturing/vatphotopolymerisation/ (accessed on Nov 22, 2020).

343. All3DP What Is Material Jetting? – 3D Printing Simply Explained Available online: https://all3dp.com/2/what-is-material-jetting-3d-printing-simply-explained/#:~:text=Material jetting (MJ) is one,to the 2D inkjet process. (accessed on Nov 21, 2020).

344. Ge, Q.; Sakhaei, A.H.; Lee, H.; Dunn, C.K.; Fang, N.X.; Dunn, M.L. Multimaterial 4D Printing with Tailorable Shape Memory Polymers. *Sci. Rep.* **2016**, *6*, 31110, doi:10.1038/srep31110.

345. Boydston, A.J.; Cao, B.; Nelson, A.; Ono, R.J.; Saha, A.; Schwartz, J.J.; Thrasher, C.J. Additive manufacturing with stimuli-responsive materials. *J. Mater. Chem. A* **2018**, *6*, 20621–20645, doi:10.1039/C8TA07716A.

346. Zhang, B.; Li, S.; Hingorani, H.; Serjouei, A.; Larush, L.; Pawar, A.A.; Goh, W.H.; Sakhaei, A.H.; Hashimoto, M.; Kowsari, K.; et al. Highly stretchable hydrogels for UV curing based high-resolution multimaterial 3D printing. *J. Mater. Chem. B* **2018**, *6*, 3246–3253, doi:10.1039/c8tb00673c.

347. Patel, D.K.; Sakhaei, A.H.; Layani, M.; Zhang, B.; Ge, Q.; Magdassi, S. Highly Stretchable and UV Curable Elastomers for Digital Light Processing Based 3D Printing. *Adv. Mater.* **2017**, *29*, 1606000, doi:10.1002/adma.201606000.

348. Tibbits, S. 4D Printing. *Archit. Des.* **2014**, *84*, 116–121, doi:10.1002/ad.1710.

349. Shanjani, Y.; Pan, C.C.; Elomaa, L.; Yang, Y. A novel bioprinting method and system for forming hybrid tissue engineering constructs. *Biofabrication* **2015**, *7*, 045008, doi:10.1088/1758-5090/7/4/045008.

350. Coats, A.L.; Harrison, J.P.; Hay, J.S.; Ramos, M.J. Stereolithography resins and methods 2005.

351. Grigorian, L. 3D printers and photocurable polymer and resin based feedstocks for 3D printers 2019.

352. Dougherty, T.K.; Elias, W.E.; Thelander, T.C.; Bhavnani, M.N. Investment casting method and pattern material comprising thermally-collapsible expanded microspheres 1995.

353. Lee, J.S. Photo-curable resin compositions and method of using the same in three-dimensional printing for manifacturing artificial teeth and denture base 2014.

354. McNair, O.D.; Janisse, A.P.; Krzeminski, D.E.; Brent, D.E.; Gould, T.E.; Rawlins, J.W.; Savin, D.A. Impact properties of thiol-ene networks. *ACS Appl. Mater. Interfaces* **2013**, *5*, 11004–11013, doi:10.1021/am403238g.

355. McNair, O.D.; Brent, D.P.; Sparks, B.J.; Patton, D.L.; Savin, D.A. Sequential Thiol Click Reactions: Formation of Ternary Thiourethane/Thiol–Ene Networks with Enhanced Thermal and Mechanical Properties. *ACS Appl. Mater. Interfaces* **2014**, *6*, 6088–6097, doi:10.1021/am405138e.

356. Esfandiari, P.; Ligon, S.C.; Lagref, J.J.; Frantz, R.; Cherkaoui, Z.; Liska, R. Efficient stabilization of thiol-ene formulations in radical photopolymerization. *J. Polym. Sci. Part A Polym. Chem.* **2013**, *51*, 4261–4266, doi:10.1002/pola.26848.

357. Ellson, G.; Wang, W.; Zhang, Y. Thiol-Ene Printable Resins for Inkjet 3D Printing 2020.

358. Uzcategui, A.C.; Muralidharan, A.; Ferguson, V.L.; Bryant, S.J.; McLeod, R.R. Understanding and Improving Mechanical Properties in 3D printed Parts Using a Dual-Cure Acrylate-Based Resin for Stereolithography. *Adv. Eng. Mater.* **2018**, *20*, 1800876, doi:10.1002/adem.201800876.

359. Baur, C.; Askin, A.; Cook, D.; Giocondi, J.; Skiles, A.J.; Sullivan, S.; Kniffel, R.; Siemon, J.T. SLA Resins and Methods of Making and Using the Same 2017.

360. Akutsu, M.; Nakayashiki, T.; Tachikawa, H.; Ohkawa, K.; Chikaoka, S. Energy Beam Curable Epoxy Resin Composition, Stereolithographic Resin Composition and Stereolithographic Method 1999.

361. Wang, D.; Kaya, K.; Garra, P.; Fouassier, J.P.; Graff, B.; Yagci, Y.; Lalevée, J. Sulfonium salt based charge transfer complexes as dual thermal and photochemical polymerization initiators for composites and 3D printing. *Polym. Chem.* **2019**, *10*, 4690–4698, doi:10.1039/c9py00913b.

362. Topa, M.; Hola, E.; Galek, M.; Petko, F.; Pilch, M.; Popielarz, R.; Morlet-Savary, F.; Graff, B.; Laleveé, J.; Ortyl, J. One-component cationic photoinitiators based on coumarin scaffold iodonium salts as highly sensitive photoacid generators for 3D printing IPN photopolymers under visible LED sources. *Polym. Chem.* **2020**, *11*, 5261–5278, doi:10.1039/d0py00677g.

363. Ligon, S.C.; Liska, R.; Stampfl, J.; Gurr, M.; Mülhaupt, R. Polymers for 3D Printing and Customized Additive Manufacturing. *Chem. Rev.* **2017**, *117*, 10212–10290, doi:10.1021/acs.chemrev.7b00074.

364. Andrzejewska, E.; Zych-Tomkowiak, D.; Andrzejewski, M.; Hug, G.L.; Marciniak, B. Heteroaromatic Thiols as Co-initiators for Type II Photoinitiating Systems Based on Camphorquinone and Isopropylthioxanthone. *Macromolecules* **2006**, *39*, 3777–3785, doi:10.1021/ma060240k.

365. Fouassier, J.P.; Allonas, X.; Lalevée, J.; Dietlin, C. Photoinitiators for Free Radical Polymerization Reactions. In *Photochemistry and Photophysics of Polymeric Materials*; Allen, N.S., Ed.; 2010 ISBN 978-0-470-13796-3.

366. Jasinski, F.; Zetterlund, P.B.; Braun, A.M.; Chemtob, A. Photopolymerization in dispersed systems. *Prog. Polym. Sci.* **2018**, *84*, 47–88, doi:10.1016/j.progpolymsci.2018.06.006.

367. Messe, L.; Chapelat, C. Curable composition 2008.

368. Kowsari, K.; Akbari, S.; Wang, D.; Fang, N.X.; Ge, Q. High-Efficiency High-Resolution Multimaterial Fabrication for Digital Light Processing-Based Three-Dimensional Printing. *3D Print. Addit. Manuf.* **2018**, *5*, 185–193, doi:10.1089/3dp.2018.0004.

369. Taormina, G.; Sciancalepore, C.; Bondioli, F.; Messori, M. Special Resins for Stereolithography: In Situ Generation of Silver Nanoparticles. *Polymers (Basel).* **2018**, *10*, 212, doi:10.3390/polym10020212.

370. Mu, Q.; Wang, L.; Dunn, C.K.; Kuang, X.; Duan, F.; Zhang, Z.; Qi, H.J.; Wang, T. Digital light processing 3D printing of conductive complex structures. *Addit. Manuf.* **2017**, *18*, 74–83, doi:10.1016/j.addma.2017.08.011.

371. Wang, F.; Chong, Y.; Wang, F.K.; He, C. Photopolymer resins for luminescent three-dimensional printing. *J. Appl. Polym. Sci.* **2017**, *134*, 1–8, doi:10.1002/app.44988.

372. Fantino, E.; Chiappone, A.; Roppolo, I.; Manfredi, D.; Bongiovanni, R.; Pirri, C.F.; Calignano, F. 3D Printing of Conductive Complex Structures with in Situ Generation of Silver Nanoparticles. *Adv. Mater.* **2016**, *28*, 3712–3717, doi:10.1002/adma.201505109.

373. Zolfagharifard, E. When science is stylish: Designer uses 3D printing to create a range of accessories that is taking the fashion world by storm Available online: https://www.dailymail.co.uk/sciencetech/article-2384802/Catherine-Wales-uses-3D-printing-create-range-accessories-taking-fashion-world-storm.html (accessed on Jul 15, 2019).

374. Kim, S.; Seong, H.; Her, Y.; Chun, J. A study of the development and improvement of fashion products using a FDM type 3D printer. *Fash. Text.* **2019**, *6*, 9, doi:10.1186/s40691-018-0162-0.

375. Pei, E.; Shen, J.; Watling, J. Direct 3D printing of polymers onto textiles: experimental studies and applications. *Rapid Prototyp. J.* **2015**, *21*, 556–571, doi:10.1108/RPJ-09-2014-0126.

376. Gross, B.C.; Erkal, J.L.; Lockwood, S.Y.; Chen, C.; Spence, D.M. Evaluation of 3D Printing and Its Potential Impact on Biotechnology and the Chemical Sciences. *Anal. Chem.* **2014**, *86*, 3240–3253, doi:10.1021/ac403397r.

377. Lu, C.; Wang, C.; Yu, J.; Wang, J.; Chu, F. Two-Step 3 D-Printing Approach toward Sustainable, Repairable, Fluorescent Shape-Memory Thermosets Derived from Cellulose and Rosin. *ChemSusChem* **2020**, *13*, 893–902, doi:10.1002/cssc.201902191.

378. Sutton, J.T.; Rajan, K.; Harper, D.P.; Chmely, S.C. Lignin-Containing Photoactive Resins for 3D Printing by Stereolithography. *ACS Appl. Mater. Interfaces* **2018**, *10*, 36456–36463, doi:10.1021/acsami.8b13031.

379. Palaganas, N.B.; Mangadlao, J.D.; de Leon, A.C.C.; Palaganas, J.O.; Pangilinan, K.D.; Lee, Y.J.; Advincula, R.C. 3D Printing of Photocurable Cellulose Nanocrystal Composite for Fabrication of

Complex Architectures via Stereolithography. *ACS Appl. Mater. Interfaces* **2017**, *9*, 34314–34324, doi:10.1021/acsami.7b09223.

380. Becker, J.; Lange, A.; Fabarius, J.; Wittmann, C. Top value platform chemicals: Bio-based production of organic acids. *Curr. Opin. Biotechnol.* **2015**, *36*, 168–175, doi:10.1016/j.copbio.2015.08.022.

381. Willke, T.; Vorlop, K.D. Biotechnological production of itaconic acid. *Appl. Microbiol. Biotechnol.* **2001**, *56*, 289–295, doi:10.1007/s002530100685.

382. Kumar, S.; Krishnan, S.; Samal, S.K.; Mohanty, S.; Nayak, S.K. Itaconic acid used as a versatile building block for the synthesis of renewable resource-based resins and polyesters for future prospective: a review. *Polym. Int.* **2017**, *66*, 1349–1363, doi:10.1002/pi.5399.

383. Winkler, M.; Lacerda, T.M.; Mack, F.; Meier, M.A.R. Renewable Polymers from Itaconic Acid by Polycondensation and Ring-Opening-Metathesis Polymerization. *Macromolecules* **2015**, *48*, 1398–1403, doi:10.1021/acs.macromol.5b00052.

384. Barrett, D.G.; Merkel, T.J.; Luft, J.C.; Yousaf, M.N. One-step syntheses of photocurable polyesters based on a renewable resource. *Macromolecules* **2010**, *43*, 9660–9667, doi:10.1021/ma1015424.

385. DataIntelo *The Global Itaconic Acid Market by Applications (Synthetic Latex, Superabsorbent Polymers, Chelant Dispersant Agents, Unsaturated Polyester Resins, Methyl Methacrylate, and Detergent Builders) and Regions (Asia Pacific, North America, Latin America, Europ*; 2019;

386. Lim, H.-W.; Cassidy, T.; Cassidy, T.D. Application Research of 3D Printing Technology on Dress Forms. *Int. J. Eng. Technol.* **2017**, *9*, 78–83, doi:10.7763/IJET.2017.V9.949.

387. Lim, K.S.; Levato, R.; Costa, P.F.; Castilho, M.D.; Alcala-Orozco, C.R.; van Dorenmalen, K.M.A.; Melchels, F.P.W.; Gawlitta, D.; Hooper, G.J.; Malda, J.; et al. Bio-resin for high resolution lithography-based biofabrication of complex cell-laden constructs. *Biofabrication* **2018**, *10*, 034101, doi:10.1088/1758-5090/aac00c.

388. Biebl, H.; Menzel, K.; Zeng, A.P.; Deckwer, W.D. Microbial production of 1,3-propanediol. *Appl. Microbiol. Biotechnol.* **1999**, *52*, 289–97.

389. Kaur, G.; Srivastava, A.K.; Chand, S. Advances in biotechnological production of 1,3-propanediol. *Biochem. Eng. J.* **2012**, *64*, 106–118, doi:10.1016/j.bej.2012.03.002.

390. Ciriminna, R.; Pina, C. Della; Rossi, M.; Pagliaro, M. Understanding the glycerol market. *Eur. J. Lipid Sci. Technol.* **2014**, *116*, 1432–1439, doi:10.1002/ejlt.201400229.

391. Fache, M.; Darroman, E.; Besse, V.; Auvergne, R.; Caillol, S.; Boutevin, B. Vanillin, a promising biobased building-block for monomer synthesis. *Green Chem.* **2014**, *16*, 1987–1998, doi:10.1039/c3gc42613k.

392. Gong, H.; Beauchamp, M.; Perry, S.; Woolley, A.T.; Nordin, G.P. Optical approach to resin formulation for 3D printed microfluidics. *RSC Adv.* **2015**, *5*, 106621–106632, doi:10.1039/C5RA23855B.

393. Somisetti, V.; Allauddin, S.; Narayan, R.; Raju, K.V.S.N. Synthesis of a novel glycerol based B3-type monomer and its application in hyperbranched polyester urethane-urea coatings. *RSC Adv.* **2015**, *5*, 74003–74011, doi:10.1039/c5ra11712g.

394. Kim, Y.; Watanabe, H.; Kim, B.K.; Seu, Y.B. Chemo-biological preparation of the chiral building block (R)-4-acetoxy-2-methyl-1-butanol using Pseudomonas putida. *Tetrahedron Asymmetry* **2011**, *22*, 1658–1661, doi:10.1016/j.tetasy.2011.09.019.

395. Alizadehgharib, S.; Östberg, A.-K.; Dahlgren, U. Effects of the methacrylate/acrylate monomers HEMA, TEGDMA, DEGDA, and EMA on the immune system. *Clin. Exp. Dent. Res.* **2017**, *3*, 227–234, doi:10.1002/cre2.93.

396. Yoshii, E. Cytotoxic effects of acrylates and methacrylates. *J. Biomed. Mater. Res.* **1997**, *37*, 517–524, doi:0021-9304/97/040517-08.

397. Mokry, J.; Karbanova, J.; Lukas, J.; Paleckova, V.; Dvorankova, B. Biocompatibility of HEMA Copolymers Designed for Treatment of CNS Diseases with Polymer-Encapsulated Cells. *Biotechnol. Prog.* **2000**, *16*, 897–904, doi:10.1021/bp000113m.

398. Zhang, Y.; Chu, D.; Zheng, M.; Kissel, T.; Agarwal, S. Biocompatible and degradable poly(2-hydroxyethyl methacrylate) based polymers for biomedical applications. *Polym. Chem.* **2012**, *3*, 2752, doi:10.1039/c2py20403g.

399. Johnson, R.P.; Jeong, Y.-I.; Choi, E.; Chung, C.-W.; Kang, D.H.; Oh, S.-O.; Suh, H.; Kim, I. Biocompatible Poly(2-hydroxyethyl methacrylate)-b-poly(L-histidine) Hybrid Materials as pH-Sensitive Intracellular Anticancer Drug Delivery. *Adv. Funct. Mater.* **2012**, *22*, 1058–1068,

doi:10.1002/adfm.201102756.

400. Zhang, K.; Woodruff, A.P.; Xiong, M.; Zhou, J.; Dhande, Y.K. A synthetic metabolic pathway for production of the platform chemical isobutyric acid. *ChemSusChem* **2011**, *4*, 1068–1070, doi:10.1002/cssc.201100045.

401. Pereira, B.; Zhang, H.; De Mey, M.; Lim, C.G.; Li, Z.J.; Stephanopoulos, G. Engineering a novel biosynthetic pathway in Escherichia coli for production of renewable ethylene glycol. *Biotechnol. Bioeng.* **2016**, *113*, 376–383, doi:10.1002/bit.25717.

402. Wang, Y.; Xian, M.; Feng, X.; Liu, M.; Zhao, G. Biosynthesis of ethylene glycol from d-xylose in recombinant escherichia coli. *Bioengineered* **2018**, *9*, 233–241, doi:10.1080/21655979.2018.1478489.

403. Liu, H.; Ramos, K.R.M.; Valdehuesa, K.N.G.; Nisola, G.M.; Lee, W.K.; Chung, W.J. Biosynthesis of ethylene glycol in Escherichia coli. *Appl. Microbiol. Biotechnol.* **2013**, *97*, 3409–3417, doi:10.1007/s00253-012-4618-7.

404. Le Nôtre, J.; Witte-van Dijk, S.C.M.; van Haveren, J.; Scott, E.L.; Sanders, J.P.M. Synthesis of Bio-Based Methacrylic Acid by Decarboxylation of Itaconic Acid and Citric Acid Catalyzed by Solid Transition-Metal Catalysts. *ChemSusChem* **2014**, *7*, 2712–2720, doi:10.1002/cssc.201402117.

405. Voet, V.S.D.; Strating, T.; Schnelting, G.H.M.; Dijkstra, P.; Tietema, M.; Xu, J.; Woortman, A.J.J.; Loos, K.; Jager, J.; Folkersma, R. Biobased Acrylate Photocurable Resin Formulation for Stereolithography 3D Printing. *ACS Omega* **2018**, *3*, 1403–1408, doi:10.1021/acsomega.7b01648.

406. Lim, D.; Morris, P.C. Polymerization Inhibitors 1986.

407. Fouassier, J.P.; Morlet-Savary, F.; Lalevée, J.; Allonas, X.; Ley, C. Dyes as photoinitiators or photosensitizers of polymerization reactions. *Materials (Basel).* **2010**, *3*, 5130–5142, doi:10.3390/ma3125130.

408. Cantrell, J.; Rohde, S.; Damiani, D.; Gurnani, R.; DiSandro, L.; Anton, J.; Young, A.; Jerez, A.; Steinbach, D.; Kroese, C.; et al. Experimental Characterization of the Mechanical Properties of 3D Printed ABS and Polycarbonate Parts. In *Advancement of Optical Methods in Experimental Mechanics*; Lamberti, L., Lin, M.-T., Furlong, C., Sciammarella, C., Reu, P.L., Sutton, M.A., Eds.; Conference Proceedings of the Society for Experimental Mechanics Series; Springer International Publishing: Cham, 2019; Vol. 3 ISBN 978-3-319-97480-4.

409. Textile Innovation Knowledge Platform Available online: http://www.tikp.co.uk/knowledge/material-functionality/luminescence/ (accessed on Aug 13, 2019).

410. Auger, A.; De Sousa Nobre, S.; Getto, D. Method for Marking a Textile Thread with a Fluorescent Element, Textile Thread Produced by the Marking Method, and Use of Said Textile Thread for Weaving an Item of Clothing 2017.

411. Sanz Casado, J.M.; Alcaraz De La Osa, R.; Moreno Garcia, F.; Gonzalez Fernandez, F.; Saiz Vega, J.M.; Aspeei, B.; Gonzalez, R.; Martinez, Z. Method for Manufacturing Long Lasting Phorsphorescent Fabrics Obtained from the same 2017.

412. Lowry, M.S.; Hudson, W.R.; Pascal, R. a; Bernhard, S. Accelerated luminophore discovery through combinatorial synthesis Supporting Information. *J. Am. Chem. Soc.* **2004**, *126*, 14129–14135, doi:10.1021/JA047156+.

413. Matteucci, E.; Baschieri, A.; Mazzanti, A.; Sambri, L.; Ávila, J.; Pertegás, A.; Bolink, H.J.; Monti, F.; Leoni, E.; Armaroli, N. Anionic Cyclometalated Iridium(III) Complexes with a Bis-Tetrazolate Ancillary Ligand for Light-Emitting Electrochemical Cells. *Inorg. Chem.* **2017**, *56*, 10584–10595, doi:10.1021/acs.inorgchem.7b01544.

414. Dumur, F.; Gigmes, D.; Fouassier, J.-P.; Lalevée, J. Organic Electronics: An El Dorado in the Quest of New Photocatalysts for Polymerization Reactions. *Acc. Chem. Res.* **2016**, *49*, 1980–1989, doi:10.1021/acs.accounts.6b00227.

415. Huo, H.; Shen, X.; Wang, C.; Zhang, L.; Röse, P.; Chen, L.-A.; Harms, K.; Marsch, M.; Hilt, G.; Meggers, E. Asymmetric photoredox transition-metal catalysis activated by visible light. *Nature* **2014**, *515*, 100–103, doi:10.1038/nature13892.

416. Gualandi, A.; Matteucci, E.; Monti, F.; Baschieri, A.; Armaroli, N.; Sambri, L.; Cozzi, P.G. Photoredox radical conjugate addition of dithiane-2-carboxylate promoted by an iridium(III) phenyl-tetrazole complex: a formal radical methylation of Michael acceptors. *Chem. Sci.* **2017**, *8*, 1613–1620, doi:10.1039/C6SC03374A.

417. Laftah, W.A.; Hashim, S.; Ibrahim, A.N. Polymer Hydrogels: A Review. *Polym. Plast. Technol. Eng.* **2011**,

50, 1475–1486, doi:10.1080/03602559.2011.593082.

418. Dragan, E.S. Design and applications of interpenetrating polymer network hydrogels. A review. *Chem. Eng. J.* **2014**, *243*, 572–590, doi:10.1016/j.cej.2014.01.065.

419. Guo, Y.; Bae, J.; Fang, Z.; Li, P.; Zhao, F.; Yu, G. Hydrogels and Hydrogel-Derived Materials for Energy and Water Sustainability. *Chem. Rev.* **2020**, *120*, 7642–7707, doi:10.1021/acs.chemrev.0c00345.

420. Hennink, W.E.; van Nostrum, C.F. Novel crosslinking methods to design hydrogels. *Adv. Drug Deliv. Rev.* **2012**, *64*, 223–236, doi:10.1016/j.addr.2012.09.009.

421. Malkoch, M.; Vestberg, R.; Gupta, N.; Mespouille, L.; Dubois, P.; Mason, A.F.; Hedrick, J.L.; Liao, Q.; Frank, C.W.; Kingsbury, K.; et al. Synthesis of well-defined hydrogel networks using Click chemistry. *Chem. Commun.* **2006**, 2774, doi:10.1039/b603438a.

422. Jungst, T.; Smolan, W.; Schacht, K.; Scheibel, T.; Groll, J. Strategies and Molecular Design Criteria for 3D Printable Hydrogels. *Chem. Rev.* **2016**, *116*, 1496–1539, doi:10.1021/acs.chemrev.5b00303.

423. Talebian, S.; Mehrali, M.; Taebnia, N.; Pennisi, C.P.; Kadumudi, F.B.; Foroughi, J.; Hasany, M.; Nikkhah, M.; Akbari, M.; Orive, G.; et al. Self-Healing Hydrogels: The Next Paradigm Shift in Tissue Engineering? *Adv. Sci.* **2019**, *6*, 1801664, doi:10.1002/advs.201801664.

424. Taylor, D.L.; in het Panhuis, M. Self-Healing Hydrogels. *Adv. Mater.* **2016**, *28*, 9060–9093, doi:10.1002/adma.201601613.

425. Wool, R.P. Self-healing materials: a review. *Soft Matter* **2008**, *4*, 400, doi:10.1039/b711716g.

426. Talebian, S.; Mehrali, M.; Taebnia, N.; Pennisi, C.P.; Kadumudi, F.B.; Foroughi, J.; Hasany, M.; Nikkhah, M.; Akbari, M.; Orive, G.; et al. Self-Healing Hydrogels: The Next Paradigm Shift in Tissue Engineering? *Adv. Sci.* **2019**, *1801664*, 1801664, doi:10.1002/advs.201801664.

427. Wang, M.X.; Chen, Y.M.; Gao, Y.; Hu, C.; Hu, J.; Tan, L.; Yang, Z. Rapid Self-Recoverable Hydrogels with High Toughness and Excellent Conductivity. *ACS Appl. Mater. Interfaces* **2018**, *10*, 26610–26617, doi:10.1021/acsami.8b06567.

428. Jacob, R.S.; Ghosh, D.; Singh, P.K.; Basu, S.K.; Jha, N.N.; Das, S.; Sukul, P.K.; Patil, S.; Sathaye, S.; Kumar, A.; et al. Self healing hydrogels composed of amyloid nano fibrils for cell culture and stem cell differentiation. *Biomaterials* **2015**, *54*, 97–105, doi:10.1016/j.biomaterials.2015.03.002.

429. Miyamae, K.; Nakahata, M.; Takashima, Y.; Harada, A. Self-Healing, Expansion-Contraction, and Shape-Memory Properties of a Preorganized Supramolecular Hydrogel through Host-Guest Interactions. *Angew. Chemie Int. Ed.* **2015**, *54*, 8984–8987, doi:10.1002/anie.201502957.

430. Li, G.; Zhang, H.; Fortin, D.; Xia, H.; Zhao, Y. Poly(vinyl alcohol)–Poly(ethylene glycol) Double-Network Hydrogel: A General Approach to Shape Memory and Self-Healing Functionalities. *Langmuir* **2015**, *31*, 11709–11716, doi:10.1021/acs.langmuir.5b03474.

431. Long, T.; Li, Y.; Fang, X.; Sun, J. Salt-Mediated Polyampholyte Hydrogels with High Mechanical Strength, Excellent Self-Healing Property, and Satisfactory Electrical Conductivity. *Adv. Funct. Mater.* **2018**, *28*, 1804416, doi:10.1002/adfm.201804416.

432. Ding, F.; Wu, S.; Wang, S.; Xiong, Y.; Li, Y.; Li, B.; Deng, H.; Du, Y.; Xiao, L.; Shi, X. A dynamic and self-crosslinked polysaccharide hydrogel with autonomous self-healing ability. *Soft Matter* **2015**, *11*, 3971–3976, doi:10.1039/C5SM00587F.

433. Wei, Z.; Zhao, J.; Chen, Y.M.; Zhang, P.; Zhang, Q. Self-healing polysaccharide-based hydrogels as injectable carriers for neural stem cells. *Sci. Rep.* **2016**, *6*, 37841, doi:10.1038/srep37841.

434. Liu, H.; Sui, X.; Xu, H.; Zhang, L.; Zhong, Y.; Mao, Z. Self-Healing Polysaccharide Hydrogel Based on Dynamic Covalent Enamine Bonds. *Macromol. Mater. Eng.* **2016**, *301*, 725–732, doi:10.1002/mame.201600042.

435. Antony, R.; Arun, T.; Manickam, S.T.D. A review on applications of chitosan-based Schiff bases. *Int. J. Biol. Macromol.* **2019**, *129*, 615–633, doi:10.1016/j.ijbiomac.2019.02.047.

436. Zhang, Y.; Tao, L.; Li, S.; Wei, Y. Synthesis of Multiresponsive and Dynamic Chitosan-Based Hydrogels for Controlled Release of Bioactive Molecules. *Biomacromolecules* **2011**, *12*, 2894–2901, doi:10.1021/bm200423f.

437. Tseng, T.C.; Tao, L.; Hsieh, F.Y.; Wei, Y.; Chiu, I.M.; Hsu, S.H. An injectable, self-healing hydrogel to repair the central nervous system. *Adv. Mater.* **2015**, *27*, 3518–3524, doi:10.1002/adma.201500762.

438. Cheng, K.-C.; Huang, C.-F.; Wei, Y.; Hsu, S. Novel chitosan–cellulose nanofiber self-healing hydrogels

to correlate self-healing properties of hydrogels with neural regeneration effects. *NPG Asia Mater.* **2019**, *11*, 25, doi:10.1038/s41427-019-0124-z.

439. Qu, J.; Zhao, X.; Ma, P.X.; Guo, B. pH-responsive self-healing injectable hydrogel based on N-carboxyethyl chitosan for hepatocellular carcinoma therapy. *Acta Biomater.* **2017**, *58*, 168–180, doi:10.1016/j.actbio.2017.06.001.

440. Wei, Z.; Yang, J.H.; Liu, Z.Q.; Xu, F.; Zhou, J.X.; Zrínyi, M.; Osada, Y.; Chen, Y.M. Novel biocompatible polysaccharide-based self-healing hydrogel. *Adv. Funct. Mater.* **2015**, *25*, 1352–1359, doi:10.1002/adfm.201401502.

441. Huang, W.; Wang, Y.; Huang, Z.; Wang, X.; Chen, L.; Zhang, Y.; Zhang, L. On-Demand Dissolvable Self-Healing Hydrogel Based on Carboxymethyl Chitosan and Cellulose Nanocrystal for Deep Partial Thickness Burn Wound Healing. *ACS Appl. Mater. Interfaces* **2018**, *10*, 41076–41088, doi:10.1021/acsami.8b14526.

442. Lü, S.; Gao, C.; Xu, X.; Bai, X.; Duan, H.; Gao, N.; Feng, C.; Xiong, Y.; Liu, M. Injectable and Self-Healing Carbohydrate-Based Hydrogel for Cell Encapsulation. *ACS Appl. Mater. Interfaces* **2015**, *7*, 13029–13037, doi:10.1021/acsami.5b03143.

443. Loebel, C.; Rodell, C.B.; Chen, M.H.; Burdick, J.A. Shear-thinning and self-healing hydrogels as injectable therapeutics and for 3D-printing. *Nat. Protoc.* **2017**, *12*, 1521–1541, doi:10.1038/nprot.2017.053.

444. Highley, C.B.; Rodell, C.B.; Burdick, J.A. Direct 3D Printing of Shear-Thinning Hydrogels into Self-Healing Hydrogels. *Adv. Mater.* **2015**, *27*, 5075–5079, doi:10.1002/adma.201501234.

445. Ashraf, S.; Park, H.K.; Park, H.; Lee, S.H. Snapshot of phase transition in thermoresponsive hydrogel PNIPAM: Role in drug delivery and tissue engineering. *Macromol. Res.* **2016**, *24*, 297–304, doi:10.1007/s13233-016-4052-2.

446. Gan, J.; Guan, X.X.; Zheng, J.; Guo, H.; Wu, K.; Liang, L.; Lu, M. Biodegradable, thermoresponsive PNIPAM-based hydrogel scaffolds for the sustained release of levofloxacin. *RSC Adv.* **2016**, *6*, 32967–32978, doi:10.1039/c6ra03045a.

447. Maia, J.; Carvalho, R.A.; Coelho, J.F.J.; Simões, P.N.; Gil, M.H. Insight on the periodate oxidation of dextran and its structural vicissitudes. *Polymer (Guildf).* **2011**, *52*, 258–265, doi:10.1016/j.polymer.2010.11.058.

448. Sun, B.; Hou, Q.; Liu, Z.; Ni, Y. Sodium periodate oxidation of cellulose nanocrystal and its application as a paper wet strength additive. *Cellulose* **2015**, *22*, 1135–1146, doi:10.1007/s10570-015-0575-5.

449. Kristiansen, K.A.; Potthast, A.; Christensen, B.E. Periodate oxidation of polysaccharides for modification of chemical and physical properties. *Carbohydr. Res.* **2010**, *345*, 1264–1271, doi:10.1016/j.carres.2010.02.011.

450. Guthrie, R.D. The "Dialdehydes" from the Periodate Oxidation of Carbohydrates. In; Shirley Instilute, Manchester, England, 1962; Vol. 34, pp. 105–158.

451. Rahmat, D.; Rahman, F.A.R.; Nurhidayati, L.; Laksmitawati, D.R. Synthesis and Characterization oh Hydroxypropylcellulose-cysteamine conjugate as a novel cationic tiomer with lipophilic properties. *Int. J. Appl. Pharm.* **2019**, *11*, 222, doi:10.22159/ijap.2019v11i1.30014.

452. Li, Q.; Sritharathikhun, P.; Motomizu, S. Development of Novel Reagent for Hantzsch Reaction for the Determination of Formaldehyde by Spectrophotometry and Fluorometry. *Anal. Sci.* **2007**, *23*, 413–417, doi:10.2116/analsci.23.413.

453. Buschmann, H.-J.; Dutkiewicz, E.; Knoche, W. The Reversible Hydration of Carbonyl Compounds in Aqueous Solution Part II: The Kinetics of the Keto/Gem-diol Transition. *Berichte der Bunsengesellschaft für Phys. Chemie* **1982**, *86*, 129–134, doi:10.1002/bbpc.19820860208.